Development of a Wind Tunnel Test Apparatus for Horizontal Axis Wind Turbine Rotor Testing

by

Michael K. McWilliam

A thesis
presented to the University of Waterloo
in fulfillment of the
thesis requirement for the degree of
Master of Applied Science
in
Mechanical Engineering

Waterloo, Ontario, Canada, 2008

I hereby declare that I am the sole author of this thesis. This is a true copy of the thesis, including any required final revisions, as accepted by my examiners.
I understand that my thesis may be made electronically available to the public.

Michael K. McWilliam

Abstract

Currently, wind energy presents an excellent opportunity to satisfy the growing demand without the supply and environmental problems associated with conventional energy. The engineering in wind turbines is not fully mature. There are still phenomenon, particularly dynamic stall, that cannot accurately be modeled or controlled. Dynamic stall contributes to fatigue stress and premature failure in many turbine components. The three dimensionality of dynamic stall makes these structures unique for wind turbines. Currently, flow visualization of dynamic stall on a wind turbine rotor has not been achieved. These visualizations can reveal a lot about the structures that contribute to dynamic stall.

Particle Image Velocimetry (PIV) is a powerful experimental technique that can take multiple non-intrusive flow measurements simultaneously of planar flow. Using high-speed cameras time resolved PIV can reveal the transient development of a given flow field. This technique is ideally suited to gain a better understanding of dynamic stall. A custom wind turbine is being built at the University of Waterloo to allow such measurements on the blade. A high speed camera is mounted on the hub and will take measurements within the rotating domain. Mirrors are used so that laser illumination rotates with the blade. The wind turbine will operate in controlled conditions provided by a large wind tunnel. High speed pressure data acquisition will be used in conjunction with PIV to get an understanding of the forces associated with the flow structures. Computational fluid dynamics was used to size the rotor within the wind tunnel. Laser based measurements required special considerations for stiffness.

Many revealing experiments will be made possible by this apparatus. First, the flow structures responsible for the various forces can be identified. Quantitative measurements of the flow field will identify the development of the stall vortex. The quantified flow structures can be used verify and improve models. The high spatial resolution of PIV can map the three dimensional flow structure in great detail. The experimental apparatus is independent of the blade geometry, as such multiple blades can be used to identify the effect of blade geometry. Finally flow control research in the field of aviation can be applied to control dynamic stall.

Acknowledgements

I would like to give thanks to my supervisor David Johnson. Dr. Johnson has been very generous in providing guidance and giving me many opportunities to showcase my work and network. I would like to thank William Thompson for keeping me grounded and maintaining my interests in wind energy. I thank Kaya McGregor for helping me realize my passion for renewable energy. Another valuable support for me is Elsie Petch. Elsie has been an amazing support always behind me. Finally I would like to thank my mother for helping me when I needed it most, ensuring that I can go forward and accomplish my dreams. The five of you have been integral in my success.

Contents

List of Tables

List of Figures

Nomenclature

DSV	Dynamic Stall Vortex
HAWT	Horizontal Axis Wind Turbine
NREL	National Renewable Energy Laboratories
PIV	Particle Image Velocimetry
TSR	Tip Speed Ratio
A	Frontal area of the turbine $[m^2]$
c	Chord of the airfoil $[m]$
C_p	Coefficient of power [-]
C_t	Coefficient of thrust [-]
D	Turbine diameter $[m]$
F	A force in a free body diagram $[N]$
F_T	Thrust force $[N]$
H	The height of the tower $[m]$
h	Turbine height $[m]$
L_n	The length of member in the tower base sub assembly $[m]$

$\hat{n}$	Unit normal vector $[m]$
N	The number of blades [-]
P	Power $[W]$
Q	Torque $[Nm]$
q	Volumetric flow $[m^3/s]$
s	distant along a path $[m]$
T	Thickness of the momentum sink volume $[m]$
U	Turbine blade speed $[m/s]$
V	Wind speed $[m/s]$
V_r	Velocity at the rotor $[m/s]$
V_θ	Angular wind velocity $[m/s]$
W	Wind speed relative to the blade $[m/s]$
α	The angle of attack, defined as the angle between the relative wind velocity (W) and the chord line $[rad]$
λ	Tip speed ratio [-]
ν	Kinematic viscosity $[Pas]$
ω	Angular speed $[rad/s]$
Φ	gap width ratio in a Savonius turbine [-]
ρ	Density of air $[kg/m^3]$
σ	Solidity [-]
υ	Blockage correction [-]

χ	Momentum sink per unit volume $[N/m^3]$
ψ	Savonius blade orientation $[rad]$
Re	Reynolds Number [-]

Chapter 1

Introduction

Today, the demand for energy is growing along with concerns over the many problems associated with conventional sources. Hydro-carbon fuel combustion has been a major source of energy for the western world for many years now. The availability of conventional sources is dwindling, alternative sources have higher costs and their supply is also subject to dwindle in the long term. The widespread use of combustion based energy sources, and the pollution associated with them, has resulted in some serious challenges for today's society [91]. Accordingly, there is a great demand for additional energy sources that are clean and renewable.

Wind energy is one such energy source that has little environmental impact, little adverse health effects, negligible security concerns, and is completely renewable. Currently wind energy is the fastest growing source of energy. As of 2006, there was 20,622 MW of installed wind energy capacity in Germany alone [110]. In Denmark, wind energy makes up 21.7% of the electricity consumed [8]. Wind energy has proven itself as a viable source. In Denmark and Germany, subsidy programs were required, to stimulate the installation of such a large wind energy capacity. As such, there is still a lot of work needed to develop the technology, so that it is cost competitive with conventional sources.

There are several areas for further development in the design of wind turbines. There are many opportunities to improve the mechanical, structural and electrical systems. The greatest potential for improvement, in both short and long term development, is in the field of aerodynamics [96]. Within this field, there are still ways turbines of similar size,

could extract more energy, however, many of these strategies increase the complexity and cost with only an incremental gain in performance. Improved aerodynamic understanding will likely yield the greatest benefits, by reducing the cost of wind energy, by minimizing some of the damaging forces generated in the blades. Wind turbine aerodynamics will be the main focus for research within this thesis.

A general discussion about wind turbine research, development and the technology is given in Appendix A. The Appendix summarizes the various turbine concepts and explains why the conventional horizontal axis wind turbines are most desirable. The major systems of a wind turbine are explained along with the associated development needs. Throughout the appendix, the effect and importance of aerodynamic development on the other areas of development is highlighted.

1.1 Review of Wind Turbine Aerodynamics

Within the field of aerodynamics there are still several separate areas of research. First, predicting aerodynamic performance is important for the design and engineering of wind turbine technology. Understanding the aerodynamics and structures in the wake are important for predicting rotor aerodynamics and flow conditions downstream. There are many active research areas in the flow about the blades, the flow at the tips is investigated to reduce noise, better airfoil prediction is dependent on improved understanding in rotational effects and stall delay, finally transient aerodynamics effects occur frequently in wind turbine operation. An extended discussion on all of these areas of aerodynamics is given in Appendix B.

One important area of unsteady aerodynamics is the effect of dynamic stall. This phenomenon is a source of damage on the blades and other components of the turbine. The apparatus under development in this thesis can be applied to many areas of aerodynamic research, however, the main focus is for research in dynamic stall. A detailed discussion of dynamic stall research in literature is given in Section 1.1.1.

There are too many deficiencies in wind turbine aerodynamic modeling, to improve the technology through studies based on computational results. It is widely recognized within literature, that experimental research is vital for improving aerodynamic understanding

[62, 85, 87, 77]. The challenges of wind turbine experimental work, is the biggest obstacle for wind turbine development. Overall, there are still several deficiencies in the information gained from experimental work. For an extended discussion refer to Appendix B. Primarily this thesis is focused on addressing these deficiencies. Section 1.1.2 discusses the details of how these can be addressed.

1.1.1 Dynamic Stall in Wind Turbine Aerodynamics

Dynamic stall can occur frequently when certain flow conditions arise, it is sensitive to yaw error and wind speed. Figure 1.1a shows how the rotor is misaligned with the wind when there is yaw error. This error, arises when the wind changes direction suddenly or there is error in the yaw orientation system. The yaw error will introduce an in-plane component to the wind, this alters the V_θ component at the blade when it is at the top or bottom. Depending on the angular direction and blade position, the additional V_θ component will be against the blade motion, and will reduce the angle of attack, see Figure 1.1b. When the blade moves to the opposite position, the additional V_θ component will be with the blade motion and increase the angle of attack, see Figure 1.1c. If the turbine is operating in high enough winds, that stall conditions are imminent, the blade will stall when the flow in Figure 1.1c occurs. Fully connected flow will resume, when the blade approaches the opposite position, and the conditions in Figure 1.1b develop. With the blade rotation, stall and flow reconnection will repeat periodically, this transient stall phenomenon is referred to as dynamic stall.

The National Renewable Energy Laboratory (NREL) Phase VI 'Unsteady Aerodynamics Experiment' results showed the forces on the blade as a result of dynamic stall. Figure 1.2 shows that the force can be triple the force expected in static stall conditions [77]. The dramatic increase in force is caused by the dynamic stall vortex, shown in Figure 1.3 [77]. Initially, it will form at the leading edge very small, eventually it will grow large enough to cover a majority of the suction surface. The dynamic stall vortex is a low pressure region covering a large area of the blade surface, resulting in the strong blade force. Once the recirculation region grows beyond the chord of the profile, it will break off and the airfoil will enter static stall conditions.

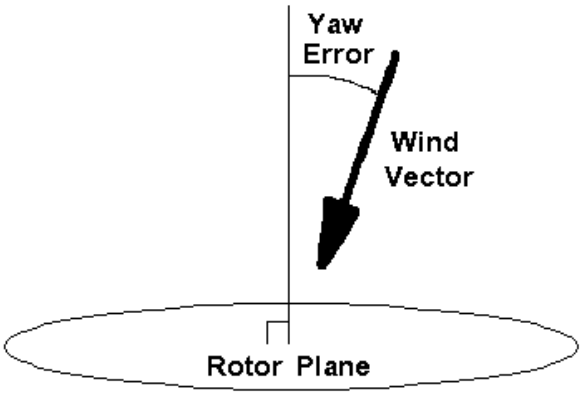

(a) Global Flow Geometry

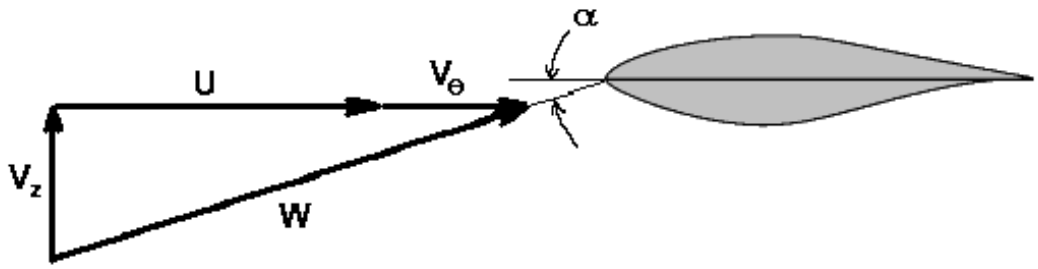

(b) Fully Connected Blade Flow Geometry

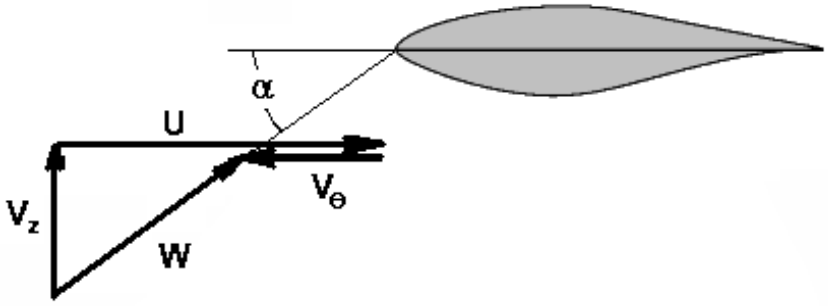

(c) Stalled Blade Flow Geometry

Figure 1.1: Wind Flow during Dynamic Stall

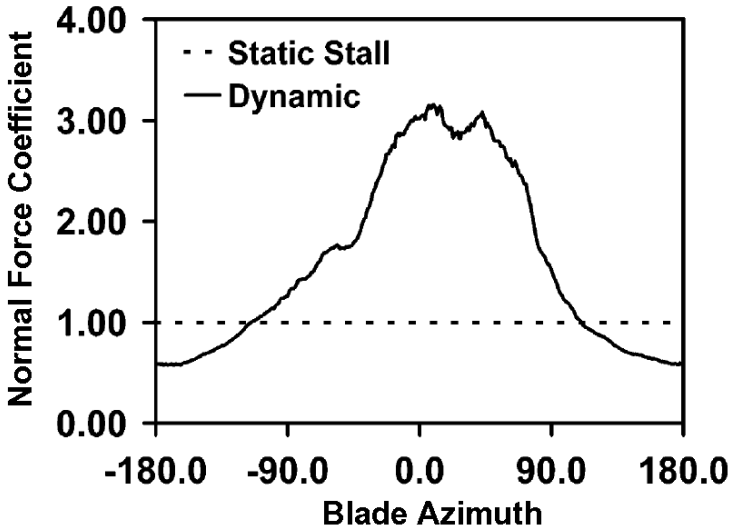

Figure 1.2: Forces on the Blade as a Result of Dynamic Stall [77]

Figure 1.3: Dynamic Stall Flow Visualization [77]

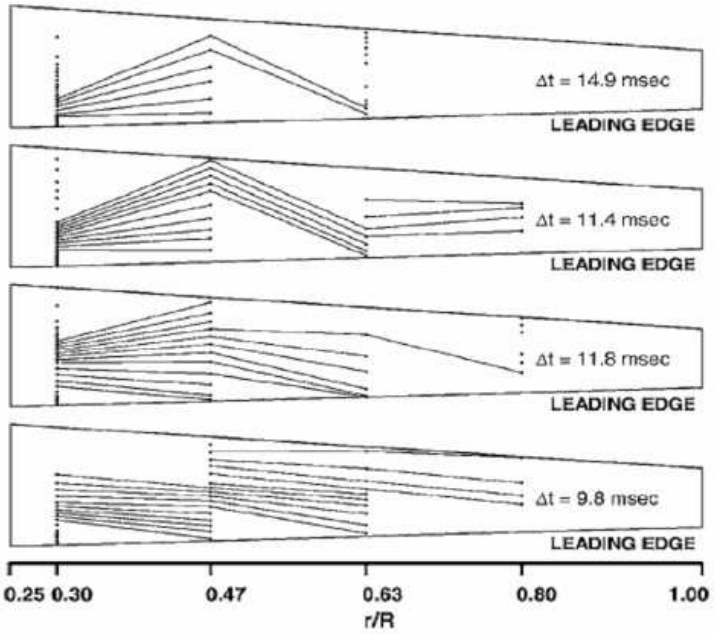

Figure 1.4: Three Dimensional Dynamic Stall Structure [73]

The results of experimental studies have shown increased complexity, with dynamic stall on wind turbines blades. The work given in Figure 1.3 was from a wing sections in two dimensional flows, on wind turbine blades there would be additional rotational effects. The work by Schreck et al. [73] has shown there are complex 3 dimensional structures, Figure 1.4. Tangler [94] extended the work of Schreck et al., using the circulation distribution, he gave evidence of a double horseshoe vortex structure, Figure 1.5. He argued that the trailing vorticity would suppress stall towards the root and promote it towards the tip. The three dimensional structure and the trailing vorticity associated with it, would have a significant effect on the aerodynamics throughout the entire blade.

Currently, no flow visualization similar to that shown in Figure 1.3, or velocimetry, has been collected in the rotating domain. The results of the NREL Phase VI 'Unsteady Aerodynamics Experiments' by Hand et al. [30] did not have sufficient spatial resolution to confirm the arguments of Tangler. The rotational effects are known to alter stall characteristics, however the spatial resolution limited the insights into what rotational effects

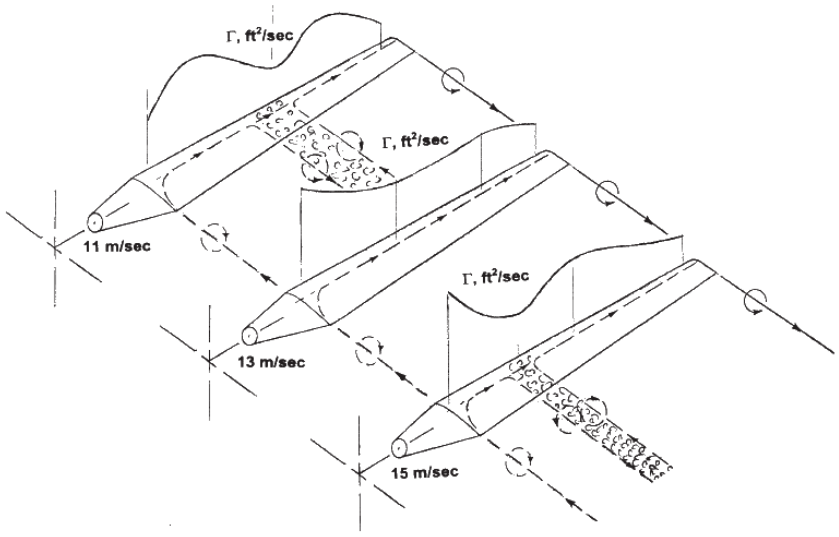

Figure 1.5: Possible Double Horseshoe Structure during Stall [94]

that could be recovered [72]. More investigations on the blade aerodynamics are required to confirm the arguments of Tangler and learn more about the role of rotation on dynamic stall structures.

1.1.2 Future Research Needs in Wind Turbine Aerodynamics

The deficiency in wind turbine aerodynamic measurements, call for a facility that can provide a long term program to continuously study wind turbines. The facility should be capable of accommodating multiple blade geometries, and needs to provide a controlled flow, so models can be accurately validated. Special attention is required to provide flow visualization and detailed measurements at the rotor blade, especially with increased resolution [78]. One experimental technique that could reveal many of the mysteries in blade aerodynamics is time resolved Particle Image Velocimetry (PIV).

Facilities are available at the University of Waterloo to provide a large controlled flow field. A flexible apparatus that can load a wind turbine rotor will allow multiple blades to be tested in this facility. Special care in design of the apparatus will allow advanced experimental techniques to be utilized. Having this apparatus in a University environment

will allow for long term research, in wind turbine aerodynamics. This will open up many opportunities to address many of the issues discussed above. The topic of this thesis is the design of an apparatus, capable of using advanced time resolved PIV on various wind turbine rotors.

1.2 Thesis Overview

A lot of the research performed on dynamic stall has relied on surface pressure measurements. Flow visualization and velocimetry is an ideal compliment to pressure data. One method ideal for collecting both types of data is laser PIV. The method has been proven for steady state two dimensional flows. Dynamic stall is a three dimensional transient phenomenon. The three dimensional structure of dynamic stall can be analyzed, by stacking the results from two dimensional sections. The transience of the flow field can be measured with time resolved PIV, or by taking phase averaged measurements. Before serious design could be initiated, the applicability of PIV for dynamic stall research, needed to be investigated. This was done by performing simple PIV experiments on Vertical Axis Wind Turbines (VAWT). The results and experience was used to determine the best equipment for dynamics stall research.

The data acquisition equipment available is not sufficient for experiments in dynamic stall research. As such, additional equipment is needed to perform the proper experiments. There are two systems needed, one for collecting surface pressure measurements, and another for collecting PIV data. The proposed experiment will analyze transient flow fields that occur in very short time periods. Thus it is important that high sampling rates can be achieved to accurately capture the events. Previous work in this area is limited, due to insufficient resolution, thus the data acquisition system needs to have many channels and high resolution.

Detailed measurements of this type are very difficult to achieve in the field. Thus a controlled environment from a wind tunnel will be utilized to create the flow fields. Wind tunnels introduce their own error, from the flow conditions at the boundaries of the test area. Walls tend to limit the flow expansion typically seen in nature, while shear layers promote flow expansion. To ensure that the wind tunnel experiments represent

environmental flows, commercial CFD codes were used to predict the flow within a wind turbine. The results of the wind tunnel models were compared with that of a turbine in an infinite flow field. The comparison showed the ideal rotor position and the largest rotor size acceptable for the wind tunnel.

Control of the rotor motion is necessary to reproduce turbine flows, this requires a system to provide and absorb torque to and from the rotor. A wind turbine rotor is designed to operate at specific rotational speeds at various wind speeds. Under a range of operating conditions a specific rotor will produce a range of torque. The torque response will also vary with rotor geometry. Special care is required, in the design of the torque supply and absorption system, to reproduce all the different operating conditions. The control of the torque can be achieved with either passive or active methods. Passive methods use internal inertia to limit short term speed variation, yet operator input is still required for long term compensation. Active methods employ closed loop feedback, to continuously adjust the torque, for constant speed operation.

Determination of the rotor size and location in the wind tunnel, along with the structure of the load device, allows for the mechanical design of the test apparatus itself. The test apparatus needs to accommodate the rotor and all the experimental equipment, yet also fit within existing wind tunnel facilities. The structural integrity of the wind turbine rotor and rig is very important. The blades and shaft were analyzed under both static and dynamic cases. The components were designed to keep the fundamental frequency above that of rotation, to avoid sympathetic vibrations. A high fundamental frequency is also associated with high stiffness, this is desirable when taking laser based measurements. As such the fundamental frequency was maximized for all other components that would hold laser optics. Static analysis was employed on all other components. Tight restrictions on maximum stress were placed on rotary components for fatigue and deflection considerations.

Chapter 2

Preliminary Experiments in Particle Image Velocimetry[1]

2.1 The purpose of the experiment

If laser Particle Image Velocimetry (PIV) is used to investigate dynamic stall in Horizontal Axis Wind Turbines (HAWT), preliminary experiments need to be conducted to evaluate the applicability of this technique. Vertical Axis Wind Turbines (VAWT) operate in a transient flow field that yield separation and strong vortices, similar to the flow of interest in HAWT's. Measuring the flow about a small VAWT was conducted, to determine whether the available equipment is capable of identifying key flow structures and whether any additional equipment is required.

Modern laser PIV techniques have been developed over the last 20 years, and continue today in advanced analysis techniques [100, 24]. One powerful technique uses the PIV data to find information about the pressure field. This information is necessary to understand the forces caused by various flow structures. There are several sophisticated methods for determining the pressure field. For the sake of evaluation, a simple approach based on finite difference methods was developed. The method was used to further understand

[1] A substantial portion of this Chapter appears in the literature. *International Journal of Green Energy*, 5:55–68, 2008 [51]

the capabilities of current PIV equipment and evaluate the applicability to pressure field determination.

2.1.1 VAWT Aerodynamics in literature

In a typical wind turbine design there are numerous design variables that must be considered in order to optimize the power output for a given wind regime. Savonius based VAWT are no exception and studies have been reported that consider various geometric and flow variables. A typical Savonius design consists of two or more vertical blades aligned with the rotating shaft (rotor) as shown in Figure 2.1 [67]. This study considers variants of the Savonius vertical axis wind turbine. Studies have been reported evaluating the overall performance of the rotor based on the average power and torque produced. One study considered the number of blades, the aspect ratio, the space between rotors and the tip speed ratio, allowing the optimum configuration to be known [7]. One issue with Savonius rotors is that the torque generated varies considerably with rotor orientation or phase angle. Typically the varying torque issue is resolved by stacking two rotors separated by 90 degrees [53]. A recent study evaluated the effect of twisted blades compared to straight blades, finding that small degrees of twist were effective, but greater degrees of twist reduced the overall performance [64]. A method to use particle tracking velocimetry (PTV) to determine the pressure forces and torque at several phase angles is described by Murai et al. [57], for a standard Savonius design. The work by Murai et al. revealed many details of the flow field about the Savonius rotor, showing that lift like forces contribute to the overall power of rotor.

These studies do not provide any details of the mechanism of energy extraction. Due to the geometrical arrangement, significant variations in torque and power are present for different orientations of the rotor. Flow visualization studies and circumferential pressure measurements are reported in Fujisawa [20]. That study and Blackwell et al. [7] report an optimum value of the ratio of the distance the blades overlap (gap) to the blade diameter (Φ) to be 0.15, see Figure 2.2a for the geometric convention for the gap and blade diameter. This overlap is reported to allow a Coanda-like flow to develop on the convex side of an advancing blade surface, essentially a curved wall jet. This allows a fluid jet to be directed onto the following blade where momentum transfer may take place. A low speed water

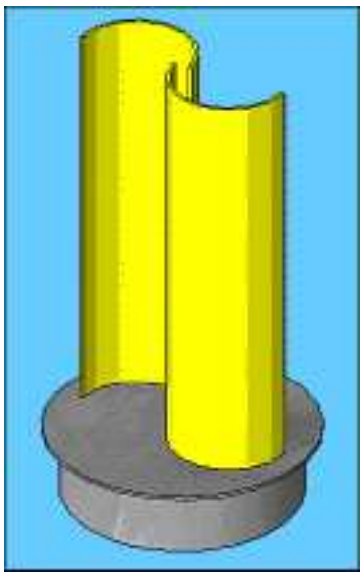

Figure 2.1: Typical Savonius Rotor

based study is reported by the same author using an early PIV system [21]. A numerical study is reported by Modi and Fernando for a rotor with a continuous blade and no overlap [55]. They report flow separation from the tips of the blades from a vertical position to ψ of 30 degrees past the vertical direction, see Figure 2.3.

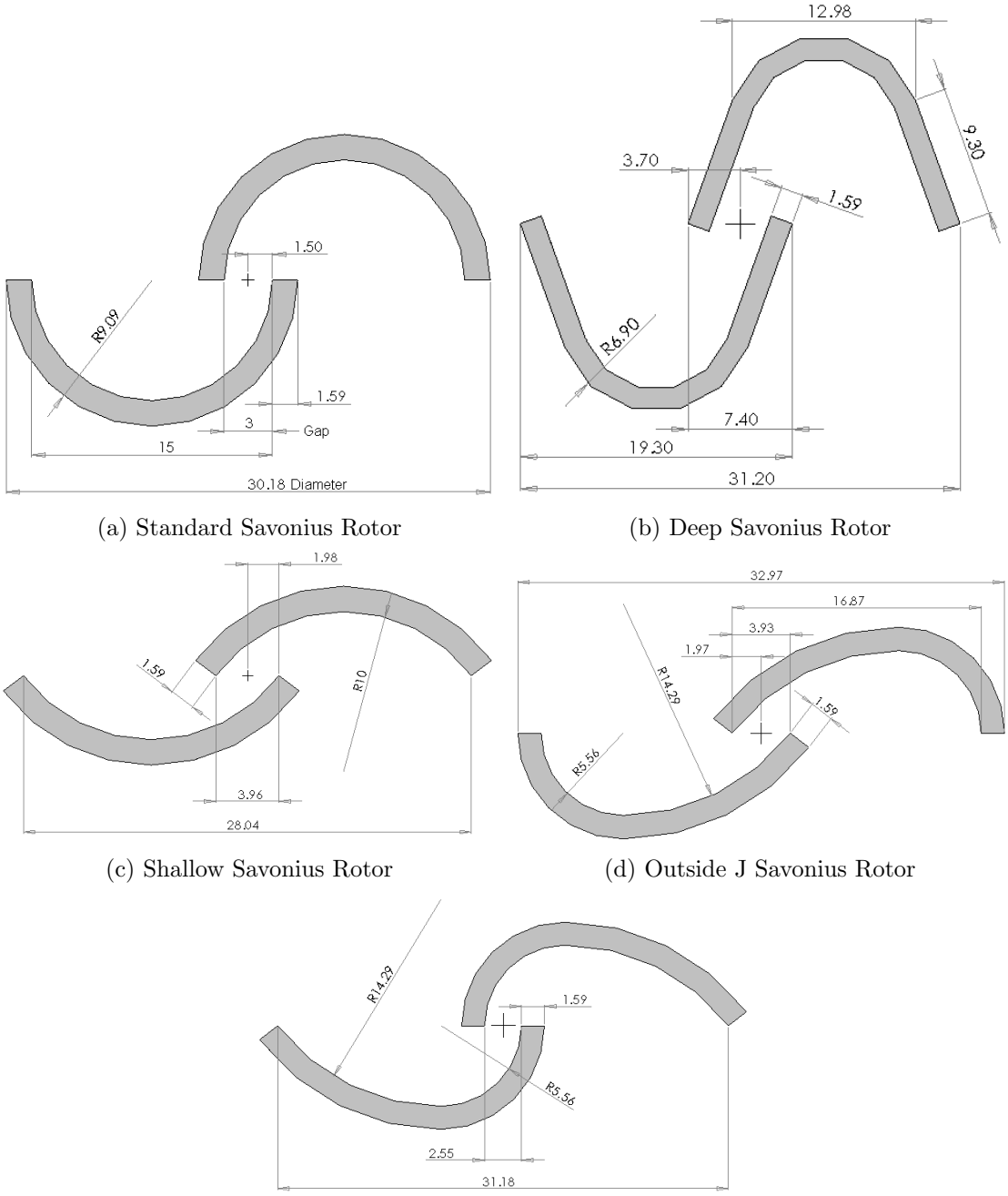

(a) Standard Savonius Rotor

(b) Deep Savonius Rotor

(c) Shallow Savonius Rotor

(d) Outside J Savonius Rotor

(e) Inside J Savonius Rotor

Figure 2.2: Geometry for a Various Test Rotors

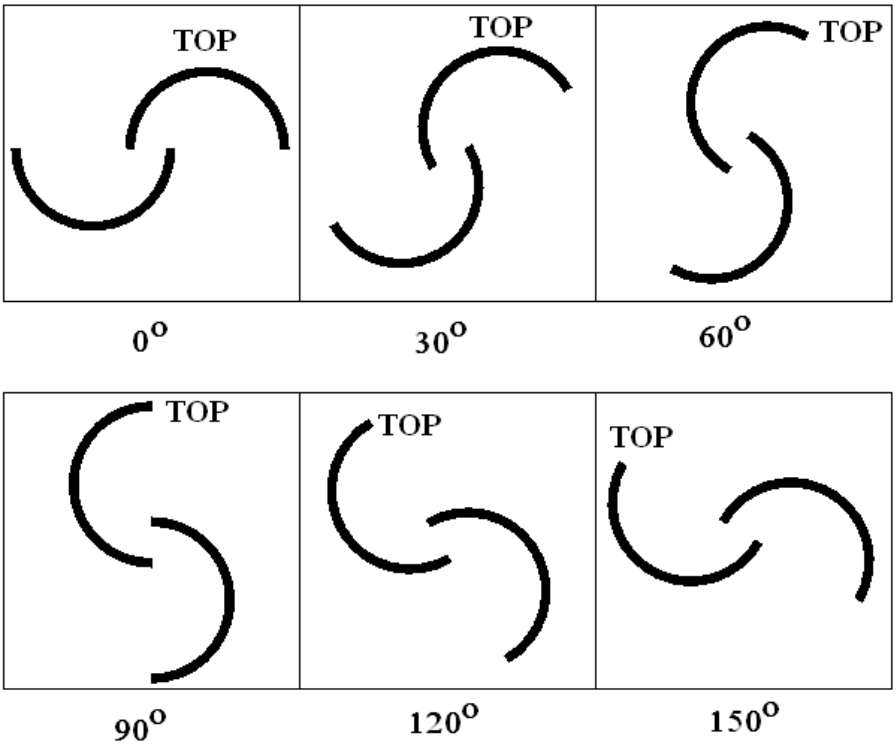

Figure 2.3: Angular Definition for Savonius Orientation

The work presented here attempts to further identify the complex flow structures around a Savonius wind turbine and other variants of that design. The structures were evaluated as a function of rotor orientation. In addition to identifying these structures, this study evaluated how variations in geometry affected these flow structures. Further analysis was applied to identify the role played by the gap between the rotor blades. The PIV technique was utilized as it allows non-intrusive simultaneous flow measurements on a plane. In this application of PIV the details of the flow structures and the flow around the turbine rotors were revealed.

2.2 The experimental set-up

2.2.1 Turbines

The test Savonius rotors had two blades fabricated from clear acrylic sheet with a constant overlap between them. Five different blade configurations were evaluated as shown in Figure 2.2. For these comparative studies some geometry and flow variables were fixed in order to make comparison with blade geometry variables. The overlap between the blades was fixed at the optimum value 0.15D based on previous studies [21] and the aspect ratio (h/D) was fixed at 4. In these studies, the rotor rotation speed ω was constant at 163 rad/s (1560 rpm) to give a tip speed ratio (TSR =V/U) of 0.8 nominally (variations in the blade design changed this value slightly). This value is consistent with the peak power production in other studies [79, 7]. Typical Reynolds numbers (VD/ν) for these model turbines are 6000 consistent with other studies [57]. For each rotor geometry, at least six constant phase orientations of the rotor were chosen. Figure 2.3 shows the different orientations and labels the blade that is referenced as the top blade.

2.2.2 Wind Tunnel

Uniform air flow was produced by a variable speed closed-circuit type wind tunnel. The working section was an acrylic test section 152mm x 152mm x 450mm. A photograph of the wind tunnel is shown in Figure 2.4. The turbine rotor to be tested was placed in the tunnel centre and 300 mm downstream of the nozzle exit. The blockage correction υ for complex

shapes given by Rae and Pope defined as Equation 2.1 was 0.039 [63]. No corrections were made to the velocities presented. Further details of the wind tunnel performance may be found in [90]. For the studies reported here the wind tunnel was run at a constant velocity of 3m/s (V) in the working section.

$$\upsilon = \frac{1 \text{ Model Frontal Area}}{4 \text{ Test Section Area}} \tag{2.1}$$

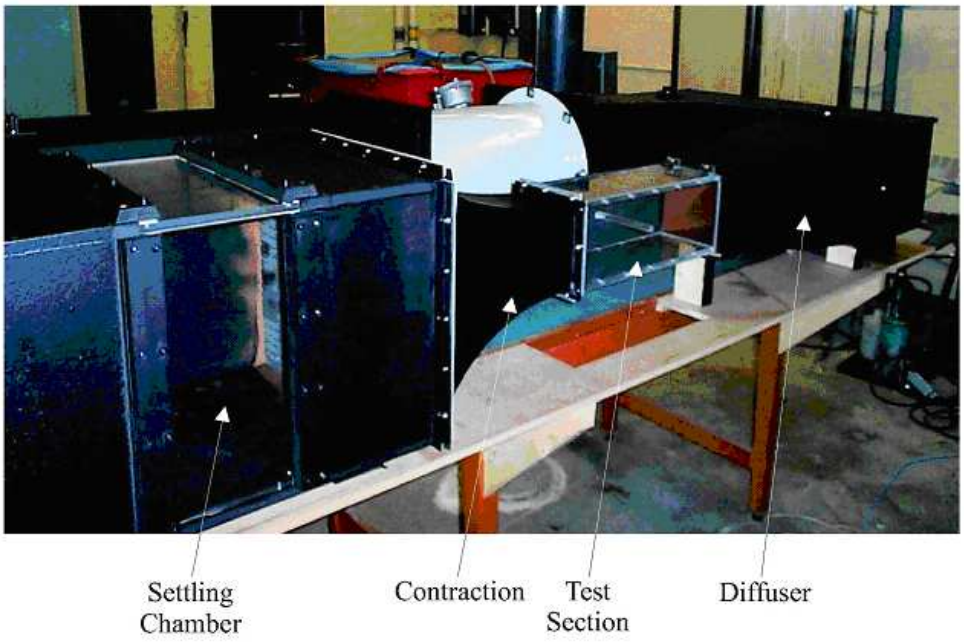

Figure 2.4: Small Closed Circuit Wind Tunnel

2.2.3 Particle Image Velocimetry

The PIV arrangement was designed for an unobstructed view of the flow within the transparent working section, as shown in Figure 2.5. The flow in the working section was illuminated with a 120mJ double-cavity 532 nm Nd:YAG laser capable of operating at 15 Hz with a pulse duration of 5 ns that created a light sheet 3 mm in thickness spanning the region of interest. A Kodak ES 1K x 1K CCD camera was used to capture the particle

images. It was equipped with a 108 mm, F/2.5 zoom lens. A field-of-view of approximately 100 x 100 mm was used. A 532 nm optical cut-off filter was attached to the lens to transmit only the laser wavelength light. The camera was positioned perpendicular to the laser sheet above the turbine and working section. It was mounted on a specially designed bench, which allowed movement in three axes for easy positioning. A custom designed optical trigger was connected to the turbine shaft to serve as a photo-gate trigger. This provided the once-per-revolution signal, which triggered the PIV data acquisition. With the trigger, it was possible to obtain a large number of instantaneous data at the same circumferential position of the turbine (phase average). The laser and CCD camera were linked through a Dantec Flowmap PIV 1100 processor. Vaporized mineral oil has been shown to follow airflow quite well and was used as the seeding medium. The smoke was introduced into the enclosure well upstream of the measurement region around the rotor. As well, the smoke was allowed to stabilize in the closed circuit wind tunnel before measurements were obtained. In all cases above, 500 image pairs were collected for each rotor orientation and the resultant velocity vectors were ensemble averaged at each position. Each test was repeated for at least three orientations of the rotor. Typical laser pulse separations ranged from 50 to 150 μs in order to size the particle displacements appropriately for the interrogation area size. The cross-correlation method with interrogation area of 32 x 32 pixels and 50% overlap was used to process the images to obtain the velocity vectors. This resulted in 62 x 62 vectors per vector map with a distance of approximately 1 mm between each vector. Peak validation with a correlation peak signal-to-noise ratio in the range of 1.2-1.5 was used to remove spurious vectors. Errors inherent in PIV velocity measurements are estimated to be of the order of 1% [105]. Individual vector maps were subsequently averaged to provide an averaged flow map and velocity statistics.

The individual rotors were mounted vertically in the wind tunnel in the centre of the working section. For the studies reported here, the laser light sheet was horizontal and passed through the acrylic blades at the mid height of the blade ($h/2$). The CCD camera was mounted above the wind tunnel.

A sample of one image with particle seeding is shown in Figure 2.6. The lines seen in the image are due to the reflection and refraction of the laser light due to the clear acrylic blades.

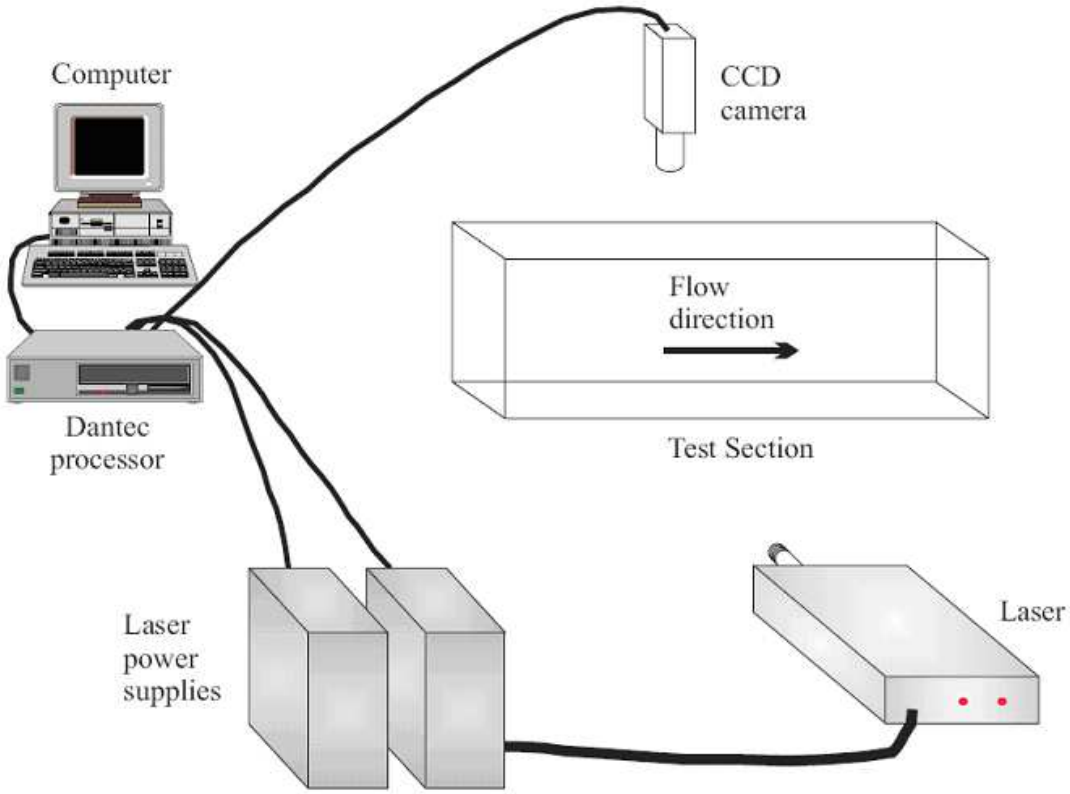

Figure 2.5: Schematic of Particle Image Velocimetry System

2.3 The results of the experiment

Velocity vector results for the standard design are shown in Figure 2.7 for six orientations of the rotor. Each vector plot represent the phase averaged velocity flow field from 500 individual velocity realization images. The phase averaged results show strong resemblance to each of the individual correlations indicating a stable, repeatable flow field. The number of vectors has been reduced by 2 in both X and Y directions to aid the presentation of the vectors. In all the Figures shown the blades are rotating in a counter-clockwise direction.

Figure 2.6: Sample Image from PIV

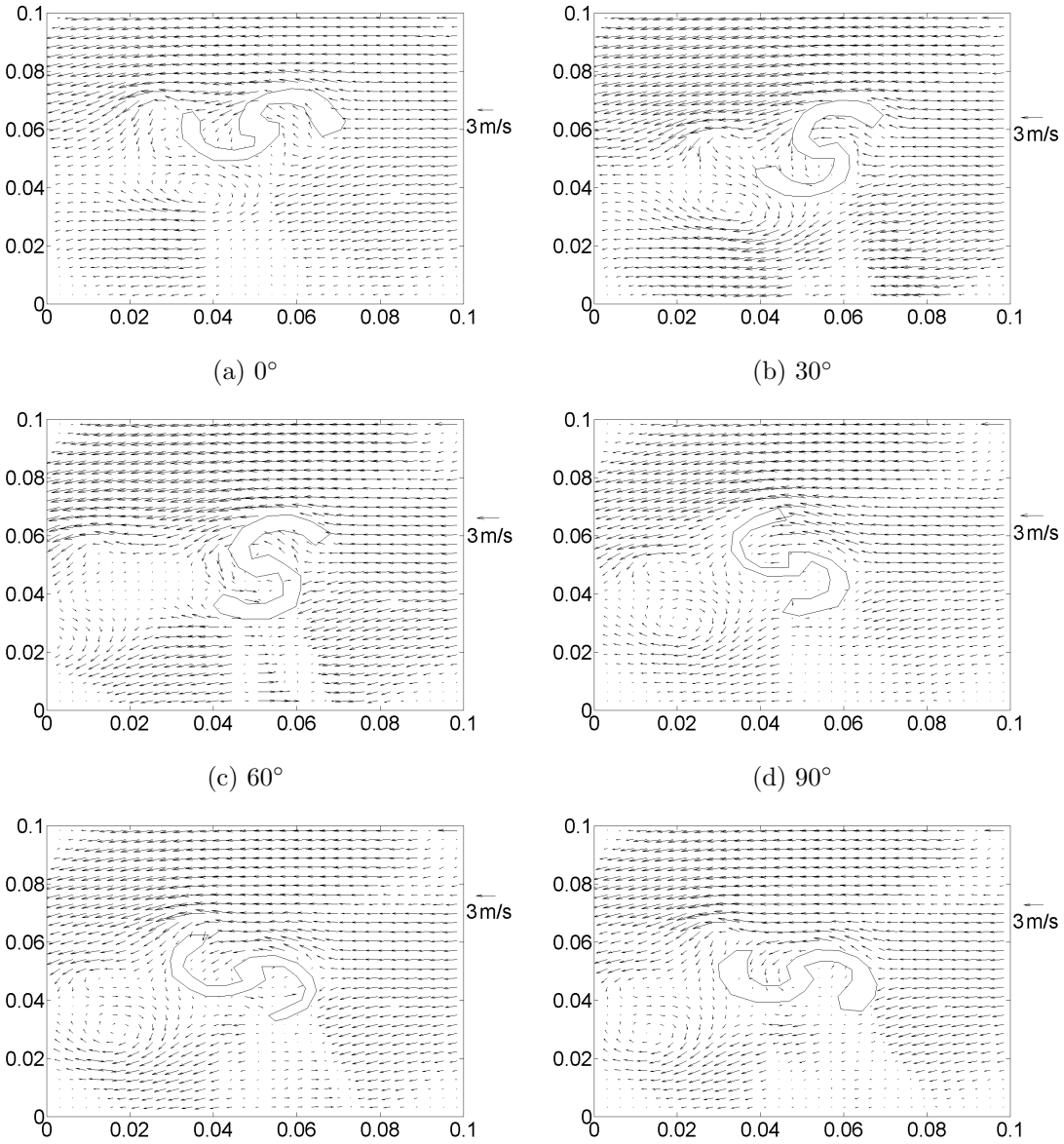

(a) 0°

(b) 30°

(c) 60°

(d) 90°

(e) 120°

(f) 150°

Figure 2.7: Vector Maps for the Standard Rotor

2.3.1 Standard Design

Figure 2.7 shows the flow over a standard Savonius rotor. At small phase angles the flow over the top blade is turned into the bottom blade. Figure 2.3 shows what blade is top and bottom at each orientation. At the trailing edge of the bottom rotor a vortex starts to form and eventually separates and convects downstream. At large phase angles the flow over the concave portion of the blade separates and is no longer turned into the bottom blade. As the top blade increases in phase angle more flow enters the convex section. A small degree of divergence forms as the top blade reaches 90 degrees. This may indicate that the gap between blades is insufficient. The laser entered the test section from the top of the Figures; shadows from the rotor distorted many of the results below the rotor. As such there are few conclusions about the flow directly below the blade. The wake of the bottom flow indicates that a second vortex forms and eventually separates and convects downstream.

Figure 2.7a through 2.7c and 2.7e through 2.7f shows flow acceleration over the top blade as indicated by increased flow velocity over the concave surface. This shows that there are lift-like forces on the blade particularly evident at the 30 and 60 degree orientations (Figure 2.7b and 2.7c). These results are consistent with Murai et al. where a peak lift coefficient was found at a 30 degree orientation [57]. Their results indicate a negative lift coefficient at 150 degrees and this would be consistent with the results presented here (120-150 degrees) as the acceleration over the bottom blade moving into the flow creates a force in the clockwise direction. Thus, the rotor does not operate purely with drag differential as the only contributing force. The flow at the trailing edge of the top blade follows the bottom blade. This suppresses flow separation until angles beyond 60 degrees as shown in Figure 2.7c. Figures 2.7a through 2.7f show that with each rotor revolution, two vortices are being shed from the blades. The first vortex is shed off the tip of the bottom blade at 0 degrees. The first vortex is much stronger than the second vortex suggesting a net transfer an angular momentum to the rotor. Shadows hide the exact phase angle when the second vortex is shed. The wake in Figure 2.7d shows that the second vortex is shed closely behind the first spatially. The first vortex is shed closer to the center of the wake, while the second is shed towards the outside. These results are qualitatively similar to

Angle [°]	Top Blade Flow $\left[\frac{m^2}{s}\right]$	Bottom Blade Flow $\left[\frac{m^2}{s}\right]$
0	NA	-0.0045
30	NA	-0.0043
60	0.0025	-0.0045
90	0.0007	NA
120	0.0020	NA
150	-0.0001	NA

Table 2.1: Flow into Convex Region of Standard Savonius Blade per Unit Height

the streamlines shown in Murai et al. obtained with spatio-temporal interpolation of PTV results [57]. Murai et al. only consider a standard design.

The flow into each of the convex sections of the blades was evaluated using the two-dimensional flow Equation 2.2 along a line from the inner tip of one blade to the outer tip of the opposite blade. The results are given in Table 2.1. The flow into the convex region of the bottom blade is always negative. The flow behind the bottom blade is following the blade and drawing more air through the gap. Previous work (Fujisawa, 1992) suggested that a Coanda flow is responsible for transferring momentum onto the bottom blade. The results here show that the apparent jet is really part of the wake of the bottom blade. The net flow out of the bottom blade shows that there is an inflow at the gap. Flow into the top blade shows that there is a net transfer of mass from the top blade to the bottom blade at nearly all phase angles. The flow at the gap would act to increase the pressure behind the bottom blade reducing the drag as the blade travels upwind. The error in mass balance at 60 degrees is likely due to shadows distorting the results along the small section of line integral.

$$q = \int \left(\vec{V} - \vec{\omega} \times \vec{r}\right) \cdot \hat{n} ds \tag{2.2}$$

2.3.2 The results of Alternate Turbine Geometries

Many of the same flow structures are present in modified rotors. There are small differences in each rotor, none of which are significant enough to change the major conclusions on the applicability of laser PIV techniques for dynamic stall research. For reference, the details are given in Appendix C.

2.4 Methods in extending Particle Image Velocimetry results

PIV results alone only give information about the speed of the flow. For dynamic stall research and other aerodynamic research the forces on an object are the primary interest. Laser PIV can become a much more powerful tool if force information could be derived from the velocimetry. The benefits of extending PIV data have prompted a lot of research into extending the methods [98, 100, 24, 101, 57]. Some of these techniques use control volume analysis to determine the forces, others attempt at determining the pressure field. Pressure field results can be extended further to find the overall force, knowing the pressure field has further benefits by identifying the dominant flow structures associated with the forces.

The dynamic stall flow field by nature is unsteady, stall being a viscous phenomenon, viscosity is expected to play a major role. Finally with the high Reynolds number associated with wind turbines operation turbulence is also expected to play a role. None of the techniques in literature account for all these effects, using the PIV techniques that will be applied to dynamic stall research. A more advanced and comprehensive technique similar to those of Murai et al. was applied to the PIV data collected for the vertical axis turbines [57]. The details of the method are given in Appendix D.

Overall, the methods were successful in identifying the expected pressure trends of the major structures. However there was a lot of noise in the final pressure solution. It is suspected that much of the noise is from poor resolution in the original data. The effect of Eularian terms, temporal terms and Reynolds stress terms were explored separately. The

Reynolds stress terms were highly sensitive to error, so multiple methods of evaluating these terms were also evaluated.

The investigation showed that high spatial and temporal resolution is very important for accurate pressure field determination. This is an important conclusion for selecting the PIV data acquisition system, high sampling rates at high resolution are important for force determination. Another important conclusion is the Reynolds stress sensitivity to noise. Different methods for evaluating this term showed varying degrees of sensitivity to noise, however it is very unlikely that any method will be perfectly insensitive. Further work is needed to improve these methods.

2.5 Summary of the preliminary experiment

Overall, the preliminary results show that laser PIV will be a powerful method in exploring wind turbine rotor flows. The velocimetry results can show many of the critical flow structures in a transient flow field. Further analysis showed that the results can be extended to give insight on the pressure field. The current equipment is not sufficient to collect pressure field data in irregular HAWT flows. The temporal resolution is too coarse to capture transient flows. Phase triggering can be used on regular flows however little can be done for irregular flows. The spatial resolution is sufficient to reveal many details of the flow. A new laser PIV system is needed to explore HAWT aerodynamics, 1 mega pixel resolution is acceptable, however sampling rates of kHz magnitude is mandatory. Issues with the Reynolds stress term in finding pressure have little dependency on the data acquisition. Resolving Reynolds stress issues will require further work on the methods themselves.

Chapter 3

Selection of Data Acquisition System

3.1 Types of Data to be Recorded

The primary focus for the apparatus is to collect information about flow physics at the blade. Here, the main areas of data are the pressure at the surface and the flow about the blade. Once integrated, information about pressure leads to the forces generated and all other critical information needed by engineers. Particle Image Velocimetry (PIV) can reveal a lot about what flow structures are creating specific pressure signals. It will also give vital information about the flow structures that occur in wind turbine aerodynamics. There is a large deficiency in flow visualization and velocimetry at the blades. Potentially there are new insights to be gained from detailed measurements at the blade.

Finally this equipment needs to be controlled and the information from the data acquisition needs to be downloaded. This is complicated given that all the equipment, except for the laser is mounted in the rotating domain. This adds unique criteria to the selection and demands that specialized equipment is used for the system. This chapter discusses alternatives and the final selection of each sub system. The first sub-system is the pressure acquisition system, then the PIV system, finally the computer used to control and access the data.

3.2 Pressure Data Acquisition System

3.2.1 Criteria for Pressure Data Acquisition

The formation and movement of a Dynamic Stall Vortex (DSV) is to be monitored with surface mounted pressure taps. Important parameters in specifying the pressure taps are the frequency of data collection and the physical spacing between pressure taps. There are no analytical models for the DSV. Empirical data presented by Schreck et al. were used to determine the physical characteristics of the DSV [78].

Pressure signals from a wind turbine experiment, that captured dynamic stall events, are given in Figure 3.1. Figure 3.2 shows the physical locations of the pressure taps [78]. The data gives the pressure with respect to the azimuth position of the blade. The reference states that the rotational speed of the blade is 71.6 RPM [78]. From this, the time can be determined between various azimuth positions. This in-turn allowed for various statistics to be determined.

Further data reduction was performed to determine the timing for the proposed experiment. The rotational speed for the University of Waterloo experiment is 2.8 times faster because the wind turbine rotor is 36% the size of the experimental rotor used in the work of Schreck et al. [78]. Thus, all the times of the Ames experiment are reduced by a factor of 2.8.

The pressure traces give three pieces of information. It first gives the period of the pressure spike from the DSV on the pressure signals. Second, it gives the time it takes for the DSV to traverse the entire blade section. Finally it gives the physical size of the DSV by pairing up pressure traces where the DSV spike end and starts at the same time. Red lines mark pressure trace pairs where the DSV starts and ends on Figure 3.1.

The width of the pressure spike determines the minimum frequency for sampling an individual pressure tap. For the experiment the expected average pressure spike period is 42ms while the smallest pressure spike period is 6.5ms. For four data points this corresponds to a frequency of 95Hz and 609Hz respectively. The traverse time determines the length of time required to capture one DSV event. That time is 102ms. The proposed PIV sampling frequency is 1000Hz. Thus, 102 image pairs are sufficient to capture a DSV event. Finally, the size of the DSV was determined with 4 pressure trace pairs. The size

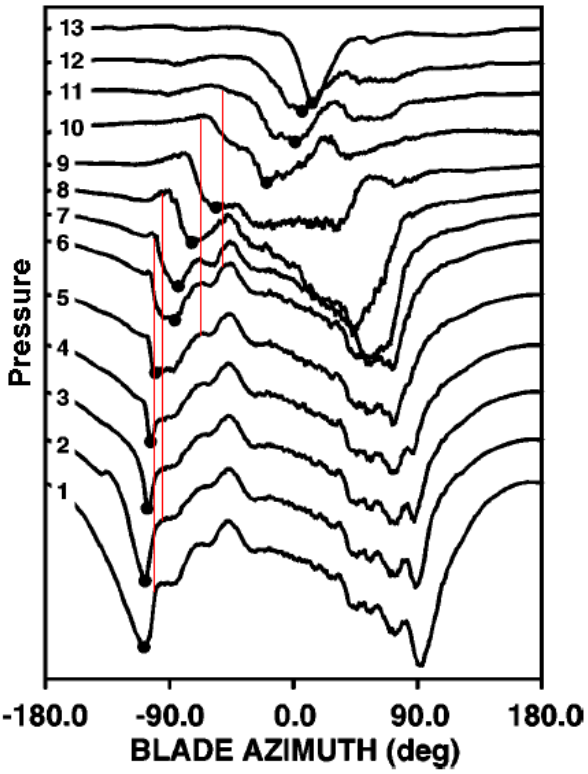

Figure 3.1: Pressure Trace of Dynamic Stall Vortex [78]

of the DSV for each pair is 10, 20, 40 and 50 in percent chord. The pressure tap spacing should be about 5% chord. Thus 20 pressure taps are required for the suction surface.

The wind turbine rotor will be operating at a tip speed ratio between 2 and 4. The range of wind speeds will be 8-13 m/s. The smallest pressure coefficient on the surface will be greater than -7 while the largest will be 1. The fluid velocity about the blade will be between 9 and 54 m/s. The smallest pressure range along one chord section will be between 47.2 and -330.4 Pa while the largest pressure range will be between 1,695 and -11,865 Pa. The system specifications are summarized in Table 3.1.

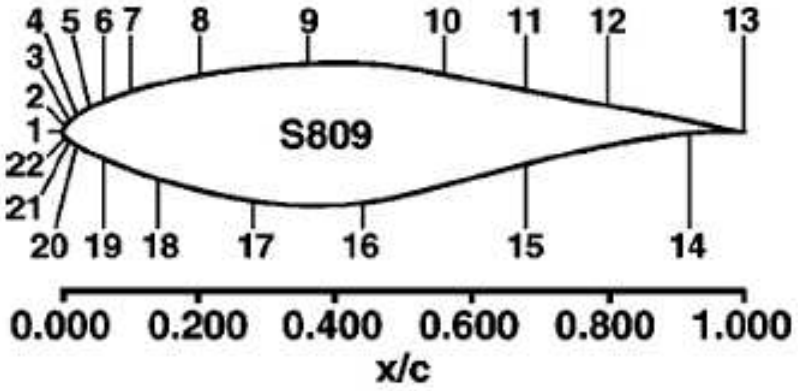

Figure 3.2: Pressure Port Locations [78]

Minimum Number of Channels	24
Minimum Sampling Rate [Hz]	609
Minimum Pressure Range [kPa]	0.05 - 0.33
Maximum Pressure Range [kPa]	-12 - 1.7

Table 3.1: System Specification Summary

3.2.2 Pressure Sensor Selection

The available technology for collecting pressure data was investigated. The details of this investigation are given in Appendix E. Technology similar to the integrated multi-sensor systems used in the NREL Phase VI experiments was investigated [30]. Individual sensor technology was also investigated. Individual sensors require a separate data acquisition system, two types were evaluated, one based on extending personal computers, the second being self contained.

Using individual pressure sensors provides a more flexible solution that better fits the criteria. For the current application the best solution is the Honeywell 26PC full bridge pressure sensor.

However, this solution adds increased complexity. Unlike the integrated multi-sensor systems there is no dedicated acquisition system accompanying the pressure sensors. The Compact DAQ architecture from National Instruments was chosen for the data acquisition. At an acceptable cost the system will be capable of sampling 32 channels at 50 kHz in a small package that will offer the greatest flexibility. The system offers excellent applicability for future applications. The modules are dedicated for full bridge strain gauge measurements thus setup and debugging will be greatly simplified with this system versus custom excitation and amplification circuitry.

3.3 Particle Image Velocimetry Data Acquisition

3.3.1 Criteria and Constraints of the Equipment Selections

The flow physics of interest are unsteady and can be large and complex. Analysis of pressure signals indicated a minimum sampling rate of 609 Hz. However, this was to capture four samples of the DSV as it is convected along the suction side of the blade. One can assume that there will be other details far from the blade that may occur at higher frequency. Chapter 2 shows an accurate understanding of the transient flow fields requires high temporal resolution. As such the PIV camera needs to have as high of a frame rate as possible to give maximum detail of transient phenomenon.

Experiments in two dimensional wind tunnels studying dynamic stall indicate that the DSV can be quite large [77]. A large DSV would have a significant influence on flow in the proximity of the blade. For its temporary residence it would act as an extra large blade, augmenting solidity effects. Solidity effects are already known to have a small effect on the wind turbine aerodynamics [89, 54], a large DSV will amplify this. It is theorized that rotation affects the boundary layer to induce radial components in the flow [13]. These same effects should also influence the behavior of the DSV, thus there will be deviation from two dimensional DSV behavior. It is important to accurately capture the far extent of the flow while still being able to resolve the small details in the DSV itself. Both of these criteria demand that the image area be quite large and good results have been collected with mega pixel images. As such a resolution smaller the 1024x1024 pixels should be avoided.

Light sensitivity is known to decrease as resolution and speed increase. Powerful laser based illumination will be critical to collect data, it is important that any laser used is powerful enough to illuminate the flows of interest. The cameras will be evaluated with existing lasers while the results of the evaluation will be used to determine what laser will be best suited.

The speed of the camera also places constraints on the laser speed, the timing of image exposures is controlled by pulses of the laser. The required inter-frame timing is too fast to perform true time resolved PIV. To overcome this shortcoming frame straddling can be used. Frame straddling is achieved by pulsing the laser at the end of one frame, then again soon after the opening of the next frame. To achieve this the pulsed laser needs to be capable of double pulsing at repetition rates no lower than half that of the camera. Continuous wave lasers can behave like pulsed lasers with a shutter, with a continuous wave laser the pulsing requirements are applied to the shutter. The constraint on shutters is not an issue, however pulsed lasers give superior illumination, with strong intensity and short flash time, hence a pulsed laser is the preferred solution.

3.3.2 Investigations in Camera and Laser Selection

The available technology for collecting PIV data was investigated. Both the cameras and the lasers were evaluated. Experiments and various trials were used to assess the

capabilities of each of the components. The details of these studies is given in Appendix F. The major conclusions from these studies are given below.

Summary of the Camera Investigation

Several cameras were investigated to explore each cameras capabilities and limitations for PIV data acquisition. Experiments were used to test three cameras, the APX intensified camera from Photron, another from Dantec, finally a non-intensified camera from Photron. Each camera was evaluated with different light sources, small continuous wave argon laser, a 5W continuous wave argon laser and an Nd:YAG pulsed laser. The results of the experiments were used to select the best camera

Provided that the light source is intense enough the SA-1 camera is superior. The camera was capable of taking good images with 5W continuous wave laser. Good images were also collected with the Nd:YAG laser at an attenuation of 75. In most cases the large bit depth of the SA-1 was needed to amplify the camera. In extreme cases over amplification causes banding. Many good images were taken with small amplification with the Argon Laser and the Nd:YAG Laser. Thus, the camera can be used with equipment available to us now.

The intensified cameras have an advantage of gating and intensification. This allows the cameras to be used to evaluate high speed flows, with weaker lasers or with continuous lasers. The intensified cameras are better suited, in instances were powerful light sources are not available. The test matrix given makes is difficult to compare the two intensified cameras. Both cameras have different noise characteristics. The Dantec camera gave sharper images, however gave more noise. The noise of the Dantec camera appeared as isolated bright spots. The noise in the APX resembled a haze. The isolated bright spots can be identified and ignored where a uniform haze cannot and will surely disrupt PIV correlations. Thus the Dantec camera is better than the APX.

Comparisons with the Nd:YAG laser show one shortcoming of intensifiers. Under pulsed conditions, where the pulse width is of ns scale, there is little increase in light sensitivity with intensification. Since pulsed lasers are preferred, this property shows reduced benefits with an intensified camera. The nonlinearity of the attenuator gives uncertainty in the

actual light sensitivity under pulsed conditions. Accordingly further evaluation in the light sensitivity is required.

Laser Selection Summary

The criterion was that the laser and camera combination was able to image a 0.3 meter window for analyzing the flow about a wind turbine blade. The SA-1 camera is superior due to speed and bit depth. The speed will allow the capture of faster phenomenon. The bit depth allows the camera to capture information at low light. The intensifier in the Dantec camera failed to give a strong response in pulsed light.

At both 1 kHz and maximum SA-1 camera speed the Pegasus laser with the SA-1 camera can be used for time resolved PIV with image windows of 1.60m and 1.15m respectively. Thus the Pegasus laser with the SA-1 is sufficiently powerful for the original criterion. The Darwin Duo with the same camera at 1kHz and maximum SA-1 camera speed will capture 2.53m and 1.89m windows respectively. With the SA-1 both lasers far exceed the minimum window length criteria, thus both lasers can be used to study larger structures. The Darwin Duo will allow the imaging of very large structures, it is unlikely that there will be structures of interest exceeding the maximum area found with the Pegasus. As such the Pegasus is considered adequate, the extra power of the Darwin Duo is not justified.

3.3.3 Final Laser and Camera Selection

Overall, the Pegasus laser with the Photron SA-1 camera is the best combination. The laser is powerful enough, for full meter imaging at 2.7 kHz. This combination will give the fastest sampling with superior image quality. If higher bit depth is needed the Darwin Duo will allow 0.47m window lengths at the maximum speed and full bit depth of the camera. It is unlikely these stringent requirements will apply.

3.4 Data Acquisition System Control

A proposed experiment will take pressure and laser PIV measurements of an air flow about a rotating rotor. These measurements require a camera and a data acquisition system attached onto the rotating rotor. To control and configure these components a computer needs to be mounted in the rotating domain along with these components. This section outlines the computer requirements of each of these components. In addition, it outlines the overall architecture of a computer system that will satisfy these requirements. Finally, this section proposes a set of components that will fulfill all the requirements of the system.

3.4.1 System Architecture

Figure 3.3 shows a proposed architecture of the system. The data acquisition and camera are in the rotating domain. A computer is on the rotating domain to control both devices. Slip rings are used to transmit AC power onto the rotating domain to power all of the components. The rotating computer can communicate with the stationary computer via wireless communication.

3.4.2 Criteria and Constraints of the System

There are two components on the rotating domain. The first is the Photron SA-1 camera that will record laser PIV data. The second is the National instrument compact DAQ data acquisition system. The Photron SA-1 manual shows that the camera requires a Gigabit Ethernet connection to interface with a computer. The manual for the National Instruments Compact DAQ shows that the system requires a USB connection to interface with the computer.

The computer will require a means to communicate beyond the rotating domain. Modern operating systems like Linux and Windows XP can be operated remotely via various remote desktop protocols. The external communication will require a second Ethernet connection. RJ45 cables require 8 wires to work. It would be impractical to use eight slip rings to transmit the Ethernet connection. Wireless communication can be transmitted

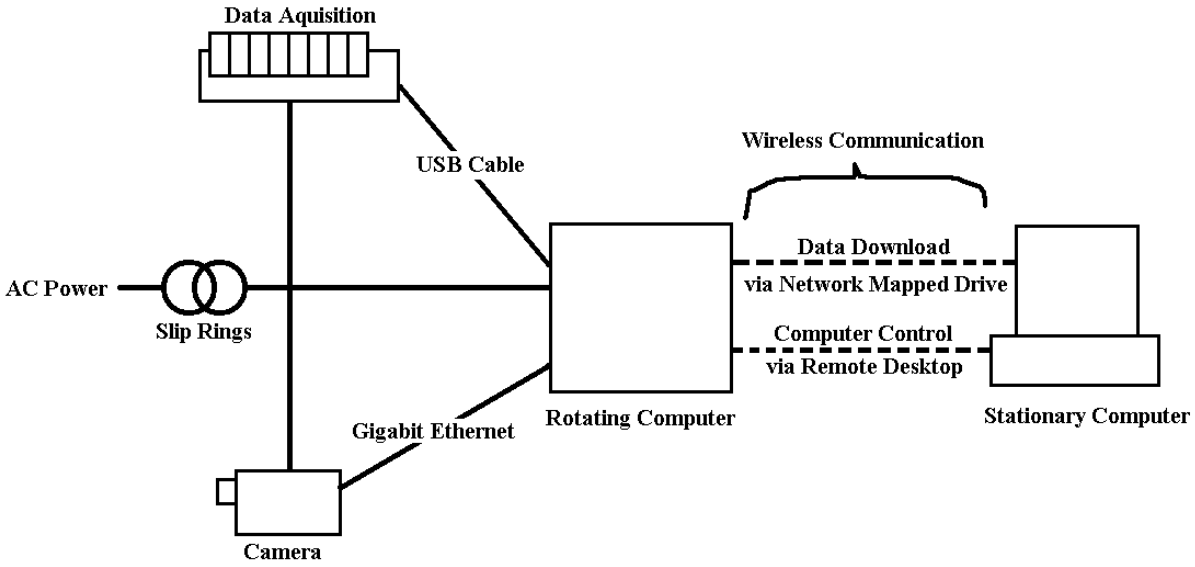

Figure 3.3: Data Acquisition System Architecture

between the rotating and stationary domain without slip rings. The computer will require a wireless Ethernet capabilities.

The pressure data needs to be collected simultaneously with the Laser PIV data. The data acquisition system for the pressure data interfaces with Labview software. Labview software will allow the pressure acquisition to be collected simultaneously. Labview software requires 1.2 GB of hard disk space and 512MB of RAM. Most software is written for the Windows XP operating system. Thus Windows XP will be the operating system of choice. The published requirements of Windows XP are 1.5 GB of hard disk space and 128 MB of RAM. In total the two software packages require 2.7 GB of disk space and 640 MB of RAM. The camera can generate a maximum of 16 GB of data in a single experiment. The windows operating system allows a network share to be connected as a drive. Utilizing this functionality will allow the rotating computer to download the camera data without using any of the local hard disk space.

AC power is required by the camera and the data acquisition system. The AC power will be provided to the system through slip rings. Since AC power will already be made

available the computer will not have to run off a battery. As such any standard personal computer system will suffice.

The computer will be mounted onto the rotating domain. The center of gravity of the computer will be mounted off the axis of rotation. The weight of the computer will contribute to a mass imbalance of the rotor. Minimizing the mass of the computer will minimize the mass imbalance. The computer system will be mounted externally in the mean airflow. A large bulky system will influence the airflow and could possibly disrupt the measurements. The size of the system needs to be minimized to maintain a proper airflow. Due to the rotor rotation gyroscopic forces will be induced in additional rotating components of the computer system. As such a fan or a disk based hard drive would fail prematurely.

3.4.3 Final Computer Selection

The mini ITX form factor is amongst the smallest of personal computers available. Of this form factor the EPIA EN main board by VIA Technologies is the only that has a Gigabit Ethernet controller standard for communication with the camera. The EPIA EN has a CPU embedded in the main board. Also, the system can host the Windows XP operating system. The system has 6 USB connections. The first will be needed to communicate with the National Instruments Compact DAQ. The remainder can be used for 8 GB USB Flash drives in place of conventional hard disks. A Wireless Ethernet card will be plugged into the PCI slot for communication with a stationary computer. Finally 1GB of RAM will be needed along with an ATX power supply. The system will be powered by standard AC power through slip rings. The system will also have no rotating components to cause gyroscopic forces. The above system will satisfy all the requirements of the rotating computer, while being exceedingly compact.

Chapter 4

Computational Study on Wind Tunnel Facility

4.1 Purpose of the study

In the case of an operating wind turbine, the flow is constrained by the ground on one side and all other sides are open to atmosphere. In the field the ground complicates the flow a great deal, by increasing turbulence and producing an uneven flow profile. These complications have made it difficult to gain a fundamental understanding of many of the flow physics [85, 87, 77]. Wind tunnel testing allows one to analyze an idealized case for wind turbines. This idealized case involves low turbulence, uniform flow in an infinite domain.

The majority of the wind energy generated in the world will come from large multi-megawatt wind turbines operating in open environmental conditions. These wind turbines exhibit rotor diameters approaching 80m. Testing these turbines in wind tunnel facilities is completely impractical. Hence, we must rely on scale models to understand the flow physics. The practice of using scale models is well understood. All the physical parameters of a given flow case can be expressed in non-dimensional terms, provided that the non-dimensional terms between two flow cases are equal, the two cases can be considered similar.

Typically wind turbines operate with the tips at a Mach number no greater than 0.3, as such one can assume that the flow is incompressible. This assumption leaves the momentum in the flow, the geometry and the motion of the rotor, to be non-dimensionalized. There is a long standing convention to non-dimensionalize the momentum using the Reynolds number Re, as defined in equation 4.1, based on the chord (c) of a given airfoil section. The section profile and various angles by definition are non-dimensional, however the chord (c) is not. This is non-dimensionalized as the section solidity (σ), given in Equation 4.2. Finally, the motion of the rotor is non-dimensionalized as the tip speed ratio (λ), given in Equation 4.3.

$$Re \equiv \frac{\rho V c}{\mu} \tag{4.1}$$

$$\sigma \equiv \frac{Nc}{2\pi r} \tag{4.2}$$

$$\lambda \equiv \frac{\omega R}{V} \tag{4.3}$$

In Equations 4.1 through 4.3 ρ is the density, V is the wind speed, μ is the dynamic viscosity, N is the number of blades, r is the radial location along the blade, ω is the rotational speed.

Matching the solidity and the tip speed ratio is achieved with a specific chord in the blades and rotational rate of the rotor. The wind tunnel itself presents no limits on these parameters. The Reynolds number is proportional to the air speed and the overall size of the rotor. The Reynolds numbers of multi-megawatt wind turbines are of the order 10^7. The maximum wind speed of the tunnel is constrained by the maximum power of the fans driving the flow. The size of the rotor is constrained by the size of the test section. Matching the Reynolds number preserves the flow similarity local to the blades, otherwise known as the local flow similarity. Matching this Reynolds number in a scaled down test is very difficult, since it cannot be perfectly matched, the Reynolds number needs to be maximized to maintain maximum similarity.

When testing in a wind tunnel there are additional constraints on the size. The boundary conditions of the test section will influence the flow of interest, differences in these

boundary conditions will compromise the flow similarity. Open jet tunnels exhibit flow divergence and shear layers about the test section, where walls will generate constraining boundary layers and prevent any flow divergence. The effect of these boundary conditions decreases by decreasing the size of the model, thus distancing the flow of interest from the unrealistic boundary flow. Minimizing the size of the model preserves the similarity about the model, otherwise known as the global flow similarity.

The contradicting constraint of maintaining local flow similarity and global flow similarity on the model size forces the experimenter to make a compromise. Achieving the best combination of global and local flow similarity results in an optimization problem. The methods applied and the results therein of such a optimization study are the subject of this chapter. The limited information given in literature pertinent to wind turbine testing gave insights into dealing with this problem. Computational fluid dynamics was applied to evaluate the flow similarity of the wind tunnel at the University of Waterloo.

4.2 Flow Similarity Studies within Literature

4.2.1 Reynolds Number Effect on Local Similarity

The order of magnitude of Reynolds number for a multi-megawatt machines is of 10^7. Practically the range of Reynolds number that can be achieved in a large wind tunnel is between 10^5 and 10^6. These differences can potentially create vastly different flow structures. The results from vastly different flows in a wind tunnel will not be applicable to those of a multi-megawatt wind turbine.

The effect of Reynolds number on airfoil aerodynamics has been known for many years. Appendix G summarizes a comprehensive study by Jacobs [43]. The stall process is most sensitive to the Reynolds number. At low Reynolds number laminar separation is the dominant stall mechanism, with increasing Reynolds number turbulent reattachment occurs. At even higher Reynolds number turbulent separation will occur and eventually dominate the stall phenomenon at even higher Reynolds number.

The results given by Jacobs [43] show that the stall mechanism of multi-megawatt wind turbines would be dominated by turbulent separation. Unfortunately at Reynolds numbers

below 10^6 reproducing stall dominated by turbulent separation is challenging. For airfoil profiles typically used in wind turbine studies higher Reynolds number effects did not start to appear until Reynolds numbers of about $9 \cdot 10^5$. For the same profiles laminar flow effects are present up until Reynolds of about $8 \cdot 10^6$. Close to 10^6 turbulent separation will still occur but laminar separation and turbulent reattachment still play a role. The increased complication will make it challenging to extend the results to provide insights into multi-megawatt turbine aerodynamics.

4.2.2 Evaluating the Global Similarity

Only one peer-reviewed article was found in literature on evaluating global similarity for wind tunnel studies of wind turbines. Some of the literature referring to wind tunnel experiments cites documents that discuss the global similarity of the particular experiment. However, many of the cited research is not publicly available. The one article that was found, evaluated the global similarity for studying the wake structure [103]. The article did not look at inflow conditions, only similarity in the wake [103].

The article by Wang et al. [103] focused on numerical techniques for evaluating the effect of wind tunnel walls on the wake of a wind turbine. The author employed the panel method to represent the effect of the walls. A prescribed wake model was used to model the wake structure of the wind turbine. The boundary condition of no flow across the panels is used to set the source strength. The resulting error of testing in wind tunnels is the flow solution of the wall sources alone [103]. Overall the method agreed well with experimental results, however there was some error in the conservation of mass, higher order panels can correct for this.

The study did not look at the wall effect on inflow condition, it focused on the wall effect on the wake structure. The authors showed how the wake in a wind tunnel will be modified. The authors analyzed a 1.0m diameter rotor operating in a closed 2.13m by 1.61m rectangular test section. This gives an inscribed circle blockage ratio of 0.386 [25].

The results show that under these conditions the axial velocity is 9-10% slower in a wind tunnel than the infinite domain [103]. The radial expansion of the wake reduced by 17-18% as well [103]. The reduced divergence of the wake would concentrate the vorticity and amplify the induction. There would be similar error in the axial and radial flow component

close to the blades. A 5% error in velocity, results in a 10% error in the pressure and force estimation, thus velocimetry error should be kept within 5%. Assuming that inflow error is similar to wake error, this blockage ratio is considered too high for accurate wind tunnel testing.

For other tunnel configurations similar studies are required to understand the error. The method employed for this study is based on inviscid flow theory, open jet test sections are bordered by viscous shear layers, and thus the method is only acceptable for closed test sections. Further research is needed to determine the maximum blockage ratio for a given level of error in a given wind tunnel configuration.

4.3 Wind Tunnel Studies of HAWT's in the Literature

In the literature, 56 different experiments and field tests of HAWT's were found, 36 of which were conducted in wind tunnels [38, 47, 58, 81, 65, 102, 36, 109, 2, 4, 30, 12, 68, 108, 82, 99, 66, 56, 29, 52, 25, 16, 15, 17, 50, 106, 83, 84, 69]. The large proportion of wind tunnel tests are not a result of preferences with wind tunnels, the article by Vermeer et. al. cited nearly all the wind tunnel experiments conducted since 1978 where most of the other articles cite work conducted since the 1990's, leading to a bias in the number of experiments found [102].

Only the aforementioned work by Wang et al. address the issue of global and local similarity, many of the articles give enough details to determine the critical statistics for similarity. Most of the wind tunnel experiments gave details of the test section and the size of the rotor, allowing for blockage ratio determination. Some articles cited the Reynolds number achieved. For others the Reynolds number was estimated when the blade geometry and test conditions were known. Not all articles provided enough information to determine the blockage ratio or Reynolds number. The resulting statistics are given in Figures 4.1, 4.2 and 4.3.

Achieving both global and local similarity is difficult and requires compromise, global similarity can be improved by sacrificing local and vice versa. The scatter plot in Figure 4.1 shows how previous researchers compromised. The plot shows that three experiments that

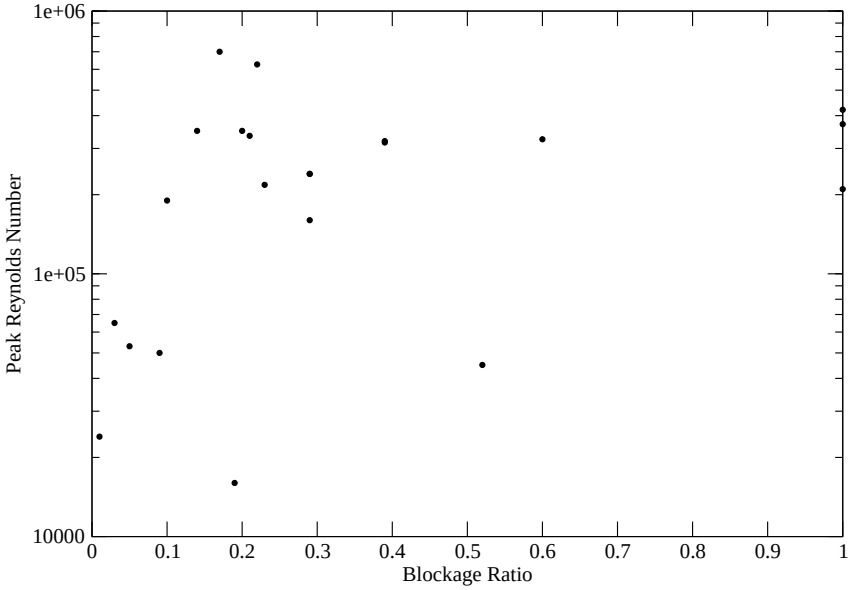

Figure 4.1: Reynolds Number vs. Blockage Ratio

sacrificed global similarity using a maximum blockage ratio of unity to achieve a Reynolds numbers between $2.1 \cdot 10^5$ and $4.2 \cdot 10^5$. Three other experiments sacrificed local similarity, operating at Reynolds numbers between $2.4 \cdot 10^4$ and $6.5 \cdot 10^4$ to achieve a blockage ratio of less than 10%. The majority of the experiments operated with a blockage ratio between 0.1 and 0.4 achieving Reynolds numbers between $1.9 \cdot 10^5$ and $3.5 \cdot 10^5$.

Two notable experiments achieved a Reynolds number of $7 \cdot 10^5$ and $6.3 \cdot 10^5$ operating at a blockage ratio of 17% and 22% respectively. These two tests would give the best results achieving the best in local similarity with small blockage ratios. The first test was conducted in a 24.4m by 36.6m wind tunnel with a full scale 10.1m diameter wind turbine hence there was no scaling error. The wind turbine used is much smaller than the 80m diameter multi-megawatt wind turbines used in the field. The second experiment was conducted in a 9.5m square tunnel with a 4.5m rotor diameter. These two notable

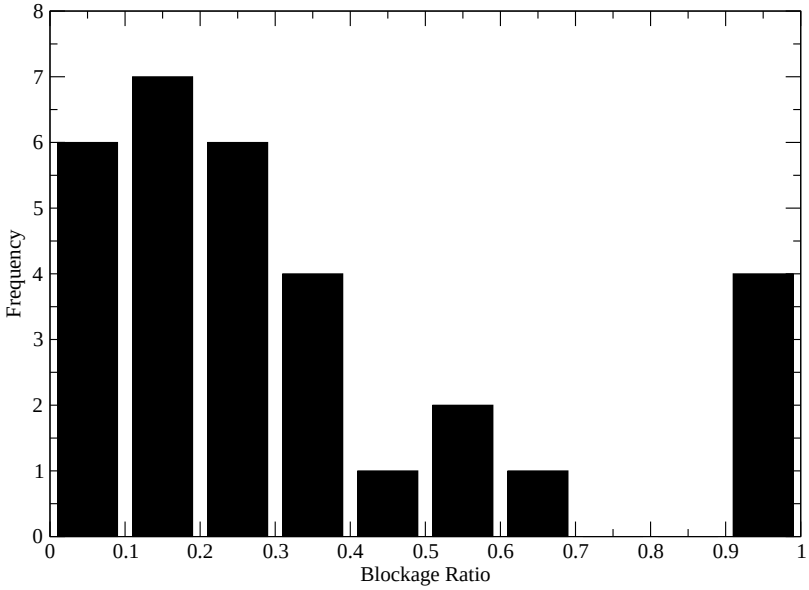

Figure 4.2: Frequency of Blockage Ratio's

experiments were able to achieve the high Reynolds number and low blockage ratio by using unique large scale facilities. Wind tunnel experiments for wind turbines are ideally suited to large facilities.

The frequency plots shown in Figures 4.2 and 4.3 include experiments that did not have blockage information or Reynolds number information. Looking at the blockage ratio plots a large majority of the experiments operated below a blockage ratio of 40%. Operating at a blockage ratio between 10% and 20% is most common. The frequency of Reynolds Number operation shows that a large majority of experiments operated below 10^5, at this level the airfoils would exhibit strong viscous and laminar flow effects. It is unlikely that turbulent boundary layers would develop, causing early separation. If they did form there would also be large separation bubbles causing large drag. Hence there is reduced certainty that these experiments would be representative of multi-megawatt wind turbines.

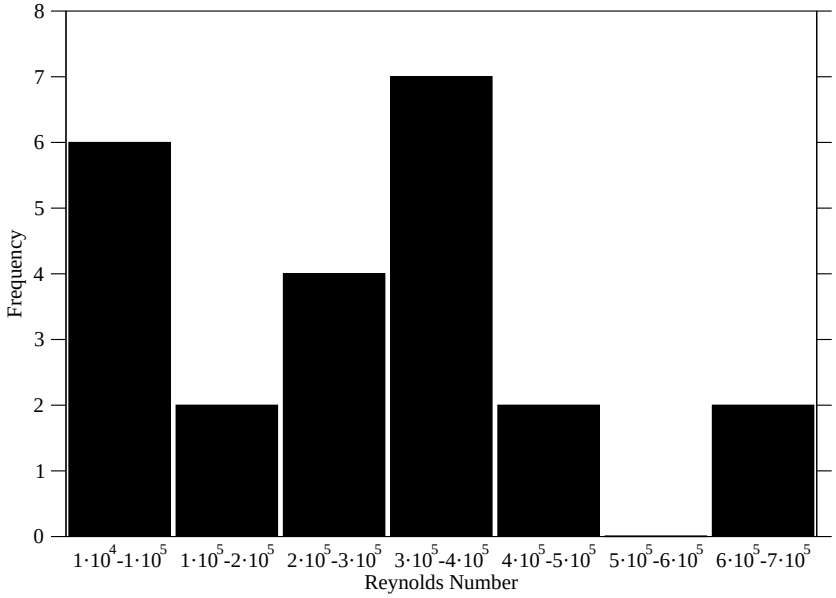

Figure 4.3: Blockage and Reynolds Number Statistics

Aside from the two notable experiments none of the tests exceeded the minimum Reynolds number of $4.5 \cdot 10^5$. This indicates that many researchers are violating the Reynolds number criteria due to the difficulty of high Reynolds number testing. This will shed much uncertainty on the results of these experiments. The importance of high Reynolds number wind tunnel testing is reinforced by Snel, he cites that much of the wind tunnel testing at a Reynolds number of $3.5 \cdot 10^5$ is too low and needs to approach $1 \cdot 10^6$ to be representative [85].

The experiment by Grant et al. [25] was performed with a blockage ratio of 38.6% in a closed section, Wang et al. [103] reported wake axial and radial expansion errors approaching 10% and 18% respectively. No details on in-flow conditions were given, yet it is likely that the inflow error would be unacceptable for pressure and load evaluation. The work by Schepers et al. cites a detailed computational fluid study into global similarity

to size the rotor in an open jet wind tunnel with a blockage ratio of 22% [69]. The cited report and details of this similarity study are not publicly available, one would expect that the rotor would be sized for acceptable global similarity. There is evidence that a blockage ratio of 22% is acceptable in open jet wind tunnels. Further research is needed to confirm this.

4.4 Description of the facility

The largest wind tunnel available at the University of Waterloo is at the Fire Research Facility. The wind tunnel has an open jet, open circuit configuration. Six 74.6 kW fans are used to drive the flow into a settling chamber to eliminate turbulence and other flow structures. The fans are driven by induction motors connected to variable frequency drives to give variable speed control. Flow straighteners are used at the jet exit to give a straight and uniform flow. The exit of the jet is 5.8m high and 8.2m wide. The jet exits along the floor of the test area.

Figure 4.4 shows a wire frame image of the tunnels geometry. Hidden lines are drawn at a finer weight. The approximate location of the fans is tinted red. The exit door of the test region is tinted blue. The flow travels from the red plane to the blue plane.

The test area is large open area inside a barn shaped building. The width of the test area is 15.4m, the maximum height is 12.964m. The roof of the test area is sloped towards the sides of the test area. At the side of the test area the roof height is 7.4m. The test area is 19.5m long.

At the opposite end the flow exits the test area through a large door, the door is 7.92m tall and 7.48m wide. Behind the door there is an obstruction to the flow, a large house used for fire research. The house sits 3.658m behind the exit. The shape of the house is similar of the test area, it is rectangular with a roof sloping to the side. The width of the house is 7.4m, the length 8.65m, at the peak the roof is 7.85m tall, and at the side walls the roof is 6m tall.

A flow characterization study was performed on the wind tunnel by Weisinger [104].

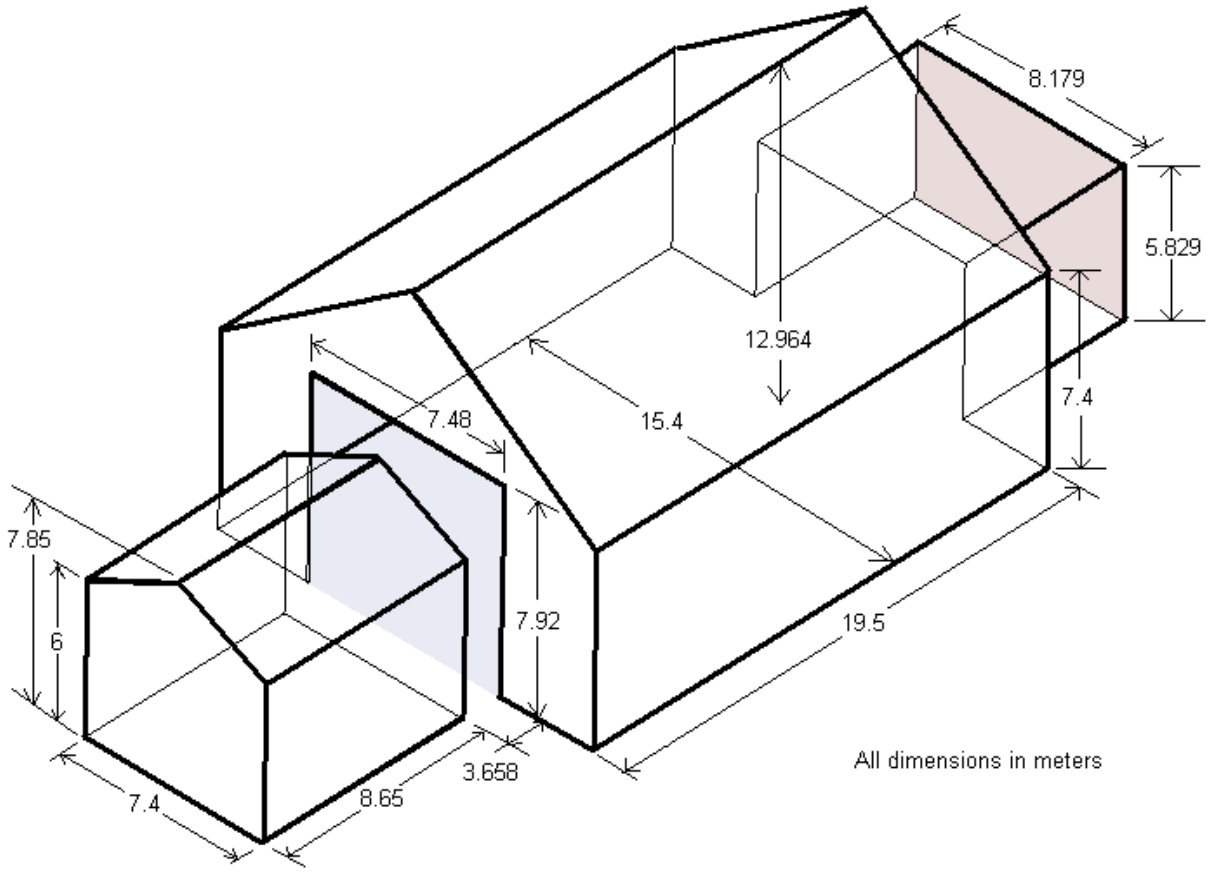

Figure 4.4: Wind Tunnel Geometry

4.5 Description of the method

As stated in the Section 4.1 there are two contradicting constraints to wind tunnel testing. The first is achieving local similarity by having chord Reynolds number approaching that of large scale wind turbines. The second is achieving global similarity by simulating the effects of an infinite domain. Achieving the first means maximizing the size of the turbine. The second constraint is violated, when the rotor size is increased, up to the point where boundary effects have a significant contribution. Thus, the size of the rotor needs to be as large as possible, without significant boundary effects.

The ideal size can be found by comparing the wind tunnel flow field, with an infinite domain flow field. In both cases the flow fields for a wide range of rotor sizes would need to be known. The effect of the boundary conditions in the wind tunnel flow, would show up in the differences between the two flow regimes. The largest rotor where the differences were acceptable would be the ideal rotor size.

An infinite domain is a hypothetical environment and does not exist. Only numerical computation can determine the wind turbine flow within such a domain. The effects of the wind tunnel can be created and tested, however this would require considerable design effort, designing multiple rotors and an apparatus capable of loading each rotor. This would be prohibitively expensive, instead numerical computations can be used to estimate the flow within the wind tunnel. The commercial computational fluid dynamic package CFX 10.0 from ANSYS [40] will be used to predict the flow within the infinite domain and the wind tunnel.

A rotor with a diameter of 3.272m will be evaluated. It represents a blockage ratio of 25%. This blockage ratio is close to the median of blockage ratio's reported within literature. Accurate solutions to the wind tunnel flow proved to be very difficult, the study is focused on confirming the applicability of this rotor.

Typically wind turbines operate over a wide range of conditions. The speed of the flow can vary as well as the axial thrust of the turbine. The axial thrust of the turbine causes the flow to diverge ahead of and in the wake of the rotor. Boundary effects would have a strong influence on the degree of divergence. The divergence itself is strongly affected by the wind speed and the axial thrust of the turbine. Like the degree of divergence, the

undesirable effects of the boundaries could also vary with wind speed and axial thrust. All models were tested with three different wind speeds and three different axial thrusts.

The maximum wind speed of the wind tunnel, 13 m/s, was one test condition. The minimum operational wind speed for a wind turbine is about 5 m/s, this speed was used as another test condition. Finally an intermediate wind speed of 9 m/s was used as a third test condition.

The axial thrust of a wind turbine is dependent on the rotor size and the wind speed. Flow fields of the same thrust would not be comparable. The smaller rotors would need to generate a very high pressure drops to achieve the same thrust of a larger rotor. A stable flow field requires the pressure drop to be below the dynamic pressure of the flow. If a pressure drop within the flow approaches the dynamic pressure, the flow will decelerate and instabilities could arise, these instabilities could create large turbulent flow structures [34]. With the same pressure drop, a high speed flow would exhibit negligible effects compared to the effects in a low speed flow.

To make models of similar thrust, with differing rotor sizes and wind speeds, comparable, the non-dimensional thrust is made constant. The non-dimensional thrust is referred to as the coefficient of thrust (C_t). It is defined in Equation 4.4. The Betz limit is based on a turbine operating at an optimum thrust coefficient. Most wind turbines are designed to operate near this point. That optimum thrust coefficient is 8/9 [48]. This optimal thrust coefficient was used as a test case. When the coefficient of thrust approaches 1 the pressure drop across the rotor is approaching the dynamic pressure. Beyond that instabilities generate large turbulent flow structures [34], it is not unusual for wind turbine to operate within these unstable flow fields. To represent that condition, a thrust coefficient of 11/9 was used as a test case. The opposite extreme is a lightly loaded rotor, this was represented by test cases with a coefficient of thrust of 5/9.

0 0

$$C_t \equiv \frac{2F_T}{\rho A V^2} \tag{4.4}$$

Wind turbines also impart tangential forces on the flow. This causes the flow to swirl about the rotor axis. The resulting rotation in the wake is lost energy. To minimize these losses wind turbines are designed to generate power through high speed rotation, under

Wind Speed $[m/s]$	Coefficient of Thrust	χ $[kg/m^2s^2]$
5	5/9	750/9
	8/9	1200/9
	11/9	1650/9
9	5/9	270
	8/9	432
	11/9	594
13	5/9	5070/9
	8/9	8112/9
	11/9	11154/9

Table 4.1: Momentum sink Parameters for Actuator Disc Modeling

low torque. The lower torque minimizes the rotation in the flow. For these reasons, the rotation in the wake is small. With a small rotation in the wake, its effects can be ignored compared to the strong effects of the axial thrust.

Ignoring the swirl, solidity effects, and assuming the rotor is evenly loaded, allows it to be modeled as an actuator disk. An actuator disc extracts momentum from any flow passing through it. Ansys CFX 10.0 [40] does not allow a surface momentum sink to be defined, instead a thin volumetric one was used. The momentum extracted within the volume is set as a momentum per unit volume parameter. Equation 4.5 was used to set the momentum sink. Equation 4.5 is independent of the rotor area, it is only dependent on the thickness T of the volume used. For the 3.272m diameter rotors a thickness of 0.1 was used. A different thickness was used for some of the smaller rotors. V in Equation 4.5 is the axial speed of the flow through the volume, the nominal speed of the tunnel was used. Divergence in the flow would reduce the speed to a small degree, slightly increasing the resulting thrust. This effect is being neglected in the results. Table 4.1 shows the χ parameters used in modeling the 3.727m diameter rotors.

$$\chi = \frac{C_t \rho V^2}{2T} \tag{4.5}$$

Laterally the test facility is symmetric, vertically there is a floor on the bottom and a shear layer at the top of the jet. The two different boundary conditions will have differing effects on the flow. The wall constrains the flow and will act to reduce the divergence. The flow beyond the shear layer will have no momentum to resist any flow divergence, thus would accentuate it. An open boundary condition could accentuate divergence more than the floor could constrain it, or the opposite. Thus the optimum height of the turbine may not be at the centerline. To estimate the optimum height, the wind tunnel rotor was tested at the centerline and 0.40m above and below it.

4.5.1 Computational Model Details

The specific details of the computational models for both the infinite domain and wind tunnel models is given in Appendix H. In all cases, symmetry was used whenever possible to simplify the model. For both models a domain and grid convergence study were attempted. In the infinite domain models it was completed successfully. Computational resources limited the number of elements in the wind tunnel models. The maximum possible number of nodes were used in the wind tunnel models.

A highly stringent convergence criteria was placed on the infinite domain model. Oscillations within the solution prevented the same criteria from being achieved in the wind tunnel models. It is expected that the oscillations are physical and not a numerical artifact, overall they were quite small. To reflect a steady state solution in the wind tunnel the long term results of a transient model were averaged.

Overall, both models showed similar flow structures indicating that the wind tunnel can successfully reproduce much of the phenomenon in wind turbine flows. The wind tunnel model results also showed many of the flow features associated with the specific wind tunnel.

4.6 Results of the Global Similarity Study

The results of the open domain study represent the ideal turbine flow field for testing. The results of the wind tunnel model represents what will likely be achieved in the actual

experiment. An open domain model corresponds with a wind tunnel model if the wind speed and coefficient of thrust are common.

In both sets of results, the data can be plotted against the radius on the rotor plane. Results of corresponding models correspond provided they are at the same radius. Differences in the grids caused the results to lie on different radial locations. Linear interpolation was used to determine open domain variable values at locations between result points. The error of the wind tunnel model is found at each point by subtracting the corresponding result in the corresponding open domain model.

The proposed experiment will likely be executed at a high velocity, with a low coefficient of thrust. The set of results for 13m/s wind speed and a thrust coefficient of 5/9 is representative of this case. The error results for this case with a turbine height at the mid plane are given in Figure 4.5. The absolute error results represent the error without adjustment. When the error is relative, all the values of the wind tunnel have been adjusted by a constant amount so the area weighted average of both result sets are the same. The absolute error of velocity is shown since the flow physics are governed by the magnitude of velocity. The absolute pressure error was very high, the wind tunnel flow has more obstructions between the inlet and outlet, hence increased pressure drop. In the Navier Stokes equation it is the pressure gradient that affect the momentum. The magnitude of pressure only matters when the flow is compressible, here the Mach number is well below 0.3, thus it is incompressible. Since the flow is incompressible, the relative pressure error is a better statistic for evaluating error in the pressure field.

The wind tunnel results have a reduced axial velocity by approximately 0.5m/s or 4%. This indicates that the axial induction factors are amplified slightly in the wind tunnel. The likely cause of the decreased velocity is the increased divergence, in three directions there is quiescent air giving little resistance to expanding flow. Overall, the trends in axial velocity are the same. The radial velocity of the wind tunnel results agree well with the open domain results. The tangential velocity error seems to indicate a swirl, however only one half of the rotor was modeled. Since nearly all the wind tunnel results indicate a positive tangential velocity it is likely that the flow is traveling parallel to the plane of symmetry. The wide scatter of the tangential error would result from the tangential component being small at the top and bottom and large in the middle. The trend of

the relative pressure error is similar to the open domain results, the highest pressure is in the center, forcing the flow to diverge. The error shows that the pressure gradient is larger in the wind tunnel. Increased pressure gradient would cause increased divergence and reduced axial velocity. This is further proof that the shear layers of the wind tunnel cannot accurately constrain the flow.

Figure 4.6 shows where the error is located on the rotor plane. The contour plots are not perfect, the results are located at scattered point locations. Two dimensional fifth degree polynomial regression was used to interpolate the results for the contour. There is some uncertainty in the values, however overall the plots show where the error was the strongest and the regions where the error was positive or negative.

The error in axial velocity is located towards the outside of the rotor. This shows that there is increased divergence at the outside closer to the boundaries of the jet flow. The radial error is concentrated towards the top of the rotor closest to the nearest shear layer, this shows the flow there is deflected up. The tangential error is greatest in the center of the rotor, showing more flow being deflected up. Overall this show that there is a small upward flow in the wind tunnel. The error in the radial velocity is slightly negative at the bottom of the rotor, the divergence here is being constrained slightly by the floor. The relative pressure error is high in the center and low towards the outside. This indicates there are additional pressure forces causing additional divergence in the wind tunnel flow.

All of the error results presented above showed the error for one specific case at one specific rotor height. The study evaluated many cases over three rotor heights. The results of each case were similar to the above results. To understand how other variables affected error, the error for each case was consolidated into one statistic, the Root Mean Square (RMS). The RMS velocity error was normalized by the inlet velocity, the RMS pressure error was normalized by the dynamic pressure of the inlet velocity. The RMS error statistics are shown in Figure 4.7, in the figures, the results of a common coefficient of thrust are plotted against turbine height. For each series a parabolic curve fit was added to give an indication of what turbine height would give the minimal error. In each series there are three points at the same height, these points are from each of the three wind speeds.

The different wind speed points of common thrust and height were very close together. This shows that the velocity has little influence on the normalized error.

The coefficient of thrust had a strong influence on normalized error, a higher thrust yielded increased error. A high thrust forces increases divergence, resulting in a larger flow field overall. A larger flow field would be more sensitive to boundary influences. The increased error of these cases shows that tunnel error is not strictly dependent on the rotors blockage ratio alone, but on the effective blockage ratio of the flow field.

The parabolic curve fits on all sets of data were used to find the location of minimum error. The average of all minimum error locations was a turbine height of 3.1m. The apparatus will be designed to hold the rotor at this height. This shows that the error of shear layer at the top is less than the error from the floor at the bottom. For these reasons, open jet wind tunnels are more suitable to wind turbine testing then closed test sections.

4.7 Summary of the Wind Tunnel CFD Study

For the proposed experiment the normalized RMS error in velocity was less than 3%, the largest normalized error comes from the relative pressure, with 17%. The dynamic stall is affected by the flow velocity. While the forces are generated by the pressure differentials around the blade, not the average pressure at a section. It is unlikely that the increased pressure error will affect the dynamic stall phenomenon too much. The velocity error of 3% results in a pressure error of 6%, this is reasonably small enough to understanding the forces generated for dynamic stall.

The study also looked at different axial thrust conditions and wind speeds. Overall wind speed had little influence on the normalized error. The axial thrust did have a strong influence, increased thrust resulted in increased error. The increased thrust would cause increased divergence making a larger flow field overall. This larger flow field would be more sensitive to the boundary conditions of the wind tunnel. This shows that a blockage ratio based on the rotor diameter alone is not sufficient for indicating the tunnel error of an experiment. Instead the effective blockage ratio of the flow field is a better indicator of error.

The axial and vertical placement of the wind turbine within the wind tunnel also has an affect on the error. Without a wind turbine, the ideal infinite domain flow would exhibit no pressure drop, and a zero pressure gradient. This premise was used to determine the

ideal axial placement. A solution for the wind tunnel model was found without a wind turbine, the location of minimum pressure gradient determined the ideal axial placement. Vertical placement was explored, by solving the flow field at all conditions of interest, with three different rotor heights. The three different heights allowed for a parabolic curve to be fit to the error data with respect to turbine height. The location of minimum error on the parabolic curve indicated the ideal turbine placement. The curve showed that placing the turbine 3.1m above the ground gave the best results. The mid-plane of the jet is 2.9m above the ground. An ideal placement above this shows that an open shear layer has a weaker effect on error than the constraining floor. This indicates that a open jet wind tunnel is more suitable than a closed test section.

The wind tunnel study has given many insights into wind turbine testing within wind tunnels. However the most important result is that the error will be very low for a 3.272m diameter rotor. The study successfully confirmed the reasonable global similarity with a rotor diameter of 3.272m for accurate testing within the University of Waterloo Fire Research Facility.

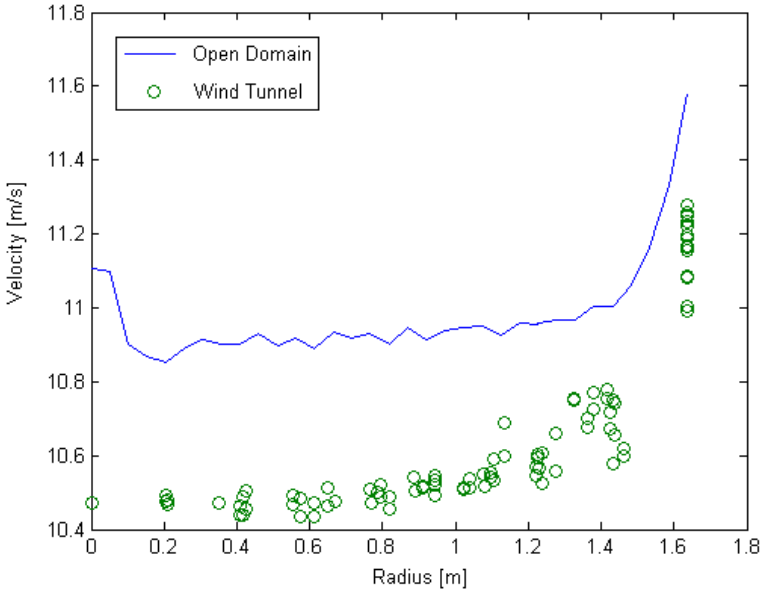

(a) Absolute Axial Velocity

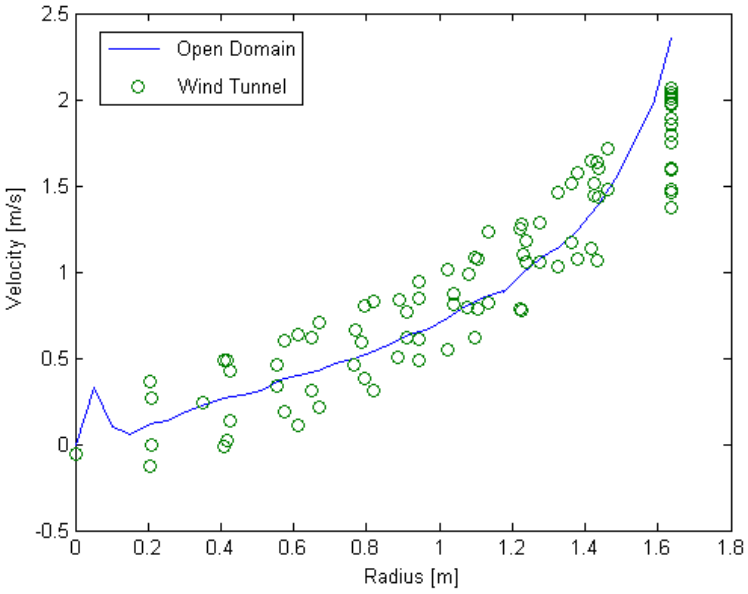

(b) Absolute Radial Velocity

Figure 4.5: Example Velocity and Pressure Results vs. Radius

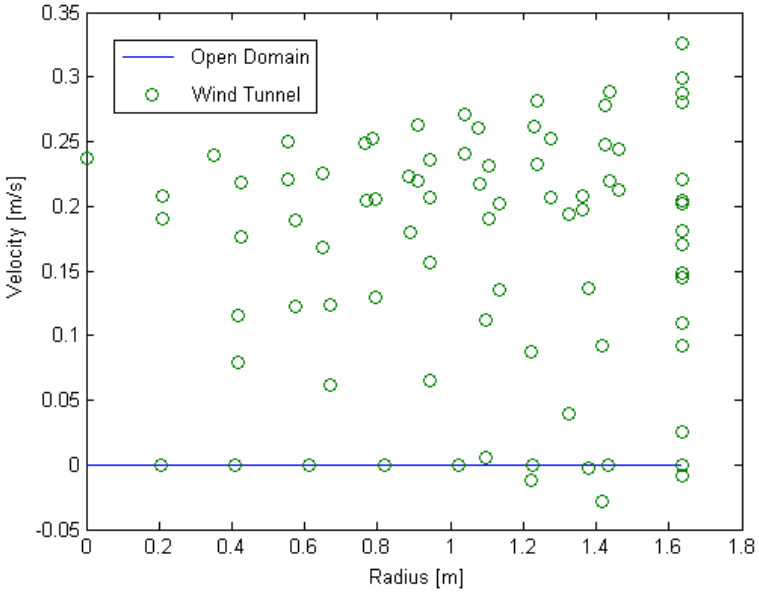

(c) Absolute Tangential Velocity

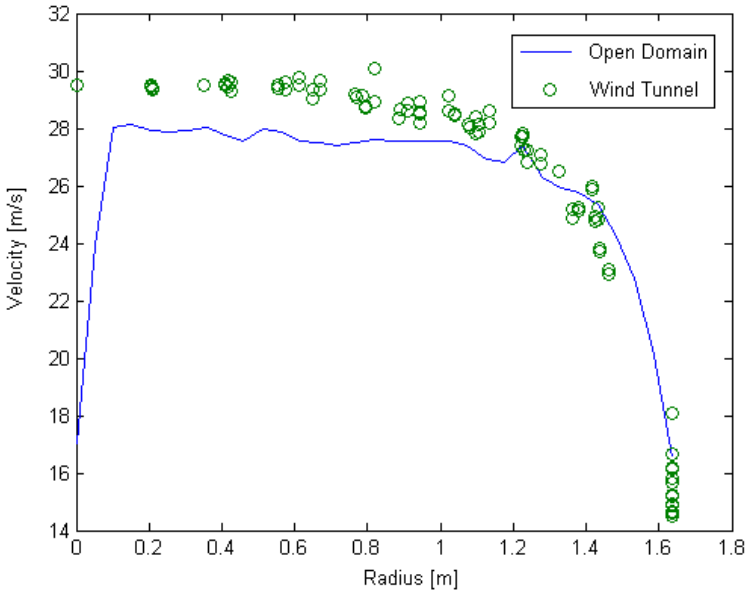

(d) Relative Pressure Error

Figure 4.5: Example Velocity and Pressure Results vs. Radius - Continued

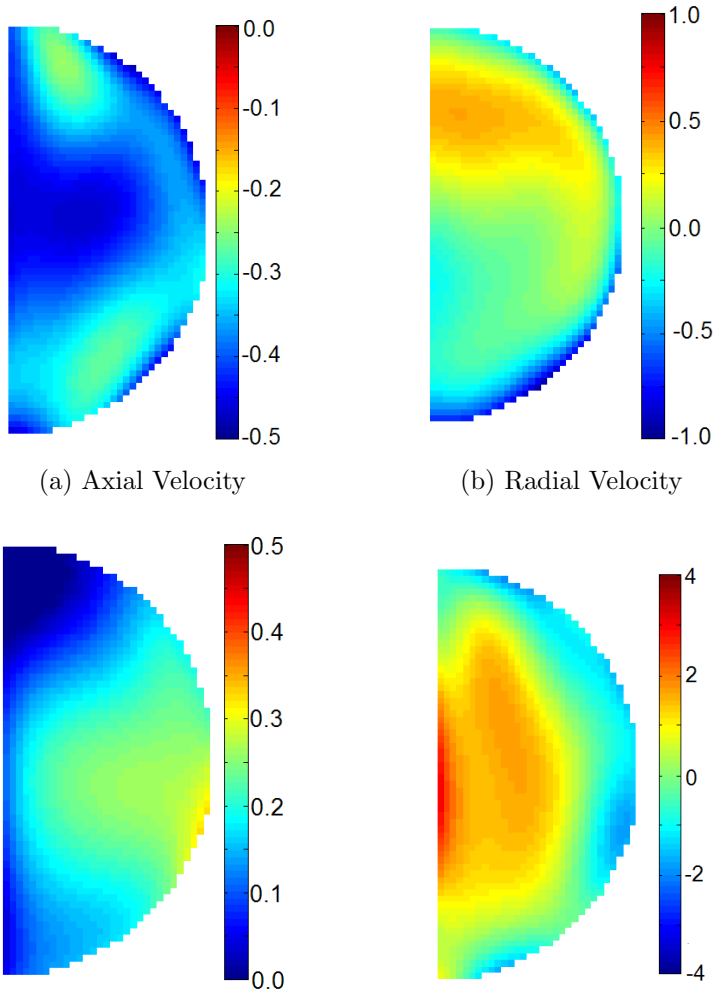

(a) Axial Velocity

(b) Radial Velocity

(c) Tangential Velocity

(d) Relative Pressure

Figure 4.6: Wind Tunnel Error at the Rotor Plane

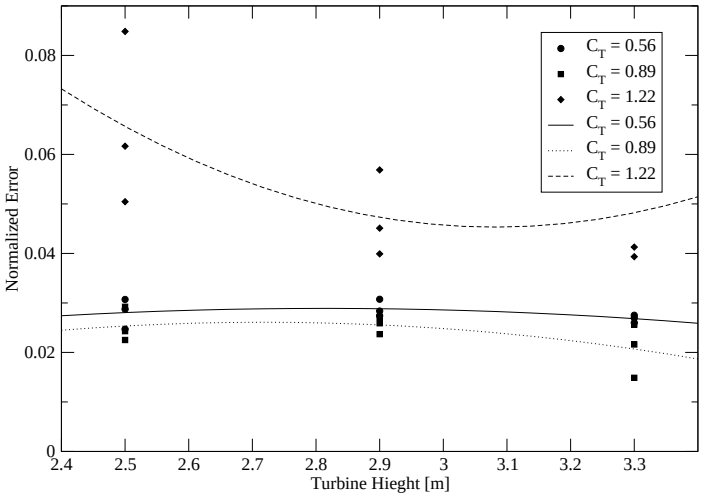

(a) Absolute Axial Velocity Error

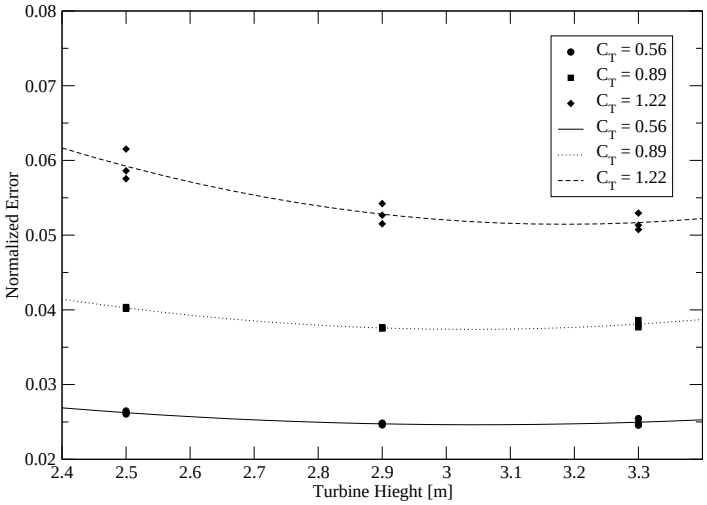

(b) Absolute Radial Velocity Error

Figure 4.7: Root Mean Square Wind Tunnel Error

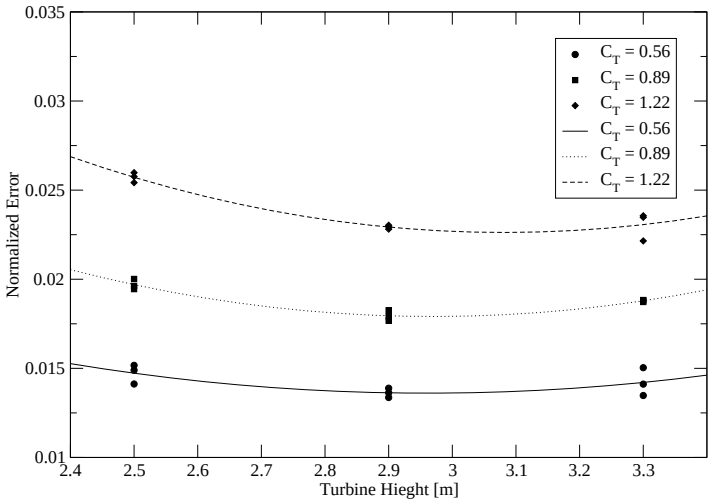

(c) Absolute Tangential Velocity Error

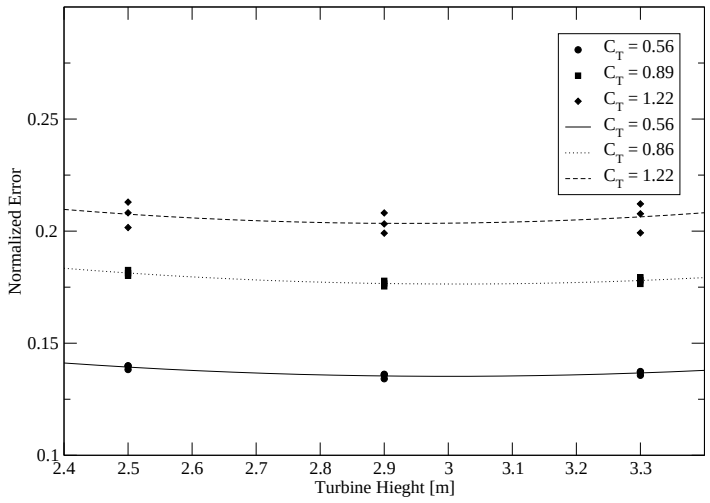

(d) Relative Pressure Error

Figure 4.7: Root Mean Square Wind Tunnel Error - Continued

Chapter 5

Loading a Wind Turbine Rotor for Test Purposes

By application, wind turbines are meant to produce a positive torque, producing power. Thus, experiments with wind turbines will require a resisting torque to maintain the rotor at a specific speed; hence the rotor needs to be loaded. The problem of supplying this torque is complicated by the fact that various experiments will require varying amounts of resisting torques at varying speeds, while others will require power into the rotor to maintain speed. The mechanism to supply torque needs to be flexible, capable of supplying a range at both positive and negative torque at a wide range of speeds. There are many systems, electrical, hydraulic and mechanical that could achieve this. Selecting the correct system is based on the expected speeds and powers of the experiments and the available resources to build this system. This chapter discusses the design of torque supply system, it outlines the criteria and constraints, various architectures applied in literature and architectures considered for the current apparatus. Finally the chapter gives the final design of the system.

5.1 Rotor Loading in Literature

Within the literature there are articles discussing the results of 20 different field tests where measurements were taken from wind turbines operating in the natural atmosphere [47, 58, 109, 12, 68, 108, 66, 16, 50, 83, 84]. By application a large majority of wind turbines

are meant to generate electricity and are electrically loaded. Many of the wind turbines used in these field tests were commercial machines, or were meant to behave as commercial machines. All the wind turbines used in field tests used electrical loading, it was not explicitly stated, however it is likely that the choice of electrical loading was based on reproducing the behavior of wind turbines operating in electrical generation applications. Figure 5.1 shows the frequency of various electrical architectures in the field tests. As with most wind turbines, alternators are common in low power machines and induction generators most common in high power machines.

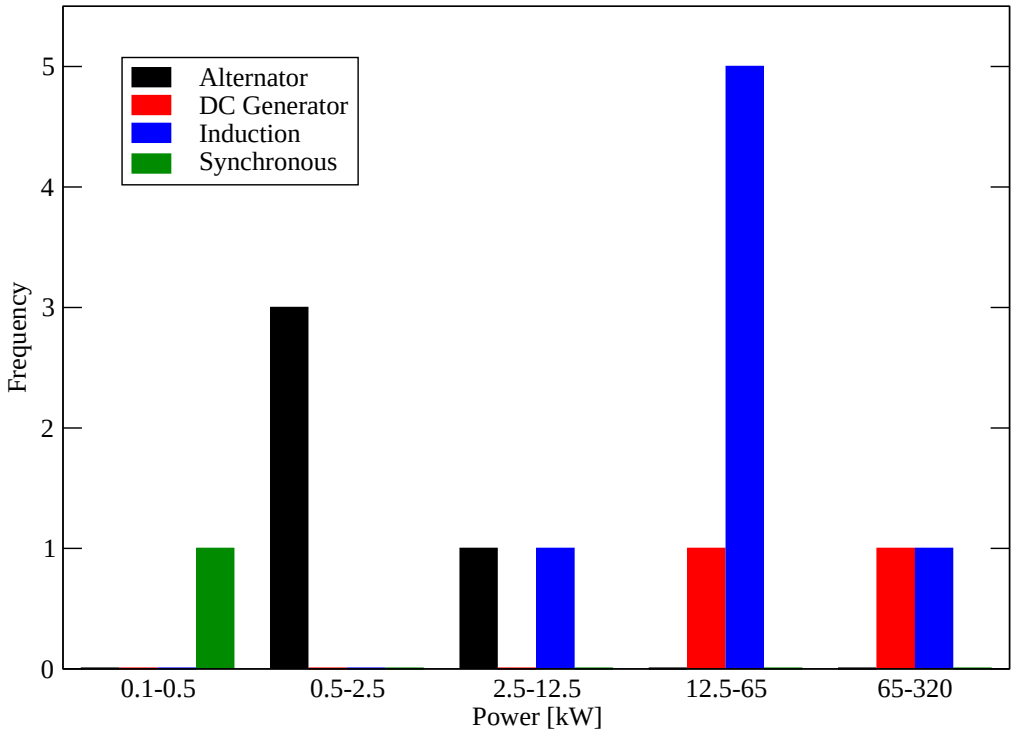

Figure 5.1: Frequency of Loading Architecture in Field Tests

Many more articles were found discussing results taken from 36 different wind tunnel tests of HAWT's [38, 81, 65, 102, 36, 2, 4, 30, 82, 99, 56, 29, 52, 25, 15, 17, 106, 69]. Wind tunnel testing of HAWT's is mainly focused on the aerodynamics, not the drive train and the overall dynamics of the machine. In wind tunnel applications the drive train is not constrained to reproducing electrical generation behavior, as such the experimenter is free to select the loading architecture that is best suited for the experiment. The loading statistics for wind tunnel experiments will be more applicable to designing a loading mechanism because these systems share similar application and criteria.

Many of the articles on wind tunnel experiments do not give the nominal power of the loading apparatus. In many of these articles the power of the apparatus is not important; however the diameter of the rotor is important and is typically reported. The power of a wind turbine can be estimated with Equation 5.2, the definition of C_p is given in Equation 5.1. The power of the rotor loading mechanisms were estimated using the rotor size, assuming a wind speed of $10m/s$ and an air density of $1.2kg/m^3$. The nominal power is estimated using a C_p of 0.35 while the lower and upper bounds of power uses a C_p of 0.2 and 0.5 respectively.

$$C_p \equiv \frac{P}{\frac{1}{2}\rho A V^3} \tag{5.1}$$

$$P = \frac{1}{8} C_p \rho \pi D^2 V^3 \tag{5.2}$$

The speed at a specific power can influence the architecture of the loading system. The speed and power of the experiments with known operating parameters was plotted in Figure 5.2. The error bars are given in speed when the experiments were conducted over a range of speeds. The error bars are given for power when the nominal power was not specified and needed to be estimated, the bars cover the estimated upper and lower limits of power.

Power law regression was performed on all the speed vs. power points. The resulting equation is shown as Equation 5.3. The R-Squared value for the power law regression is 0.919, indicating a strong curve fit. The strong curve fit shows that the speed is dependent on the power which in-turn is dependent on the rotor size. This is expected, HAWT rotors are designed to operate at tip speed ratios between 3 and 6, hence much of the testing is

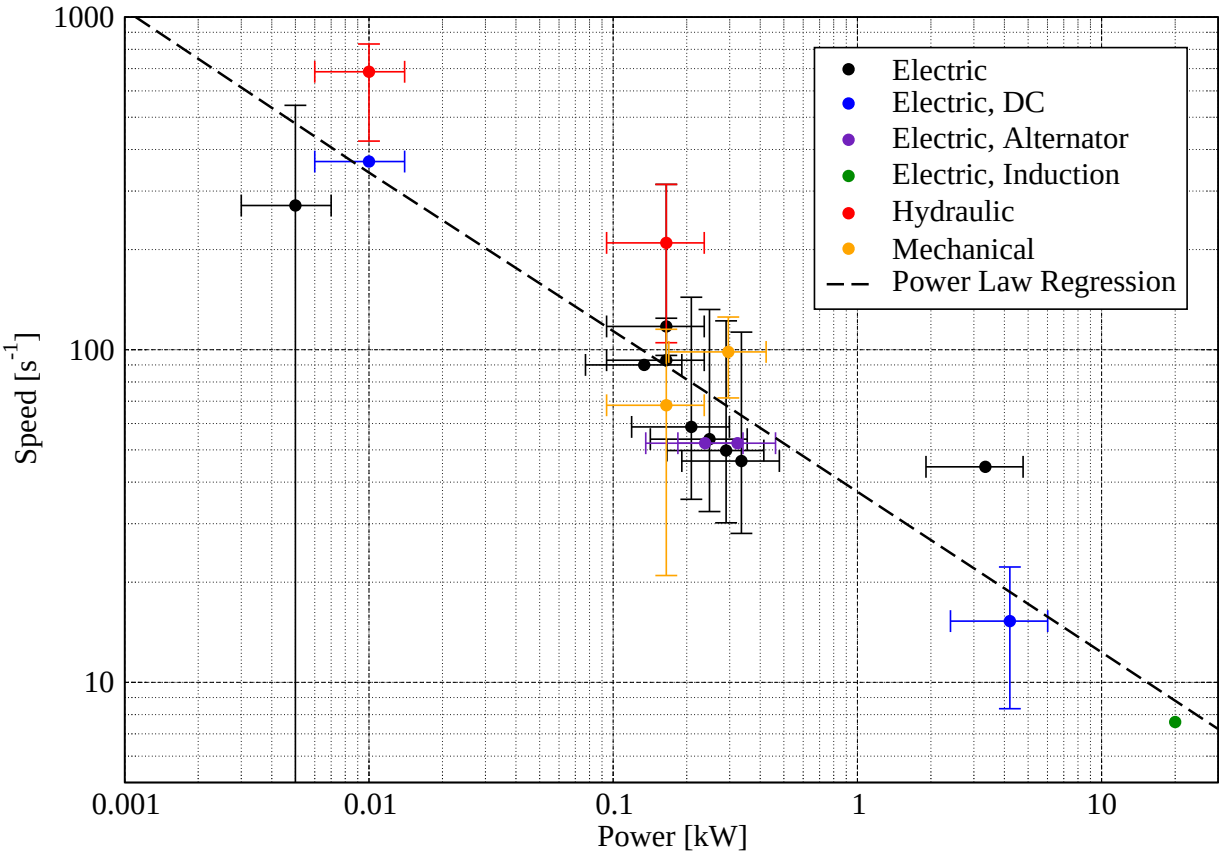

Figure 5.2: Speed vs. Power in Wind Tunnel Experiments

performed in the same range of tip speed ratios. The power law coefficient of 37.43 shows that most of the experiments were conducted at tip speed ratios of approximately 4.6. At constant tip speed ratio the rotor speed varies inversely proportional to the diameter, where the power is proportional to the diameter squared. These two proportionalities would give a power law exponent of -0.5, the regression coefficient of -0.483 confirms that these proportionalities are governing the speed vs. power trends. As such the loading architecture can be evaluated on power alone.

$$\omega = 37.43\,(P\ \ [kW])^{-0.483}\ \ \left[s^{-1}\right] \tag{5.3}$$

Not all wind turbine experiments reported in literature give the speed and could not be plotted in Figure 5.2. These additional experiments are included in Figure 5.3. A large majority of the experiments use electrical loading, the specific architecture is not reported in most articles. Within the literature where the architecture is reported, both DC motor and alternator loading are most popular. There are no experiments reporting the use of an alternator with powers above 1kW, while DC generators are used at powers between 10W and 4kW. At 20kW an induction generator was used. Hydraulic and mechanical systems have been employed when the power is below 320W.

5.2 Criteria and Constraints on the Loading System

5.2.1 Speed Sensitivity

Dynamic stall is strongly dependant on the angle of attack. For consistency in the experiment it is important that the angle of attack varies only from the yaw error and not from variation in the speed of either the rotor or the flow. Ideally maximum variation of angle of attack would be less than 0.5 degrees.

The simplest way of maintaining constant speed is to increase the inertia in the system to absorb high frequency variation of torque. Long term, low frequency torque variation can be controlled manually by the operator. It is assumed that the dominant source of high frequency torque variation will be from the dynamic stall itself.

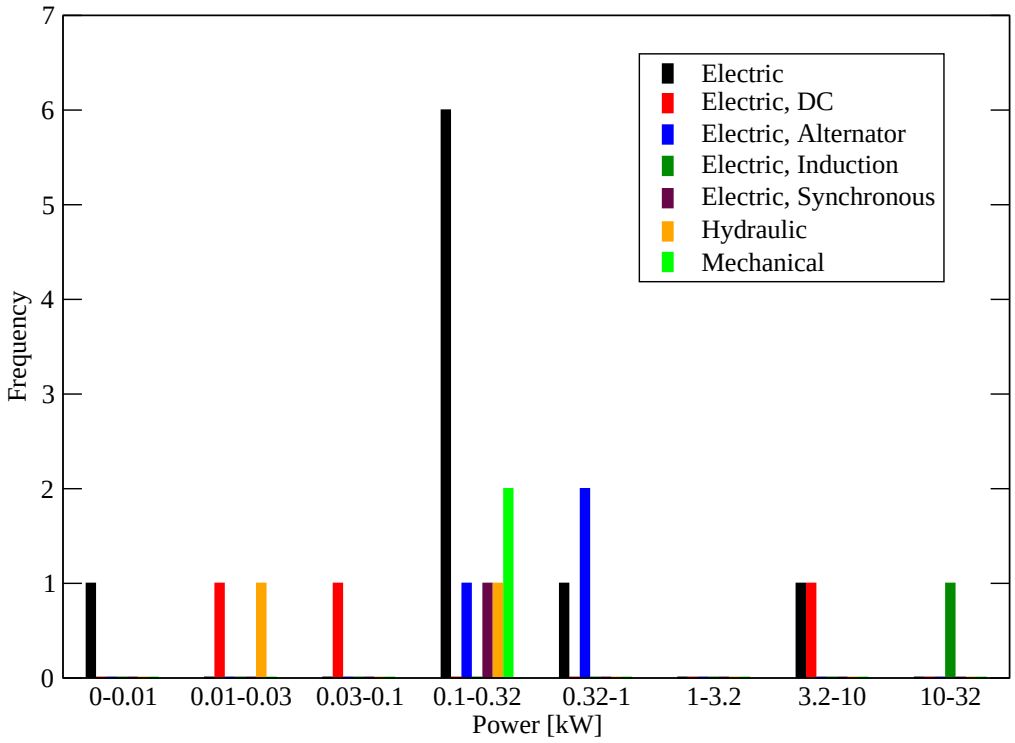

Figure 5.3: Loading Architecture Frequency in Wind Tunnel Experiments

A study given in Appendix I was performed on the sensitivity of dynamic stall to variation in the rotor speed. The study focused on determining the minimum inertia required on the high speed shaft to absorb the high frequency torque variation of dynamic stall. The study relied on a simplified BEM model to determine the angle of attack and speed and torque characteristics. The dynamic stall was modeled with a simplified stall hysteresis.

The final results of the study are given in Figure 5.4. The results show that a small additional inertia should be sufficient to maintain constant speed, thus adding inertia to assist in constant speed operation is feasible.

5.2.2 Power Requirements

The expected power of the experiment is a general statistic indicating the size of the rotor loading device. The statistic is important for sizing the electrical supply and absorption equipment. The study given in Appendix I also looked at the power requirements of the system. The study showed that under best condition the maximum power of the turbine rotor is 6459 W. Under the expected experimental conditions for dynamic stall the maximum power is 917 W. The power alone does not give enough information to design the entire system. The engineering of many of the energy conversion devices depend on the speed and torque characteristics of the rotor.

5.2.3 Rotor Speed and Torque Operating Conditions

The main focus of the apparatus design is for research into dynamic stall. However the apparatus can be used to research other areas of wind turbine aerodynamics. Implementing the drive train will require purchasing several expensive components. To avoid purchasing these components again for other experiments it is important the drive train is designed to accommodate these other possible experiments.

The aerodynamics of a wind turbine depend on the speed of the rotor. At a given power and speed the rotor torque can be found with Equation 5.4. A range of operating conditions is defined by a range of torque and speed conditions.

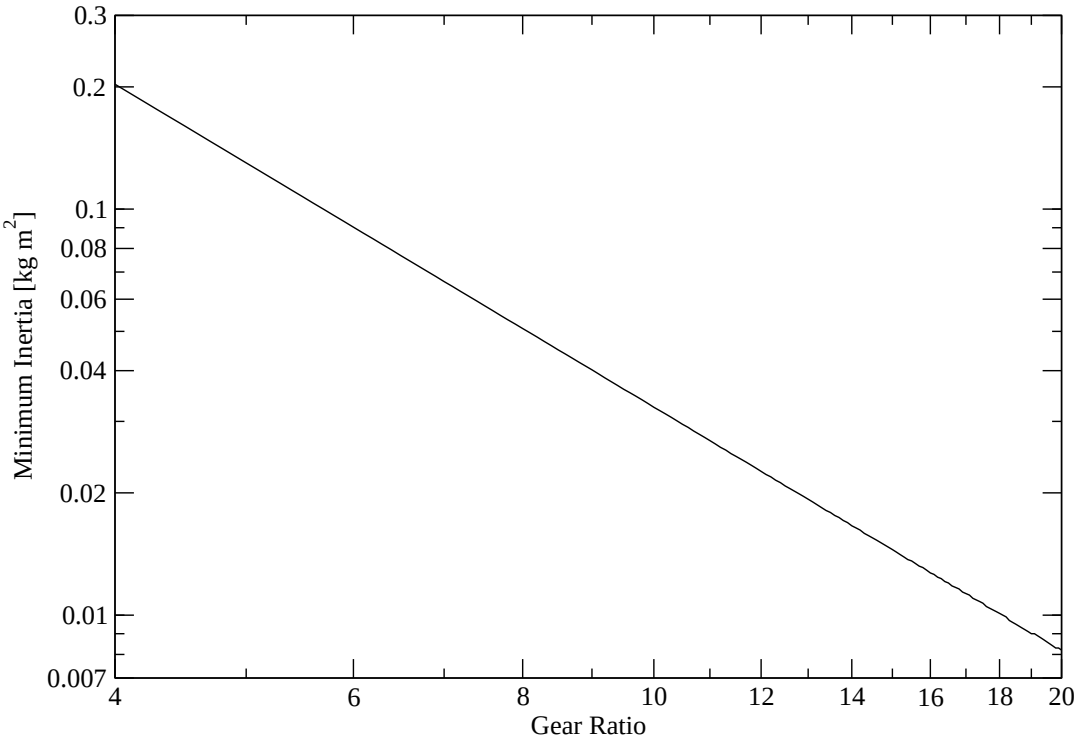

Figure 5.4: Minimum Inertia vs. Gear Ratio

Tip Speed Ratio	Speed [radian/s]
4.207	25.7
3.442	21.0
2.913	17.8
2.524	15.4

Table 5.1: Operating Conditions for the Dynamic Stall Experiments

$$Q = \frac{P}{\omega} \tag{5.4}$$

The rotational speed of a wind turbine is non-dimensionalized as the tip speed ratio, defined in Equation 4.3. The upper limit of speed occurs when the turbine reaches the upper limit of the tip speed ratio. Typically, the upper limit of tip speed ratio is 18. The lower limit in speed occurs at the lower limit in tip speed ratio. Under normal operation, this lower limit is 2.

Using Equation 5.2 and the range of wind tunnel operating conditions, one can define the range of rotor power by a range of C_P. With Equation 5.4 the torque range for a given speed can then be defined by a range of coefficients of power. Theoretically the maximum coefficient of power is 16/27 [48]. The coefficient of power could go as low as 0.05.

For the dynamic stall experiments the range of tip speed ratios will be between 2 and 4.21. During dynamic stall conditions the rotor is yawed and operating far from ideal conditions. It is likely that the coefficient of power under these conditions will be small. It is estimated that the range of the power coefficient will be between 0.05 and 0.2.

The required rotor speeds to achieve the desired tip speed ratios is given in Table 5.1.

Figure 5.5 shows the speed and torque of the operating windows discussed above. The window defined by power coefficients and tip speed ratios for full wind turbine operating conditions is shown as the 'Overall' window. The window defined by power coefficients and tip speed ratios for the dynamic stall experiments is shown as the 'Experiment' window. The points labeled 'Experiment Speed' are the results from Table 5.1.

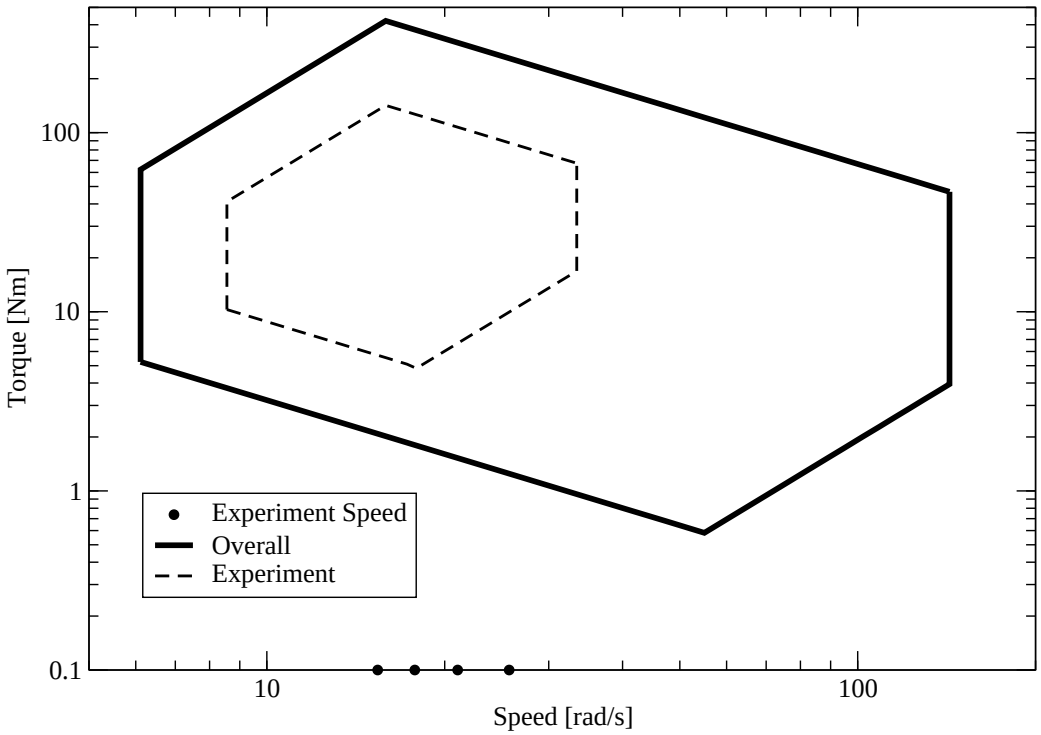

Figure 5.5: Expected Operating Conditions for Experimental Wind Turbine Rotors

The overall window represents the ideal criteria for the rotor loading. This is based on the absolute maximum power and speed one could ever expect in a wind turbine experiment. The experiment window is the criteria to perform dynamic stall experiments in the wind tunnel. The rotor loading system must achieve the experiment criteria at minimum and cover as much of the overall window as possible. The 'Experiment Speed' points confirm the parameters of the experimental window.

The operating windows in Figure 5.5 assume that in all cases the rotor will be producing a positive torque, where energy will have to be absorbed from the system. There are conditions where the rotor will operate in off design circumstances, here the rotor produces negative torque and requires additional power. There is potential for research into wind turbine operating under these off design conditions. It is difficult to know now what would be the largest negative torque generated for a given speed. Since by application wind turbine rotors are meant to produce positive torque, it is reasonable to assume the largest magnitude of negative torque will be less than the largest magnitude of positive torque. This assumption allows the operating windows in Figure 5.5 to be used in both positive and negative torque situations. It is important the rotor loading system can absorb and supply power within these operating windows.

5.3 The design of the current loading system

5.3.1 Drive Train Load Devices

Two possible load devices are readily available. The first is a DC motor. They are electrical devices that can absorb and supply power in either direction of rotation. In the literature, a very large majority of wind tunnel experiments were loaded electrically. In most articles the type of electrical loading is not specified, however in three articles DC motors were used, the smallest was approximately 10W while the most powerful motor was 4.21kW. In field tests, DC motors have be successfully used in wind turbines with rated powers up to 300kW. The wide range of applicability of DC motors and the popularity of electrical loading in wind turbine experiments makes the DC motor well suited for the application.

Maximum Power [kW]	3.5
Maximum Speed [RPM]	3300
Maximum Speed [rad/s]	345.6
Maximum Torque [Nm]	10.13
Maximum Field Voltage [V]	240
Maximum Field Current [Amp]	0.76
Maximum Armature Voltage [V]	240
Maximum Armature Current [Amp]	15

Table 5.2: Properties of the DC Motor

The performance statistics for the motor are given in table 5.2. The unmodified performance of the DC motor is not sufficient to cover any of the operational windows. The power though shows that it is sufficiently sized to cover the experiment operating window. Gearing will have to be employed to increase the torque up the levels expected at the rotor.

The second loading device is a mechanical brake specially used for setting specific torsion loads. The brake consists of a drum with a rope wrapped around it, the weights on the rope apply a constant torque on the drum giving a steady load. The energy absorbed is drawn from the brake by cooling it with water. The brake has already been successfully used in many experiments, in those experiments a maximum torque of 27.9Nm was achieved, the brake was successfully operated at a maximum speed of 77.0 radians per second. The maximum power achieved was 1.613kW at a speed of 60.737 radians per second and a torque of 26.6 Nm.

5.3.2 Drive Train Gear Configuration

There are several ways of achieving a gear ratio in a drive train. Toothed gears, chains and belt drives can all increase and decrease the speed and torque of mechanical power. It is expected that the torque under dynamic stall conditions could go from positive to negative. Toothed gears and chains are not well suited for torque reversals. While loaded the teeth of the gears and sprockets are not constrained in the opposite direction of the

torque. When the torque is reversed the gear and sprocket will rotate freely until it impacts the tooth or chain link on the other side. The dead zone in the drive train will make precise control impossible, repetitive torque reversals will wear out the drive train quickly. For these reasons the belt drive is best for the drive train.

There are several types of belt drives, V belts are the most economical but can slip and can complicate precise speed control. Toothed belts are best suited to achieve precise speed control. There are several standard tooth belt architectures, however only the PolyChain and PolyGrip architectures by Gates (www.gates.com) are suited for the expected loads of either operating window.

The speed of the DC motor will need to be reduced by 2.416 to match the maximum speed of the overall operating window. At this gear ratio the torque of the DC motor can only load a rotor at torques below 24.5 Nm. The DC motor cannot be used to load the rotor over the overall operating window. At this gear ratio the DC motor would fail to load rotors over much of the experiment operating window. Therefore, the maximum torque is 142Nm.

To cover all the operating conditions within the experiment operating window a second gear ratio is required. The speed of the DC motor needs to be reduced by 10.330 to achieve the maximum speed of the experiment operating conditions. At this ratio the motor can load rotors with torque loads as high as 104.64. This is still less than the maximum of 142 Nm however this shortfall could be absorbed by the mechanical brake.

Using two gear stages will allow both gear ratios to be achieved using the same sprockets. One of the stages could be reversed to alter the overall gear ratio. The ideal gear ratios to achieve this can be found by solving Equations 5.5 and 5.6 simultaneously. The solution to system is the first stage is set to a gear ratio of 4.996 and the second stage is set to 2.068. In the sprocket catalogs those two gear ratios cannot be perfectly replicated. The closest gear ratio for the first stage is 5.090 and the closest ratio for the second ratio is 2.045.

$$10.330 = N_1 N_2 \tag{5.5}$$

$$2.416 = \frac{N_1}{N_2} \tag{5.6}$$

Figure 5.6 shows the same operating windows as shown in Figure 5.5. The figure also shows the maximum rotor torque that can be absorbed by the DC motor. The gear ratio is not suitable to perfectly match the maximum speeds of the operating windows. The DC motor would have to run over speed by 0.8% and 3% to match the maximum speeds of the experiment and overall operating windows respectively. This is a very small over speed condition that would be acceptable for short periods of time. The figure also shows the additional torque required from the rope brake to cover the respective window.

Figure 5.7 plots the required rope brake torque for each of the respective operating windows with the known limits of the rope brake. The required rope brake torques for the overall operating window is larger than the torque absorbed by the DC motor. Looking at Figure 5.7 the required torque for the overall operating window is 315Nm, this is larger than the maximum known torque achieved in previous experiments. It is unlikely that the system will supply enough torque over the entire overall operating window. The required braking torque in Figure 5.7 for the experiment window is still larger than the maximum torque but is sufficiently small to be feasible. The system will be able to absorb torque over the experiment window. Overall, the system is suitable for the experiment window and partially suitable for the overall window.

5.3.3 Drive Train Flywheel

The criteria and constraints require an additional inertia to be added to the drive train to absorb some of the high frequency torque variation. A readily available flywheel was analyzed to determine its applicability. The details of the analysis are found in Appendix J. The study found that the flywheels inertia of $0.313 kgm^2$ far exceeded the minimum given in Section 5.2.1. The study in Appendix J also performed a structural analysis on the flywheel to ensure that catastrophic failure was highly unlikely under worst case conditions.

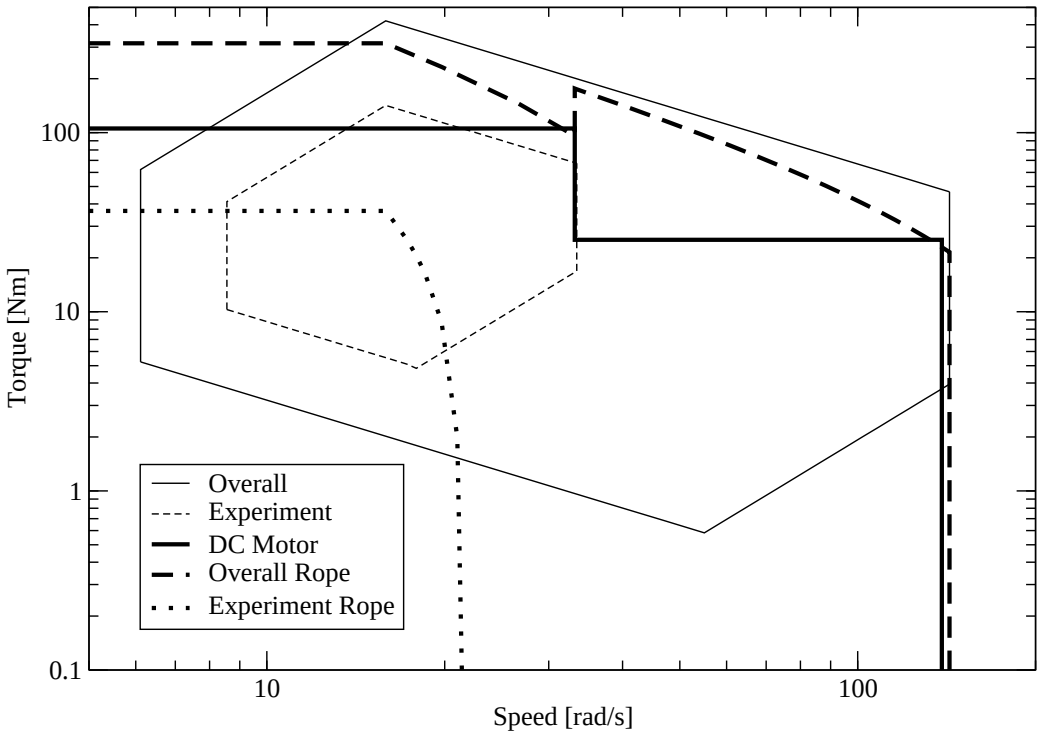

Figure 5.6: System Operating Window

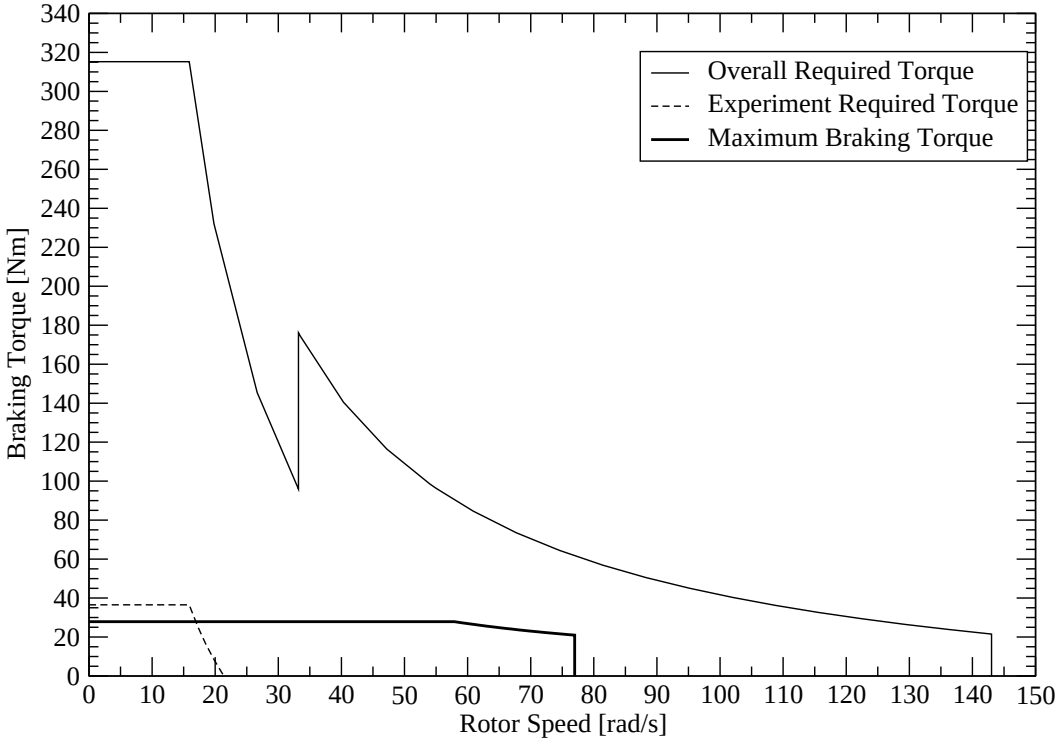

Figure 5.7: Required Braking Torque

5.4 Rotor Load Control

It is important that users of the apparatus can control the speed of rotor. The most sophisticated methods for such control is to use control electronics based on closed feedback loops. Several such commercially available controllers were considered. Alternatively, a passive controller can be assembled based on freely available equipment. The passive controller cannot automatically maintain a constant speed, only allow an operator to have control over the load torque.

At this time the ideal control mechanism is still under investigation. The results of investigating multiple load control strategies is given in Appendix K. Two different commercially available architectures were evaluated. In the appendix a design for a passive controller using readily available equipment is given.

The appendix also discusses how in the future various load control mechanisms could be implemented in the future. Overall the current rotor loading system maybe inadequate for long term research goals. Acquiring and installing a commercial controller requires a large investment that may not be required for the intended experiment. Instead the passive controller will meet the needs of the dynamic stall experiments with little investment. Once the apparatus is built and experience is gained from its use a better understanding of the rotor loading limitations will be understood. At this point an educated decision on a rotor loading mechanism with closed loop speed control can be made.

Chapter 6

Mechanical Design of the Wind Turbine Frame

6.1 Aspects of Mechanical Design

6.1.1 Design Criteria

The primary purpose for building this apparatus is to test wind turbine rotors for long term aerodynamic research. The first application of this apparatus is to perform PIV measurements on the blades in the rotating domain. If designed properly, the apparatus can be flexible enough to address other issues like stall delay, wake structures and other issues.

Most applications of this apparatus will be to investigate the aerodynamics. The aerodynamics of an actual wind turbine rotor are complicated by many of the objects and fluid structures beyond the rotor, these objects include the nacelle and tower, but also the atmosphere and ground objects. These complications have made it difficult to gain a strong understanding of the aerodynamics. Eliminating the unpredictable effects of the field along with secondary effects from structures is the key benefit to testing in a wind tunnel. It is important that these benefits are preserved. Chapter 4 discusses a detailed study to preserve the integrity of the flow field in the wind tunnel independent of the structure of

the apparatus itself. The nacelle, hub and tower will affect the flow, it is important that this effect is minimized.

The hub and nacelle are located in the center of the rotor, this area has very little contribution to the aerodynamics of interest. The hub and nacelle needs to be designed aerodynamically to minimize its influence on the flow field of interest. This can be accomplished by adding an aerodynamic cowling around the apparatus. The detrimental effect of the tower is ubiquitous in the field. Economic and structural considerations force turbine manufactures to compromise on the rotor and tower spacing. The tower effect is prominent because the tower is in the annular space of interest. The additional complications of spacing the rotor and tower for minimized effect is justified for experimental applications. Using the potential flow Equation 6.1, the tower needs to be 5 tower diameters away from the rotor plane to have a 1% effect on the flow.

$$\frac{V_\infty - V_r}{V_\infty} = \left(\frac{r}{x}\right)^2 \tag{6.1}$$

Having laser optics in the stationary and rotating domain complicates the design further. Lasers are highly sensitive to deflection in the structure, erroneous deflection and movement of the laser beam will distort the results. The various loading conditions will induce deflection, the operation of a wind turbine is unsteady by nature hence much of the loading will be as well. This unsteady loading can induce further deflections through vibrations and other dynamic effects. The effect of steady deflection can be corrected by adjusting the optics, however nothing can be done for varying deflection. It is critical that vibrations are minimized in the apparatus. Maximizing stiffness will contribute to minimize deflection in both static and dynamic loading conditions. Overall much of the structure will be designed for maximized stiffness. Under dynamic conditions there is a larger contribution from mass on the deflection. For critical components, dynamic analysis will be used to minimize vibrations and other dynamic effects.

Primarily, the apparatus is being designed for PIV measurements of the blade in the rotating domain. However there are many other applications for the apparatus, the requirements for other experiments in these areas is unknown at the time of design. To accommodate unknown requirements, the flexibility of the rig is to be maximized. This can be done by implementing adjustability in the apparatus. It is expected that physical

modifications will be made to the apparatus to allow future experiments, flexibility is given by minimizing the potential for these modifications. Permanent means of fastening parts like welding and bonding will be avoided in preference for removable fasteners like bolts. Making the apparatus large allows future additions without modifying the apparatus to fit the addition, thus the size is expanded when there are little aerodynamic effects.

6.1.2 Velocimetry Acquisition in the Rotating Domain

Additional considerations are needed in the design of the hub. This sub-assembly holds many of the components necessary for performing the Laser PIV and pressure acquisition. Since much understanding about airfoil aerodynamics is relative to the airfoil, there is a lot of information that could be gained from measurements in the rotating domain. To achieve this the hub needs to be specially designed to provide illumination and image acquisition.

Figure 6.1 shows a diagram of how a custom turbine can collect PIV measurements in the rotating domain. The laser emits the beam down the hollow shaft. A rotating mirror at the end reflects it out radially along the boom. At a specific location a second mirror is coupled with sheet optics to reflect a laser sheet on the blade section of interest. The camera mounted within the hub collects images of scattered laser light. The images are then used to determine the flow field. Simultaneous measurements of pressure are taken with the PIV measurements. The data acquisition system is mounted within the rotating domain as well.

To collect these measurements the hub needs to support a camera pointing radially behind the blades. To provide illumination the nacelle needs to support the laser head. Two things need to be designed into the hub to transmit the light to the blade. First a hollow shaft will allow the beam to travel along the axis of rotation. The mirror mounted in the rotating domain can only give consistent radial reflections if it is reflected at the axis of rotations, this can only be achieved if the beam travels axially in a hollow section. The second feature to be designed into the hub is a boom to support the laser optics behind the blade. Finally, mounting the pressure sensors in the blade requires the pressure data acquisition system to be mounted in the rotating domain, hence in the hub.

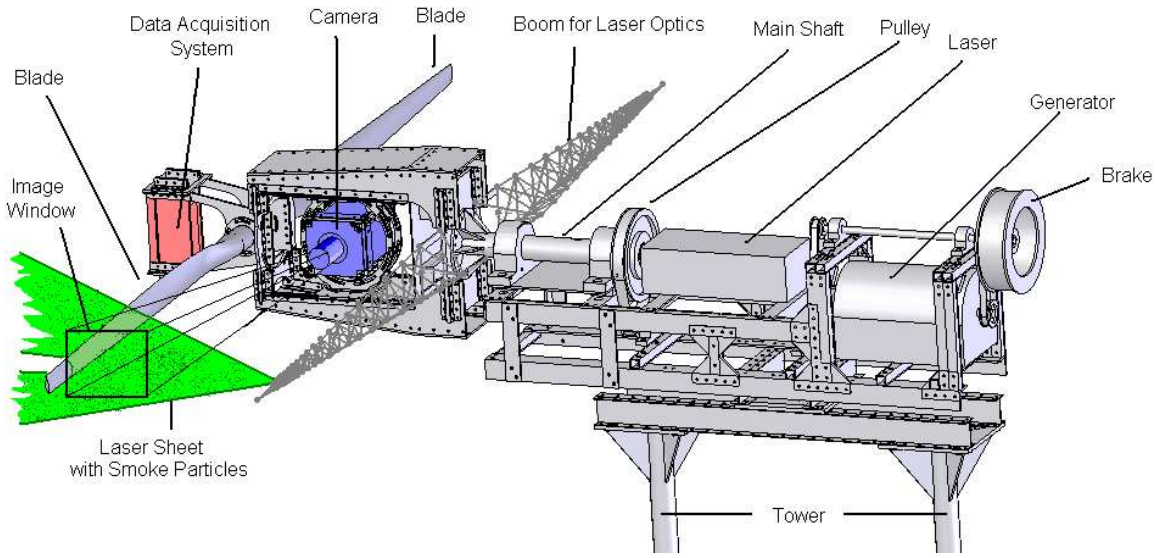

Figure 6.1: Diagram of Laser PIV Acquisitions in the Rotating Domain

6.1.3 Sub-assemblies of the Apparatus

Most of the apparatus can be divided into five major sub-assemblies. The design of two assemblies was already discussed in dedicated chapters. The first sub assembly is the data acquisition system found in Chapter 3. Second is the system to counter the aerodynamic loading, this is covered in Chapter 5. The sub assemblies documented in this chapter are the tower and the base, nacelle and the hub.

The tower and base are meant to hold all the other assemblies up to the height for optimal rotor operation. The engineering of this assembly ensures that it is structurally sound to resist all the forces that will generated in the rotor. The analysis looked at worst case static conditions. Dynamic effects were neglected, the consequences of vibration will be analyzed when the rotor is in operation. This assembly was not designed with guy wires so that it could be reinforced to counter any particular vibration mode.

The nacelle is designed to house all the components in the stationary domain and the mountings for the rotational domain. This includes the motor, the shafts and any experimental equipment in addition to the laser head. The nacelle is made to be long for flexibility in the wind direction but compact else where for minimized aerodynamic effects.

Further flexibility is engineered in the nacelle by making yaw, shaft position and tower position adjustable. Adjustable yaw allows the testing of different yaw errors, with the base fixed in the wind tunnel, adjustable yaw error is critical for dynamic stall research. Adjustable shaft positions allow fine tuning of the rotors axis of rotation. Adjustability on the intermediate shaft allows different sprockets for different gear ratios to be installed. The nacelle is mounted onto the tower at its center of gravity, future experiments may have a different weight distribution, and this will require a different mounting on the tower.

The application of the hub in this apparatus is complicated, the conventional purpose of holding the blades is preserved, and additional requirements are added for experimental purposes. The hub holds all the components that are on the rotational domain, the camera, the pressure data acquisition system, the communication and control computer and the optics for illumination on the rotational domain. The flexibility of this assembly was the main criteria invoked for mounting the camera, many axis of adjustment were included to allow for precise positioning of the camera. Compacting this assembly forced the camera to be mounted in the center, with the structural members straddling the camera. This architecture complicated the design and required extensive analysis to ensure structural integrity. The rotation and beam loading complicates the loading case, while additional fatigue considerations force a more stringent maximum stress constraint. Dynamic effects were analyzed with a simplified model, the results showed that vibrations are most sensitive to the blade properties. The stringent stress constraints made for a hub much stiffer than in the simplified model, thus dynamic effects were further mitigated.

6.2 Finite Element Based Truss Analysis Methods

In the mechanical design several truss type structures were used to support various components. To aid in the design and structural analysis two different FEM based structural analysis codes were developed. The analysis codes enabled the structure to be optimized by expediting the analysis. The finite element method incorporated the effect of non-linear behavior. Without the analysis code this would have been too difficult to determine manually.

The first code is meant to analyze a truss that is defined within 3 dimensions. The element orientation, force and displacements are all in three dimensions. In each element, bending loads are assumed to be negligible, so rod elements are used for the elements. This code is referred to as the three dimensional Rod based method, it is discussed in Section L.1 of Appendix L. The second code is meant to analyze structures that are designed to resist shear and bending loads. Here a beam element is used instead of a rod element. Coupling compression and bending loads can lead to early non-linear failure like buckling, iterative methods were implemented to account for these non-linearity's. Beams defined in two dimensions are significantly simpler than three dimensions, hence the two dimensional code was implemented. Two dimensional codes can only analyze structures defined in two dimensions where all forces and displacement are in the same two dimensions. This analysis code is referred to as the two dimensional beam based method, and is discussed in Section L.2 of Appendix L.

6.3 Design of the Base and Tower

6.3.1 Overall Architecture of Base and Tower

Structural integrity is an important consideration for developing the architecture of this assembly. Figure 6.2 shows the free body diagram for the assembly. Equation 6.2 gives the thrust for a wind turbine rotor, maximum values occur when the turbine is operating in the turbulent wake state [48]. A typical coefficient of thrust (C_t) for this state is 1.2 [48], the acceptable rotor diameter was found in Chapter 4 to be 3.272m, the maximum velocity of the wind tunnel is 13m/s and the density of air was assumed to be $1.2kg/m^3$. Using these values the thrust was 1.0kN for F_2. To account for dynamic effects and give a safety factor F_2 was assumed to be 2.0kN. The combined weight of the nacelle, the hub, blades and all the experimental equipment was assumed to be 1kN.

$$F_T = \frac{1}{8} C_t \rho \pi D^2 V^2 \tag{6.2}$$

The first challenge was to determine how to counteract the forces F_1 and F_2 overall. At the base F_1 and F_2 result in a 1kN normal force, 2kN shear, 6.2kNm bending moment.

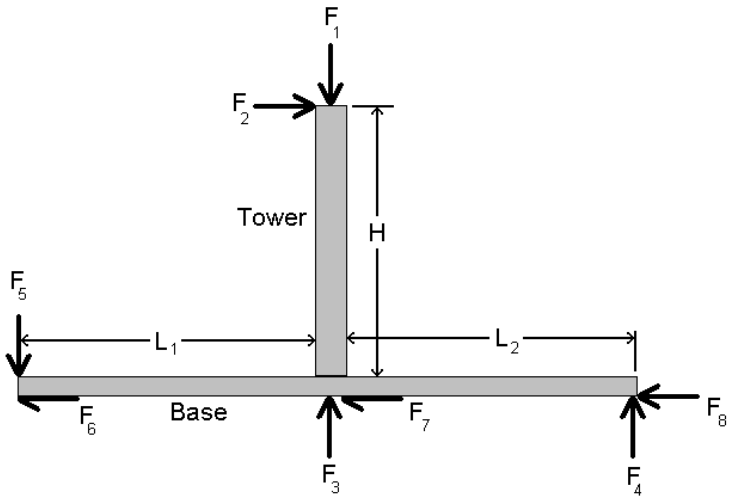

Figure 6.2: Free Body Diagram of Tower and Base Assembly

Assuming that the base could not be bolted to the floor, F_5 could only contribute to the moment with weights. Countering 6.2kNm moment would require mass of the order of 100kg or more. Having this mass upstream would have an effect of the flow at the rotor plane, thus weighting the base upstream is not desirable. Without floor mounts F_5 would be zero, only F_4 would be able to counteract the moment. The maximum force of F_4 is 1kN, hence L_2 would be at least 6.2m. Without solid floor connections the shear forces would have to be countered by friction. Several 2.409m long 2mm walled 53x30mm angle iron members are freely available. Several holes have been pre-drilled to allow four of them to be bolted together to form I beams. Neglecting the effect of the holes, these I beams are amongst the strongest members available. With the high bending moment in the base, these members are ideal for the base. The I beams could be bolted together to extend out to 6.2m.

Extending the I beams will compromise their strength, also the overall length of the base will make it awkward to install in the facility. There is uncertainty in the maximum static friction force available to counter the shear forces. Bolting the assembly to the floor of the wind tunnel eliminates any uncertainty in countering the shear force and relaxes the L_2 length requirements. To reduce the forces on the floor mounts, maximizing the

lengths of the base is still desirable. Thus the final architecture for the base entails using a 2.4m long structure out in all four directions, then bolting the beams to the floor in a pre-stressed state that will counter the large moment. The magnitude of F_4 and F_5 by distributing the moment evenly is 1.3kN, well below the expected strength of the floor mounts. Using multiple floor mounts at the ends will further reduce the forces on the floor mounts and increase the safety factor.

The poor aerodynamic properties of the I beams make them unsuitable for the tower members. Three 3m long tubes are freely available. The outside diameter is 76.2mm with a wall thickness of 1.8mm, making them very stiff. The round cross section gives better aerodynamic properties, and buckling strength in all directions. Initially, a single tube tower like those in the field was considered. Yet unlike turbines in the field, the direction of the flow in a wind tunnel is constant. Adding a second member down wind of a tower member will have negligible effect on the aerodynamics. As the force F_2 is applied, a single vertical member would bend back pointing the rotor up and introducing yaw error. The second vertical member adds more desirable deflection characteristics, as force F_2 is applied the base two vertical members and top section will deform as a parallelogram. This shape will not introduce yaw error to the rotor flow. The final architecture for the tower entails two tubular members either upwind or downwind from each other. An example of this architecture is given in a computer generated image in Figure 6.3.

6.3.2 Highly Loaded Tower Architecture

Given that the frame is the heaviest component contributing to the gravitational load, it is unlikely to vary greatly over the life of the apparatus. The axial loading from the aerodynamic forces could vary greatly. Larger rotors operating at higher wind speeds at larger thrust coefficients would give significant increases in the thrust forces. The rotor could operate at thrust coefficients higher than 1.2. Under these unique situations the tower structure may not be strong enough to resist the thrust.

Optional tower reinforcement has been designed for these special cases. The reinforcement needs to support the increased axial loading of the structure, but not the gravitational loads. The strut will be placed between the top rear corner of the top and the far rear location of the base, Figure 6.4 shows a schematic of where the additional struts are. Here

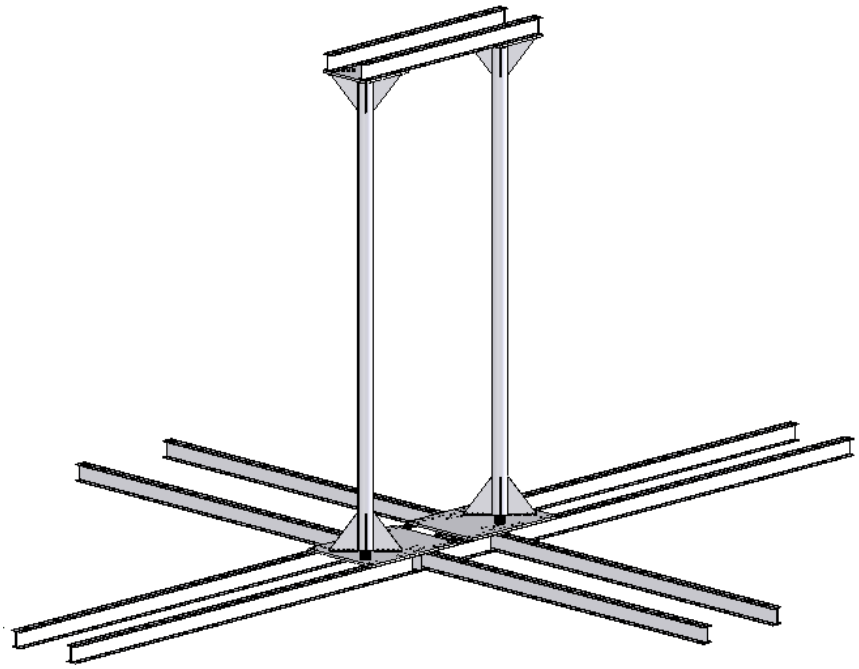

Figure 6.3: Tower and Base Architecture

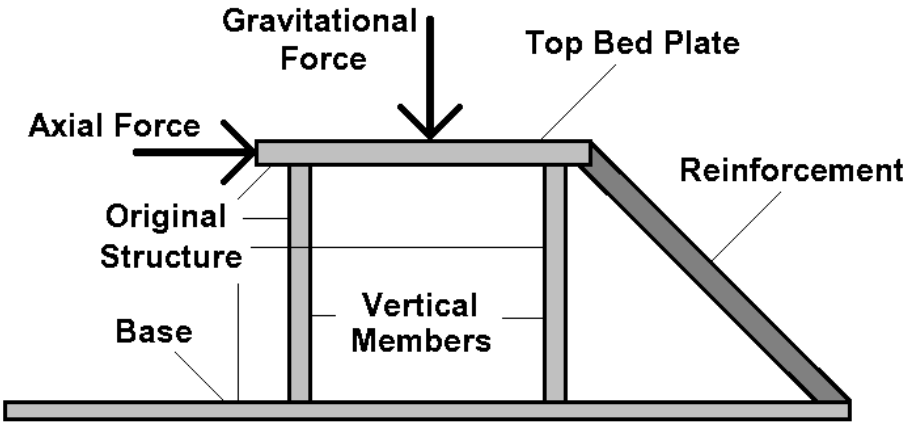

Figure 6.4: Reinforced Tower Architecture

the struts will transmit the axial loads from the tower top to the base. The two vertical tower section will still support a majority of the weight, making the structure stronger overall. This version of the tower is referred to as the highly loaded tower, the original tower is referred to as the lightly loaded tower.

6.3.3 Tower Structural Analysis

An extensive study in the structural integrity of the tower was performed. The details of the study are given in Appendix M. The study looked at the stress in both architectures of the tower over a wide range of axial thrust loads. The study also used the finite element based solid modeling software package Abaqus 6.5-1 [41] of the gusset connections of the vertical members.

Overall, the study found for the lightly loaded architecture the horizontal placement of the nacelle had negligible effects on the safety factor. With an axial load of 1000N the safety factor is about 3.4. The stress in the lightly loaded architecture started to approach dangerous levels when the axial thrust exceeded 1000N. Under worst case scenarios the gusset connections did not add any additional stress due to stress concentrations. The maximum stress in the reinforced architecture was relatively insensitive to the axial load. At an axial load of 4000N the safety factor was 6.7.

6.4 Design of the Nacelle

6.4.1 Architecture of the Nacelle

The nacelle holds the motor, the bearings for the main shaft, the remainder of the drive train and the laser head. Overall the nacelle is a frame assembly that holds all these components together. Basic structural integrity criteria apply for most of the frame, however the laser head is critical in collecting data. It is important that there is little relative motion between the laser head and the main shaft, hence additional stiffness is needed here. The nacelle should be compact to avoid disturbing the flow at the rotor plane.

The relative position of all the components is needed before the frame can be designed around them. Several concepts for components placement were considered. The concept shown in Figure 6.5 was chosen because it gave more space for additions and its shape had the smallest frontal area.

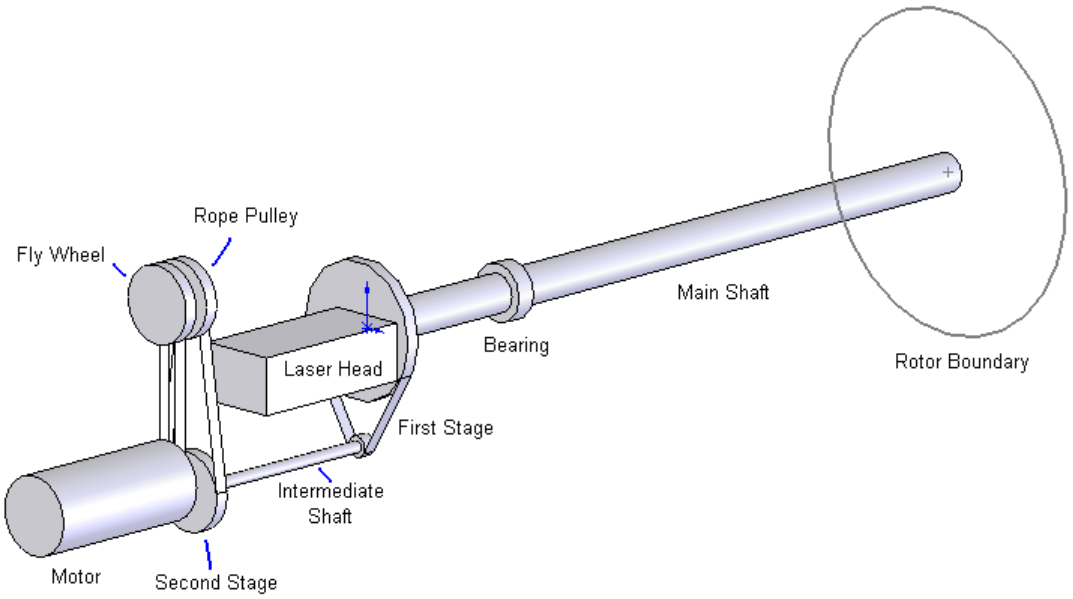

(a) Perspective View

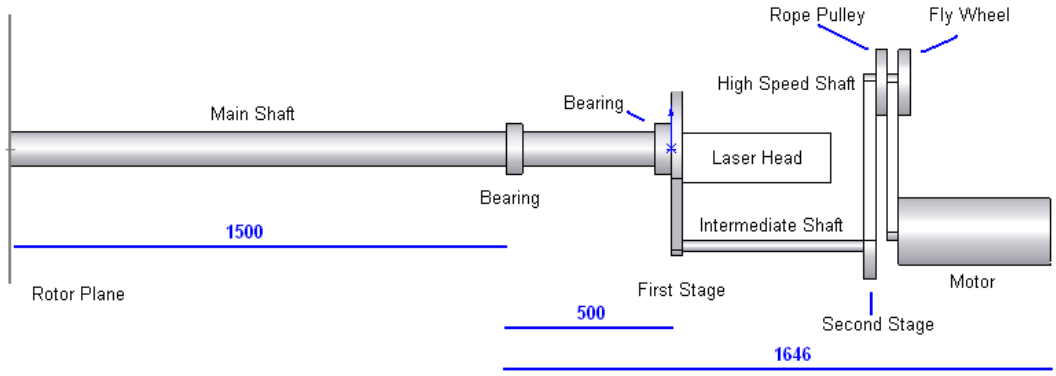

(b) Side View

Figure 6.5: First Component Placement Concept

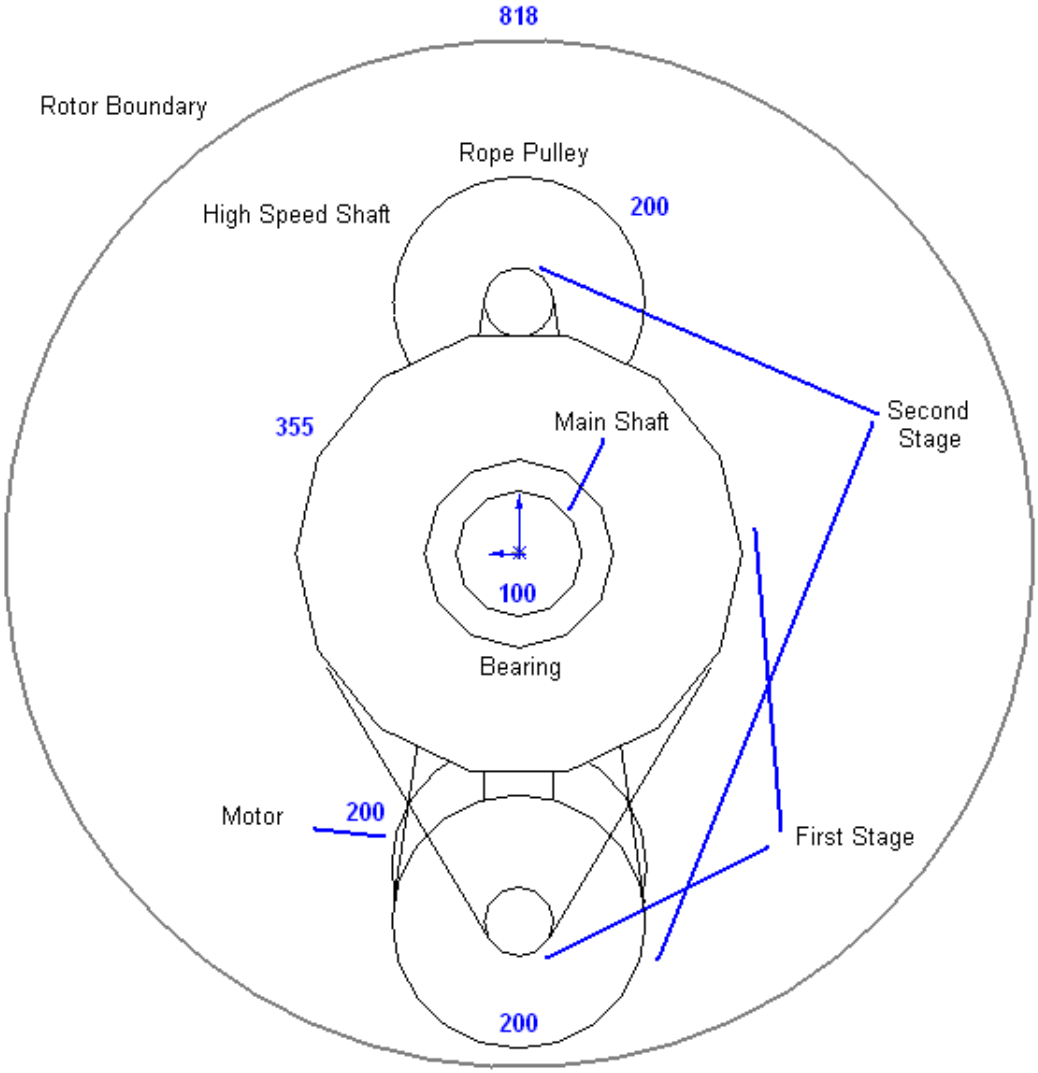

(c) Front View

Figure 6.5: First Component Placement Concept - Continued

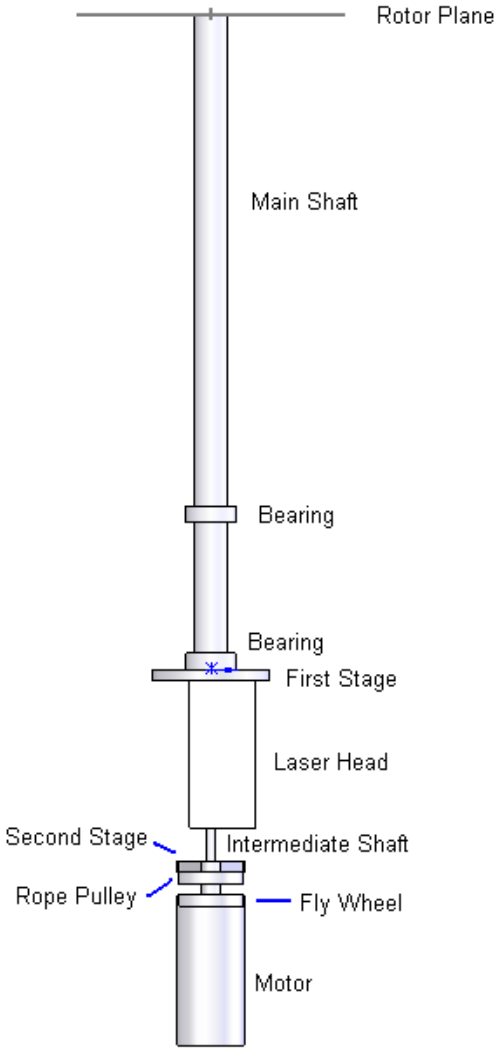

(d) Top View

Figure 6.5: First Component Placement Concept - Continued

The conceptual drawings in Figure 6.5 shows the belts driving the generator at the front. This orientation was changed early in the detailed design phase. Driving the generator from the back reduces the aerodynamic impact of the brake and flywheel and prevents water getting on the motor if and when the brake is water cooled. Another modification had the secondary shaft shifted laterally to accommodate cables going to the laser head or fiber optics in place of the laser head.

Further details on the design of the nacelle are given Appendix N.

6.5 Design of the Hub and Rotary Components

6.5.1 Architecture of the Hub

The function of the hub is to hold all the components on the rotating domain. These components include the blades, the data acquisition system, the camera, the computer for control and communication and the laser optics. The camera placement is constrained by it ability to collect data, the camera needs to the area of interest with an unobstructed view. The area of interest for the current application and many other applications is the flow at the blades. Flexibility in the camera mount will allow fine adjustment on the camera to capture good images of the area of interest. Maximizing what the camera can image will allow many other areas of research. The hub needs to be compact to minimize aerodynamic distortion.

Several concepts were considered for the Hub. The first pair of concepts explored the use of a central shaft, with the camera mounted on the outside. In both concepts the inner boundary of the aerodynamically active region was too close to the camera. A more inward mounting of the camera on the shaft is achieved, by eliminating the adjustability, however the aerodynamically active region was still too close. A third concept shown in Figure 6.6, gave the best camera position, by mounting the camera in the center of the hub. The structural elements fork out and around the camera. This concept has 5 axis of adjustment for the camera. First, azimuth position of the blades can be adjusted. Second, the lateral position of the camera along the axis of rotation can be adjusted. Third, the angle between the axis of rotation and the camera view is adjustable. Forth, the camera can rotate about

its own view axis, this allows the image orientation to match that of the phenomenon. Fifth, the camera can translate along its own view axis, when the phenomenon is within the minimum focal length the camera itself can be moved back. Due to its high degree of adjustability and its smaller frontal profile the third concept in Figure 6.6 was chosen.

6.5.2 Dynamic Analysis of the Shaft and Rotor

Reducing vibrations in the rotor and the shaft is important for collecting undistorted laser based measurements. To minimize vibrations a study into the dynamics of these components was conducted. The study attempted to minimize the first fundamental frequency of these components. It is assumed that high fundamental frequencies will make the structure resistant to vibration. Commercial software was used to determine the various vibration modes.

The study looked at several different geometric properties. The first was the effect of the shaft length, the second was the material thickness on the blades, third the material of the blades, finally the study also looked at the effect of material distribution on the blades.

All the details of the study are given in Appendix O. Overall the study found that with a shaft length less than 1.0m the frequency depended strongly on the stiffness of the blades. This adds further justification to having carbon fiber blades. The blade frequency was maximized when the material distribution was parabolic. With a parabolic distribution both blade and system frequency increased with increasing material thickness. A 2mm skin thickness still resulted in a frequency above the maximum expected from the rotor.

6.5.3 Design of a Mount for Laser Optics

To illuminate the flow at the blade a laser light sheet will illuminate a plane perpendicular to the blade. To achieve a perpendicular light sheet, optics will need to be mounted on a boom directly behind the blade. A laser beam will travel radially along the boom, at the specified radius the laser will reflect, into the axial direction, from a mirror. A set of sheet optics will diverge the laser light illuminating the desired plane. The camera and the laser will be set to collect data from a specific plane. If the laser is deflected a different plane

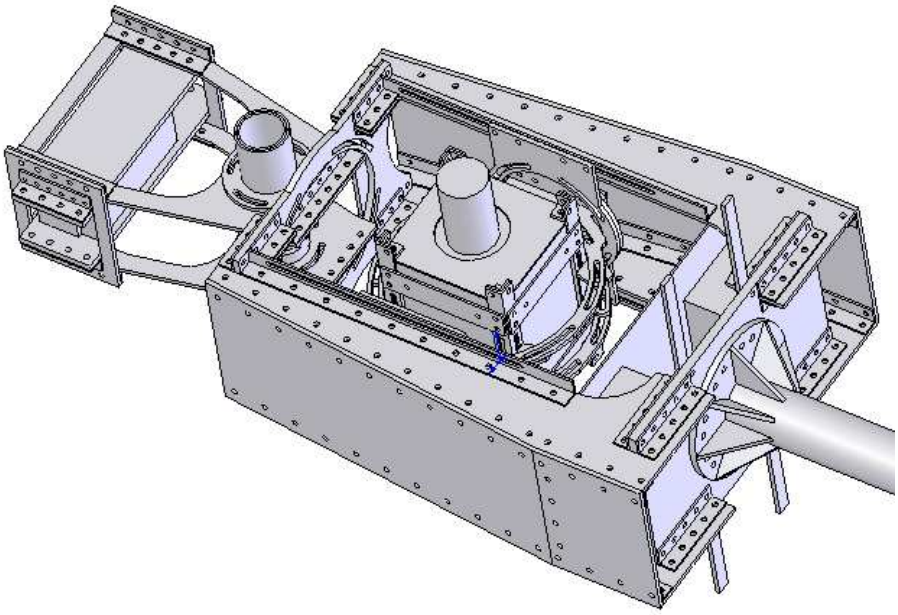

(a) Perspective View

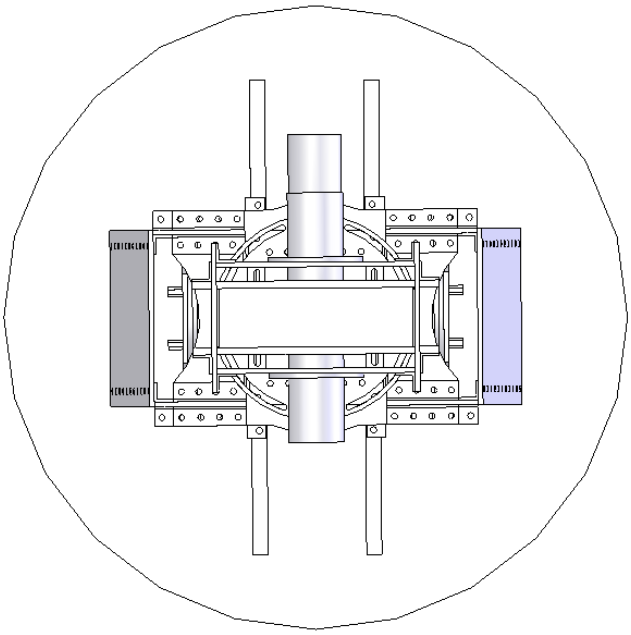

(b) Front View

Figure 6.6: Hub Concept 3

will be illuminated, the image would be out of focus and the results will be distorted. It is critical that deflection is minimized.

Steady state deflection can be corrected iteratively, by continuously adjusting the camera and optics. Varying deflection during an experiment will be impossible to correct. Hence, steady loading will have little impact, while varying loads will vary deflection and induce vibrations. The boom will be subjected to three forces, the centripetal acceleration of rotation, aerodynamic loading and gravity. Centripetal acceleration will be constant with constant rotation and minimal radial motion. Variable aerodynamic loading is expected since the boom will be moving through a turbulent flow field. Regular variable loading is expected from gravity, relative to the rotating boom, the direction of gravitational pull will be continuously changing.

Deflection will be minimized by maximizing the stiffness of the boom. The regular loading on the boom could excite a given mode of vibration. To avoid sympathetic vibrations, the boom will be engineered so the lowest natural frequency is greater than the expected rotation. Generally the stiffness is proportional to the materials modulus of elasticity and the structures area perpendicular to the deflection. Generally the fundamental frequency increases with stiffness and decreases with mass. Thus, a close to optimal stiffness along with reduced gravitational loading should be obtained if the fundamental frequency is maximized. Material selection should maximize the modulus of elasticity while minimizing the density. The structure needs to minimize mass by minimizing the amount of material used, the material should be used efficiently to give a lot of area perpendicular to the loading.

Truss architecture will be used for the boom structure. When a truss is loaded, there are dominant axial loads in the members, while bending moments are negligible. Axial loading is most efficient since all the material is equally stressed. This loading property of a truss will give maximum area perpendicular to the loading, while minimizing the material usage. There are aerodynamic benefits to a truss, flow can pass through the structure, the only interference being very small truss members. This should minimize the aerodynamic loading on the boom.

Several materials were considered. Comparing the mechanical properties steel was selected for the boom due to its high stiffness to density ratio. This should minimize vibration and deflection.

The members of the truss arranged to form triangles throughout the structure. Three main members spanned the length of the truss, the main members meet at a point at the end of the structure. The distance between the main members at the base was set to be as large as possible for the space available in the overall design. A set of secondary members connected between each of the main members in a zig zag pattern. The structure overall would act as a beam, throughout a beam there is a constant shear stress. Shear loading is axial at 45 degree orientations. The inside angle in the zig zag was chosen so shear loading would be axial in the truss. The three dimensional shape made it awkward for 45 degree angles so 43.2 degrees was chosen instead. At a certain distance along the boom the main members were too close to accommodate anymore secondary members. At the base of the boom a set of members were added to anchor the structure to the mounting points. Figure 6.7 shows a computer generated image of roughly what the truss would look like.

Under loading the forces carried in the main members would increase from the end to the base. To minimize stress and maximize the fundamental frequency, the thickness of the members would increase in thickness from the end to the base. The forces in the secondary members would be less than in the main members and would be the similar for every secondary member. The same thin rod stock can be used for the secondary members. Three different available rod sizes were considered for the main elements, 1.6mm, 3.2mm and 6.4mm diameter.

The placement of the different stocks along the main member resulted in an optimization problem. Using thin material to make it lightweight would reduce the stiffness, while using the thick material to make it stiff would increase the mass. The mass needs to be reduced while the stiffness increased to maximize the lowest fundamental frequency. The optimization requires a means to evaluate the fundamental frequency of the design, the details of the analysis is given in Section L.1 of Appendix L. Simple techniques were employed for the optimization. A large set of viable solutions were analyzed, the one with the best properties were selected.

The details of the geometry for the boom are given in Appendix P. The details and results of a structural and dynamic analysis on the boom are also given in the appendix.

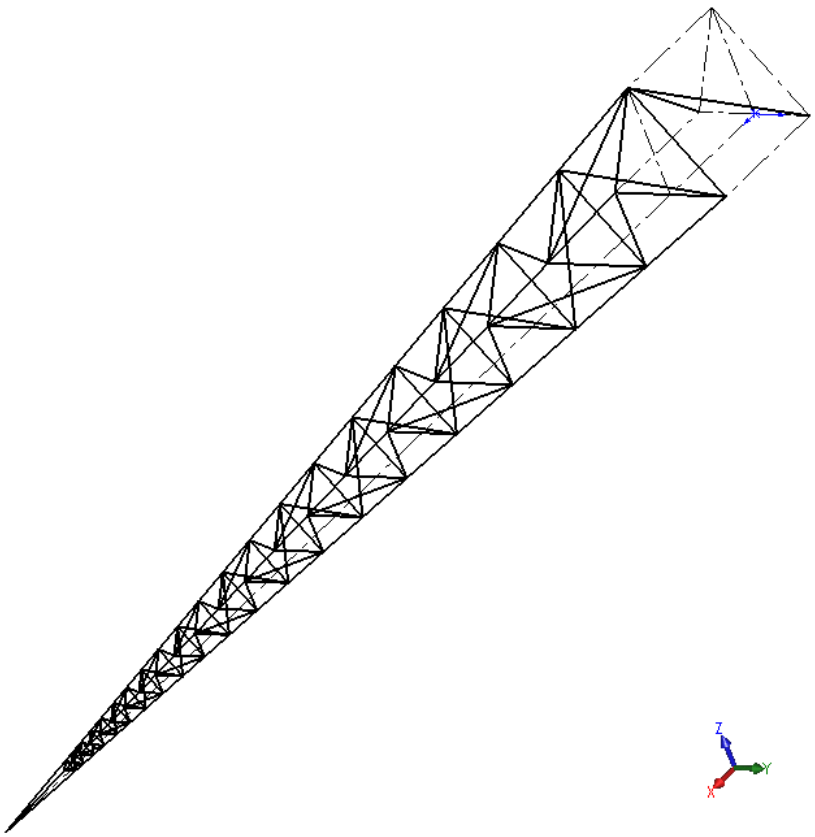

Figure 6.7: The Structure for the Boom

6.5.4 Structural Analysis of the Hub

Fatigue and deflection considerations made a structural analysis on the hub critical. To satisfy both considerations and simplify the design a stringent safety factor criteria of 10 was set on all components in the hub. In the analysis the worst case loading was used to evaluate the stress. In actual operation it is likely that the safety factor will be higher. This will make fatigue failure very unlikely, second the minimal strain will reduce deflection and overall the increased stiffness will maximize the fundamental frequency.

The commercial finite element based software Abaqus 6.5-1 [41] was used to model the stress in all the components in the hub. The limits of the commercial software prevented the analysis of the entire structure. The hub was analyzed by breaking up the structure into several overlapping solid models. The loads were determined based on beam theory. For further details refer to Appendix Q.

Chapter 7

Conclusions

There is still much understanding to be gained about the aerodynamics of the blades of wind turbines. Rotational effects are known to alter the stall characteristics and cause stall delay. With increased turbulence close to the ground unsteady effects are prevalent. One particular detrimental unsteady effect is dynamic stall. It is known to have strong forces associated with it and is difficult to accurately model. It is affected by a wide range of conditions; yaw angle, wind speed, turbulence level just to name a few. It is also known to have a complex three dimensional structure and can potentially create additional point of trailing vorticity. Dynamic stall will be the main area of research for the apparatus. There are other areas that are receiving much attention, flow at the tips is a potential inefficiency and a major source of noise. The flow itself is very complex and highly three dimensional. Overall, many studies are required for the blade to understand these issues.

Laser Particle Image Velocimetry (PIV) is a powerful non-intrusive technique for measure the flow field. It uses lasers to illuminate a two dimensional flow field and image it with a camera. The camera captures the scattered light from particles entrained in the flow. Two subsequent images are compared with statistical techniques to determine the displacement of the particles and the resulting flow speed. The method is powerful allowing the simultaneous measurement of a two dimensional flow field. Increased accuracy is achieved by not disturbing the flow field. For many of the blade flows this is an ideal measurement technique.

An important result of the flow field is the forces generated. To measure this pressure sensors are mounted to sample the surface conditions. A high speed data acquisition system is capable of resolving transient phenomenon.

Most aerodynamic understanding of airfoils is based on the domain relative to the airfoil itself. Extending that knowledge to wind turbine blades has proven challenging. The rotational effects are impossible to replicate with a static airfoil. Thus, achieving the wide range of experiments will require PIV measurements to be made in the rotating domain. To achieve this a custom wind turbine has been designed to operate within a wind tunnel.

Several preliminary investigations were required to finalize the design of the apparatus. First, a study was performed evaluating the applicability of Laser PIV measurements for transient flow fields was performed. The key conclusions are given in Section 7.1. The turbine was designed to operate within a wind tunnel, wind tunnels themselves have their own error associated with them. A study using computational fluid dynamics was performed to evaluate this error, the conclusions are given in Section 7.2. With all the major components of the experiment sourced out a system is needed to hold and control everything. A frame and loading system was designed to support everything and control the rotor potion. Section 7.3 explains all the major conclusions in the mechanical design.

7.1 Particle Image Velocimetry on Transient Flows

Experiments with vertical axis wind turbines were conducted to evaluate the applicability of PIV for transient flow measurements. Overall the method was able to capture the flow fields successfully. The system available was not able to capture time resolved images. Instead, phase averaged results were collected. This managed to capture many of the major structures in the flow.

There are techniques being explored within the literature, and the research group in extending PIV data to determine forces. The method requires the determination of the pressure field. The original PIV data was extended with these methods to determine the pressure. Several different versions were used, some ignored the transient terms, other ignored the Reynolds stress terms. It was found that more accurate estimation of the

transient term is needed. Also, accurate quantification of the Reynolds stress term is crucial. This particular term is sensitive to random error. Different ways of finding this term was tried with marginal success. Overall a time resolved PIV system, is better suited.

The high sample frequency gives better transient approximations and can potentially eliminate the need for resolving the Reynolds stress term. Using the conclusions mentioned above, and results from literature the data acquisition system was specified. The Photron SA-1 high speed camera was used to capture the images. The Pegasus dual head pulsed laser will provide the laser illumination. In addition to the PIV system a pressure data acquisition system was found. Many blade mounted small piezo-resistive sensors will sampled by the National Instruments compact DAQ system. To control all the equipment, a compact computer system has been sourced.

7.2 Wind Tunnel Effects on Turbine Flows

Ideally the flow of a large scale wind turbine would be perfectly replicated. Yet this is far too difficult, instead scale models will be tested. The use of scale models can introduce scaling error. Matching the non-dimensional Reynolds number is nearly impossible with the facilities at hand. To minimize the error, the turbine needs to be built as large as possible. A large turbine in a wind tunnel will introduce its own error. The boundaries of the tunnel flow will effect the flow and cause deviations from the ideal. To investigate these effects and to confirm a large rotor size computational fluid dynamics (CFD) was used to determine the error.

The commercial modeling package Ansys CFX 10.0 [40] was used to solve the flow fields of several wind turbine models. The control case was an infinite domain with no obstructions or boundaries. The results here represent the ideal turbine flow for testing. Several results of the turbine inside the tunnel was solved. The effect of thrust, wind speed and rotor placement on error was explored.

Overall it was found that the error was minimized when the rotor was placed slightly higher than the mid-plane. The normalized error was insensitive to the wind speed by varied greatly with thrust. The greatest error was a slight upwards deflection of the flow

and increased divergence. Overall the error was acceptable and a 3.272m diameter rotor will be use.

7.3 Mechanical Design of the Apparatus

With all the major components designed and specified the design of the frame and loading system can be conducted. The mechanical design entails the drive train supplying and absorbing energy to and from the rotor under constant speed control and the frame the support all the components and all the loads therein.

The rotor drive train and loading was designed based on components that were freely available. A 3.5kW DC electric motor was used as the main energy conversion device. Within the literature DC electric motors have been successfully used in wind turbine studies for a wide range of turbine sizes. Strict requirements were paced on the design of the rotor loading system, to ensure that the speed does not vary too much to alter the aerodynamics too much. To achieve constant speed operation a freely available flywheel was installed to provide sufficient inertia. As a back-up, additional mechanical brake is freely available to provide additional power absorption.

There are two torque and speed scenarios for loading the wind turbine. The first covers the wide range of experiments that could possibly be executed on the apparatus. This window is defined by high wind speeds high power coefficient and low tip speed ratio for the peak torque conditions. The peak speed is achieved at high tip speed ratios and wind speeds. A second operating window was defined for the dynamic stall experiments. This experimental window assumed lower power coefficients and a smaller range of rotational speeds. The loading devices could not cover the entire overall window but can load the turbine within the experimental window. Thus dynamic stall experiments will still be conducted on the apparatus.

There are two possible control systems. The first is based on freely available equipment. A variable transformer and variable resistance circuits have been designed to provide passive control. Given that the loading system may not be perfectly applicable for all research it may change. For these reasons the inexpensive passive controller will be used for ini-

tial experiments. At a later date when more is known about long term research goals, a commercial controller with closed loop active control can be used to control the system.

The frame design was divided into three sub assemblies. The first is the base and tower, the second the nacelle and the third the rotary hub. The sub assemblies were designed to provide maximum flexibility, and minimal aerodynamic interference. The use of laser based anemometry requires that deflections are minimized. In the rotary components where laser beams are being directed the frame has been designed to be very stiff.

The tower architecture was chosen to not introduce yaw error when loaded. Given that axial load can increase while gravitational is constant future experiments could have dramatically increased thrust. For these special case a reinforcement can be added to make the tower stiffer in the axial direction. The original structure was statically determinant and analyzed as such. At low axial thrust forces it was acceptable. The reinforced structure is statically indeterminate and was analyzed with a custom finite element based tool capable of accounting for non-linear behavior. The maximum stress in the reinforced structure has low sensitivity to the axial thrust. A safety factor of 6.66 was achieved for a thrust of 4kN.

The nacelle was designed with material that was freely available. The stiffest members were used to support the main shaft and the rotor components. The basic architecture is a long slender nacelle. This allows a lot of space for many additional components and gives a small profile for the oncoming wind.

The rotary hub holds the camera laser optics and data acquisition. Maximum flexibility was achieved by giving the camera mount three axis of rotation and two axis of translation. The aerodynamic interference was minimized by mounting the camera at the axis of rotation. The stringent constraints were placed on the components in the rotary hub. This sub assembly is facing fatigue loading and is directing laser beams. It is important the deflection is minimized and that stress it well below the endurance limits of steel. To accomplish both objectives the components were designed with safety factors of 10. Abaqus version 6.5-1 [41] was used for all the stress analysis. Abaqus 6.5-1 [41] was also used in a dynamic analysis to ensure that the first harmonic is above the rotational speed of the turbine. This will minimize vibrations and avoid sympathetic vibrations.

7.4 Overall Conclusions

Performing laser PIV in the rotational domain will reveal many valuable insights into wind turbine aerodynamics. A custom built wind turbine has been designed to perform these exact experiments. The applications include studying tip aerodynamics, the effect rotational forces and dynamic stall. Dynamic stall can lead to component failure and needs the most attention, as such it will be the main focus of the research.

Preliminary experiments were conducted to source the right equipment for the experiments. Computational fluid dynamic studies were conducted on the wind tunnel to ensure the flow represented one that would be seen in the field. The frame and rotor loading system has been designed for maximum flexibility without compromising the data acquisitions and phenomenon of interest. Overall, care has been taken to ensure successful measurements of dynamic stall. Adjustments may be required but no major re-designs should be needed.

The important conclusion of this apparatus is that it enables and experiment that has never been conduction. The measurements collected will be a first of its kind. Velocimetry has been applied to dynamic stall flow fields in two dimensional non-rotating conditions, this will be the first set of measurements in realistic flow conditions. This is crucial to develop a definitive understanding of this flow phenomenon in wind turbine blades. The true potential of this research is unknown but it could eventually lead to solving the dynamic stall phenomenon and extending the life of turbines making wind energy cheaper overall.

Appendix A

Review of Wind Turbine Technology and Development

Since the inception of the wind turbine in Persia in 900 AD there have been many configurations for wind energy conversion [89]. In the modern era commercial firms have based their success on three configurations. The Horizontal Axis Wind Turbine (HAWT), is a lift based propeller type turbine [89]. The Darrieus is a vertical axis lift based turbine [89]. Finally the Savonius wind turbine is a drag based vertical axis wind turbine. Commercially only the HAWT has achieved long term success [89]. They are more efficient than the Savonius [107], yet more robust than the Darrieus [92]. As such they are superior, thus will be the main focus of this thesis. The work in this thesis includes investigations in Savonius wind turbines, however this work was done to reveal information needed to investigate HAWT's further.

Modern day HAWT's convert kinetic energy in the air into electrical energy primarily for the electrical distribution grid. There are up to three secondary conversions to accomplish this. First the rotor blades convert the kinetic energy of the air into mechanical energy in the shaft. Optionally there is a second mechanical conversion in the gear box. The use of this conversion is dependent on the third conversion, mechanical to electrical. The electrical conversion will consist of a generator and possible a tertiary conversion to condition the electrical energy to a form suitable for the electrical distribution network. Many strong forces are created in the aerodynamic conversion, all these forces are carried by the nacelle

and down to the tower. Hence another critical component of wind turbine engineering is ensuring the structural integrity of the wind turbine.

Of all the critical components of wind turbine engineering, the aerodynamics is of primary importance. The engineering in aero-dynamics aims to maximize the forces that contribute to energy conversion while minimizing the forces that damage the turbine and demand excessive use of material. Accurate estimations of the energy production under a wide range of conditions are needed to properly design all the other energy conversion components. All the forces applied in conjunction with energy extraction dictate the size and materials used in all the structural components of the turbine. Given that wind turbines operate in varying environments, there are situations where the environmental conditions exceed safe and economical operating limits. These limiting parameters are used to design control systems that will maximize viable energy production while protecting the turbine from catastrophic failure. Thus accurate understanding of aerodynamic conversion is critical in advancing and engineering modern wind turbines in all areas of wind turbine engineering.

The economic viability of a wind turbine is based on maximizing energy conversion while minimizing manufacturing and construction costs. Actuator theory developed by R. E. Froude and W.J.M. Rankine was extended by A. Betz for wind turbines [23]. He determined that the maximum power of a given wind turbine by a coefficient of power of 16 parts of 27, this is referred to as the Betz Limit. The coefficient of power is defined with equation A.1. That limit is based on several assumptions that are not perfectly applicable to modern turbines, however Glauert has shown that these assumptions are conservative and the actual limit is slightly less than the Betz limit [48].

$$C_p \equiv \frac{P}{\frac{1}{2}\rho A V^3} \tag{A.1}$$

Improving the aerodynamic performance requires additional aerodynamic surfaces and rotor plane geometries, unaccounted for in the work of Betz and Glauert. Conning the rotor forward increases the maximum Cp slightly [11]. The mathematics for accurately modeling the effect of coning is complicated, this understanding is further complicated by aero-elastic effects, constantly altering the effective conning in operation. Research has shown that tip vanes improve the performance of a wind turbine slightly, the effectiveness of

tip vanes decreases with increasing Reynolds number [81, 80]. Despite reduced effectiveness commercial firms have adopted the use of tip vanes in large wind turbines. In addition there has been a lot of work in using diffusers to increase the mass flow through the rotor [59, 33, 19, 26, 6, 46, 49, 1, 39]. This type of wind turbine is referred to as a Diffuser Augmented Wind Turbine (DAWT). It has been proven by Sorensen and Hansen that the maximum Cp of a DAWT exceeds the Betz Limit [33]. Despite large performance gains, DAWT's are only economical for small rotors [19], overall they are not economically viable at the sizes of modern wind turbines [92]. Some experimental work has been done in co-rotating turbine rotors, this concept leaves a non-rotating wake thus more energy can be extracted [99, 45]. Modern turbines operate at high tip speed ratios and have little energy lost in wake rotation, as such the added mechanical problems and stiffness issues with extra blades is not justified.

Much of the aerodynamic work to advance rotor performance yields marginal improvements solving exceedingly complicated problems, have already been adopted, or are not financially feasible for modern wind turbines. Hence aerodynamic research is most likely to yield significant gains by improving the understanding, so that the costs of wind turbines are decreased. Given that aerodynamics influence the engineering of all components, improvements in aerodynamics should lead to cost improvements in other components. Hence the nature of which aerodynamic effects, influence the ideal architecture, highlight how aerodynamics can decrease costs.

The overall architecture of a wind turbine is chosen to maximize the energy conversion while minimizing the cost of energy conversion and structural integrity [87]. As stated before little improvement in performance is possible, so focus is paid to minimizing costs. The forces on a wind turbine increase by the square of the wind speed while the energy generated increase by the cube of the wind speed. Under extreme conditions the maximum forces and energy available will exceed the limits of the machine. Control is vital to shed some of the excess energy and forces in high wind conditions. Initially simple and inexpensive stall regulated wind turbines were found effective [5]. Uncertainty in the forces at stall forced industry to over enforce stall regulated turbines [92, 32]. As turbines increased in size this configuration proved prohibitively expensive. More complicated pitch regulated wind turbines were then adopted by the industry [92, 31, 5].

The architecture of early wind turbines was dependent on well developed technology at the time. The mechanical to electrical conversion needed to operate with small variation in rotational rates due to fluctuations in the wind conditions. The simplest solution was using high speed asynchronous generators [5]. These generators could operate on a small range of rotational speeds with no power electronic for conditioning. The high speed of the generators demanded gear boxes to increase the speed of generator shaft. As turbines increased in size, the rotational rates decreased to keep tip speeds low to avoid noise and other losses. This intern required gear boxes with greater gear ratios. Increased gear ratios prompted the industry to move away from parallel shaft gears to planetary gears. Increased complication in the gear sets increased the likelihood of failure. Larger more structurally sound gear boxes are not viable given the extra weight placed significant demands on the tower. As such the weight of the gear boxes is typically minimized, thus further increasing the chance of failure. Increased failure rates are further compounded by random perturbations of force from unsteady aerodynamic effects. These random forces are carried from the rotor to the shaft and through the gear box. This adds to increased fatigue stress and increased maintenance costs [35]. Given this weakness there is a lot of work in improving the strength of gear boxes without increasing the weight [35].

The weakness in the gear box has influenced some manufacturers to adopt direct drive architecture [5]. The slow speed of the shaft, forces the direct drive manufacturers to use more expensive, more complicated and less efficient synchronous generators [5]. The variation in rotor speed requires the use of power electronics with synchronous generators. Power electronics add more complication, more costs and more losses [5]. Direct drive configurations place greater demands on electrical conversion, it has prompted a lot of research in generator and power electronic research. Removing the gear box reduces the mechanical damping of random perturbations of force, giving increased structural constraints on the generator. Direct drive architecture is still adversely impacted by scaling trends. As turbines increase in power the required generator size increases parabolic. The cost of increasing the generator size is much greater than that of increasing the size of a gear box. Hence there are limits to the maximum size of direct drive turbines.

The existence of two architectures, each demanding improvements in various fields, shows that there is still a lot of innovation in the wind industry. Economies of scale and

increased interest in off-shore applications, is prompting the industry to develop larger wind turbines [61, 31, 37, 5]. Given that this scaling adversely effects the cost efficiency of both architectures, to varying degrees, there is uncertainty in what is the ideal architecture. This uncertainty has fueled a lot of development activity in improving both mechanical conversion and electrical conversion. Yet in both architectures the uncertainty is largely as result of uncertainty in the forces due to unsteady aerodynamics. The demands in development in all other areas can be relaxed with further understanding in aerodynamics.

Industry trends indicate wind turbines have been and will be increasing in size [62, 87, 5]. This in-turn increases the aerodynamic forces and greatly increases the costs of many of the components of a modern wind turbine. These increased costs have prompted the industry to adopt more complicated control strategies and architectures. Within the industry there is divergence in the overall architecture of wind turbines. This divergence is prompting a lot of demand for further research in many areas of wind engineering. The problem of increasing the size of wind turbines and the economies of scale has lead to further complication in the engineering of wind turbines. In all cases this complication is a result of uncertainty in the aerodynamics [87, 92]. Thus research in wind turbine aerodynamics is of vital importance to advance wind turbine technology.

Appendix B

Review of Wind Turbine Aerodynamics

B.1 Wind Turbine Aerodynamic Modeling

As stated above there is great potential to improve the cost competitiveness of wind energy by gaining better understanding to the aerodynamics. Given that a lot of wind turbine aerodynamics cannot be accurately predicted, the field is not mature. Accordingly there is a lot of on-going research, in many areas, trying to gain a better understanding. Understanding the full extent of each area is critical to know the best approach to enable much advancement in the field. First an understanding in the deficiencies of modeling wind turbine aerodynamics is needed, from that the details of unresolved physical phenomenon can be discussed.

The aerodynamic modeling is not just for predicting the power and forces under normal operation it is an important factor in evaluating the stall conditions, aeroelastic stability and the dynamics of the wind turbine. In the past engineers would avoid detailed dynamic analysis by making the blades exceedingly stiff. For large megawatt scale wind turbines the mass and the stress therein is prompting the industry to develop lighter more flexible blades. New blade designs absorb turbulent energy with blade motion, as appose to strain energy, risking crack propagating [62]. The reliance on aeroelastic behavior is placing greater demand on improving unsteady aerodynamic modeling.

Currently the best analytical description of flow physics is the Navier Stokes equations. However a Navier Stokes solution by numerical means is impossible with today's technology [87]. Thus simplifications are required, one such is dividing the solution domain by two. The first domain is the far field flow, both upstream and in the wake. The flow field upstream determines the flow at the blades, while the wake flow influences much of the upstream flow. The second domain is that of the blades which creates the wake and affects the entire far field flow [85]. The results of the two flow fields influence each other thus the two domains create a coupled system. In all cases numerical methods are needed to iteratively solve the problem. The goal in modeling wind turbines is to achieve reasonable accuracy that will allow the design of reliable wind turbines, while being fast and efficient enough to be a useful tool in an iterative design process.

The most commonly used model for far field flow physics is the balance of axial and angular momentum in annular stream tubes [62]. Empirical models are made for highly loaded rotors. The annular momentum balances assumes radial independence of the flow. This assumption is invalid for coned and yawed rotors [85]. For the rotor flow field, blade element models with 2 dimensional wind tunnel results are most commonly used. Using blade element theory for three dimensional rotors introduces error and requires corrections for vortex effects near the tips and roots [9]. The 3 dimensional, and rotation effects cause the profile performance to deviate from 2 dimensional approaching stall and in stall [93, 85]. The combination of these two models is considered the Blade Element Momentum (BEM) model. Despite its shortcomings and simplicity it is considered amongst the more reliable methods [62]. As such nearly all commercial codes rely on BEM for evaluating aerodynamic loads and properties [85, 77].

There are two common modeling methods within the research environment, Reynolds Averaged Navier Stokes (RANS) and lifting line models. RANS is based on the Navier Stokes equation, however it averages out the turbulent fluctuations and accounts for its effect by turbulence model. Successful applications of this method have revealed information on the effect of rotation. The choice of turbulence model can potentially introduce much error. Promising results have been achieved by combining $k\omega$ models with Large Eddy Simulation (LES), this method is called Detached Eddy Simulation (DES) [87]. RANS modeling still suffers from uncertainty in determining the transition from turbulent

to laminar boundary layers and separation [85]. RANS modeling is not well suited for modeling unsteady aerodynamic behavior [85].

Lifting line models solves the Euler equation by tracking vortex elements in the solution domain. The method is ideal for modeling the structure in the wake and the resultant induction factors [62, 11]. The method is also well suited for unsteady aerodynamic behavior and is used for exploring the effect of gusts, changing winds and yawed flowed [85, 62]. Most implementations of this model rely on blade element theory, thus suffers from many of the deficiencies in the blade element theory [85]. Attempts to model the blade profile with the panel method demand considerably more computational power with little gain in results [85]. In wind turbine aerodynamics the curvilinear vortex line elements create an inherent instability [85]. Empirical corrections are required to achieved converged results [85].

The computational requirements for both RANS and potential flow modeling exclude their use outside a research environment [85]. Their use is primarily to gain better understanding and provide a means of correcting and improving BEM models [85, 11]. However research into advanced modeling techniques cannot solve many of uncertainty issues of HAWT aerodynamics. Each of these methods has error associated with them and requires validation [87]. There is a growing body of validation data however none of it is sufficient to perfectly validate any of models. Further high quality measurements are still required, experts in the field feel that measurements are the only way to improve models not just by validation but also by gaining better understanding to create better models.

B.2 Wake Aerodynamics

Much of the uncertainty in modeling wind turbine aerodynamics come from two areas, the behavior of the far field flow and the forces generated at the blade. The inflow imparting on the blades is influenced by the vorticity distribution in the wake, this influence is referred to as induction. Much of the uncertainty is quantifying this induction at the blades, thus there is great interest in understanding the vorticity distribution in the wake. There are two sources of vorticity, trailing vorticity is generated by changes in circulation along the blade, while shed vorticity is generated when the blade circulation changes in time [85]. In

steady axial flow conditions the induction is well understood, it is in the off design cases where much of the research is focusing [11, 28].

With high turbulent intensity in the atmosphere boundary layer, turbine flow is rarely steady. The change in trailing vorticity is predictable but its influence on induction is not. The trailing vorticity will convect downstream and have a changing influence on the induction, the convection itself is also influenced by induction and the surrounding vorticity. Predicting the structure of an unsteady wake is a challenging task. The best method at modeling the wake is with a dynamic wake model this does take into account the convection and changing wake in time [62]. However dynamic wake methods are highly computationally intensive, two simple methods do exist but neither is as accurate as the dynamic wake. Frozen wake models use an average vorticity distribution and keep the induction effects constant [62]. Finally steady wake models assume the wake achieves steady state conditions immediately [62]. Little research has given consideration to shed vorticity but its effect is important. Shed vorticity is contained within the wake and is most sensitive to the induction [87]. Thus modeling this vorticity is most challenging.

For a variety of reasons it is not un-typical for a wind turbine to be operating in a yawed flow situation. Under these conditions the wake is skewed and will have varying induction depending on the azimuth [10, 29, 97, 88]. Shed vorticity is still a factor under yawed conditions, given the angle of attack at the blades is continuously changing in time, the circulation of the blades is also changing in time. Under conditions of extreme yaw the blade can enter stall and then reattach periodically, this causes particularly strong shed vortices [78].

In most models it is assumed that vorticity is generated at the blades then convected in the far stream. This assumption is false under highly loaded conditions, under these conditions the shear layer between the turbine wake and free stream flow gives way to an instability that can generate large turbulent vortices. In extreme conditions these shear layer vortices will coalesce and form a large toroid vortex of similar scale to the rotor itself [85]. These turbulent vortices will mix the wake flow with the free stream flow. This mixing effect negates the accurate use of simple momentum balances. Lifting line modes are not suitable for this flow given that it is a result of viscous interaction. Very little research has been done in this area, highly loaded wake conditions occur in low winds where little

power can be generated. Despite the fact it occurs frequently it is responsible for little of the energy production. Hence a 20% error in the turbulent wake modeling results in a 4% error in the energy production [85].

B.3 Wind Turbine Tip Flow

Much of the aforementioned discussion focused on vorticity in the far field influencing the flow at the rotor plane. There is also an effect from vorticity shed immediately at the blade. This effect is referred to as tip loss effect given most shed vorticity is at the tip. The tip loss correction given by Prandtl has been very successful despite its simplicity [9]. However it does not reflect the effect of various tip geometries. Also, much of the noise of a wind turbine is generated at the tip [92]. The noise and the need for improved tip loss models have made the tip aerodynamics another area of research.

B.4 Rotational Augmentation and Stall Delay

Much of the modeling in wind turbines use airfoil performance results from two dimensional wind tunnel experiments. Comparison of these models to actual operation has shown that actual airfoil performance on the wind turbine differs. This discrepancy is most noticeable around the static stall region. This deviation is attributed to the effect of rotation. As the blade approaches two dimensional stall characteristics centrifugal and coriolis effects become significant in the boundary layer [13, 71]. These effects will energize the flow and induce radial flow in the boundary layer. This in turn dampens the pressure gradient and acts to suppress the stall [13]. This effect is referred to as stall delay or rotational augmentation.

This effect is dangerous when engineering stall regulated wind turbines. The maximum power given by the rotor must be within the maximum power of the generator. For stall regulated turbines this maximum power condition is met by allowing the rotor to stall before the generator is over-powered. Stall delay causes the rotor to increase in power with increasing winds beyond the predicted maximum power of the generator. The uncertainty of stall was accommodated by compromising the air foil selection. Airfoils with a high

lift over drag ratio have deep stall characteristics, as such there was a dramatic change in performance whether the blade was stalled or not. Airfoils with low lift had stall forces similar to lift forces, despite the loss in performance these airfoils were much more forgiving in peak power prediction [22]. This uncertainty in stall limits the size of stall regulated wind turbines.

As turbines becomes more powerful with increased rotor size, the weight of the blade increases even greater. To deal with this engineers lighten the blade by reducing the solidity, using high lift airfoils to get the same forces [92]. The undesirable effects of stall delay are mitigated by using variable speed and/or variable pitch technology, complicating the overall turbine [5]. Stall delay still occurs but it is relegated to the root of the blade where aerodynamic forces have a lessened impact on the power and forces.

Efforts to model stall delay can be grouped into two methods. The first is semi-empirical and attempts to estimate the rotational augmentation based on two dimensional performance and rotor conditions [77, 95]. The other corrections take an analytical approach, performing an order of magnitude analysis on the boundary layer equation in a rotating frame of reference [77]. The low order terms are ignored leading to a means of correcting two dimensional airfoil performance. The analytical method is effective towards the tip however since it ignores the coriolis effect it deviates towards the root [87].

B.5 Dynamic Stall in Wind Turbine Aerodynamics

Stall delay and rotational augmentation are issues under normal yaw operation. However in many cases wind turbines will operate with a yaw error with respect to the wind direction. This will happen when the wind changes in direction or there is error between the wind direction and the sensor on the wind turbine. Under these conditions there is a theta component on the top and bottom of the rotor plane. This will cause the angle of attack to vary as it travels through the rotor plane. If the wind turbine is close to stall conditions the variation in angle of attack will cause dynamic stall. Discussion about dynamic stall in Horizontal Axis Wind Turbines (HAWT) started to appear in literature in 1992 [4, 109, 36]. It is associated with a periodic stall where soon after the flow will re-attach, the process is repeated with every rotation. The behavior of dynamic stall is of interest for a variety

of reasons. It is a major cause of fatigue damage, and has implications in aeroelastic modeling.

When the blade stalls the effect is not immediate. The flow will start to separate at the leading edge forming a small circulation region on the suction surface of the blade [78]. This circulation region is referred to as the dynamic stall vortex. This circulation will grow covering a large part of the suction surface of the blade [78]. In this region there is very low pressure that increases the lift of the airfoil, this increased lift force will grow as the circulation region grows [78]. Once the circulation region grows beyond the trailing edge of the blade it will separate and convect downstream [78]. Once separated the lift of the airfoil will quickly decline to that of stall condition. When the angle of attack returns to connected flow conditions there is a similar transient response before the blade returns to normal steady flow response [76, 27, 60].

Measurements have shown that the dynamic stall vortex is capable of creating lift forces three times that of the static stall force [77]. This strong increase in force followed by a quick decrease in force makes for a large load variation that has significant impacts on fatigue damage [78]. The delayed response between blade force and the angle of attack creates a hysteresis loop. This hysteresis has implications for aeroelastics, in flap wise bending it dampens the vibrations, however the stall has been known to excite edgewise vibrations [32, 85]. Dynamic stall also has implications for grid connection issues, it can delay the shutdown generating dangerous levels of current [44].

Dynamic stall has a complicated three dimensional structure, the dynamic stall vortices will form closer to the root [73]. With strong wind or large yaw error the vortices will form in the mid-span regions as well [73]. The vortices seem to be pinned at the root while they form and convect quicker further from the root [73]. The nature of the stall formation overall is complicated. Analysis into the result of the Ames wind tunnel test shows evidence of a double horseshoe formation [94]. The induction of the double horse shoe will promote stall towards the tip, but suppress it towards the root [94]. The existence of the double horse shoe will complicate the prediction of overall blade performance under yawed conditions.

Dynamic stall is not unique to wind turbine flows. The phenomenon is a large research topic in helicopter rotor flows. However the models used for helicopters are not

applicable for wind turbines [109]. For wind turbines two models are used to account for the hysteresis in dynamic stall. The most common is the Beddoes-Lieshman model, it is semi-empirical using steady airfoil performance to generate a hypothetical hysteresis [77]. The Beddoes-Lieshman lacks the physical fidelity to understand the dynamic stall process. Another more complicated model is the more ONERA model, despite the complexity it is a better physical representation [77]. Since acceptable results are achieved with the simpler Beddoes-Lieshman model [60], it is most popular within engineering and research circles. Experiments have shown that stall and dynamic stall is sensitive to the turbulence levels as such these dynamic stall models can only provide approximations [3].

Understanding dynamic stall through two dimensional experimentation negates the effect of rotation. It is well understand that rotation alters the stall behavior. The results of some two dimensional studies has shown that the Magnus effect can influence the behavior [18]. Also the formation of the dynamic stall vortex is sensitive to trailing vortex [18]. These two effects can distort two dimensional wind tunnel results. However they can also have implications in wind turbine flows. Towards the root there is trailing vortices. Currently there is research in the benefits of individual blade pitch . The idea is to continuously pitch the blade to account for the effect of wind shear. Continuous pitching blades can introduce a Magnus effect to the blade flow.

B.6 Experimental work in wind turbine aerodynamics

Further understanding is needed to adapt popular BEM methods to overcome limitations with yawed flows, coned rotors or unsteady flows. Most work in understanding wind turbine aerodynamics has relied on computer modeling. This has proven to be a difficult technique, but it has revealed a lot of insights into wind turbine flow fields. Many of these numerical investigations rely on semi-empirical models for the turbulence, blade forces and boundary layer conditions. Numerical methods are also limited for unsteady flows or other off design conditions. These limitations cast doubt on the accuracy. Much of the simplifications employed to simplify the models can potentially hide actual behavior.

Insights into many areas can be found with detailed measurements of wind turbine flows. As such there is great demand for physical measurements. The induction at the rotor inflow from the wake structure is of great interest [87]. Detailed measurements of the wake with corresponding rotor inflow measurements will reveal much about how the wake and the rotor inflow interact. Ideally these measurements will validate many of the numerical investigations [87]. Studies have shown that varying degrees of coning can either increase the power or reduce some of the damaging forces [11]. Thus there is need to investigate many different rotor geometries to understand how coning changes the wake and rotor inflow interactions.

Investigations into the wake will expand the capabilities of BEM methods. Yet much of the uncertainty in BEM methods is from a lack of understanding in the flow at the rotor [93]. The importance of understanding the blade flows is further compounded by ever increasing rotor size [62, 92]. The engineering of larger blades is demanding more reliable methods for fatigue and aeroelastic dynamics [62, 92]. Thus there is a great need to know the flow at the rotor and the corresponding forces of these flows. There are several unresolved issues in blade flows, there is still much doubt on the applicability of using lift and drag polar's for rotor flow [93]. So far there is not a suitable analogy for the angle of attack in a wind turbine flow [68]. Further experiments in the effects of rotation on the blade forces is needed to accurately account for stall delay [78]. Many airfoils are tested in two dimensional experiments to determine there sensitivity to grit roughness. Experiments in rotating three dimensional conditions could confirm roughened profiles under actual conditions. It is hypothesized that dynamic stall and stall in general create complicated transient and three dimensional structures [94, 73]. Measurements with high resolution in time and space are vital to confirm and understand these structures [78]. Better understanding of dynamic stall is most important as its effect on wind turbines is most detrimental [78, 87].

There are few high quality experiments or field tests to validate these models. The IEA field tests have given a large database of wind turbine operation under a variety of conditions [68]. With all field tests there is uncertainty in the actual inflow conditions, as such models cannot be perfectly validated with these results [87]. The first high quality wind tunnel experiments were at the Ames wind tunnel facility [75, 30]. An un-coned

10.1 meter diameter rotor was tested in a large closed wind tunnel [75, 30]. The blade was equipped with many high speed surface pressure sensors and pitot probes for inflow conditions [75, 30]. These experiments revealed many new insights into the detailed aerodynamics at the blade. However flow visualization could only be achieved in the far field. Limitations in mounting pressure sensor in a blade limited the spatial resolution of the surface flows. Analysis of the results indicates the existence of complicated three dimensional structures, but the details of the structure could not be captured [94, 73]. Without flow visualization, researchers were forced to make many hypothetical assertions without confirmation. Recently a wind tunnel experiment referred to as "Model Experiments In Controlled Conditions" (MEXICO) tested a 3 bladed un-coned 4.5m diameter turbine in an open wind tunnel [86]. The researchers employed particle image velocimetry (PIV) in the wake to track the dominate vortices in the wake under a variety of conditions [86]. The blades in the MEXICO project were also mounted with pressure sensors [86]. Only stationary domain results were collected through PIV, thus there is still much of the same uncertainty in the blade flows. These results will be valuable for modeling far field flow but the effect of shed vorticity could not be captured with the PIV setup.

The various measurements in field tests and wind tunnel tests give a much improved set of results to understand wind turbine aerodynamics and validate numerical models. However there is still a need for more experimentation. Detailed measurements of blade flow with high resolution in time and space is not available [87, 77]. Also in most detailed measurements of the wake only one set of blade geometry was used. Some of these experiments have indicated that there is previously unknown phenomenon that requires more detailed investigation [94]. There is a need for long term active research in experimental wind turbine aerodynamics. This requires a specially designed wind turbine suitable for experiments. Only tufts have been successfully applied in flow visualizations of three dimensional rotating wind turbine flows, the applicability of these results is in doubt [89, 28]. Surface measurements of pressure are common place but only laser Doppler anemometry and hot wire anemometry are available for velocity measurements close to the blade [4, 28]. These measurements provide insight however given that the blade flows have complicated three dimensional structures in the rotating domain, point measurements in the stationary domain fail to capture everything that is happening.

Appendix C

Aerodynamics of Alternate Savonius Turbines

C.1 Deep Rotor

Figure C.1 shows the velocity fields for the Deep rotor. The small radius of curvature on the concave side of the top blade causes the flow to separate at 60 degrees phase angle. A vortex follows the bottom blade at phase angles between 0° and 60°. This shows that the depth of the blades acts more as a bluff body and fails to direct flow around the bottom blade. The flow separation on the top blade and the recirculation region behind the bottom blade will reduce the momentum transfer to the blade.

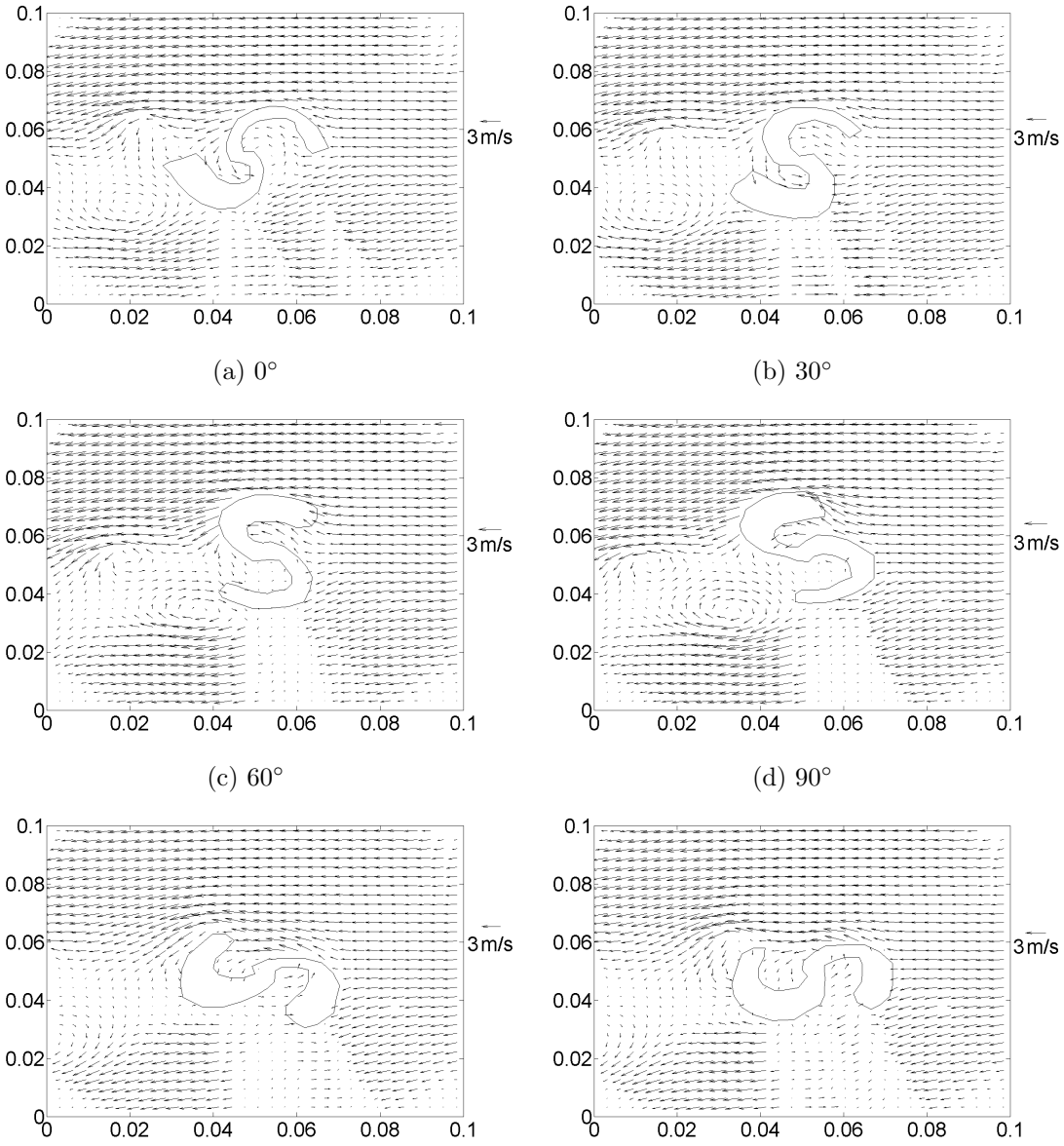

(a) 0°

(b) 30°

(c) 60°

(d) 90°

(e) 120°

(f) 150°

Figure C.1: Vector Maps for the Deep Rotor

C.2 Shallow Rotor

Figure C.2 shows the vector fields for the Shallow rotor. The flow acceleration over the concave surface of the top blade is weaker. This weakens the lifting mechanism reducing the overall momentum transfer. The vortices in the wake are also weaker further showing reduced momentum transfer. There is greater divergence in the flow in front of the top rotor at 90 degrees. This suggests that less flow is passing through the gap between the shallow blades. On the top blade there would be greater drag however less flow behind the bottom blade increases the drag of the bottom blade. Both these flows have opposite effects on the overall momentum transfer.

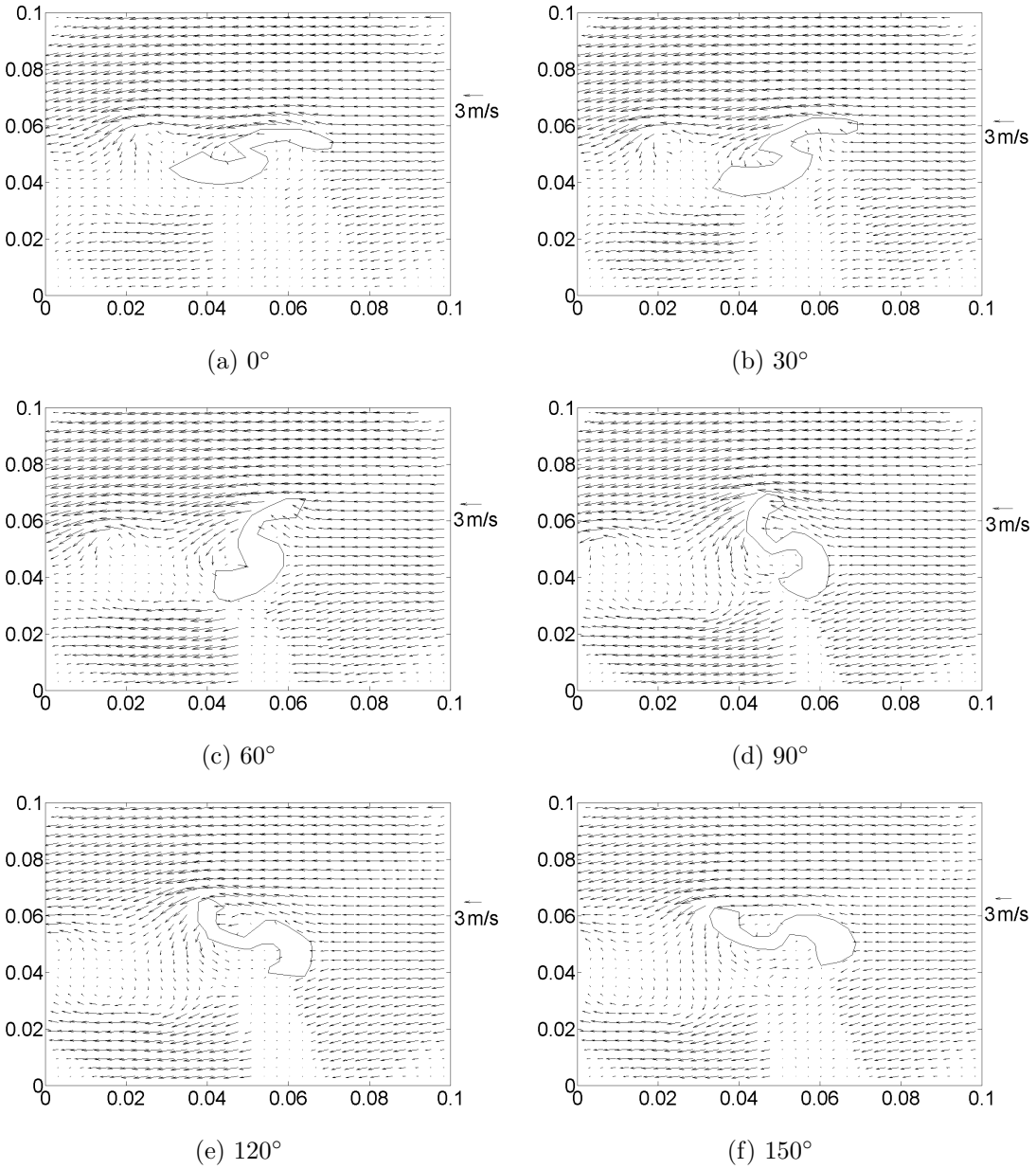

(a) 0°

(b) 30°

(c) 60°

(d) 90°

(e) 120°

(f) 150°

Figure C.2: Vector Maps for the Shallow Rotor

C.3 Outside J

Figure C.3 shows the velocity plots for the Outside J rotor. The major difference in the Outside J is that the shedding of the bottom vortex is delayed compared to that of the standard rotor. The wake of the bottom blade flow is pulling flow from the top blade through a higher phase angle. The outside tip of the outer J has a smaller radius than all other rotors. This causes a stronger vortex towards the outside of the bottom blade wake, which indicates lower pressures to pull flow off the top blade. The geometry also shields the vortex from the mean flow and allows it to stay attached longer. The vortex behind the bottom blade will increase the drag of the bottom blade.

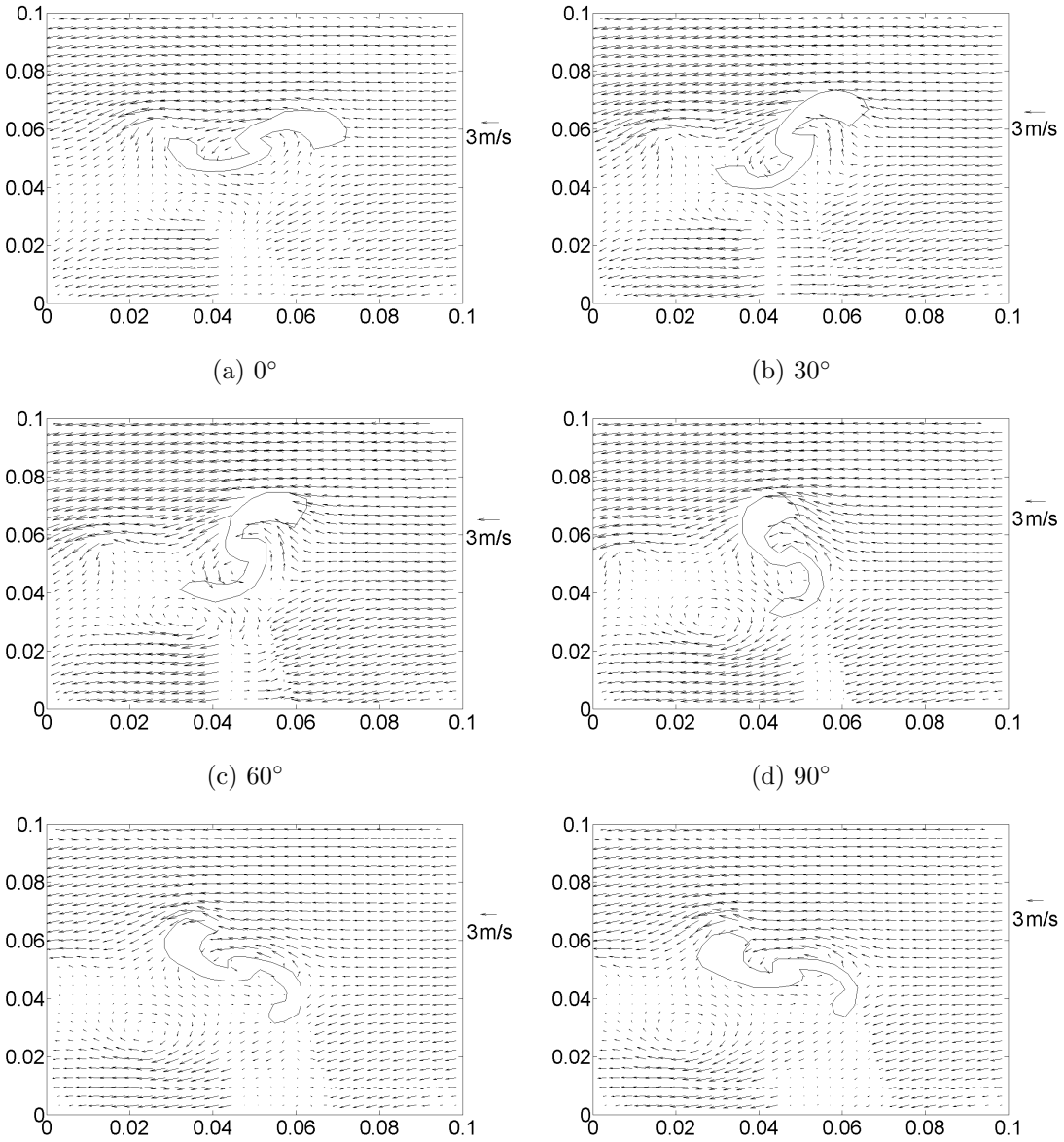

(a) 0°

(b) 30°

(c) 60°

(d) 90°

(e) 120°

(f) 150°

Figure C.3: Vector Maps for the Outside "J" Rotor

C.4 Inside J

Figure C.4 shows the velocity plots for the Inside J Rotor. Shadows had a smaller impact on the PIV results on the Inside J rotor at 60 degrees. This revealed that the bottom vortex is shed at 60 degrees. It is likely that the bottom vortex is shed at similar phase angles for all rotors. The better results also revealed that the flow follows the bottom blade through phase angles between 0 and 120 degrees. The flow into the top blade has greater divergence suggesting that there is reduced flow through the gap. This reduced flow will have the same effect as in the shallow rotor.

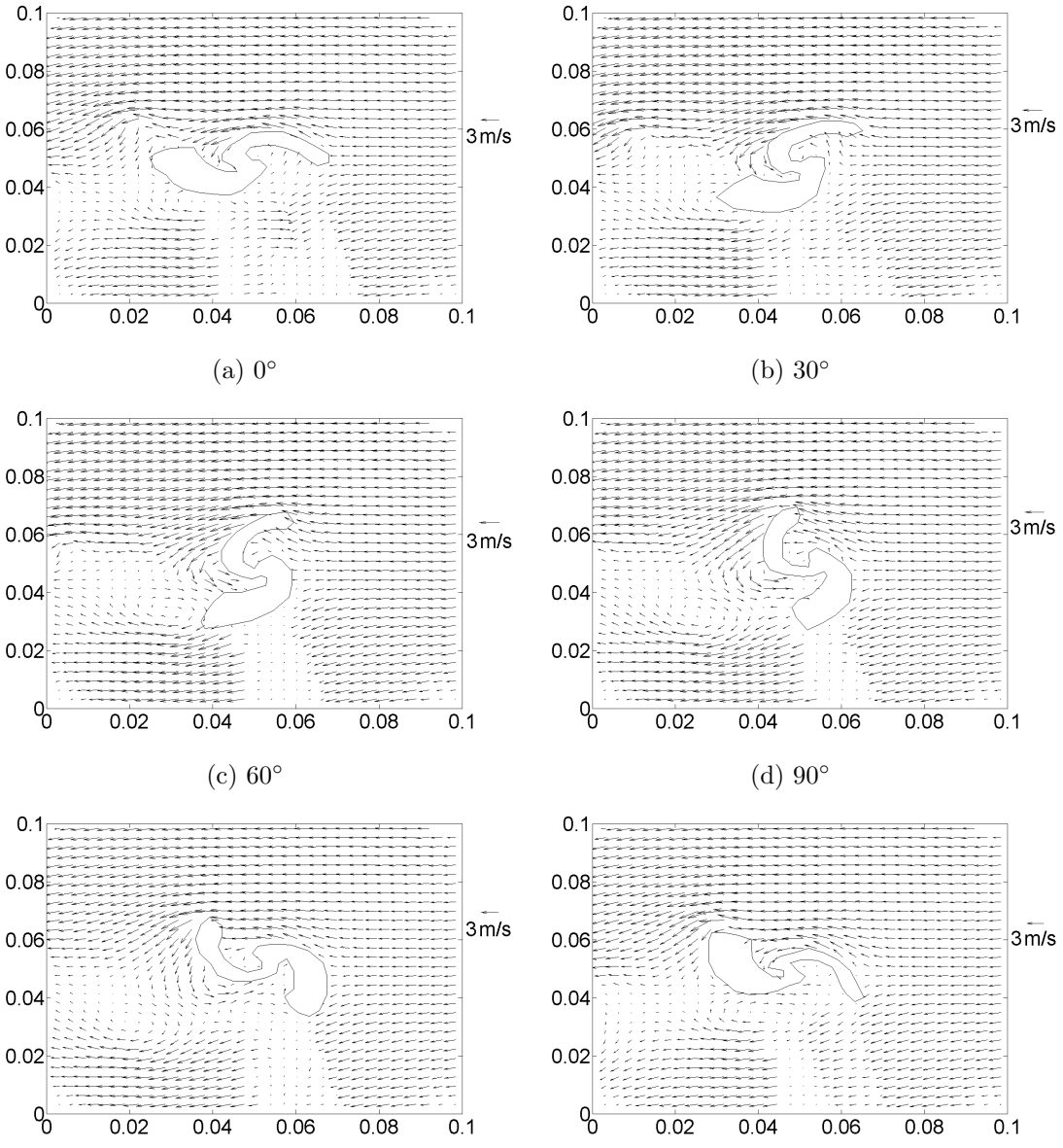

(a) 0°

(b) 30°

(c) 60°

(d) 90°

(e) 120°

(f) 150°

Figure C.4: Vector Maps for the Inside "J" Rotor

Appendix D

Extending Velocimetry Data

Future developments in wind turbine aerodynamics will need to focus on the forces generated by the wind. Velocimetry data alone reveals little how flow structures contribute to the forces. Researchers have been using control volume momentum balance techniques on PIV to determine the overall forces. These methods are well suited for integral forces on objects, but fail to show where on the surface the forces are being applied. Surface pressure measurements will provide force information at the surface, however it is difficult to measure the pressure in the free stream, hence it will be difficult to measure how extended flow structures contribute to the forces at the surfaces.

To resolve these issues and determine how flow structures contribute to forces at the blade surface, free stream pressure results are needed in conjunction with the velocimetry data. Techniques are needed to extend the PIV data to estimate the pressure at the data points. This section explores methods of determining the aerodynamic forces and the pressure fields using PIV data.

D.1 Advanced PIV analysis techniques in Literature

In much of the literature, PIV data is being extended to determine the forces on a submersed body. Early methods relied on control volume balance of momentum [98]. Most terms in the momentum balance are evaluated directly from the velocimetry, except for the pressure [98]. Determining the effect of pressure requires the integration of Navier Stokes

about the boundary of the control volume [98]. The work by Unal et al. attempted to determine the instantaneous data and required the area integration of a temporal derivative [98].

Work by van Oudheusden et al. attempted to determine the time averaged force [100]. The time averaging eliminates the temporal derivative and the area integration, however it requires the use of the Reynolds Averaged Navier Stokes Equation (RANS) [100]. The RANS equations introduces the Reynolds Stress term, this term can only be evaluated averaging the fluctuating momentum transfer over many samples. This method is better suited for steady yet turbulent flows. In special cases the momentum balance does not require a control volume, van Oudheusden et al. successfully performed a line integral of the momentum deficit in the wake to determine the drag of an airfoil [100].

The control volume methods are not exclusively applied to momentum balances. The work of Grant et al. performed a control volume analysis of vorticity in the wake of a wing to determine the induced drag and lift [24]. The vorticity is determined by invoking the differential definition. The derivative terms are evaluated by taking a finite difference of velocimetry on a regular grid [24]. Grant et al. used particle tracking methods thus required the velocity to be interpolated onto grid points [24]. The circulation is then determined by integrating the vorticity [24].

Most of the control volume work assumed incompressible flow, however van Oudheusden et al. extended the method to compressible flows [101]. Compressibility introduces a new unknown, density, this is dealt with by invoking the adiabatic assumption, and ideal gas law [101]. van Oudheusden et al. also determined the pressure field over the entire flow field but did not give the details on how this was done.

The work by Murai et al. explored different methods for determining the pressure field [57]. The author applied his techniques to a transient flow field to find the instantaneous pressure field [57]. Particle tracking methods were used to gather velocimetry data, the author used a cubic equation to interpolate the results on the a finely spaced grid [57]. High speed digital imaging gave fine temporal resolution, critical for evaluating temporal derivatives [57]. Two governing equations were considered for evaluating the pressure field, the pressure Poisson equation and the Navier Stokes equation [57]. The pressure Poisson equation eliminated the need to evaluate temporal derivatives, but ignores viscous effects

and requires boundary conditions to be specified, leading to a source of additional error [57]. The Navier stokes was more sensitive to noise however the author showed that low pass filters can eliminate this, thus the Navier Stokes equation gave greater certainty [57]. Both methods required integration of a pressure gradient, the author used least square curve fit of the finite difference definition to perform this [57]. Turbulent effects on the mesoscale were captured with this method, however the author explored the use of turbulence models on the sub grid level, finding a 3% effect on the solution.

D.2 Determining Pressure Fields from PIV Vector Maps

The phase averaged results from the Savonius wind turbine experiments are used to explore methods for estimating the pressure field. Given that the flow field is turbulent and transient the Reynolds Averaged Navier Stokes equation is used as a starting point, equation D.1. The PIV measurements taken in this experiment can only capture two dimensions of velocity along a two dimensional plan hence any gradients and velocity perpendicular to the measurement plane are unknown. The measurements were taken at the mid point of the turbine thus by symmetry it can be assumed that there are negligible flow and gradients perpendicular to the measurement plane. For all the flows of interest body forces have a negligible effect thus are ignored.

$$\rho\frac{\partial\bar{u}_i}{\partial t}+\rho\frac{\partial\bar{u}_j\bar{u}_i}{\partial x_j}=\rho\bar{f}_i+\frac{\partial}{\partial x_j}\left[-\bar{p}\delta_{ij}+\mu\left(\frac{\partial\bar{u}_i}{\partial x_j}+\frac{\partial\bar{u}_j}{\partial x_i}\right)-\rho\overline{u_i'u_j'}\right] \tag{D.1}$$

Various differencing schemes can be used to determine any of the gradients. For gradients central differencing was used when possible, equation D.2. At the boundaries forward or backwards differencing is used, equation D.3. A first order differencing scheme was used for the double derivatives, equation D.4. For spatial gradients, information at adjacent data points in the same set of results can be used. For temporal gradients, data from previous or future data sets can be used. The time between phases is determined by dividing the difference in phase angles by the angular speed.

$$\frac{\partial \phi}{\partial s} = \frac{\phi_{i+1} - \phi_{i-1}}{s_{i+1} - s_{i-1}} \tag{D.2}$$

$$\frac{\partial \phi}{\partial s} = \pm \frac{\phi_i - \phi_{i\mp 1}}{s_{i+1} - s_{i-1}} \tag{D.3}$$

$$\frac{\partial^2 \phi}{\partial s^2} = \frac{\phi_{i-1} + \phi_{i+1} - 2\phi_i}{(s_{i+1} - s_i)(s_i - s_{i-1})} \tag{D.4}$$

The Reynolds stress term is measured by taking many PIV measurements at the same phase angle. Once filtered the results are averaged, the filtered results along with the average can be used to determine the fluctuating component. Thus for every data set the $\overline{u_i' u_j'}$ term is known.

Once all the velocity gradient terms are known the pressure gradient can be found using equation D.1. It is assumed that the actual pressure at a given point is the average of the sum of pressure and the gradient contribution at adjacent terms. The central location and the adjacent location will have different gradients, thus the average gradient between points is used. Equation D.5 is assumed valid at each point.

$$P_i = \frac{1}{N} \sum_{j=0}^{N} P_j + \frac{1}{2} \Delta x_j \left(\frac{dP}{dx}_i + \frac{dP}{dx}_j \right) \text{ j=n,s,...} \tag{D.5}$$

Equation D.5 is applied only for valid points in the solution domain, invalid locations are ignored. Applying equation allows a matrix to be formed for pressure over the solution domain. The pressure terms are in the matrix while the gradient terms are in the solution vector. The system alone is indeterminate given that it is based purely on gradients. A known pressure and a known point needs to be specified to get a solution from the system. For purposes of exploration an upstream point in the center of the flow was assumed to be at 0 gauge pressure.

The method given here is similar to that in Murai et al. [57]. Differences arise in the fundamental equation, instead the RANS equation was invoked as it is in van Oudheusden et al. [101]. The computational overhead of statistical curve fits was eliminated by using a matrix solution to approximate the pressure field. The matrix method would introduce

increased error however allowed for quick results, this is deemed acceptable for qualitative purposes.

D.3 Pressure Field Results

The method described in section D.2 was applied to the vector maps for the standard Savonius rotor. The accuracy of the method is determined qualitatively. The accuracy of the terms in equation D.1 is found by comparing different results to a base case. The base case only considers the Euler and viscosity terms to determine pressure. The Reynolds stress and the temporal derivative is set to 0.

D.3.1 Base Case Pressure Fields

Figure D.1 shows the pressure fields for the base case. Ignoring the Reynolds stress and the temporal derivatives does not distort the results beyond comprehension. The pressure solution corresponds with many of the flow features identified in the velocimetry data. All of the vortices were marked with a local low pressure region. Regions of divergent flow were further highlighted by relatively high pressure regions. The pressure solution revealed possible stagnation points at each of the rotor orientations. The first at 0° upstream of the top blade, while every other upstream of the advancing blade. The pressure solution confirmed the integral flow analysis in and out of the blades. In all orientations there is a pressure difference across the gap that will drive flow from the upstream blade to the down stream blade. The method is further validated given that the order of magnitude is comparable to the dynamic pressure.

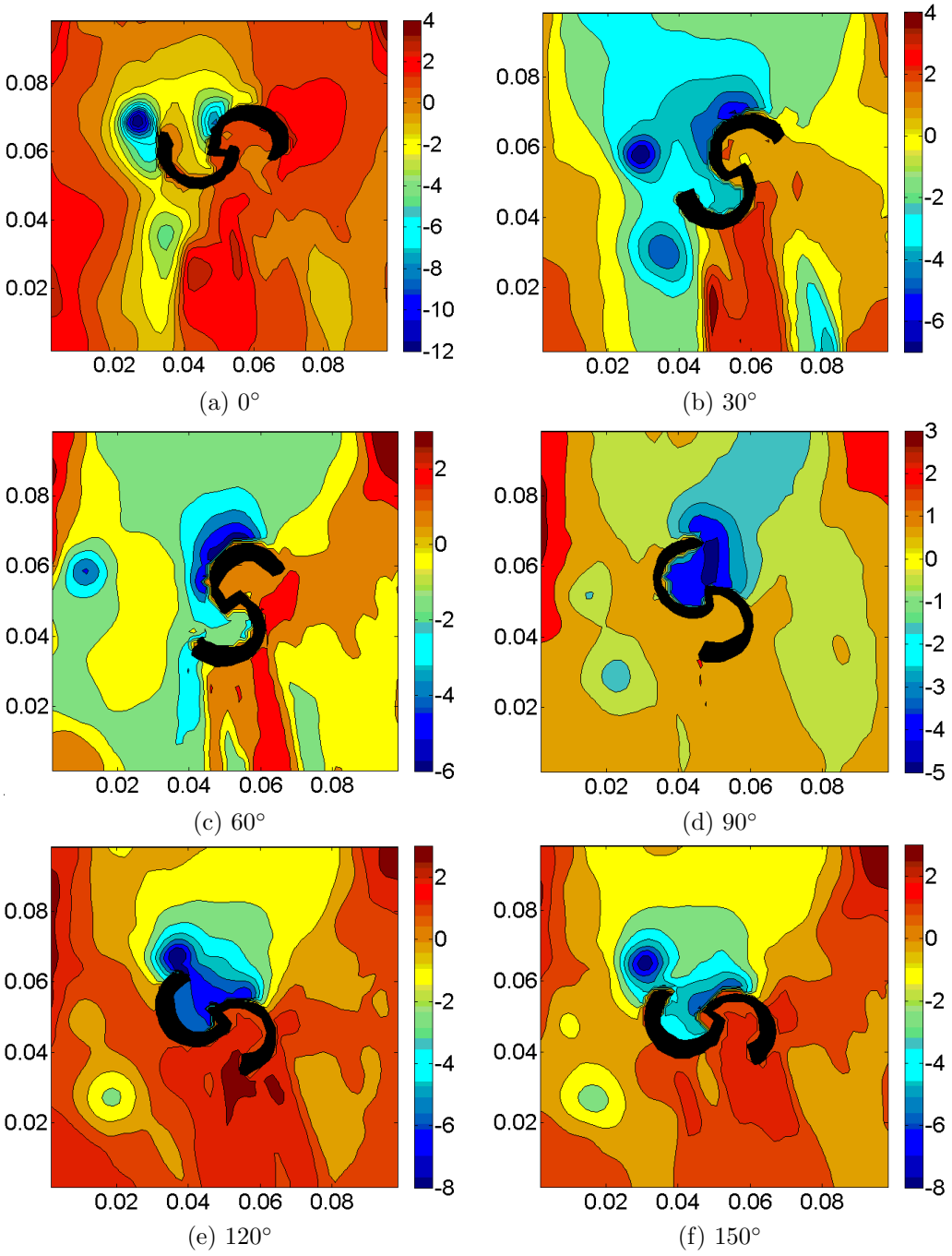

(a) 0° (b) 30°

(c) 60° (d) 90°

(e) 120° (f) 150°

Figure D.1: Base Pressure Fields for the Standard Rotor, $\Delta P = 1Pa$

Despite the consistency of the pressure solution with the velocimetry there is still many features that indicate error. The solution below the rotor would have a shadow in the images hence this data is erroneous. At the edge and corners of the domain there are strong pressure gradients, in the velocimetry the vectors in same region are erroneous. Given the aforementioned error in the velocimetry, anomalies of the pressure solution in the same region does not reflect the error in the method. Far from the rotor there are many pressure contours in the free stream flow, second these contours have an erratic shape. Given that this is the average pressure solution turbulence cannot explain this. The low pressure regions above the top blades extend far from the rotor. This could be from flow constriction between the turbine and the wall. Given that the blockage ratio is very small, it is unlikely that this would cause a 2 Pa drop in pressure.

D.3.2 Base with Transient Terms

Figure D.2 shows the pressure fields were re-calculated with the temporal derivatives. Including the temporal derivative gave a more accurate solution over many of the different phase angles. In many cases the contours were less erratic, and there was a net drop in pressure from upstream and down stream locations. The inclusion of the temporal derivative also revealed more flow structures about the rotor, there were additional stagnation points in the upwind blade while the low pressure regions extended deeper into the downwind blade. Many of the flow features in the base case were preserved.

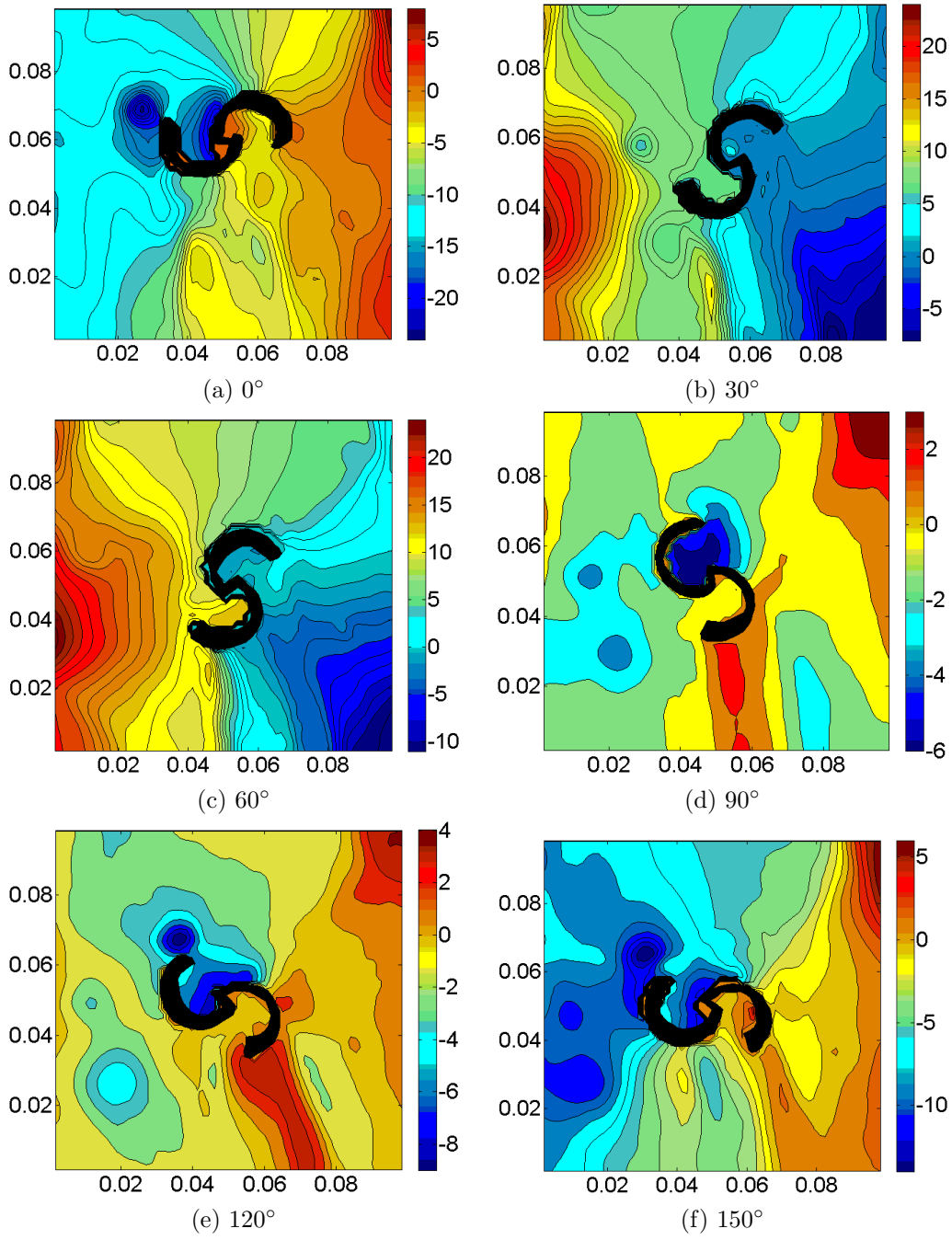

(a) 0° (b) 30°

(c) 60° (d) 90°

(e) 120° (f) 150°

Figure D.2: Temporal Pressure Fields for the Standard Rotor, $\Delta P = 1Pa$

In all cases the inclusion of the temporal derivative increased the range of pressures in the solution. At phase angles where a reasonable solution was achieved, the pressure range increase was modest. However two cases, given in figures D.2b and D.2c, show the temporal derivative had a dramatic increase in pressure range, that washed out a lot of the flow features in the base case. These resulting pressure field shows dramatic increase in pressure across the flow and increasing pressure downstream, both of which are likely false. The temporal derivative is predicted with a second order differencing scheme, in which data at both adjacent phase angles is used. There is a nominal phase difference of $\pi/3$ between adjacent phase angles, giving a course estimation of temporal gradients.

D.3.3 Base with Reynolds Stress Terms

The Reynolds stress term requires the fluctuating components of velocity, this is found by inspecting each data set for a given phase. Equation D.6 was used to determine the fluctuating component for each set. Then the appropriate product of the $u_i' u_j'$ was found. The products at a given point were averaged across all the available data sets. The Reynolds stress is found by determining the appropriate gradient through finite difference methods described above.

$$\phi = \overline{\phi} + \phi' \tag{D.6}$$

Figure D.3 shows the results of including the Reynolds stress term. In all cases the data is incomprehensible, the dominant features in the pressure fields reflect the optical set-up as appose to the flow field itself. The high pressure region in the corners is the edge of the lenses, the streaks radiating from the top are from the laser sheet being distorted by oil droplet on the window, and the semi-circle above the rotor is reflection off the edge of the rotor base. Most other features in the pressure field reflect other artifacts in the experimental set-up. Overall the inclusion of the Reynolds stress terms introduce considerable error.

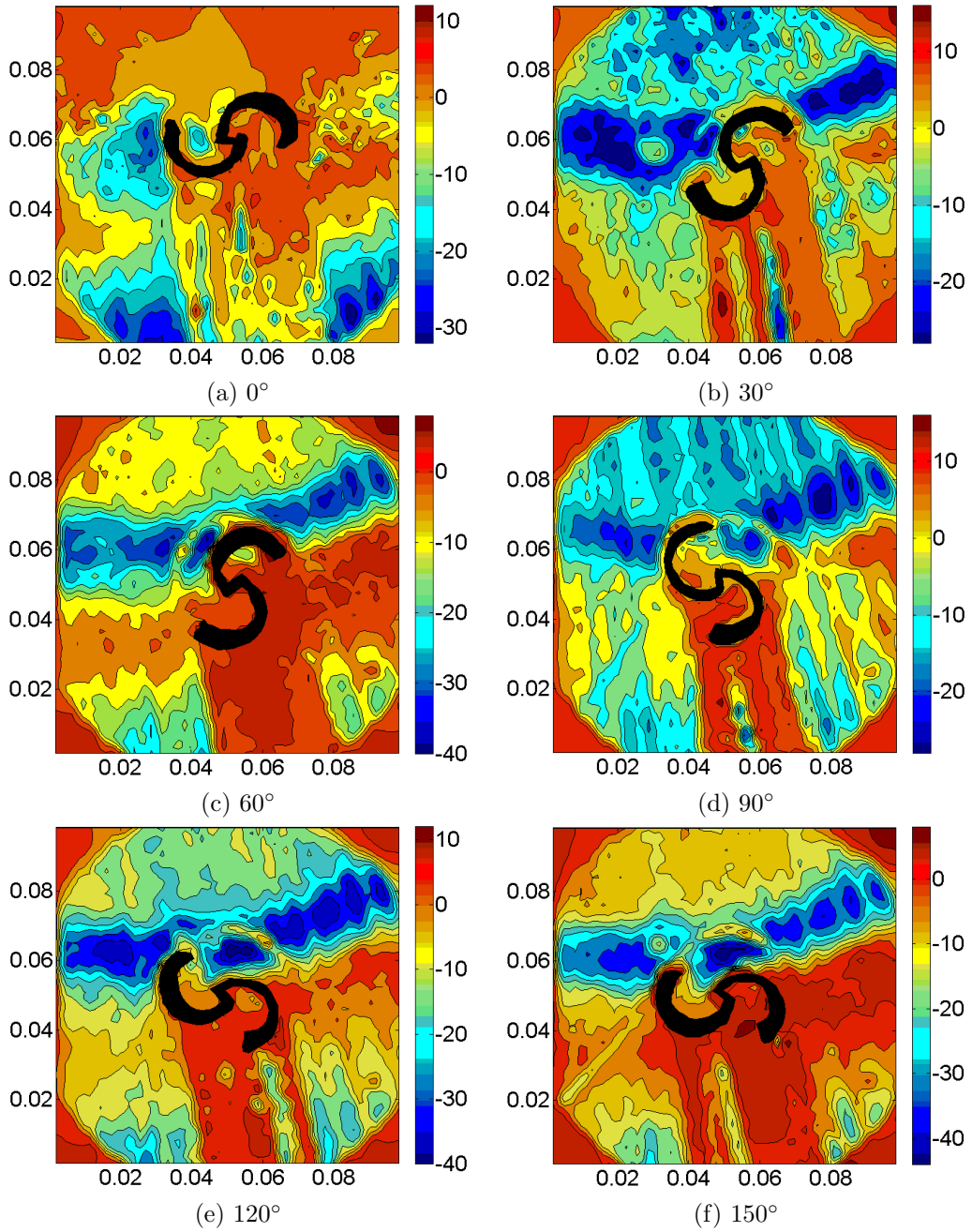

(a) 0° (b) 30°

(c) 60° (d) 90°

(e) 120° (f) 150°

Figure D.3: Reynolds Stress Pressure Fields for the Standard Rotor, $\Delta P = 4Pa$

Figures D.4 and D.5 show the histogram of average velocities in the velocimetry data. Figures D.6 and D.7 show the histogram of fluctuating velocities in the velocimetry data. Comparing the variance between corresponding histograms it is obvious that the turbulent intensity is greater than unity. It is very unlikely that the true turbulence level is similar to the results given, it is more likely that the Reynolds stress term is picking up more of the error than the actual turbulence. The velocimetry was calculated using spatial correlations on images, erroneous data is filtered by peak ratio statistics. These methods are not perfect and can introduce many false results that have acceptable peak ratios. These erroneous vectors have little influence on the velocimetry since the results are averaged across many data sets. Yet when finding the Reynolds stress term these errors resemble turbulent fluctuations and artificially reflect increased turbulence. Figure D.8 shows the results in figure D.6e with two normal distributions superimposed. The properties of the superimposed distributions were selected arbitrarily to highlight that erroneous data is included with data that is likely physical fluctuations. The largest issue in evaluating the Reynolds stress term is eliminating erroneous data in every data set, or reducing the sensitivity to erroneous data.

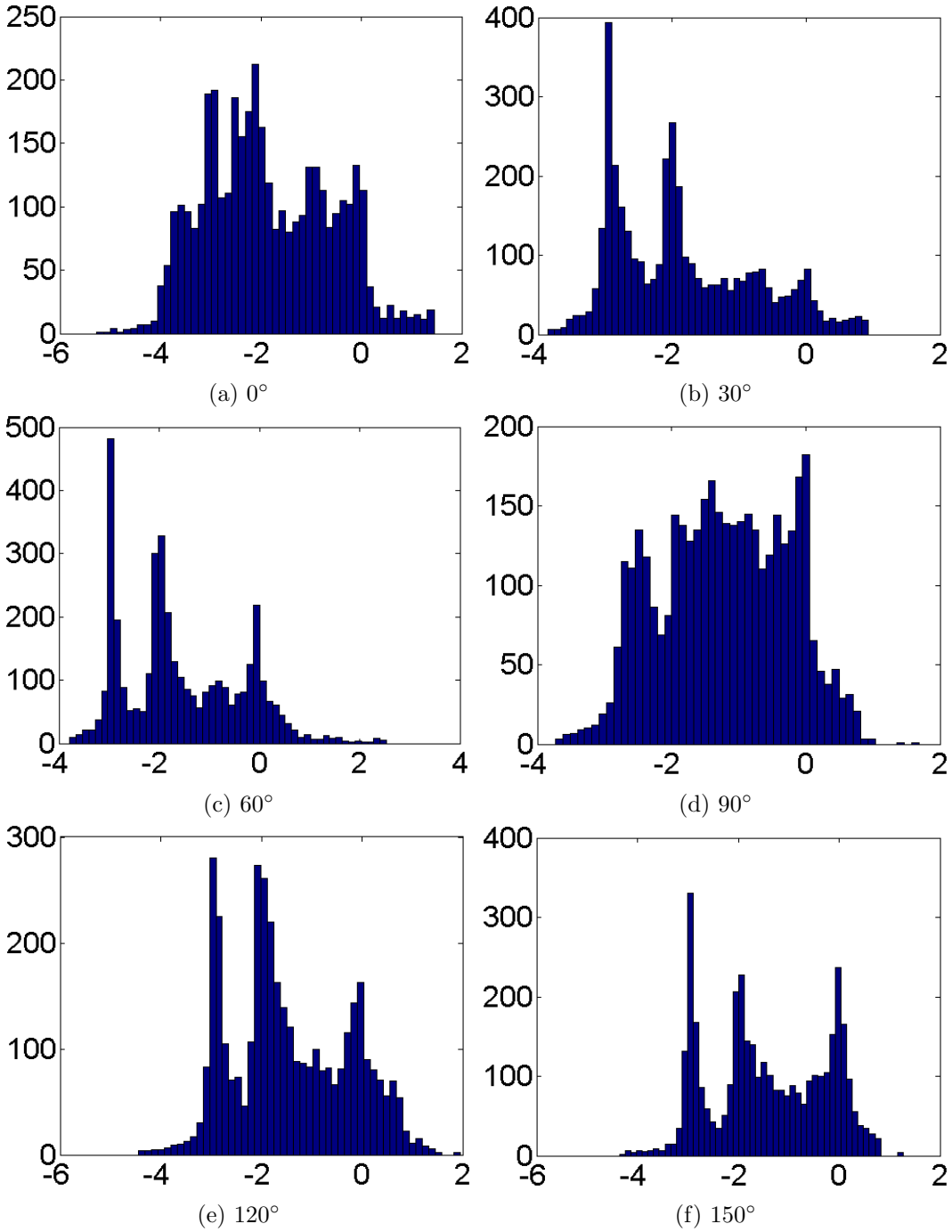

(a) 0° (b) 30°

(c) 60° (d) 90°

(e) 120° (f) 150°

Figure D.4: Frequency of Average U Velocities for the Standard Rotor

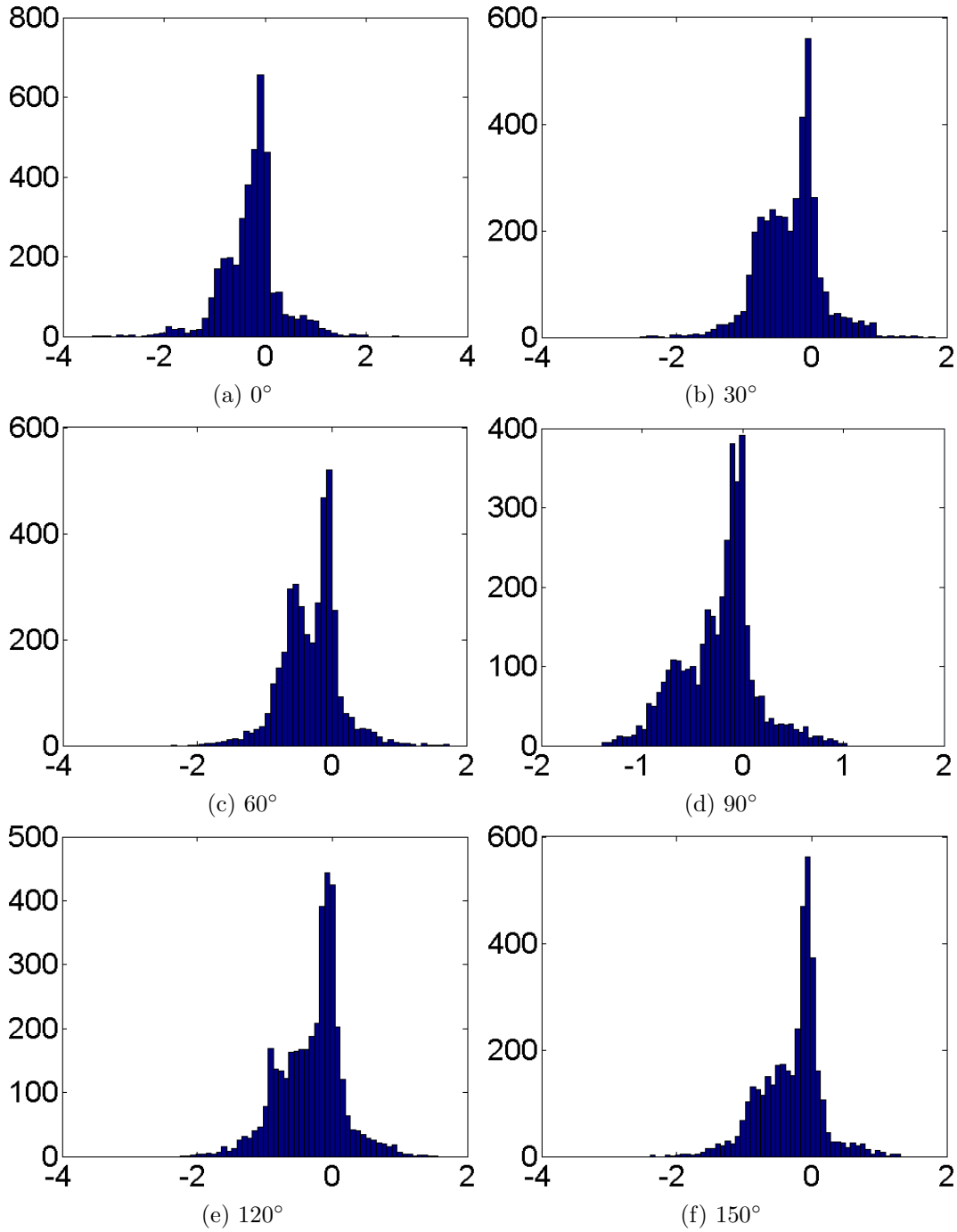

Figure D.5: Frequency of Average V Velocities for the Standard Rotor

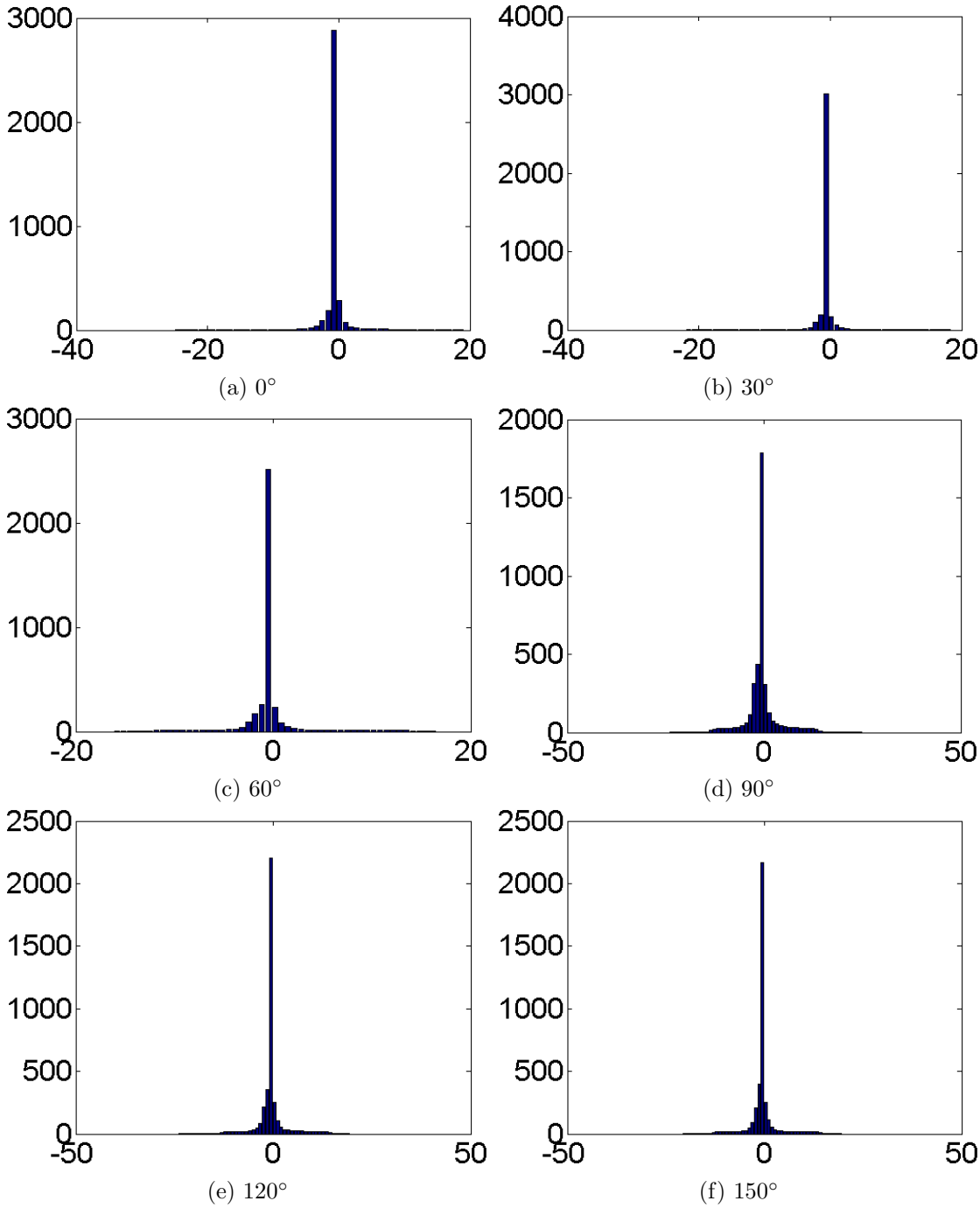

(a) 0° (b) 30°

(c) 60° (d) 90°

(e) 120° (f) 150°

Figure D.6: Frequency of U fluctuations for the Standard Rotor

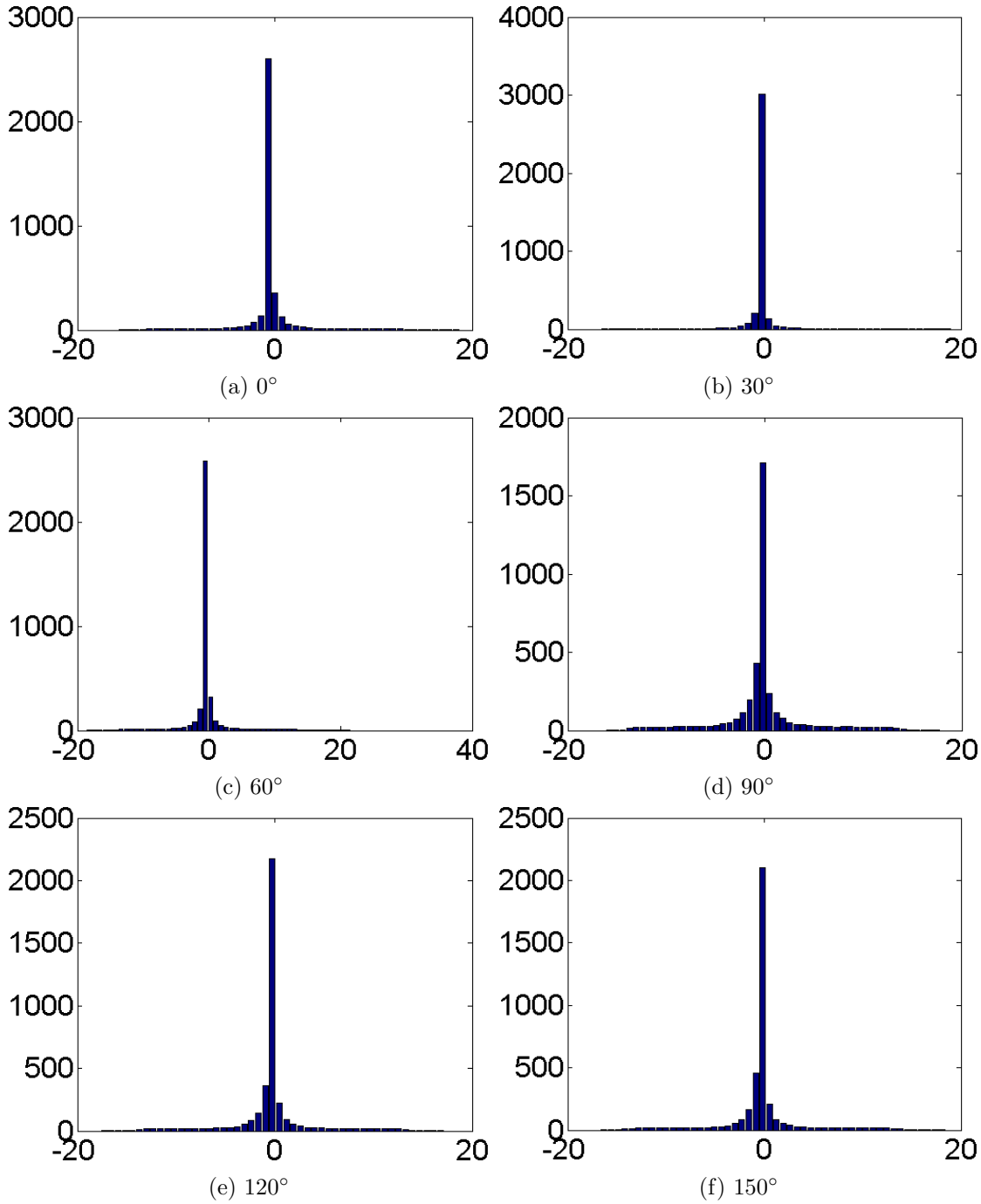

Figure D.7: Frequency of V fluctuations for the Standard Rotor

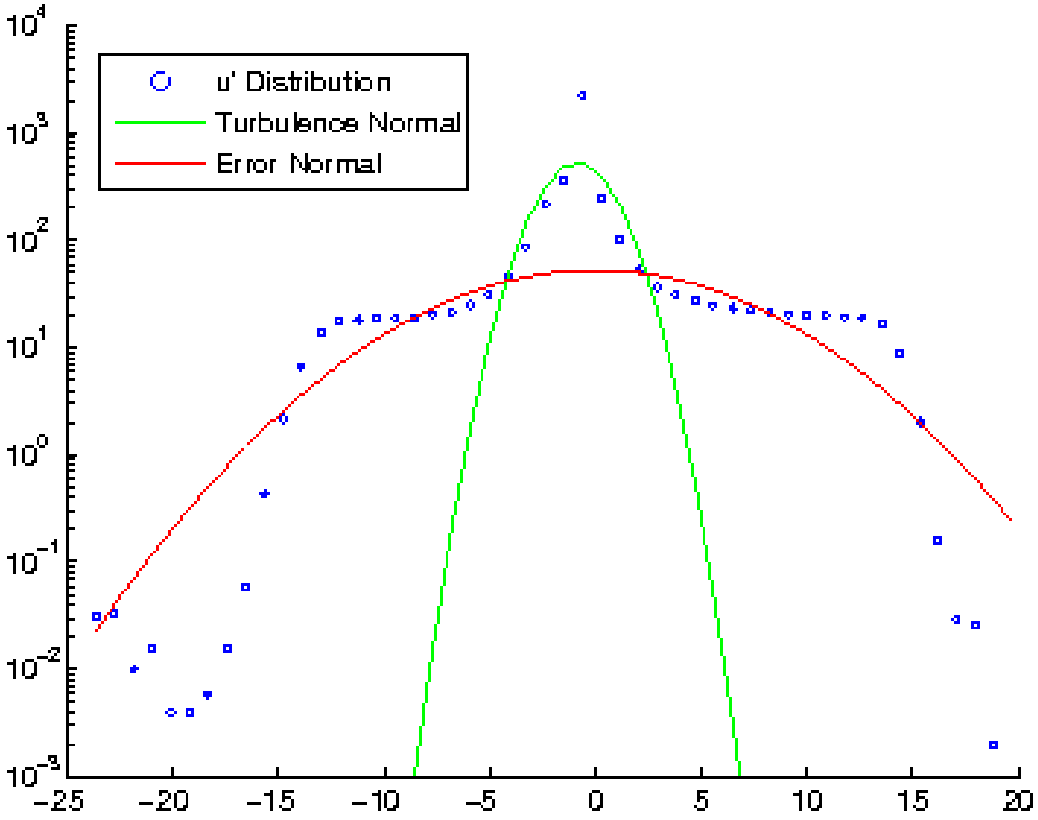

Figure D.8: Contribution of Physical and Erroneous data on Fluctuating Components

The Reynolds stress terms is a result of Reynolds averaging of the Euler terms in the Navier Stokes Equation given in equation D.7. The derivation of the Reynolds stress in equation D.1 is found by substituting equation D.6 into the Euler terms of equation D.7 and time averaging. This derivation is given in equations D.8 through D.11, equation D.9 and D.10 are equivalent given that by conservation of mass the divergence of velocity is 0. Given that all PIV measurements can only capture phenomenon in a plane, it is convenient to assume two dimensional flow in the analysis. Any physical flow in the third dimension will give error in the two dimensional divergence term. There is more error in the divergence term since erroneous data is not constrained to the principles of mass conservation. Thus the introduction of the divergence term would increase the sensitivity to error.

$$\rho\frac{\partial u_i}{\partial t} + \rho u_j\frac{\partial u_i}{\partial x_j} = \rho f_i + \frac{\partial}{\partial x_j}\left[-p\delta_{ij} + \mu\left(\frac{\partial u_i}{\partial x_j} + \frac{\partial u_j}{\partial x_i}\right)\right] \tag{D.7}$$

$$\overline{\left(\bar{u}_j + u'_j\right)\frac{\partial\left(\bar{u}_i + u'_i\right)}{\partial x_j}} = \overline{\bar{u}_j\frac{\partial\bar{u}_i}{\partial x_j} + \bar{u}_j\frac{\partial u'_i}{\partial x_j} + u'_j\frac{\partial\bar{u}_i}{\partial x_j} + u'_j\frac{\partial u'_i}{\partial x_j}} \tag{D.8}$$

$$= \bar{u}_j\frac{\partial\bar{u}_i}{\partial x_j} + \overline{u'_j\frac{\partial u'_i}{\partial x_j}} \tag{D.9}$$

$$= \bar{u}_j\frac{\partial\bar{u}_i}{\partial x_j} + \overline{u'_j\frac{\partial u'_i}{\partial x_j} + u'_i\frac{\partial u'_j}{\partial x_j}} \tag{D.10}$$

$$= \bar{u}_j\frac{\partial\bar{u}_i}{\partial x_j} + \frac{\partial\overline{u'_i u'_j}}{\partial x_j} \tag{D.11}$$

An attempt was made at redefining the Reynolds stress term, such that it was less sensitive to error, by eliminating the divergence term. Equation D.12 is based on a rearrangement of the left hand side terms in equation D.8 and the terms in equation D.11. This definition was applied to generate the pressure results in figure D.9. The results with the alternate definition have a greater range in pressure and are equally unrealistic as the original results. The second and third term on the right hand side of equation D.8 will increase the overall error. In these terms the error is being multiplied by the full velocity. In the original method the error is multiplied by a small fluctuating component. This increased range in pressure shows that the sensitivity to error is increased. There is evidence

of reduced error sensitivity by comparing the features between different sets of results. Many of the non fluid based features in the original results are not present in the alternate results. In both sets of results there is either a high or low pressure region that crosses the domain through the top rotor blade. During the experiment a smoke wand was inserted upstream to maintain seeding levels through out measurements. In some images coherent structures from the wand are visible. There could be error from the correlations locking onto the structures instead of the seeding particles.

$$\frac{\partial \overline{u_i' u_j'}}{\partial x_j} = \overline{\left(\bar{u}_j + u_j'\right) \frac{\partial \left(\bar{u}_i + u_i'\right)}{\partial x_j}} - \bar{u}_j \frac{\partial \bar{u}_i}{\partial x_j} \tag{D.12}$$

The derivation of the Reynolds stress term shows many other alternatives for accounting the effect of turbulence. The most promising implementation would be using the second term in D.8 in place of the conventional Reynolds stress term. Averaging the velocity over many data sets helped eliminate much of the error, averaging pressure the same way should have the same effect. Multiple pressure results could be found by applying the methods on each data set without the Reynolds stress term. Calculating the pressure on every set of results will dramatically increase the computational load, as such pressure averaging method will be interesting to explore only for academic purposes.

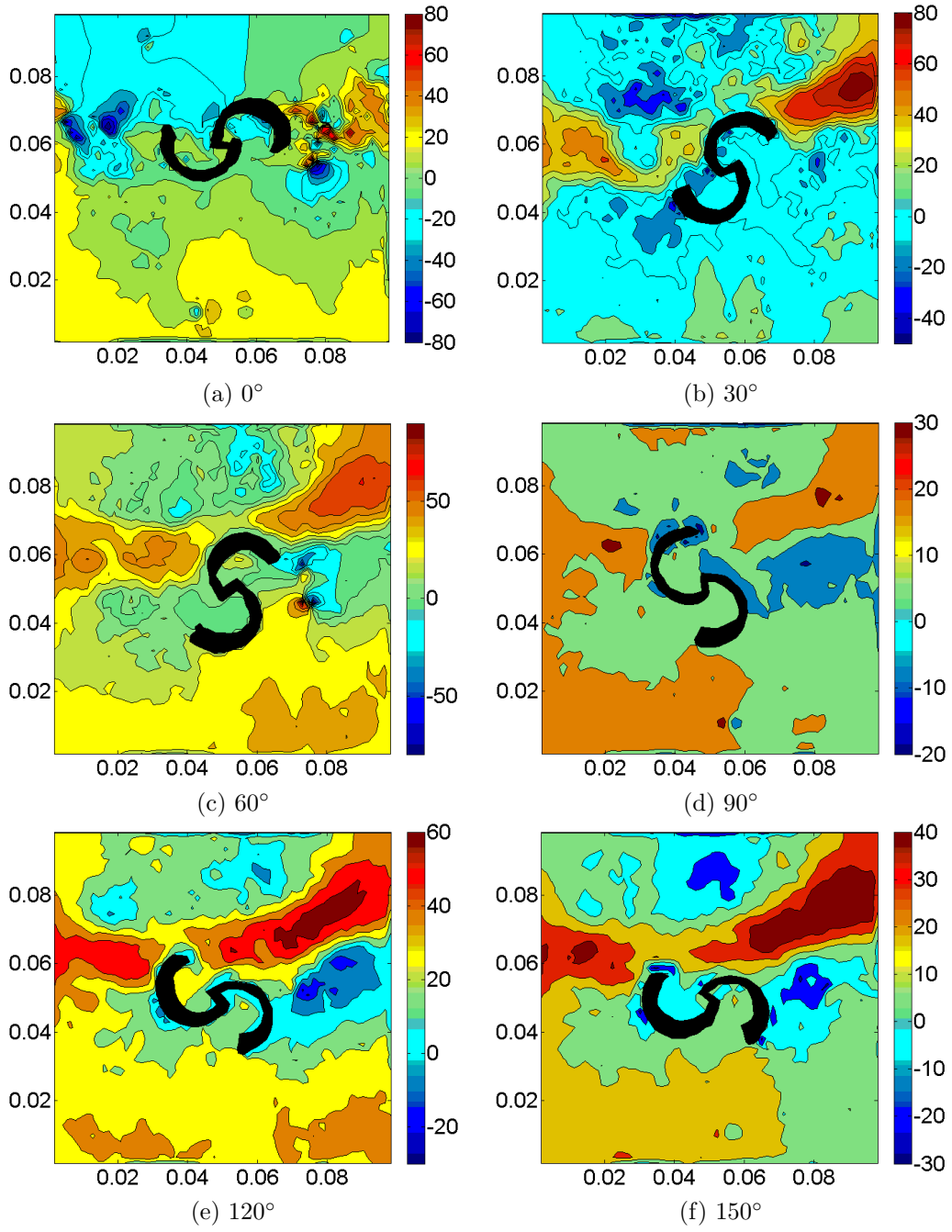

(a) 0° (b) 30°

(c) 60° (d) 90°

(e) 120° (f) 150°

Figure D.9: Alternate Reynolds Stress Pressure Field, $\Delta P = 10Pa$

D.3.4 Opportunities for Future Work

The temporal derivative is needed to capture all the details in a transient flow. The time step between results needs to be sufficiently small to minimize descretization error. Repeating the experiments at more phase angles to get better descretization will improve this error. Higher sampling rates can lead to time resolved PIV with sufficiently small time steps. Exploring the benefits of both methods will require further experimentation.

Including the effect of Reynolds stress, increases the error dramatically. This term is highly sensitive to erroneous data, since it appears as turbulent fluctuations. There are many ways to account for turbulence, only two alternatives were implemented here. The results of these methods show that the implementation affects the sensitivity. Further investigation is needed in alternate techniques. The techniques applied to screen the velocimetry for errors were based on simple statistical measures. It is expected that more sophisticated screening methods could significantly reduce the error to a point where the Reynolds stress is reasonably accurate. This too will require further investigation.

The accuracy of these methods is unknown, the effectiveness of various techniques could only be evaluated qualitatively. Determining an objective measure of quality will require extensive error analysis. This can be achieved by applying the method on velocimetry with a known pressure solution. Velocity and pressure solution sets can be developed analytically for simple geometries and numerically using computational fluid dynamic packages. However verification with experimental results is critical to evaluate the accuracy in turbulent flow applications.

Methods cited in literature used more sophisticated techniques at integrating the pressure gradients and correcting error in the velocimetry. Incremental improvements are expected with the implementation of these methods. Since specific details were not given on the implementations given in literature, more time will be required to include the same techniques in this method.

Improving the techniques to minimize the error, performing more experiments or further investigations in the accuracy is beyond the scope of the thesis. The analysis shows that PIV results can be used to give insight into the pressure field. Currently there is ongoing research on developing these techniques further. It is not critical that these advanced

techniques are fully developed for future experiments, conventional pressure probes can still be used to give reliable results.

Appendix E

Pressure Sensor Systems

Pressure data is an important component to aerodynamic research. Accurate and effective means of collecting pressure information depends on the transducers and the data acquisition systems employed to collect the information. An extensive investigation into available pressure sensors and the associated data acquisitions systems was conducted. The technical specifications and the costs of each technology and its application to proposed applications experiments is discussed below.

E.1 Integrated Multi-Sensor Systems

The experimental apparatus being sought should replicate the NREL Phase VI experiments at the Ames wind tunnel facilities. In that experiment the engineers used Scanivalve technology [30]. The Scanivalve Corporation has 3 sensors that can be used for our application. The sensor summary is given in Table E.1. Each of the sensors have a number of physical sensors, each sensor has an optional valve that doubles the number of channels. In all cases the optional valve version violates the sampling frequency constraint. For best measurements the pressure sensors will be mounted within the rotor blade, as such the physical scale of the sensor package and blade is important. The chord of the NREL Phase VI wind turbine, the S809 profile and ratio of between the size of the wind tunnel facility at the University of Waterloo and at Ames research facility gave a hypothetical blade for space approximation. Figures E.1, E.2 and E.3 show how the sensors will fit into the hypothetical

blade at various locations. The ZOC33 will not fit in any point in the blades, The ZOC22B will fit up to r/R 0.5 where the ZOC23 will fit up to r/R 0.9. To avoid dynamic effects at the highest frequency the maximum tube length is 0.014m, thus the ZOC23 will accurately measure pressure over 88% of the blade. While the ZOC 22B will violate the tube length constraint over 34% of the blade. Thus the ZOC 23 without the valve is the most suitable sensor for the application.

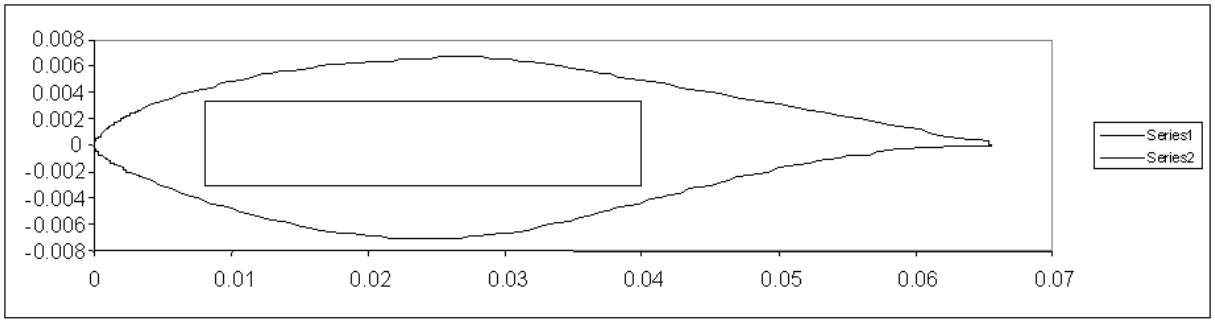

Figure E.1: ZOC 23B at r/R of 0.9

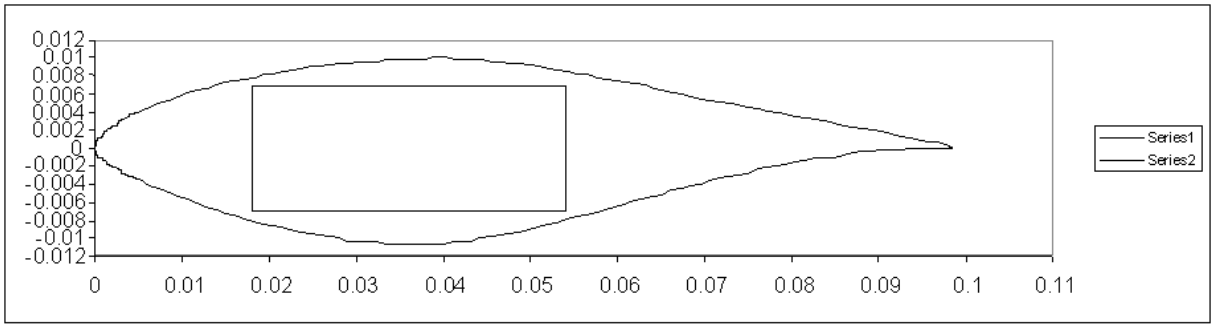

Figure E.2: ZOC 22B at r/R of 0.5

Sensor	ZOC22B64	ZOC22B32	ZOC23B64
Number of Inputs	64	32	64
Total Sampling Rate [Hz]	20000	20000	20000
Single Sampling [Hz]	312.5	625	312.5
L [m]	0.105	0.105	0.032
W [m]	0.01397	0.01397	0.00635
H [m]	0.0361	0.0361	0.03654
Min P Range [kPa]	2.5	2.5	2.5
Max P Range [kPa]	350	350	350
Error [Pa]	3.75	?3.75	3.75
Farthest Dist. r/R	0.5	0.5	0.9
Sensor	ZOC23B32	ZOC33-128	ZOC33-64
Number of Inputs	32	128	64
Total Sampling Rate [Hz]	20000	50000	50000
Single Sampling [Hz]	625	390.625	781.25
L [m]	0.032	0.126365	0.126365
W [m]	0.00635	0.036424	0.036424
H [m]	0.03654	0.042799	0.042799
Min P Range [kPa]	2.5	2.5	2.5
Max P Range [kPa]	350	350	350
Error [Pa]	3.75	3.75	3.75
Farthest Dist. r/R	0.9	NA	NA

Table E.1: Summary of Available Scanivalve Pressure Sensors

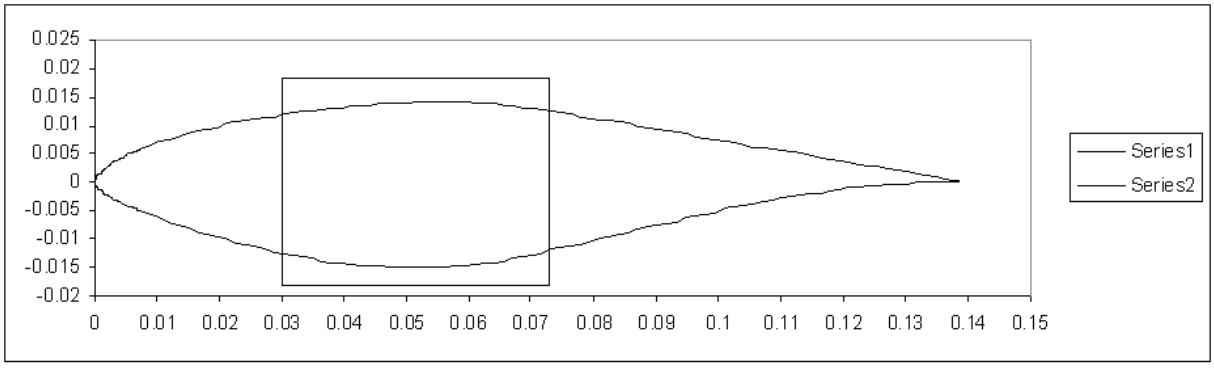

Figure E.3: ZOC33 at r/R of 0.01

The data acquisition for the Scanivalve solution is equally compact and can be digitized at the hub. The system consists of a RAD Base that does all the processing and communication to a PC. The RAD Base needs to be expanded with a RAD. The RAD is an expansion card that contains the analog to digital converter. The RAD is the device that interfaces with the sensor. The RAD Base can be expanded up to 8 RADs.

E.2 Individual Pressure Sensors

An alternative to the Scanivalve solution is using individual sensors. The individual sensor solution entails all the sensors being bought individually and connecting to the appropriate filtering and amplification circuitry. Small inexpensive sensors are used as the transducer. Then operational amplifiers, data acquisition hardware and a computer are assembled to make a custom pressure sensor data acquisition system.

The pressure ranges criteria cannot be met with one sensor. The best configuration is with one set to measure the smallest pressure range, the other for the largest pressure range. Three separate series of sensors were found for the application. Each series has similar sensors with different pressure ranges. Table E.2 outlines the merits of each sensor series. The size relative to the blade is given in figures E.4, E.5, E.6, E.7, E.8 and E.9. The Ares series has the best accuracy for the lower pressure range. However the size is too large to be utilized in significant numbers. The range and accuracy of the SX0 and 26PC series is the same. The 26PC is in a smaller package and will allow 10 sensors to be placed at the root with 2 sensors at the tip. The SX0 cannot fit beyond an r/R of 0.8. The 26PC series sensor is the least expensive at $20.00.

Series	Ares	SX0	26PC
Lower Range	1245 Pa	6895 Pa	6895 Pa
Upper Range	6895 Pa	34475 Pa	34475 Pa
Accuracy at Lower Range	3 Pa	34.5 Pa	34.5 Pa
Accuracy at Upper Range	52 Pa	172 Pa	172 Pa
Frequency	NA	10000 Hz	NA
Output Type	50 mV Range	25 mV Range	17 mV
Excitation Voltage	5 V	12 V	10 V

Table E.2: Summary of Individual Sensor Solution

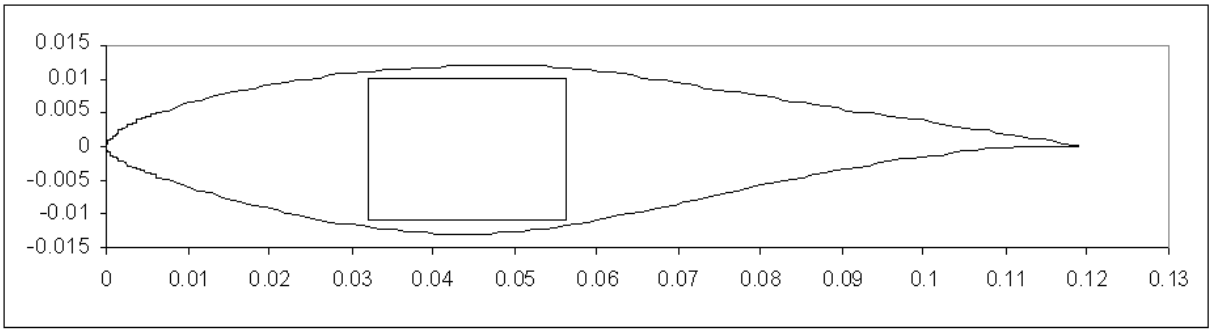

Figure E.4: 2 Ares Series Sensors at r/R 0.25

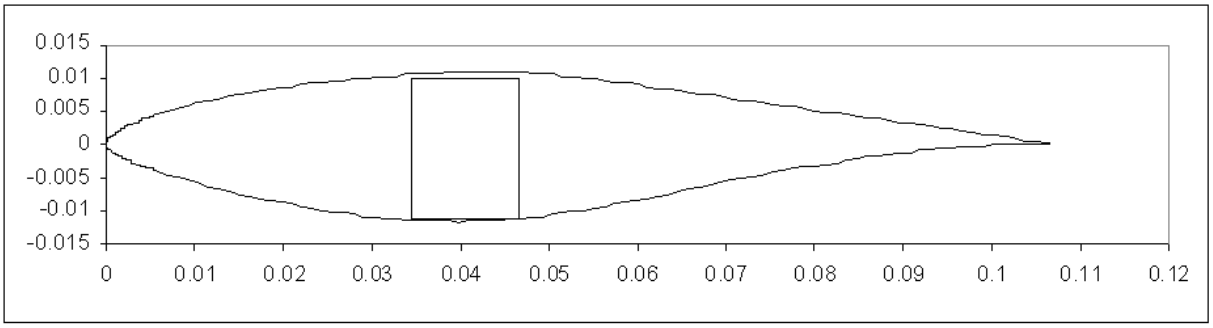

Figure E.5: 1 Ares Series Sensors at r/R 0.4

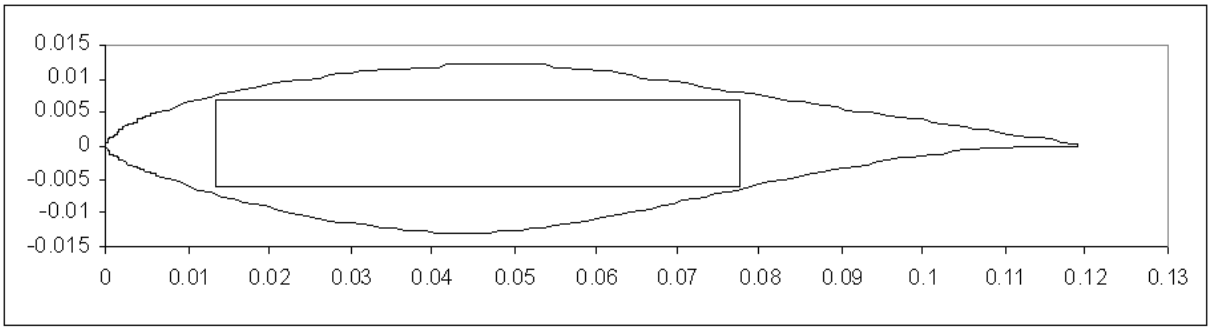

Figure E.6: 5 SX0 Series Sensors at r/R 0.25

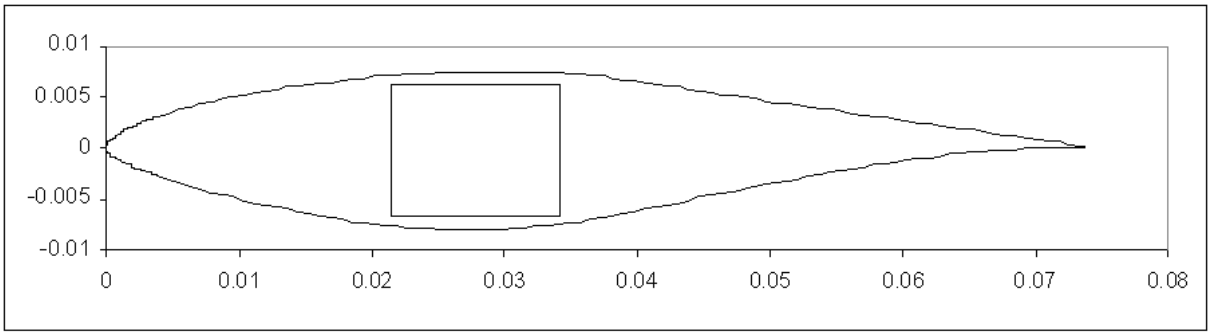

Figure E.7: 1 SX0 Series Sensors at r/R 0.8

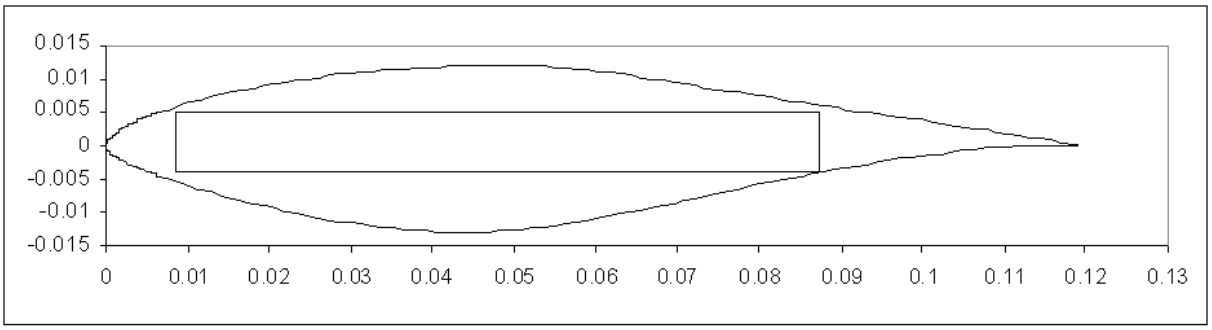

Figure E.8: 10 26PC Series Sensors at r/R 0.25

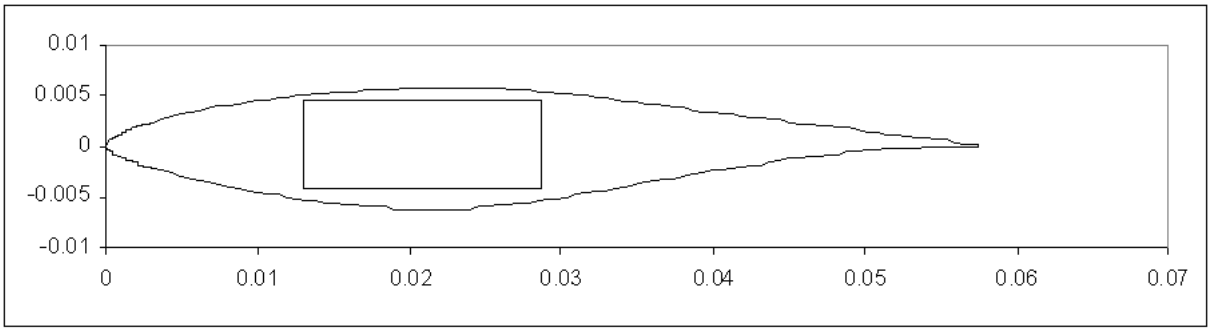

Figure E.9: 2 26PC Series Sensors at r/R 1

E.3 Computer Based Data Acquisition

Personal Computer Input\Output Card Solution

The PCI IO card solution relies on a simple analog input channel for measuring the pressure sensors. The sensors themselves require a power source and give a millivolt signal. To avoid noise the signal needs to be amplified with op-amps. This would require a separate clean DC power source for both the op-amp and the sensor. A battery would be sufficient. The op-amps would need to be soldered onto the same board as the sensor. This solution requires additional labor. A schematic of this system is given in Figure E.10.

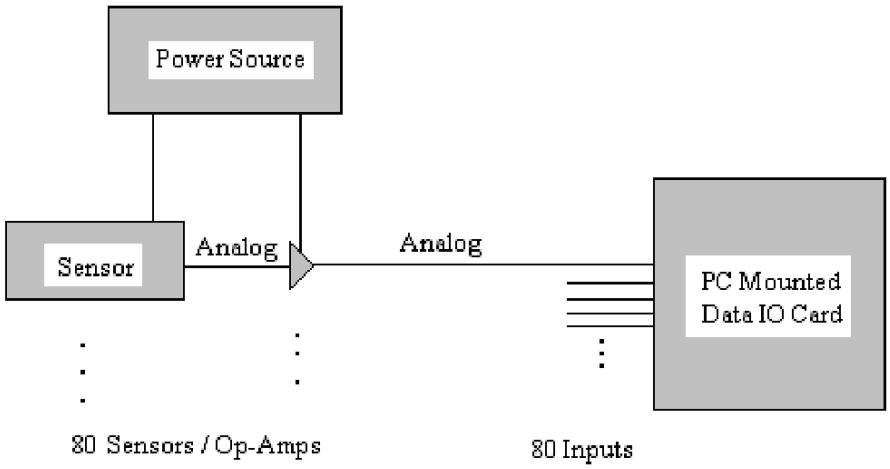

Figure E.10: Personal Computer Input\Output System Architecture

The NI PCIe-6225 is the best data acquisition card. It was chosen first for having the maximum amount of analog inputs and second for having the least cost. Another card being considered for other applications is the NI PCIe-6251. There is a possibility that two cards are needed satisfy the desired number of sensors and sampling frequency for the other application. The criteria of the thesis application are different that those of the application the card is being selected for. However these data acquisition systems still meets the criteria of the thesis application. A third acceptable data acquisition card is

	NI PCIe-6225	NI PCI-6229	2 x NI PCIe-6251
Analog Inputs	80	32	32
Resolution [bit]	16	16	16
Sampling Freq. per [Hz]	3,125	7,812.5	62,500
Analog Output	2	4	4

Table E.3: Summary of Individual Sensor Solution

given. It has the same number of analog inputs as that of the other application however it is much less expensive. The specifications are given in Table E.3.

E.4 Full Bridge Data Acquisition Systems

National Instruments offers three solutions for measuring full bridge sensors directly. The differences between systems are in the performance and the costs. The SCXI system has the best performance and the highest cost, the next best is the Compact DAQ with moderate cost and performance, finally the SC architecture has the best price but the worst performance. The details of each system are given below.

E.4.1 SCXI architecture

The first relies on the SCXI architecture. The SCXI module will read and power the sensor in analog format simultaneously. Each module gives 8 channels. For 24 channels 4 modules are needed at $3,110 a piece. The modules plug into a chassis, which multiplexes the channels and yields another analog signal for a PCI-6229 data IO card in the computer. A schematic of this architecture is given in Figure E.11. A 4 module chassis costs $842 the NI PCI-6229 data acquisition card costs $1,314. The total cost of this system is $14,595. The system is analog up to the computer data acquisition card. This allows it to be sampled at any speed. Increasing speed decreases the accuracy. The signal is not digitized until the PCI card. This can potentially add additional noise to the measurements. The SCXI offers one advantage over the other systems. There are more signal conditioning options with the SCXI data acquisition system. The modules can perform substantial signal conditioning on many more channels at larger sampling rates. With larger chassis the system can hold up to 12 modules, which would give up to 72 channels. Thus the SCXI architecture is the best system for future applications that need faster more accurate and greater number of channels.

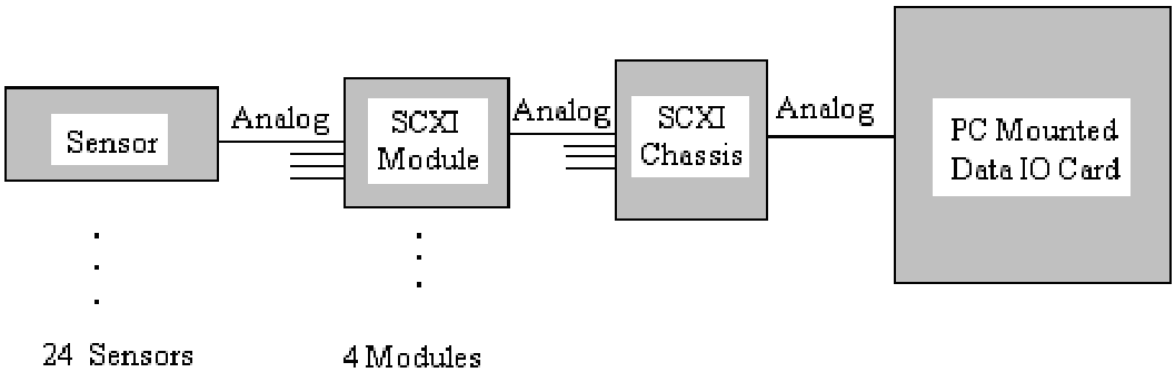

Figure E.11: SCXI Architecture

E.4.2 Compact DAQ Architecture

The second architecture is the Compact DAQ. It is similar to the SCXI system in that it is made up of modules that are mounted within a chassis that will send data to a computer. The difference is that the system digitizes the data at the module and sends the information to a computer via USB cable. Thus no additional data IO card is needed. Each module for the system takes 4 inputs from four quarter bridge sensors. The chassis can take up to 8 modules, 6 modules will allow for 24 channels and 8 will allow for 32 channels. The schematic of the architecture is given in Figure E.12. Each module costs $1,233 the chassis costs $1,120.50. National Instruments offers a %25 cost reduction for any items that are purchased at quantities of 5 or greater. With the discount the total cost of the system is $6,669 for 24 channels and $8,518 for 32 channels. The system can be sampled at 50 kHz and is digitized at the module thus the speed is sufficient and there is minimal noise introduced in the signal.

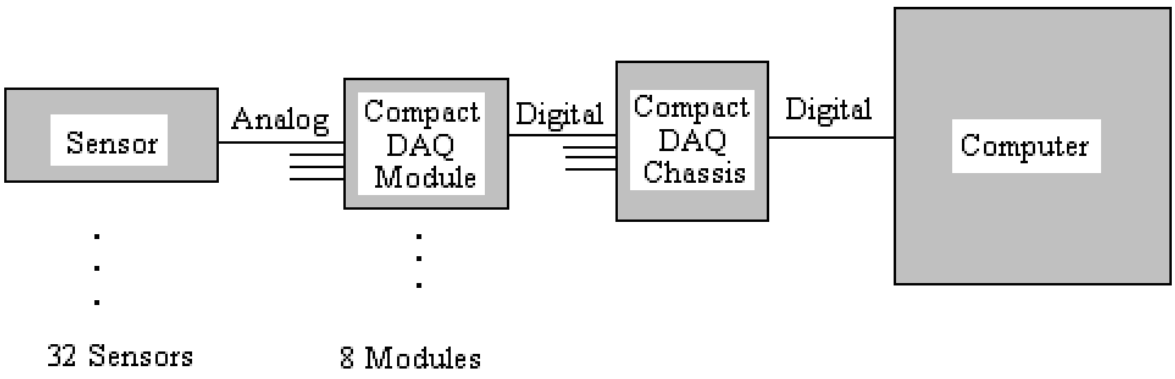

Figure E.12: Compact DAQ Architecture

E.4.3 SC Architecture

The third architecture is the SC architecture. The system relies on a similar architecture as the SCXI architecture. The signal from the sensor plugs into a module. The module is connected to a chassis and sends an analog signal to the computers Data IO card. A schematic of this architecture is given in Figure E.13. Each module will accept signals from two sensors and cost $369.00 each. The chassis is $301.50 while the NI PCI-6229 data acquisition card will be used to sample the data. The same 25% discount will apply to the SC modules. The total cost of the system is $4,936. Given that the digitizing occurs at the IO card there is an increased chance more noise will be introduced in the signal. Finally the system is further limited to a maximum sampling rate of 1.6 kHz.

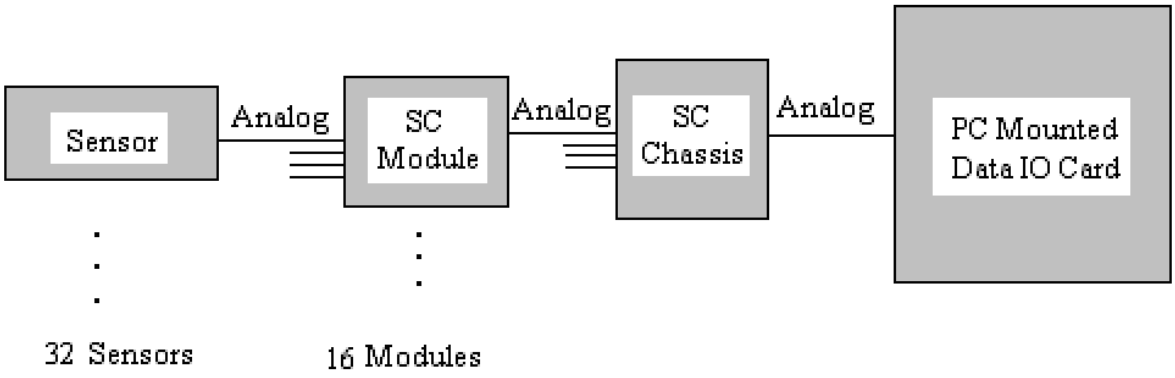

Figure E.13: SC Architecture

E.4.4 Data Acquisition System Comparison

Figure E.14 shows the size of each of the data acquisition systems. The circle represents the inner boundary of the hypothetical rotor blades active area. The rectangle in the center is the smallest area occupied by the data acquisition. All three architectures are sufficiently small enough to not affect the flow. The compact DAQ is the smallest and will provide the greatest flexibility.

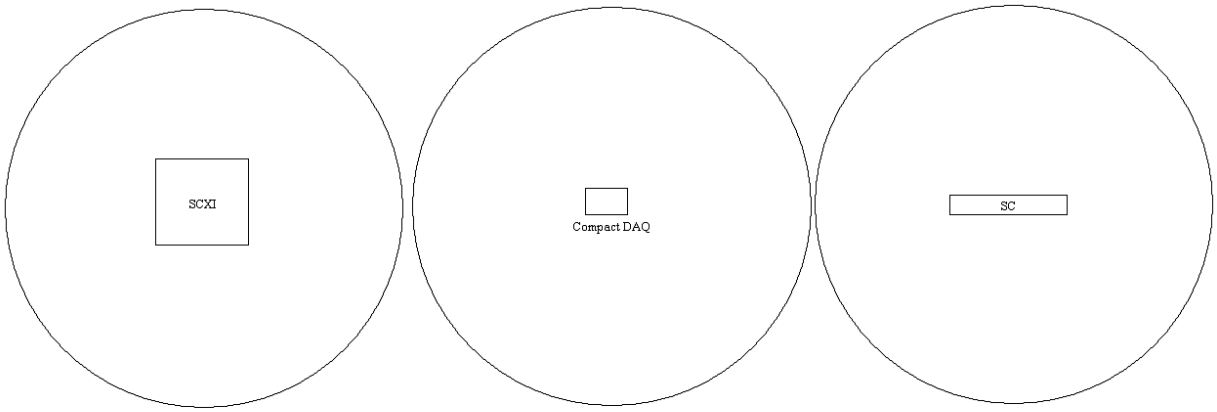

Figure E.14: Scale of Dedicated Quarter Bridge Data Acquisition Systems

Table E.4 compares the merits of all architectures. The SC Architecture is sufficient for the specifications of the experiment. However for a 32-37% cost increase the data acquisition is 31 times faster, half the size, has 50% greater bit depth and much less noise. The Compact DAQ architecture is a good system for the current needs and is moderately powerful enough to handle more powerful data acquisition. The SCXI is the most expensive but has the potential to be the most powerful system. The system can be upgraded to handle 72 channels sampled at 200 kHz with all the signal conditioning required. For the current application the SCXI advantages are above and beyond those of the experiment. It is unlikely that future applications will require the power of the SCXI architecture. The Compact DAQ architecture is sufficient for the current application and is moderately powerful enough to handle future applications. Thus the author recommends the Compact DAQ architecture.

	SCXI	Compact DAQ	SC
Maximum Channels	24	32	32
Sampling Rate [kHz]	200	50	1.6
Chassis Size L [m]	0.32	0.25	0.26
Chassis Size W [m]	0.19	0.09	0.24
Chassis Size H [m]	0.18	0.06	0.04

Table E.4: Summary of Dedicated Quarter Bridge Data Acquisition Systems

Appendix F

Cameras and Lasers for PIV

F.1 Available Cameras for Selection

The following cameras were evaluated for time resolved PIV. The critical performance statistics is the relationship between frames per second (fps) and the resolution. Most cameras will allow for very high fps with reduced resolution. The quality of PIV data degrades with resolution. Thus it was important that a camera has both high speed and excellent resolution.

- Photron SA-1 FastCam
- Photron 1024 PCI FastCam-X
- Ultima APXi2
- Ultima APX-RS
- Ultima APX
- Phanton V10.0 Mono
- Phanton V9.1 Mono
- Phanton V7.3 Mono

- Dantec TR
- Dantec iNanosense Mk7

Tables F.1, F.2 and F.3 summarizes many of the details of the cameras. All cameras in the table use CMOS technology, the Ultima APXi2 and Dantec iNanosense Mk7 use an intensified head to achieve increased light sensitivity. Typically cameras can capture frames faster when resolution is reduced. A high resolution camera like the Phantom 10.0 has a low nominal frame rate but at 1 mega pixel it has frame rates comparable to the Ultima APX and Phantom 9.1. Thus the full range of speed and resolution needs to be considered for comparison. Figure F.1 show how speed varies with resolution for each of the cameras.

Camera	Cost	Max. Res. H	Max. Res. W
Photron SA-1	150000	1024	1024
Photron 1024 PCI	40000	1024	1024
Ultima APXi2	NA	1024	1024
Ultima APX-RS	80000	1024	1024
Ultima APX	70000	1024	1024
PHANTOM V10.0 Mono	NA	2400	1800
PHANTOM V9.1 Mono	NA	1632	1200
PHANTOM V7.3 Mono	61800	800	600
Dantec TR	84750	1280	1024
Dantec iNanosense Mk7	84750	1280	1024

Table F.1: Cost and Size Summary of Available Cameras

Camera	FPS at Max Res. [Hz]	Min. Shutter [μs]	Frame τ [μs]
Photron SA-1	5400	2	185
Photron 1024 PCI	1000	1.5	1000
Photron APXi2	2000	5	500
Ultima APX-RS	3000	2	333
Ultima APX	2000	4	500
PHANTOM V10.0 Mono	480	2	2083
PHANTOM V9.1 Mono	1000	2	1000
PHANTOM V7.3 Mono	6688	2	150
Dantec TR	500	0.1	2000
Dantec iNanosense Mk7	1000	NA	1000

Table F.2: Speed Summary of Available Cameras

Camera	Pixel Size [μm]	EI Sensitivity
Photron SA-1	20	NA
Photron 1024 PCI	17	4800
Photron APXi2	17	NA
Ultima APX-RS	17	4800
Ultima APX	17	4800
PHANTOM V10.0 Mono	NA	2400
PHANTOM V9.1 Mono	NA	2400
PHANTOM V7.3 Mono	NA	4800
Dantec TR	NA	NA
Dantec iNanosense Mk7	NA	NA

Table F.3: Light Sensitivity Summary of Available Cameras

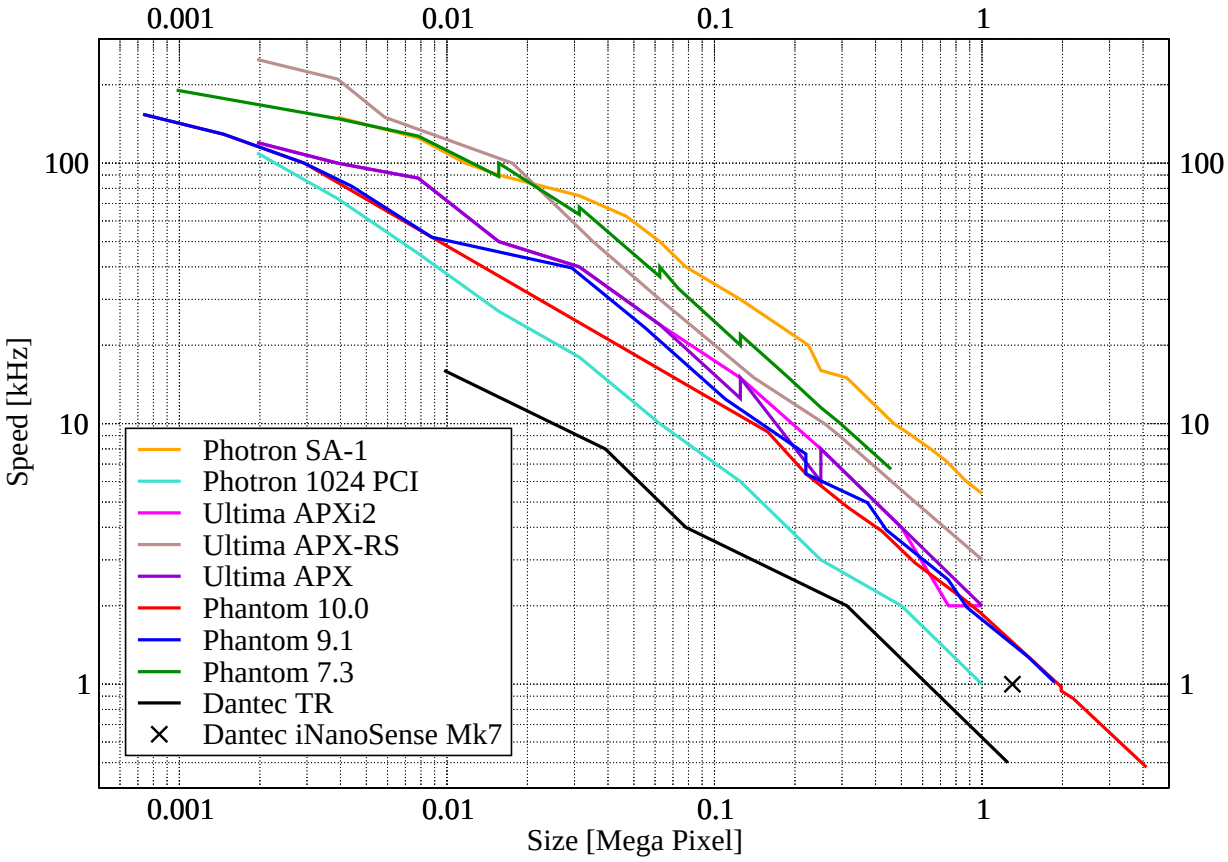

Figure F.1: Camera Speed vs. Image Size

The fastest camera available for high resolution images is the Photron SA-1. At a full mega pixel the cameral has a frame rate of 5.4 kHz. This will allow PIV images to be captured at 2.7kHz, this is nearly 4 times faster than the minimum sampling rate for pressure signals. The speed of the camera also allows its use in high speed flows, the fluid velocity would have to approach 500 m/s before the cross correlations would be compromised. The full mega pixel resolution allows for 1024 vectors with 32x32 interrogation areas. Thus this camera is superior for PIV on transient phenomenon.

Light sensitivity is a concern, hence cameras with intensified heads were considered. There are two suppliers, Dantec Dynamics, and Photron. The Dantec camera has a frame rate of 1 kHz with a resolution of 1.3 mega pixels. The frame rate of this camera gives a PIV sampling rate below the minimum sampling rate for the pressure signal. There is no information on how this camera will perform at reduced frame rates. The Photron APXi2 has a mega pixel resolution but a frame rate of 2 kHz. This would give a sampling rate of 1 kHz, sufficient according to the pressure sensor sampling criteria. Provided that the light sensitivity of the SA-1 is insufficient either of these intensified cameras could be the best choice. All other cameras fail to have comparable performance.

F.2 Experiments Testing Camera Performance

This section outlines the analysis of three cameras being considered for PIV research. The first is the Dantec iNanosense, the second is the APXi2 and finally the third is the Photron FastCam SA-1. The cameras were evaluated on light sensitivity and image quality. The test matrix each camera was submitted to was different for each camera. However there are enough one to one comparisons to get a sense of each cameras performance. Despite the variations in the camera tests, all cameras were used to image a flow over a cylinder in a small wind tunnel. For most tests a continuous wave Argon laser was used, also the Nd:YAG pulsed laser was used for two of the cameras. Many images were taken but the images given here are selected to be representative of the various aspects of the cameras performance.

There are many factors to evaluating a camera, the resolution the speed and the ease of integration, are all factors on top of light sensitivity and quality. In this section these

factors were ignored. The purpose of this is to summarize the new information given by evaluating the cameras directly.

F.2.1 Small Argon Laser Comparison

In the first comparison the cameras were given light from the air cooled argon laser. Both the Dantec and APX camera were operating with 75% intensifier and $20\mu s$ shutter speed. The SA-1 has an exposure of $333\mu s$. The comparison shows that the SA-1 and APX images are similar. They differ by exposure time. Comparing the exposure time shows that the SA-1 needs about 17 times more light.

Ignoring more significant bits also brightened the SA-1 images. This increased the brightness by a factor of 16. This brightening and increased exposure shows that the SA-1 camera needs about 272 times more light for the exact same image with 12-bit resolution. If 8-bit resolution is acceptable for the images, than 17 times more light is needed for the SA-1 over the APX.

The Dantec Camera could not be compared since the image is simply black. The F-Stop on the APX and SA-1 lens is 0.9, where as the F-Stop on the Dantec lens is 2.65. The difference in lenses will make the two Photron cameras about 4 times more powerful. See Figures F.2, F.3 and F.4 for the example images.

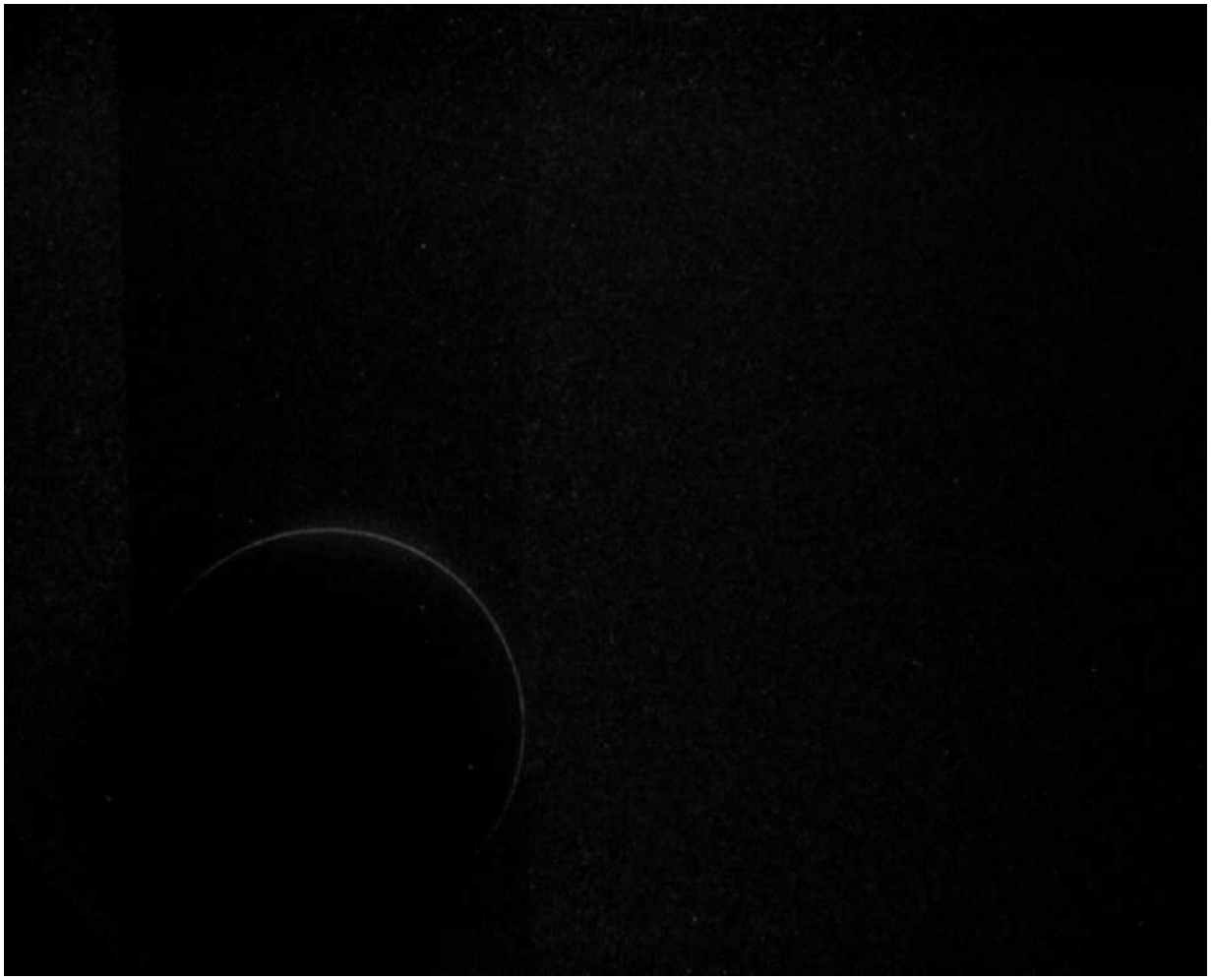

Figure F.2: Dantec Camera 20 micro shutter, air cooled argon laser, image

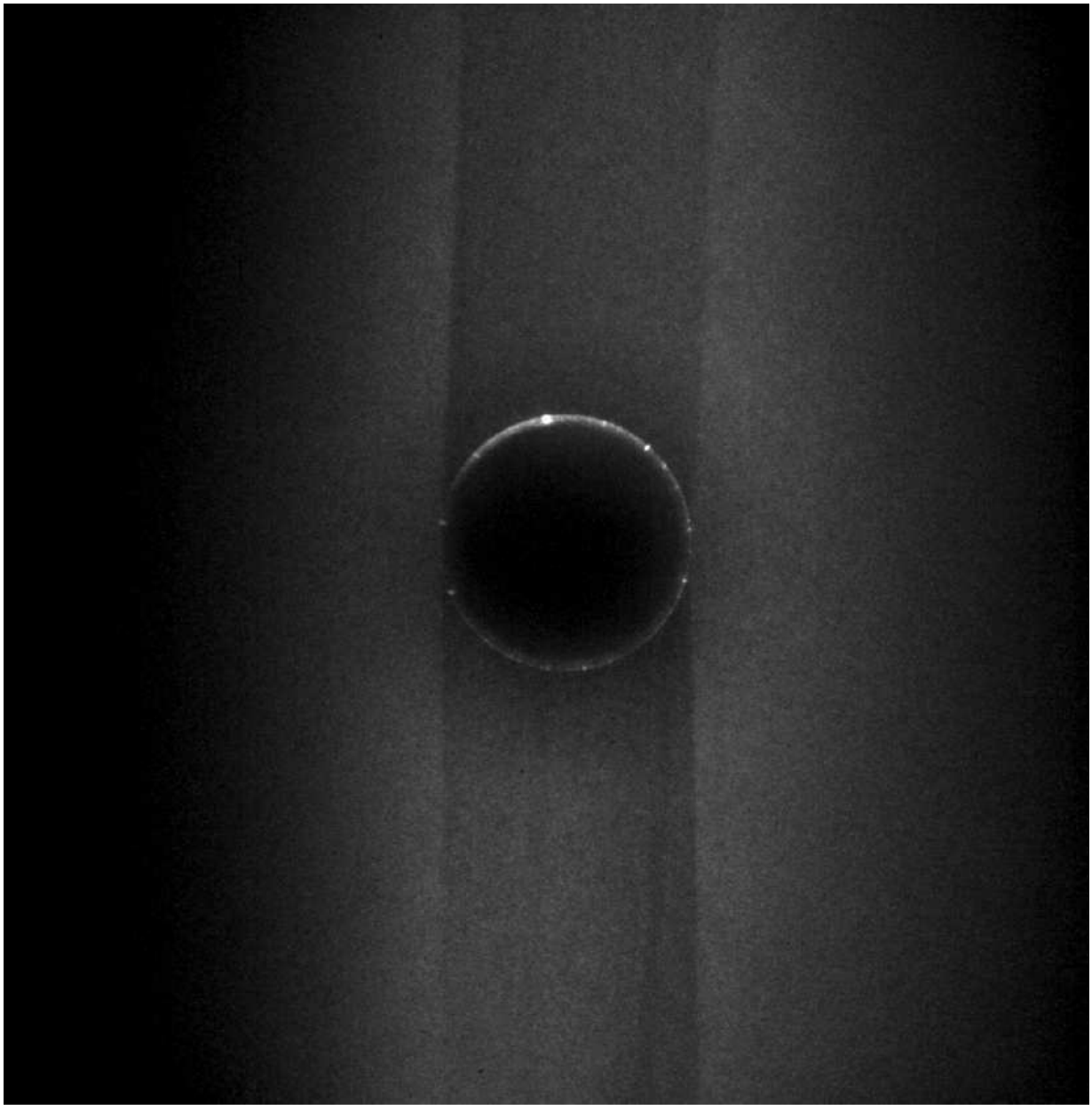

Figure F.3: APX Image 20 micro shutter, air cooled argon laser, image

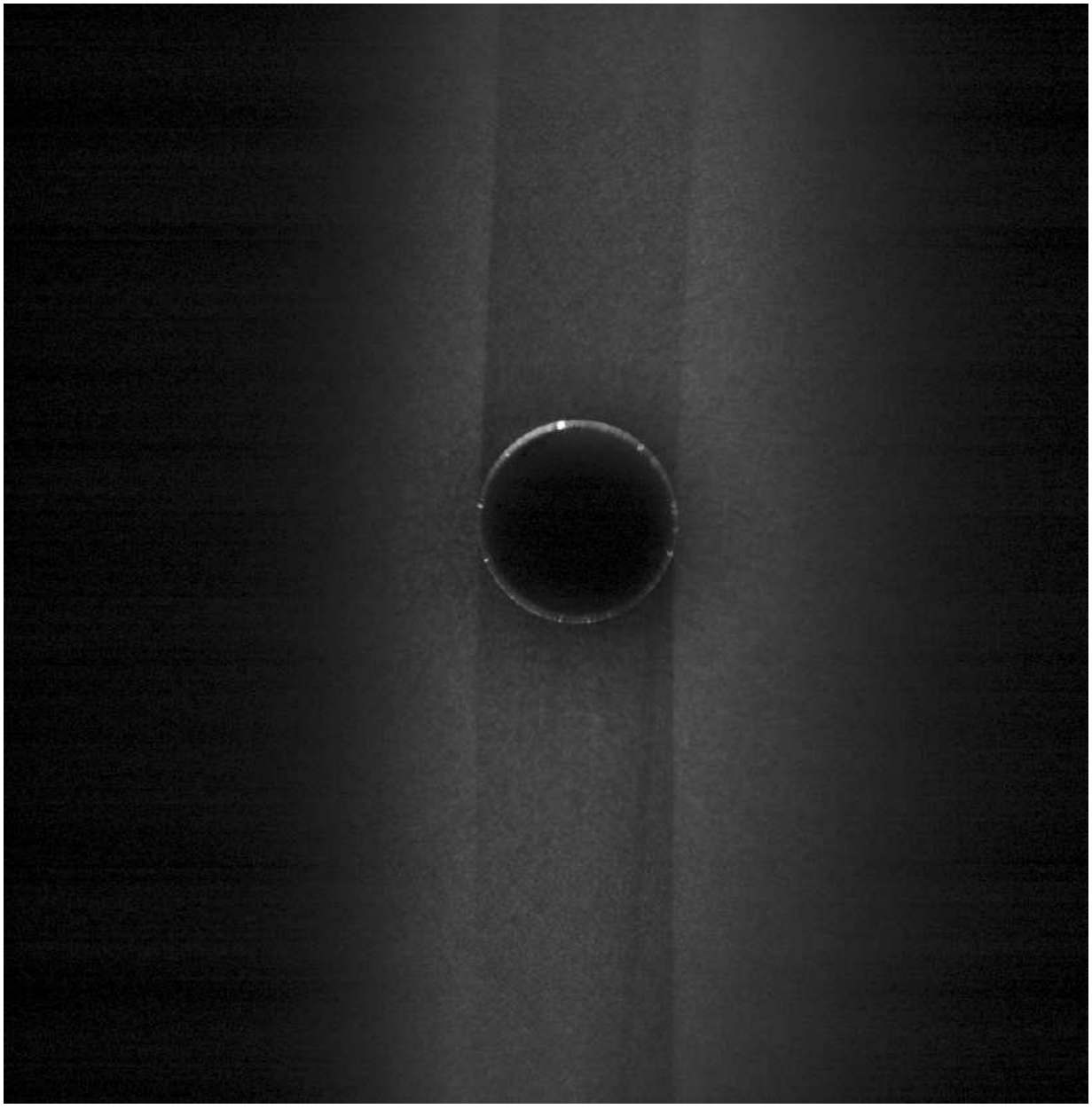

Figure F.4: SA-1 330 micro shutter, air cooled argon laser, image

F.2.2 Large Argon Laser Comparison

Several images were taken with the Photron cameras using the 5W argon laser for a light source. This allowed a second comparison of the two cameras. There are two instances where both cameras had shutter speeds of 6 microseconds. The APX camera gave a better image however the SA-1 image still shows enough detail to be useful. In the SA-1 camera the first 4 most significant bits were ignored. In this comparison the APX camera was able to capture 16 times the light.

The difference in light sensitivities with the two lasers shows nonlinearities between the cameras. This is expected since good images with a brighter light sources require less intensification. With a stronger light source the SA-1 sensitivity is comparable for 8 bit images. For full 12-bit resolution 16 times more light is needed. With weak light sources the APX is still useful where the SA-1 light sensitivity drops off considerably. Examples of each camera are given in Figures F.5 and F.6.

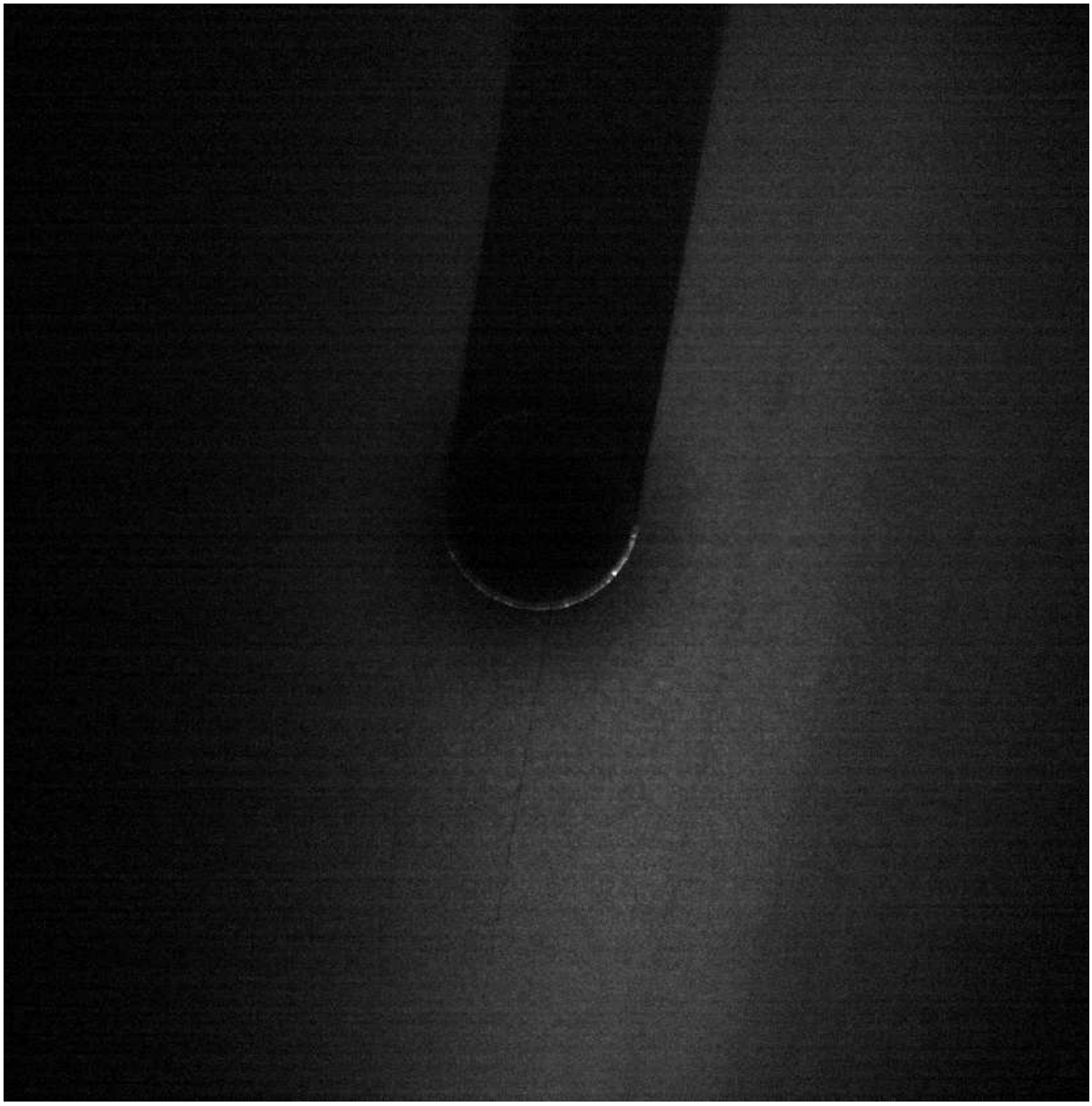

Figure F.5: SA-1 Camera, 6 microsecond shutter with 4W Argon Laser, Image

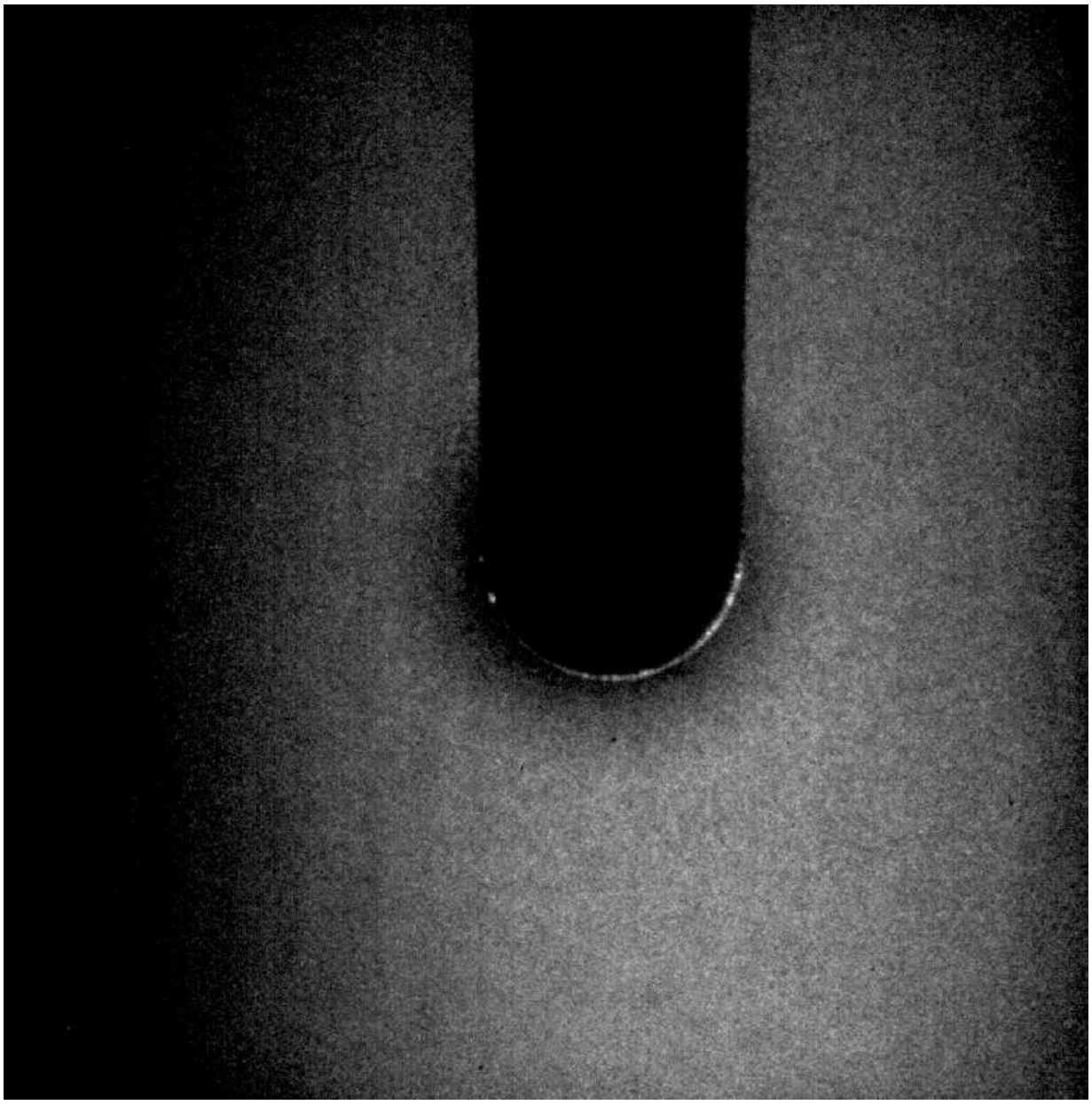

Figure F.6: APX Camera with 6 microsecond shutter, 4W Argon Laser, Image

F.2.3 Pulsed Nd:YAG Laser Power Comparison

The SA-1 and the Dantec camera were both tested with a Nd:YAG laser. The Nd:YAG laser image in Figure F.7. The images for the Dantec Camera were not collected thus cannot be given for comparison. However in both cases the Nd:YAG laser power was adjusted until the light level was sufficient to gather good images. The attenuation scale ranges from 0 to 1000 and reflects increasing intensity. According to Dantec product specifications the laser intensity increases monotonically with attenuation but not linearly. At an attenuation of 100 the intensity is 2.2% the nominal. For the SA-1 images the attenuator was at 75 whereas for the Dantec camera the attenuator was at 50. Again the Dantec camera is using a lesser lens. This shows that the two cameras have comparable performance with a pulsed laser.

The similar sensitivity cannot be attributed to stronger illumination, despite a stronger nominal illumination for the Nd:YAG laser, the attenuation setting gives a weak laser pulse. The intensifier on the Dantec camera was set to full power, unlike the weak image comparison, it seemed to have little effect on the light sensitivity. Comparing the 5ns pulse width of the Nd:YAG laser with the $20\mu s$ shutter used in other camera images, there is a large order of magnitude difference in the exposure period. The intensifier relies on chemical reactions to provide intensification, like all chemical reactions there would be transient response time associated with the reaction. Given the large orders of magnitude difference in exposure, it is very likely that the Nd:YAG pulse width is less than the response time of the intensifier, reducing the effectiveness of the intensifier.

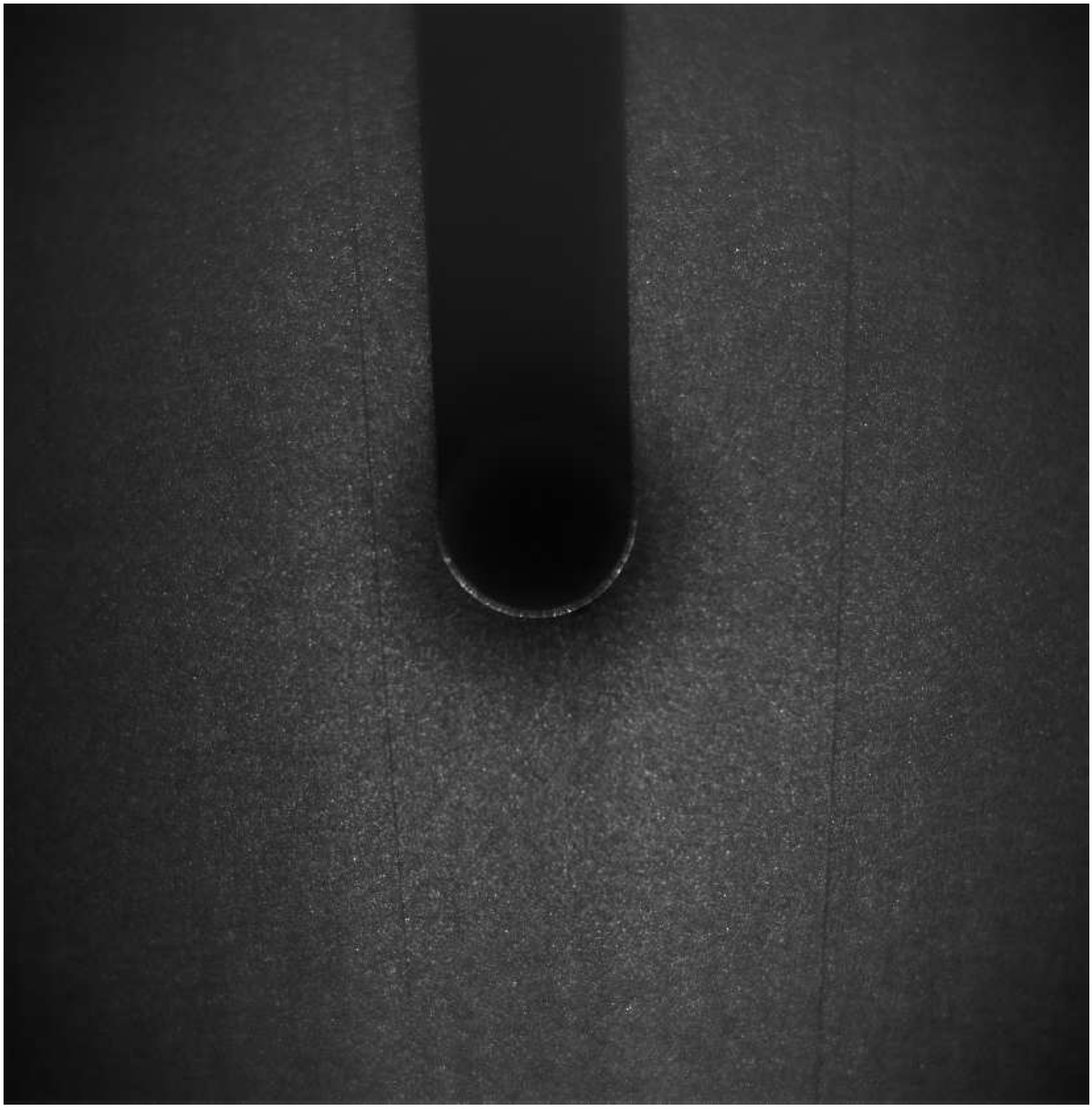

Figure F.7: SA-1 Images with the Nd:YAG Laser

F.2.4 Dantec Image Quality

The images given in Figures F.8 and F.9 were taken with a solid state pulsed laser supplied by the Dantec Salesman. The images were taken for a high speed flow. These images were selected because they show how the camera can be used for flow visualization, the smoke is such that the maximum sharpness can be evaluated, and the black shows the nature of the noise introduced by the Dantec camera. Figure 6 the intensifier is at 75% whereas Figure 7 the intensifier is at full power. Figure 7 shows bright spots in the shadows. This is the noise given by the intensifier.

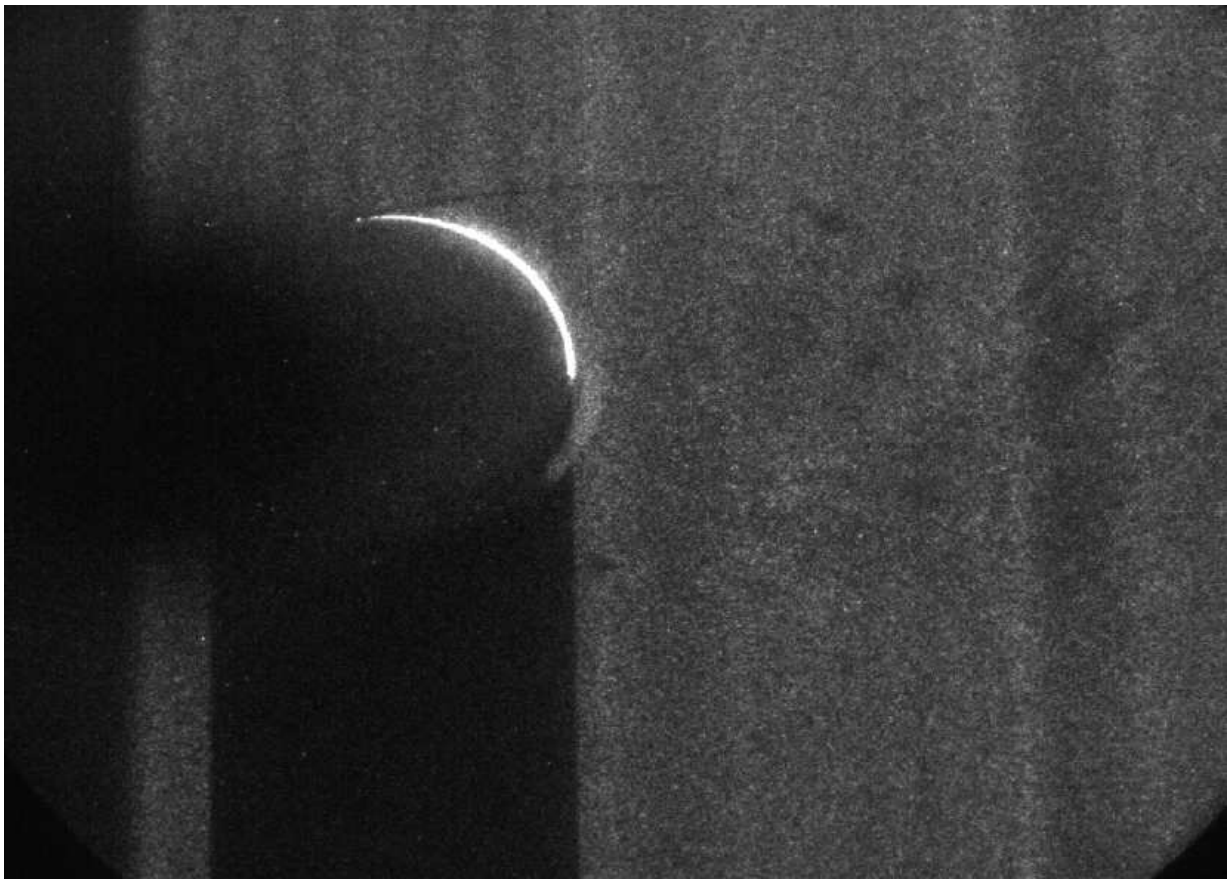

Figure F.8: Example of the Dantec Image Quality

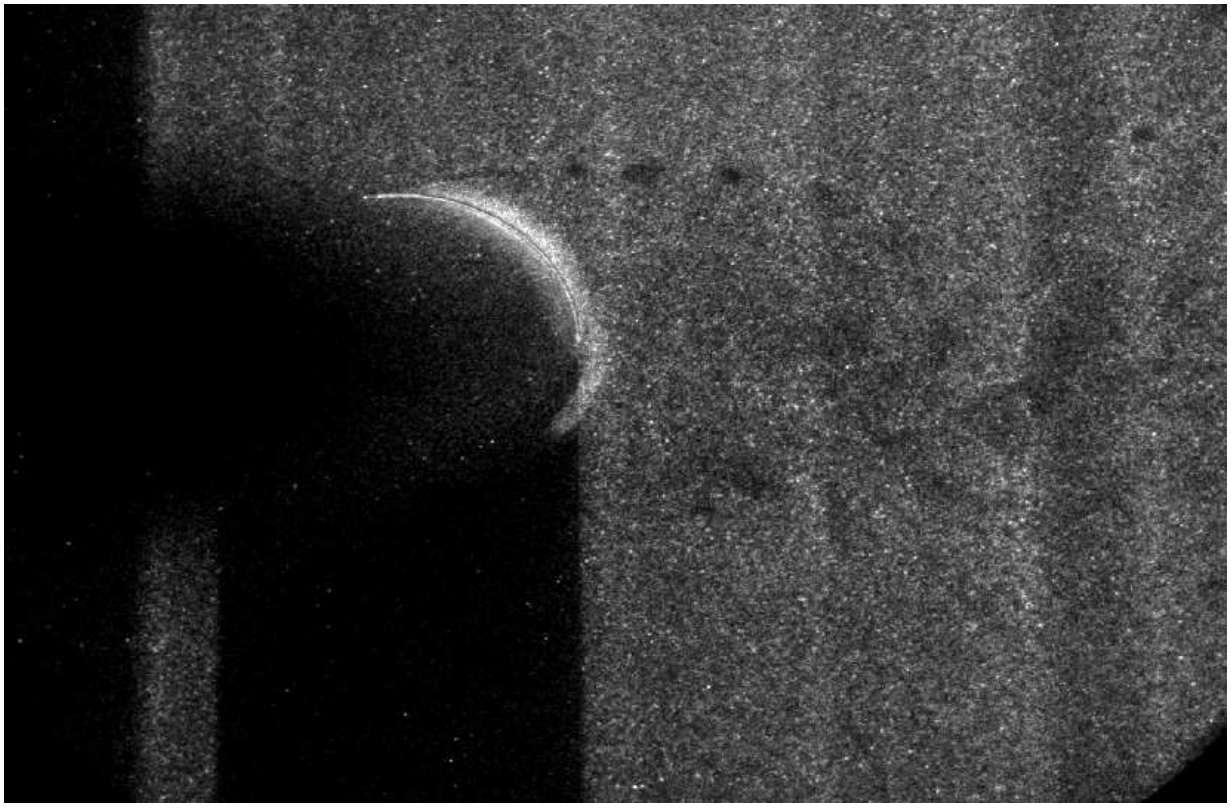

Figure F.9: Dantec Image with Full Intensification

F.2.5 APX Image Quality

Figures F.3 and F.6 show some of the best examples with the APX camera. Overall the image quality is slightly blurrier than the Dantec camera. Figure F.10 below shows some of the noise. Around the outside of the cylinder there is a small haze. This image is not the worst. The haze became very significant at full intensification to the point where the images are useless. The noise in the Dantec camera resembles isolated bright spots. The noise in the Dantec camera resembles a haze. There is more noise in the Dantec camera however the noise did not impact PIV results significantly. It is expected that a homogeneous haze will be worse than a scattering of isolated bright spots. The homogeneous haze will mix well with the image where bright spots can be easily identified.

Overall the Dantec camera gave better images. The noise is an issue however it does not render the camera useless. Figures F.8 and F.9 show the potential for flow visualization. Several PIV cross correlations were taken. Good correlations were achieved for gas speeds as high as 42 m/s. Based on light sensitivity the Dantec camera could potentially be slightly more powerful than the APX camera. If lenses had a smaller impact than the APX camera is similar in light sensitivity.

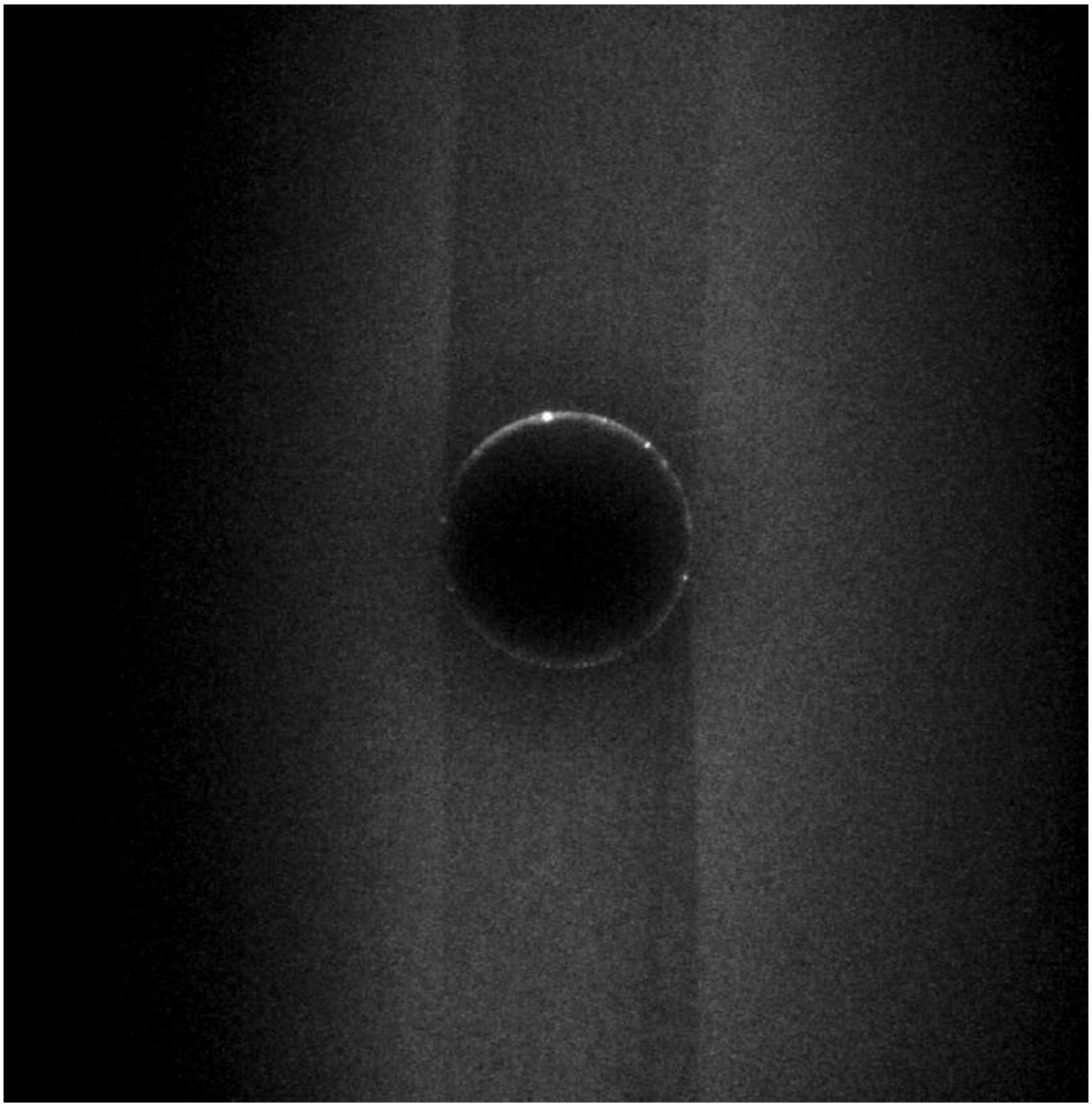

Figure F.10: Example of APX Noise

F.2.6 SA-1 Image Quality

The image in Figure F.7 was taken with the Nd:YAG laser. Zooming in on the image will allow one to see that the SA-1 is capable of picking up particles within a couple pixels. The streaks in the light sheet are very sharp with SA-1. The image quality of the SA-1 is superior to that of the intensified head cameras.

There is one limitation though. As stated before many of the SA-1 images require higher order bits to be ignored. When 4 bits are ignored and only the lower 8 bits are used banding shows up in the image. It is the author's opinion that this is caused by the down loading of the information. It is hypothesized that bright rows were sampled first, while the dark rows lost their charge. This only shows up in the lower bits because the loss in charge will be very small and should only impact the lower bits. Figure F.11 shows and example of this banding. Recalibrating the camera can diminish the problem. After recalibration the set-up used in figure F.11 was used to capture the image in figure F.12. The second image is not as bright however the banding is gone, thus the banding issue is a small problem.

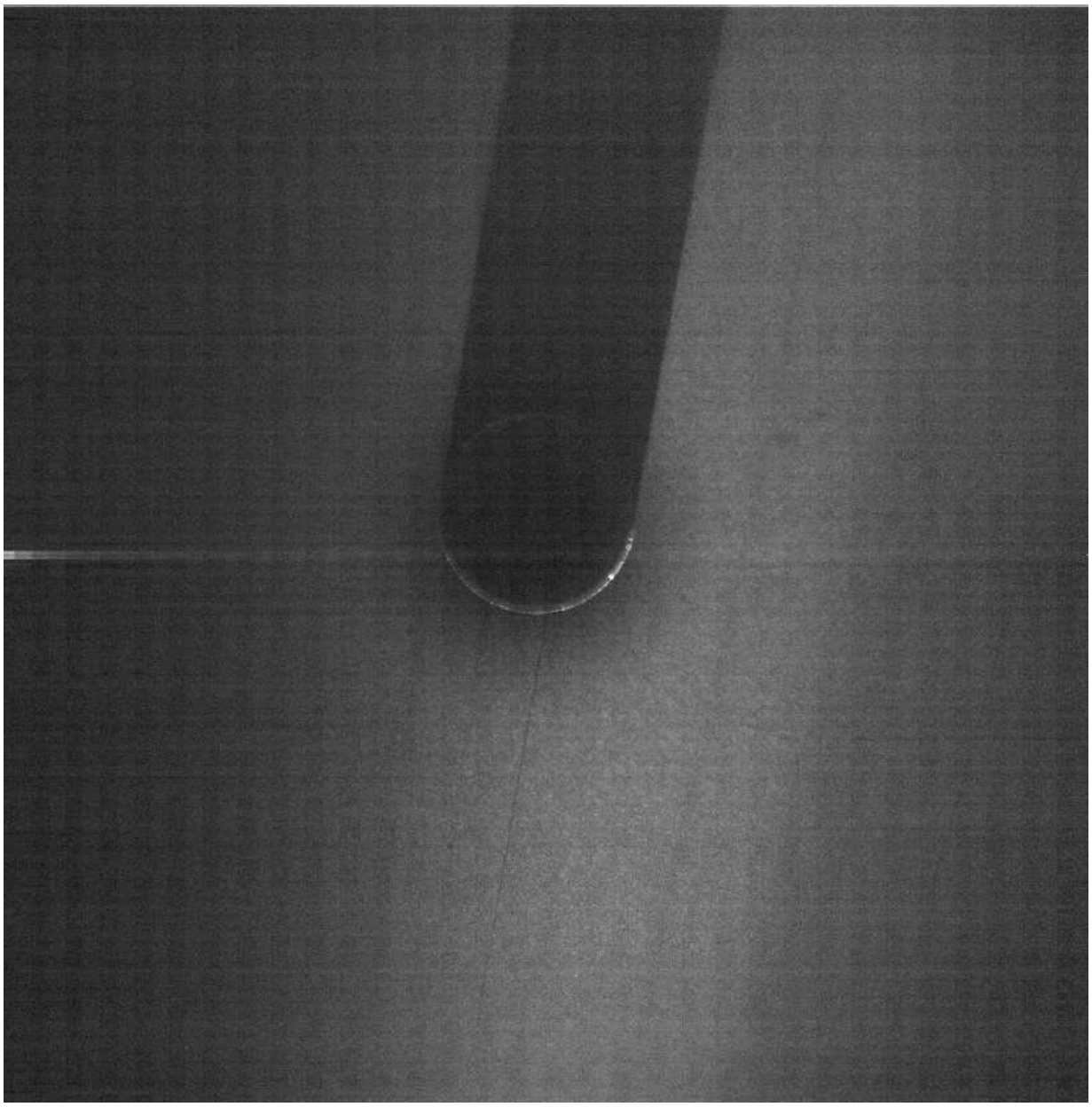

Figure F.11: SA-1 Banding

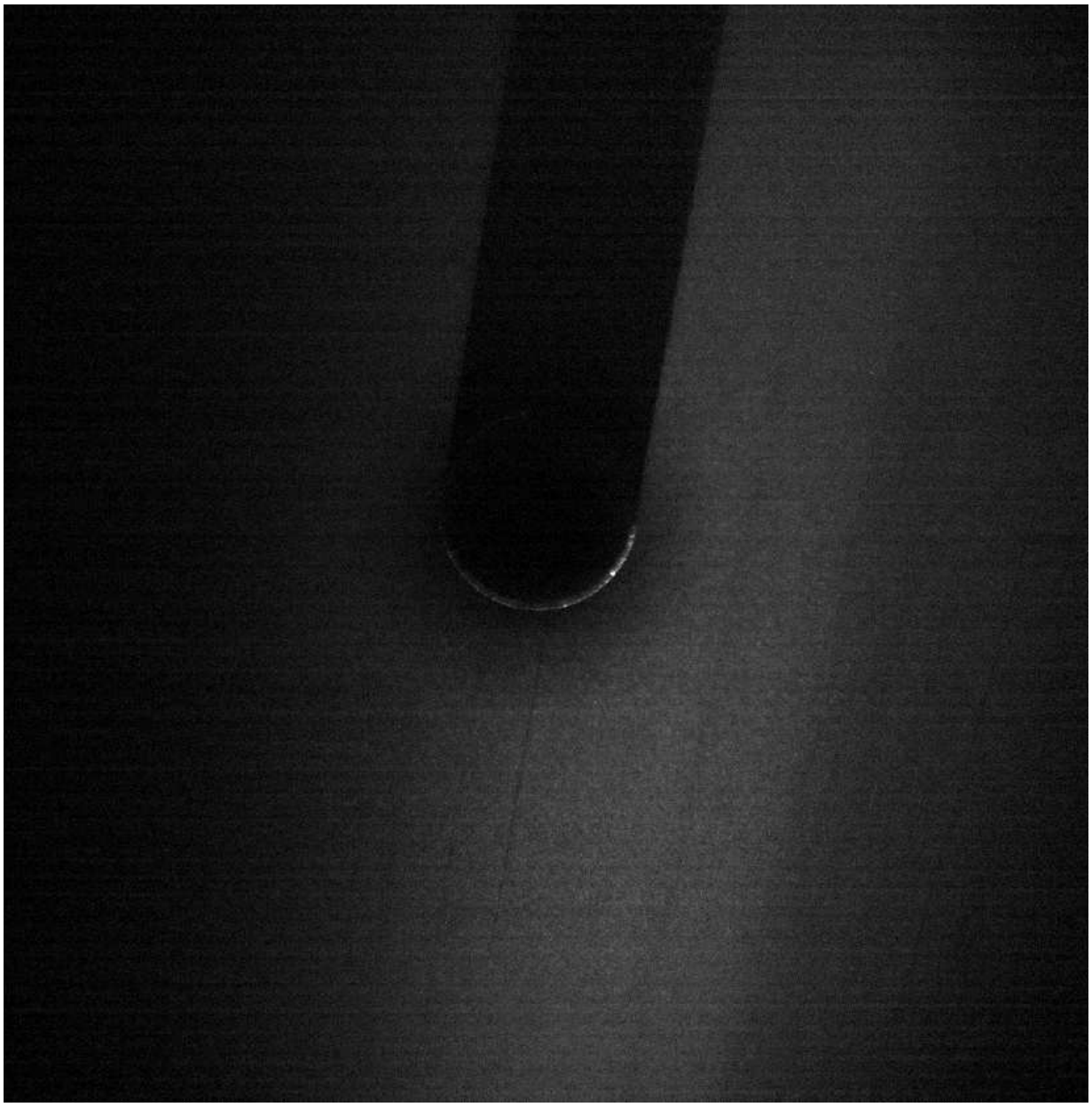

Figure F.12: SA-1 Camera Images after Calibration to Avoid Banding

F.3 Evaluation of Camera Light Sensitivity

Preliminary results of the camera evaluation show that the intensifier provides a significant benefit with weak continuous illumination. Yet pulsed lasers are preferred for PIV. Results suggest that under these conditions there is little benefit to intensification. The nonlinearities in the laser attenuator give uncertainty in these conclusions. Direct measurements of the laser power at the same attenuation levels will allow direct comparison in light sensitivity. Measuring the laser power serves a second purpose, it gives a numerical measure of light sensitivity, that can be used to determining the applicability of various lasers. This sections outlines the procedure used to measure the laser power and the subsequent results. A small discussion is given on the implications of the results on the overall camera selection.

F.3.1 Procedure

The top two cameras were both tested with the Nd:YAG laser, the pulsing of the Nd:YAG laser exposes the camera to a discrete amount of energy. As such the light sensitivity is independent of the shutter speed or time. Using a laser calorimeter, measurements of the laser power will indicate the light sensitivity of each camera. The power in watts was measured with one laser head firing at the nominal 15 Hz. The power of each pulse is determined by dividing the laser power by the nominal pulsing frequency.

Before each measurement the scale on the laser calorimeter was zeroed. For each measurement the meter was reading for several minutes to collect the steady state reading. To avoid damaging the sensor, measurements were made only at the power levels where the cameras were evaluated at. All cameras were evaluated with full flash lamp on the Nd:YAG laser. There is hysteresis in the attenuator knob of the Nd:YAG laser. To account for this, all attenuator adjustments were made by reducing the attenuation down to the desired value. This same procedure was used when evaluating the camera.

Attenuation Level	Power [mW]	Pulse Energy [mJ]
0	5.5	0.367
50	4.1	0.273
75	9.5	0.627

Table F.4: Nd:YAG Laser at Various Levels of Attenuation

F.3.2 Results

The power of the laser was measured at three levels of attenuation. Measurement at an attenuation of 0 was taken as a reference, while an attenuation of 50 and 75 reflect the conditions of the Dantec and SA-1 camera respectively. Table F.4 lists the results of each measurement.

F.3.3 Discussion

The first thing to note is the laser is more powerful at 0 attenuation than at 50 attenuation. The attenuator is highly non-linear. This increased power at 0 vs. 50 has been confirmed visually many times. Thus this reading is not erroneous.

The cameras were evaluated with field of views of approximately 10cm square. With this field of view the Dantec camera was performed well under test 2 conditions. Hence 0.27 mJ pulses are needed for the Dantec camera. With a similar field of view the Photron SA-1 camera was evaluated under test 3 conditions. Hence 0.63 mJ pulses are needed for this camera.

Another interesting thing to note is that the difference in light sensitivity is a lot less with a high powered pulse. The Photron camera needed about 2.3 times more light to capture a similar image. With continuous light sources the difference in sensitivity is 17 times greater. This confirms that the intensifiers do not respond well when capturing a short burst of light.

F.3.4 Camera Light Sensitivity Summary

Under pulsed laser conditions, both cameras were able to perform well with low energy pulses. The Dantec camera required 0.27 mJ pulses where the Photron camera required 0.63 mJ pulses. The benefit of the intensifier is reduced even further with pulsed light sources. The intensifier was only able to amplify the light by a factor of two in these conditions. With continuous light source the gains were 17 times greater. This shows that the Photron SA-1 is a better camera for time resolved PIV with pulsed lasers. The gains with the intensifier are reduced with pulsed lasers thus the compromise in image quality and speed is not justified.

In the event that a high speed pulsed laser is not available, the high powered Argon laser will be used. Camera comparisons with the 5W Argon laser show a moderate decline in the intensifier performance, yet the intensified camera is still more sensitive. The images captured with the SA-1 camera and the 5W laser were adequate with very short exposure times. Thus the light sensitivity is adequate for available lab equipment.

F.4 Laser Selection

The laser is an important aspect in any PIV set-up, it also has implications in the camera selection. Hence the top two cameras, the Dantec iNanosense and the Photron Fast-Cam SA-1, will be evaluated against the New Wave Pegasus and the Quantronix's Darwin Duo lasers. The measured pulse energy for adequate images with both cameras is being used to determine the largest sampling area that can be achieved with each laser. At minimum the maximum sampling area needs to be large enough to contain the chord of a wind turbine rotor of interest, approximately $900cm^2$ for a 30cm chord. Larger sampling areas would enable the measurement of larger fluid structures, typically found in wake of a wind turbine. This latter criteria is not mandatory, however could prove useful in deciding between similar options.

F.4.1 Details of the Study

Both cameras were used to image a 0.01 m2 window illuminated with the Nd:YAG laser. The power of the laser was increased until acceptable images were taken with the camera. The acceptability of the images was determined visually. PIV correlations can word on dark images. The limits given here represent a conservative limit. Second the images taken with SA-1 camera were evaluated with full 12-bit resolution. Darker images can be taken with the lower 8 bits. The assumed laser power needed to see 8 bit images is given by equation F.1.

$$P_8 = \frac{P_{12}}{2^4} \tag{F.1}$$

The power required by each camera to image 0.01 m2 is given in Table F.5. The Dantec camera does not perform well under pulsed laser conditions. The intensifier fails to respond well when the light is emitted in an instant. The camera still outperforms the SA-1 under 12-bit operation, however the SA-1 is superior under 8 bit operation.

Camera	Energy [mJ]
Dantec iNanosense	0.273
Photron FastCam SA-1 12-bit	0.627
Photron FastCam SA-1 8-bit	0.039

Table F.5: Laser Pulse Energy to Image $0.01m^2$ with a Given Camera

The Pegasus is a dual cavity Nd:YLF laser meant for PIV. The laser has a 10mJ pulse at 1kHz repetition rate. The laser power drops off with higher repetition. The power versus repetition is given in Table F.6. The laser has a maximum repetition rate of 10.5 kHz. The Quantronix Darwin Duo is a similar laser. It has the same Nd:YLF dual cavity laser, the major difference is increased power, 25 mJ pulses at 1 kHz. For PIV application the laser needs to fire at half the rep rate of the camera. Thus the maximum laser speed with the Dantec and SA-1 camera is 1 kHz and 2.7 kHz respectively. Both lasers have high energy pulses at these levels.

Speed [kHz]	Pegasus Power [mJ]	Darwin Duo Power [mJ]
0.5	11.5	
1.0	10.1	25.0
2.0	6.5	17.7
3.0	4.6	12.6
4.0	3.5	9.6
5.0	2.6	7.4
6.0	2.3	6.0
7.0	1.6	
8.0	1.5	
9.0	1.2	
10.0	0.9	2.8

Table F.6: Summary of Laser Power

The maximum area was estimated based on the assumption that the required laser power varies linearly with the image area. The window areas are presented as window lengths, which is the length of on edge of a square at a given area. The maximum window length for each camera and laser combination is given by equation F.2.

$$L = \sqrt{A_{ref} \frac{P}{P_{ref}}} \tag{F.2}$$

F.4.2 Results and Discussion

Figure F.13 shows how the maximum window length varies with laser repetition rate. The Darwin Duo with the SA-1 under 8-bit operation gives the largest window of 2.53 m at 1 kHz. With the Darwin Duo laser at 1 kHz, the SA-1 at 12-bit and the Dantec cameras have a maximum window length of 0.63m and 0.96m respectively. The window lengths with the Pegasus laser at 1 kHz, for the SA-1 at 8-bit, SA-1 at 12-bit and Dantec cameras are 1.60m 0.4m and 0.61m respectively. At the full speed of the SA-1 at 8-bit and 12-bit the window

lengths with the Pegasus is 1.15m and 0.29m respectively. At full speed of the SA-1 at 8-bit and 12-bit the window lengths with the Darwin Duo is 1.89m and 0.47m respectively. In nearly all cases the minimum window length criteria was met, at 12 bit resolution the SA-1 with the Pegasus laser the window length criteria is violated. Given that the bit depth is adjustable and the criteria is nearly satisfied, we can assume all combinations are acceptable.

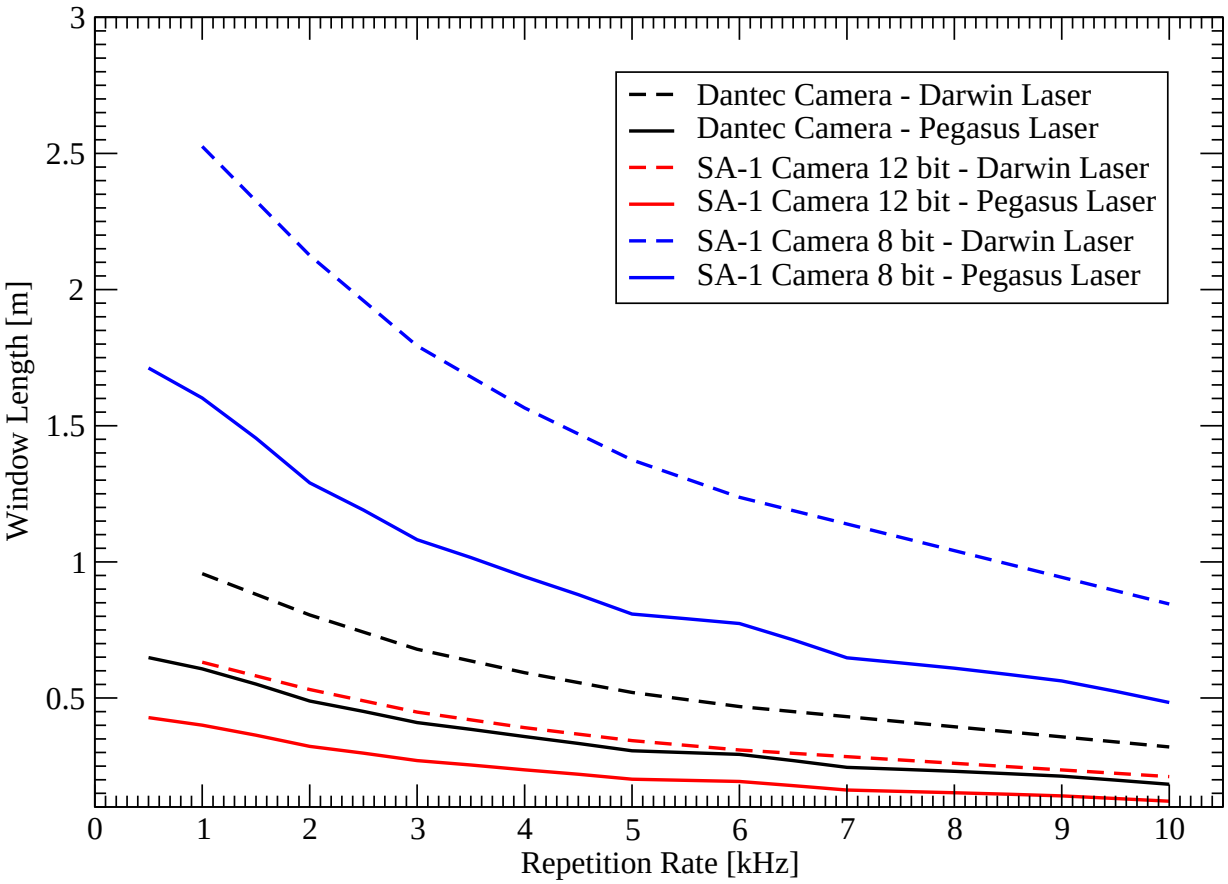

Figure F.13: Window Length of Various Laser and Camera Combinations

With the lower bits of the SA-1 camera the camera is superior with respect to the Dantec Camera. When comparing the Dantec camera with the SA-1 at full 12 bit resolution the difference is small. Thus the Dantec camera performs poorly with pulsed lasers. The

Intensifier cannot react fast enough to be effective. Hence the Photron SA-1 camera is the best for both PIV and flow visualization.

Appendix G

Effect of Reynolds Number on Airfoil Performance[1]

A study by the now defunct National Advisory Committee for Aeronautics (NACA) was performed on the effect of profile shape and Reynolds number on the section performance [43]. The study investigated the section lift drag and moment polar's from Reynolds numbers as low as 10^5 and as high as $9 \cdot 10^6$. The effect of larger Reynolds number was investigated by testing airfoils that exhibited increased sensitivity to viscous effects. The profiles and their geometric trends, analyzed in the study are given in the following list.

Varying Thickness

- NACA 0009, NACA 0012[2], NACA 0015, NACA 0018

Varying Camber

- NACA 0012[2], NACA 2412, NACA 4412[3], NACA 6412

Varying Thickness and Camber

[1] A substantial portion of this Appendix summarizes the work of Jacobs et al. [43]
[2] Airfoil has been used in wind turbine studies [102, 29]
[3] Airfoil has been used in wind turbine studies [102]

- NACA 4409, NACA 4412[3], NACA 4415[4], NACA 8318[5]

Varying Thickness Shape

- NACA 23012, NACA 23012-33

Varying Camber Shape

- NACA 0012[2], NACA 2412, NACA 23012, NACA $2R_2$12, NACA 4412[3], NACA 43012, NACA 6412, NACA 6712

Effect of Split Flap

- NACA 0012[2], NACA 23012, NACA 23015, NACA 23021, NACA 43012

Effect of External Flap

- NACA 23012

Effect of Handley-Page slot

- Clark Y[3]

The peak coefficient of lift (C_l) was most sensitive to Reynolds number. This lift coefficient is reached at the onset of stall, since stall has strong dependence on viscous effects, the trends of this coefficient give many insights into the effect of Reynolds number. Jacobs et al. argued that the nature of stall was strongly affected by the presence of laminar separation, the location of laminar turbulent transition of the boundary layer and the extent of turbulent separation. [43]

All separation phenomenon occurs in adverse pressure gradients. On an airfoil section with positive angle of attack, the lowest surface pressure occurs on the suction side, just after the leading edge on the nose, beyond this point the pressure is increasing up to the trailing edge. If the boundary layer is laminar there will be local separation soon after the minimum pressure point. At low Reynolds number, separation can occur at angles

[4]Airfoil has been used in wind turbine studies [102, 36, 56, 25]

[5]This airfoils increased sensitivity to viscous effects allowed for the insights into the effect of Reynolds numbers in excess of 10^7

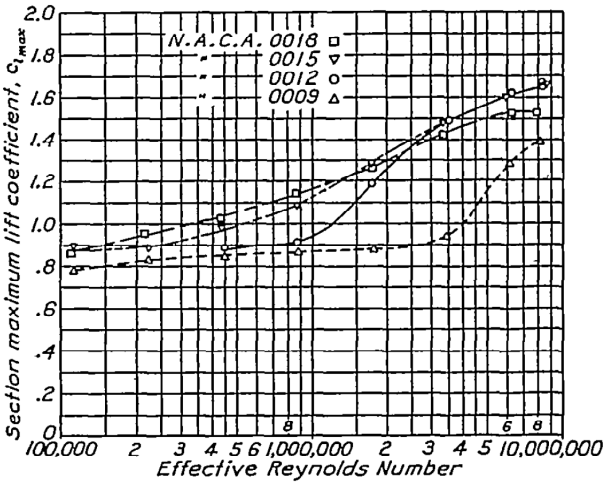

Figure G.1: Peak Lift vs. Reynolds Number of NACA 00xx Series Airfoils [43]

of attack of 0 degree. With reduced Reynolds number the early laminar separation will cause stall at smaller angles of attack and give a reduced peak lift. Another effect of low Reynolds number is the nature of stall. With separation occurring at the leading edge, there is a dramatic drop in lift, with the airfoil entering a deep stall. [43]

At increased Reynolds number, the boundary layer will transition from laminar to turbulent conditions, towards the trailing edge. The mixing effect of the turbulent state resists separation, and can reattach a flow separated from laminar separation. At angles of attack approaching stall, the reattachment process will give a small increase in lift. The biggest lift increases are due to an increased angle of attack for the onset of stall. With increasing Reynolds number this transition point moves from the trailing edge towards the leading edge, giving earlier reattachment and greater resistance to stall, further increasing the peak lift. An example of increasing lift can be seen in figure G.1. One can see that for the NACA 0012 at a Reynolds number of approximately $8 \cdot 10^5$ boundary layer transition starts to occur. The dramatic increase of the lift coefficient is the transition point moving from the trailing edge towards the leading edge. [43]

Eventually the turbulent transition point will occur before the minimum pressure point negating any laminar separation and further lift increases with Reynolds number. This seen in the NACA 8318 airfoil in figure G.2. At higher Reynolds number boundary layer

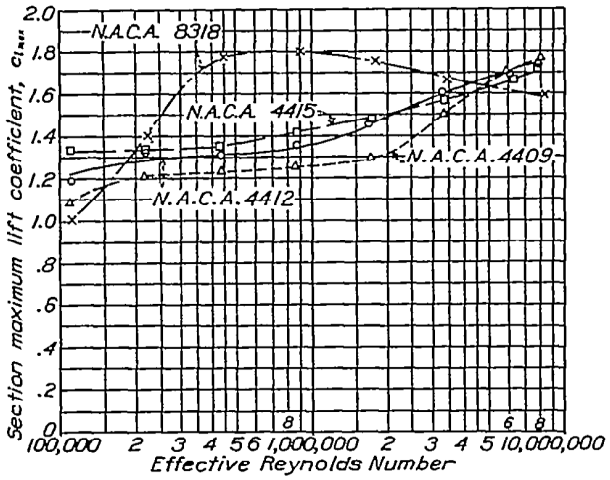

Figure G.2: Peak Lift vs. Reynolds Number of NACA 44xx Series Airfoils [43]

thickening will cause the turbulent boundary layer to separate towards trailing edge. The turbulent separation will start at the trailing edge and move further towards the leading edge with increasing Reynolds number and angle of attack. This will cause deep stall at smaller angles of attack and give smaller peak lift coefficients. Under these condition when the boundary layer is completely turbulent, the stall is more gradual. With respect to the angle of attack, the lift polar will show lift increasing at a decreasing rate up to a peak, then decreasing gradually to the deep stall point. [43]

The Reynolds number also has had effect on the profile drag. However most airfoils exhibit the similar trends of flat plate drag, with the exception of when the flow is completely laminar. In the laminar region each airfoils drag is unique with differences bearing little correlation with the various geometric parameters. Overall the drag coefficients are decreasing with increasing Reynolds number. At a Reynolds number of about $6 \cdot 10^5$ the airfoils will start show increasing drag parallel to the Prandtl-Gerber transition curve. At a Reynolds number of 10^7 the drag of nearly all the airfoils coalesce and the drag decreases parallel with flat plate drag for turbulent flows. [43]

The report by Jacobs et al. on the effect of Reynolds number shows the consequences of not achieving local similarity. First the nature of stall will change with changes of Reynolds number between 10^5 to 10^7. Table G.1 shows selected performance of airfoils

Airfoil	Peak Lift at Transition	Maximum Peak Lift	Reynolds Number for Transition	Reynolds Number Maximum Peak Lift
NACA 0012	0.91	1.66	$8.71 \cdot 10^5$	$8.37 \cdot 10^6$
NACA 4412	1.36	1.74	$8.74 \cdot 10^5$	$7.92 \cdot 10^6$
NACA 4414	1.41	1.72	$8.82 \cdot 10^5$	$7.92 \cdot 10^6$

Table G.1: Lift Properties of Selected Wind Turbine Airfoils [43]

typically used in airfoil studies. Table G.1 gives the peak lift coefficient at the onset of the transition phenomenon and the maximum lift coefficient once the turbulent transition advances towards the nose. Table G.1 also gives the respective Reynolds numbers for the two peak lift conditions. In summary between Reynolds numbers $8.71 \cdot 10^5$ and $8.37 \cdot 10^6$ the peak lift coefficient can increase by increments 0.75 and 0.31. This dramatic change in lift coefficients occurs above Reynolds numbers that are practical for wind tunnel testing and below the Reynolds found in large scale wind turbines. Overall scale model tests with these airfoils will fail to achieve flow similarity with multi-megawatt turbines.

The behavior of the NACA 8318 and other airfoils in the report shows that high Reynolds number behavior can be reproduced at Reynolds practical for testing. The peak lift tends of the NACA 8315 show that local flow similarity can be achieved at Reynolds number as low as $4.5 \cdot 10^5$. Quantitatively there would be differences in the performance of airfoils like the NACA 8315 in test conditions and the airfoils on large wind turbines. However the important qualitative features will be preserved, this is more important when trying to investigate the flow physics. Quantitative similarity is only important in predicting the performance. Other airfoils may display high Reynolds number behavior at lower Reynolds number but further investigation is required. For the current study the Reynolds number of $4.5 \cdot 10^5$ is the minimum Reynolds number for accurate testing.

The effect of scaling and the airfoil selection is complicated by the effects of rotation. It has been well documented that rotation modifies the stall behavior of an airfoil [77, 87, 85, 74, 13, 14, 72, 71, 70]. This effect is still poorly understood, hence currently results from static airfoil tests are the best source for selecting airfoils for wind turbines.

Appendix H

Details of Wind Tunnel Computational Models

H.1 Infinite Domain Model

H.1.1 Model Geometry

The flow in an infinite domain would be axis-symmetric. This simplifies the model allowing it to be modeled as a two dimensional flow. An axis-symmetric wedge was used for the flow domain. The domain of the first model is shown in figure H.1.

A periodic pair was defined between the two X faces. The periodic pair causes the mesh from one X face to be extruded to the other face. In the extrusion only one layer of elements was generated. This with the symmetry boundary conditions eliminate any X variation in the solution, making the models two dimensional.

H.1.2 Boundary Conditions

An inlet boundary condition is used on the face at the farthest negative Z direction. Medium turbulence was specified for the inlet flow. The inlet speed is specific to the model instance. An outlet boundary condition was used for the face at the farthest positive Z direction. The static pressure was set to 0 Pa. A wall with a free slip boundary condition

was set for the face in the farthest positive Y direction. A symmetry boundary condition was used for the faces on either X side of the domain.

H.1.3 Domain and Grid Convergence Study

To accurately simulate an infinite domain, the boundary conditions should have no effect on the results about the rotor. To ensure boundary effects are negligible a domain study was carried out. The distance of the inlet, wall and outlet boundary conditions, from the rotor, were all variables in the study.

The spatial resolution of the mesh is another important factor in the accuracy of the results. To ensure grid independence a grid convergence study was conducted simultaneously with the domain study. Tetrahedral elements were used for the grid. A base grid spacing was specified for the entire model, this was a parameter explored in the grid convergence study. A refined mesh was specified around the turbine, the grid spacing and the extent of the refined region were all parameters in the grid convergence study.

A convergence study is an iterative process that solves the same model several times. In each iteration there is one model considered as a base case, all others models are test models. Only one parameter is different between the base case and the other test models. The results of all the models are compared with the base case. If there are significant differences between the base case and another model, then the solution is not independent to the parameter varied in that particular test model. If significant differences are found, the parameters used to define the base case are adjusted and the process repeats itself. The process is not complete until all the test models produce the same results as the base case.

H.1.4 Final Domain and Mesh

A convergence study was successfully performed on the grid and domain. For the 3.272m diameter rotor the ideal inlet distance is 20m, the ideal outlet distance is 60m. The wall boundary has to be 23.14m to have no effect. For grid independence a base grid spacing of 0.184m was used. The radius of influence for the refined mesh is 3.272m, with a grid spacing of 0.015m.

For the models with the 3.272m diameter rotor 66604 elements were used in the mesh. Most of the elements were wedge elements. Figure H.2 shows the mesh for the entire domain. Figure H.3 shows the mesh close to the turbine.

H.1.5 Convergence Criteria

The root mean square (RMS) of the residual error of all three components of the momentum balance and mass balance was used to determine the convergence. The convergence criteria was found by solving the same model with difference convergence criteria. Noticeable differences were found between results when the RMS residuals was greater than 10^{-5}. Models solved with an RMS residual of 10^{-5} or less gave results that were independent of the convergence criteria. Hence this residual level was set as the convergence criteria. All models were successfully solved with this criteria.

H.1.6 An example of the Open Domain Results

Typically under stall flow the rotor is lightly loaded. To maximize the Reynolds number the tests will be conducted at wind speeds approaching 13m/s. The results for the 5/9 C_t at 13 m/s test case are most representative of the experiment conditions. Figure H.4 shows an example of these results. A color contour plot was overlaid with a black and white contour plot of shear strain rate, the color plot was made semi-transparent to see both sets of results simultaneously. Stream lines were added to show where the flow is going.

As expected, upstream of the rotor there is a high pressure region and down stream there is a low pressure region. This is a result of the axial thrust of the rotor. The effect of this pressure field on the flow is to create divergence. The stream lines show a small divergence, this is expected with a small coefficient of thrust. The increased divergence in the near wake of the rotor indicates rapid deceleration of the flow here. The pale region starting from the rotor tip and extending into the wake indicates there is a shear layer as a result of this deceleration.

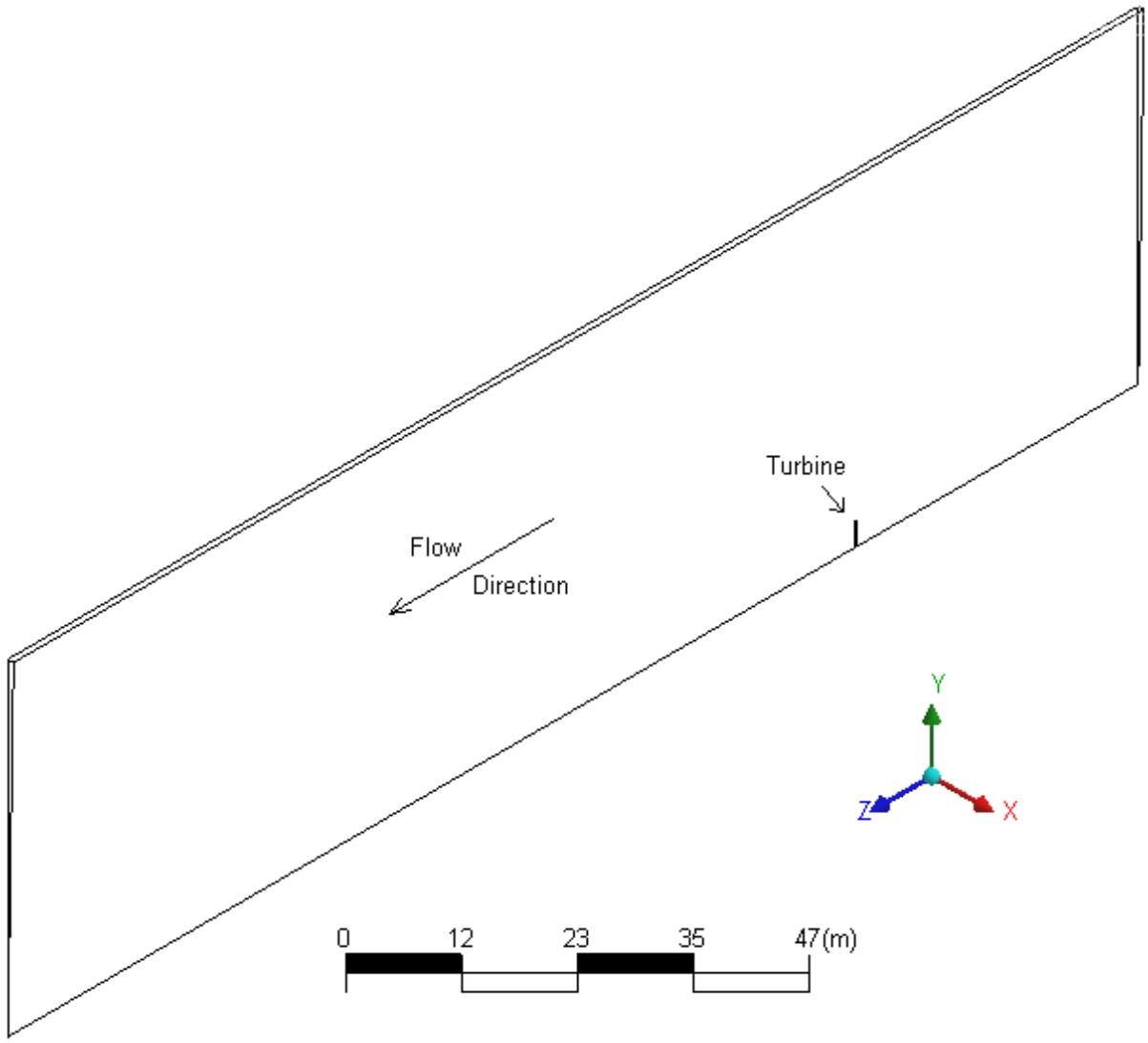

Figure H.1: Domain used for the Infinite Domain Models

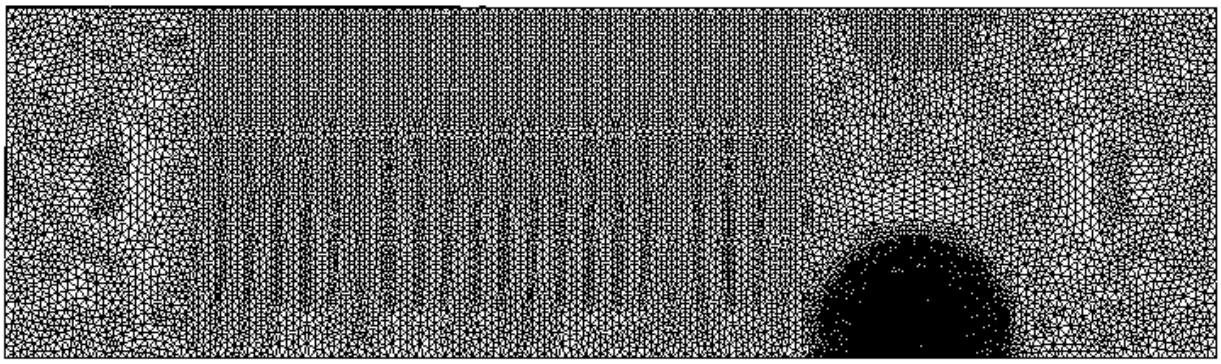

Figure H.2: Final Open Domain Mesh

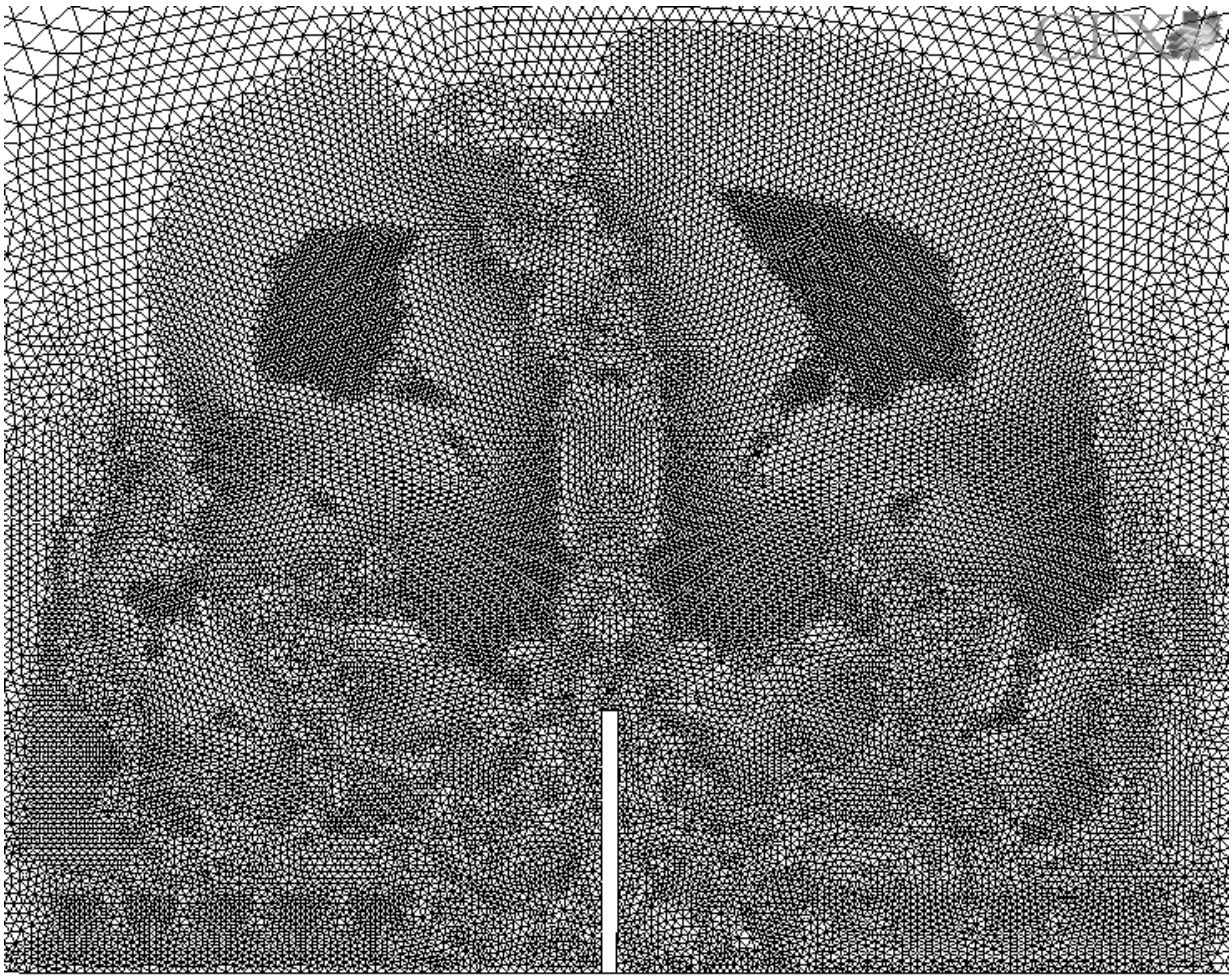

Figure H.3: Final Open Domain Mesh

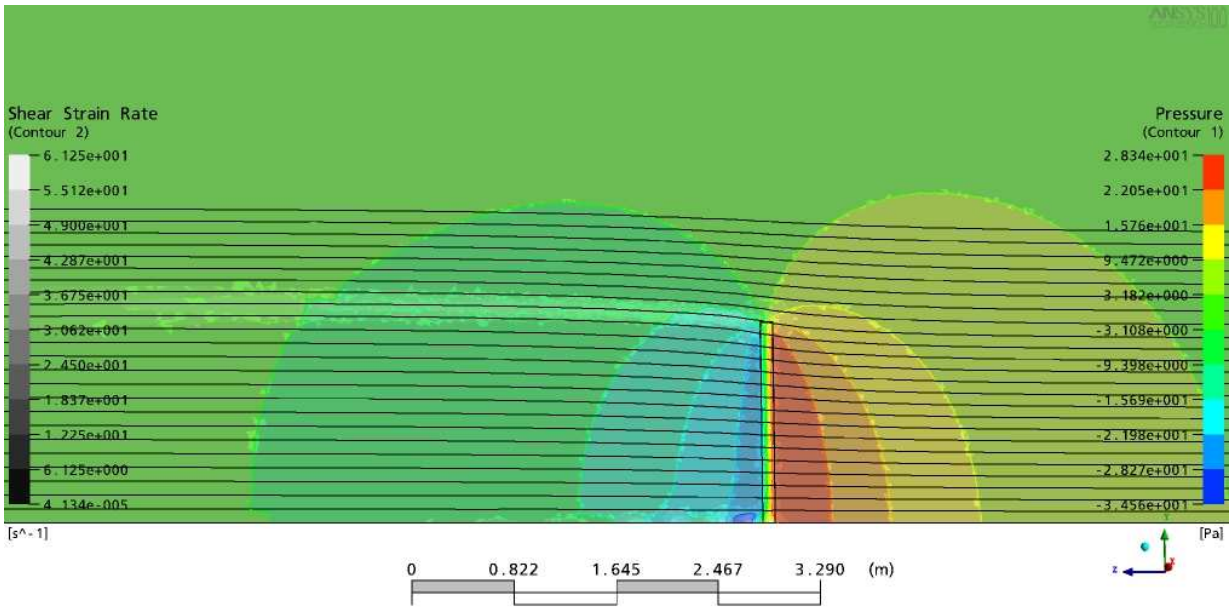

Figure H.4: Sample Results for the Open Domain Model

H.2 Wind Tunnel Model

H.2.1 Model Geometry

The geometry is symmetrical, simplifying the problem, however it is still very complex. Figure H.5 shows the geometry used in the model domain. Hidden lines are drawn with reduced weight. The inlet is tinted red, surfaces with an opening boundary condition are tinted blue.

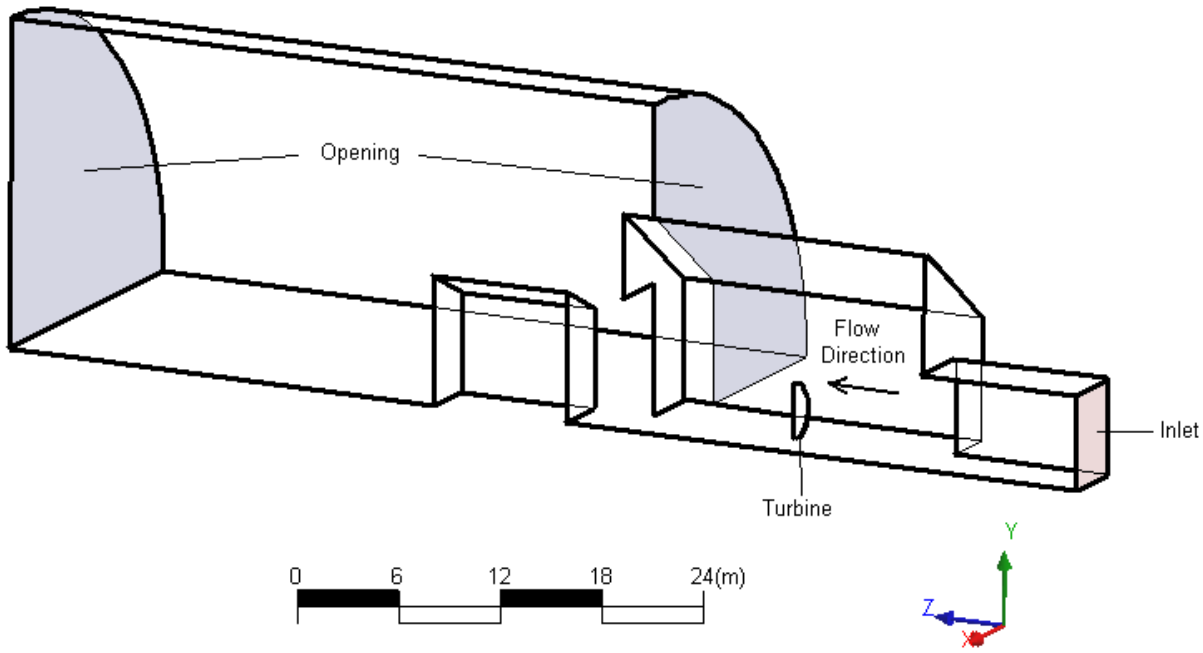

Figure H.5: Geometry for the Wind Tunnel Flow Models

The exit door has different geometry than the jet, forcing the jet to converge laterally and diverge vertically. The obstacle behind the exit door will force the flow to diverge around to pass into the open domain. The exit door and the obstacle alone will create some flow convergence and divergence. This can have some error on the wind tunnel flow. Because of these issues the wind tunnel flow may have stronger sensitivities to the

additional divergence of a wind turbine. To account for these effects the exit door, obstacle and entire test area was included into the model.

The region beyond the exit door is in an open domain. Here atmospheric air can be entrained in the flow and effect how the flow by-passes the obstacle. Accurately modeling the effect of the exit, requires the effect of an open domain to be included. This was done by including a large open volume about the obstacle and part of the test area. The walls of the test area and the open domain separated the two regions except at the exit door.

H.2.2 Boundary Conditions

The farthest surface in the negative Z direction was set as the inlet. The inlet speed was specific to the model instance. A symmetry boundary condition was specified for the surface at the plane of symmetry.

To account for entrained flow in the open domain, an opening boundary condition on the upstream face of the open domain was used. Bluff bodies, like the obstacle, can produce extended recirculation zones in the wake. These zones can not be resolved properly if they extend past an outlet boundary condition. To avoid these complication an opening boundary condition was specified for the far face of the open domain. For both opening boundary conditions the total pressure of incoming flow was set to 0, while the exiting flow had a static pressure of 0.

A free slip wall boundary condition was used for the cylindrical surface about the open domain. Using an opening boundary condition on that surface would be a better representation. Attempts were made on solving several models with opening boundary conditions here. However the large surface area of the opening boundary condition added numerical instability, making convergence difficult. Setting a wall boundary condition improved the stability greatly. Results of identical models, with the wall and with the opening boundary conditions were compared. The comparison showed that the wall boundary condition had no effect on the results at the wind turbine rotor.

A no slip wall boundary condition was specified for all other surfaces.

H.2.3 Domain and Grid Convergence Study

The flow domain is comparably well defined compared to the infinite domain model. The inlet boundary condition is close enough to the turbine to have a potential influence on the flow there. The flow exits into an open domain, here the domain is meant to be semi-infinite. The boundary conditions here influence the accuracy of the open domain flow, to a lesser extent there is potential it also effects the wind turbine flow. To ensure accuracy, a domain convergence model is required here.

The inlet jet was model by having the inlet boundary condition at the end of a rectangular channel. The length of the channel was one of the parameters in the domain study. If the open domain is set too small it will fail to represent a semi-infinite domain. For the open domain the radius, the length downstream and the length upstream were all variables in the domain study.

The size of the mesh is another source of error. Error is minimized when the solution is independent of the grid. A grid convergence study was performed to obtain mesh independent solutions. The mesh size was defined with an overall mesh spacing parameter. The geometry of the test area and the exit can potentially have a significant effect on the turbine flow, thus an improved mesh is desired here. This refined mesh was defined throughout the test area, around the exit and at leading face of the obstacle. This refined mesh was governed by the radius of influence and the mesh spacing within this region. A second refined mesh was defined within the first, the flow about the wind turbine is the main focus of the study. The mesh about the wind turbine was refined further, this refinement was governed by the radius of influence and the mesh spacing within this region. All the governing parameters were variables in the grid convergence study.

The only domain variable to affect the rotor results was the length of the inlet duct. The results were most sensitive to the mesh spacing in the refined regions. The overall mesh spacing had no effect. The size of the first refined mesh had no effect on the results, however a larger refined mesh around the turbine rotor improved results. Base case for the second iteration had a lengthened inlet duct, finer mesh in both refined regions and a larger region about the turbine.

Increasing the length of the inlet duct beyond that in the second base case had no effect on the rotor results. The limitations of computer resources prevented further exploration

of models with finer grids. The increased element count dramatically reduced the length of time required to solve a model. The test matrix called for 108 models to be solved, increasing the element count any further increased the solver time from one evening to an entire weak. Waiting 108 weeks to solve all the wind tunnel models is completely impractical. Hence the convergence study had to be completed with the second base case being the final domain and mesh.

H.2.4 Final Domain and Mesh

In the final model the inlet duct was set to being 10m long. For the open domain, the rear was 40m back from the test area exit, the radius 20m and extended forward over the building from the test exit 2m. The overall grid spacing was set to 4m. In the first refined region the radius of influence was set to 15m with a grid spacing of 0.5m. The radius of influence for the second refined region was 9.9m with a grid spacing of 0.25m.

In all meshes and in the final mesh a third refined region was defined about any of the walls with a no slip boundary condition. This was done to accurately model the boundary layers. The parameters for this region were not included in the convergence study. Regardless of the accuracy of modeling the boundary layers influence on the turbine flow would be obvious. Ten layers of square elements were used in this region, the thickness of the first layer was 9.6mm, and each subsequent layer was 1.2 times thicker than the last. The total thickness of this region was 0.25m.

Figure H.6 shows the entire domain and mesh used for the final wind tunnel models. Figure H.7 shows the mesh about the rotor. Approximately 350,000 elements were used in all meshes, most of the element were tetrahedral in shape.

H.2.5 Convergence Criteria

For the first iteration of the convergence study the same stringent convergence criteria was used. The increased element count of the final mesh resulted in decreased numerical stability. The same convergence criteria could not be achieved. Figure H.8 shows a typical residual curve for a final model. The best RMS residual that can be achieved is 20-30 times

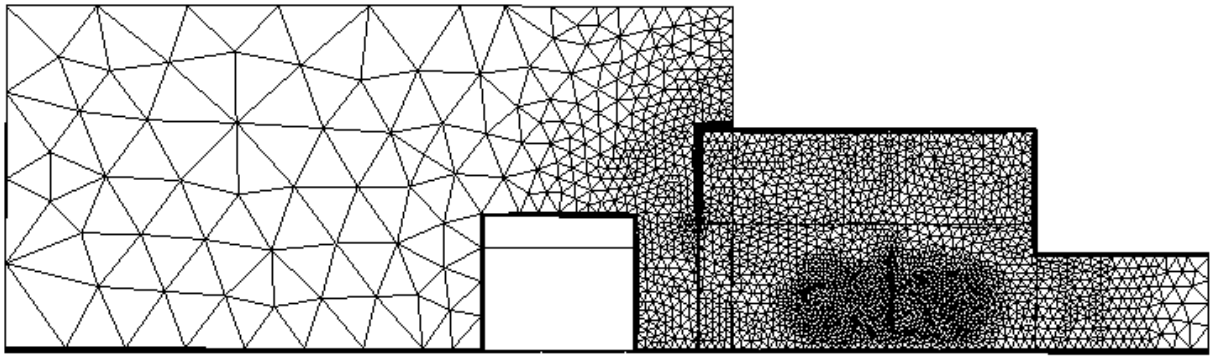

Figure H.6: Domain and Mesh for the Wind Tunnel Flow Models

greater than the residual achieved in the open domain studies. Various combinations of time step increases and decreases were attempted with no success.

Beyond 400 time steps the residual values scatter about the same magnitude. The momentum residuals seems to rise and fall with regularity. This suggests that there is an periodic phenomenon occurring in the flow preventing a further decline in the residual. The results of 100 subsequent time steps, after 1000, were extracted from a representative model. Figure H.9 shows how the z component of velocity varied at one element at the rotor inlet over the 100 time steps. This one figure represents one variable from many. Velocity in all directions, pressure, and turbulence model parameters were all plotted against time step. These variable were all plotted for all the elements at the rotor inlet. All other plots showed similar trends.

A discrete Fourier transforms were performed over all variables at all elements with respect to the time step. Figure H.10 shows an example of one of the Fourier transform results. This result was taken from the axial component of velocity from an element at the inlet to the wind turbine. This plot is typical of all other variables at all other elements. The Fourier confirms that there is one dominant periodic phenomenon dominating the flow. It is quite clear that this phenomenon is quite regular. The magnitude of the peak shows the variation on the rotor inflow is negligible. The high residual caused by this oscillation is likely located elsewhere in the solution domain.

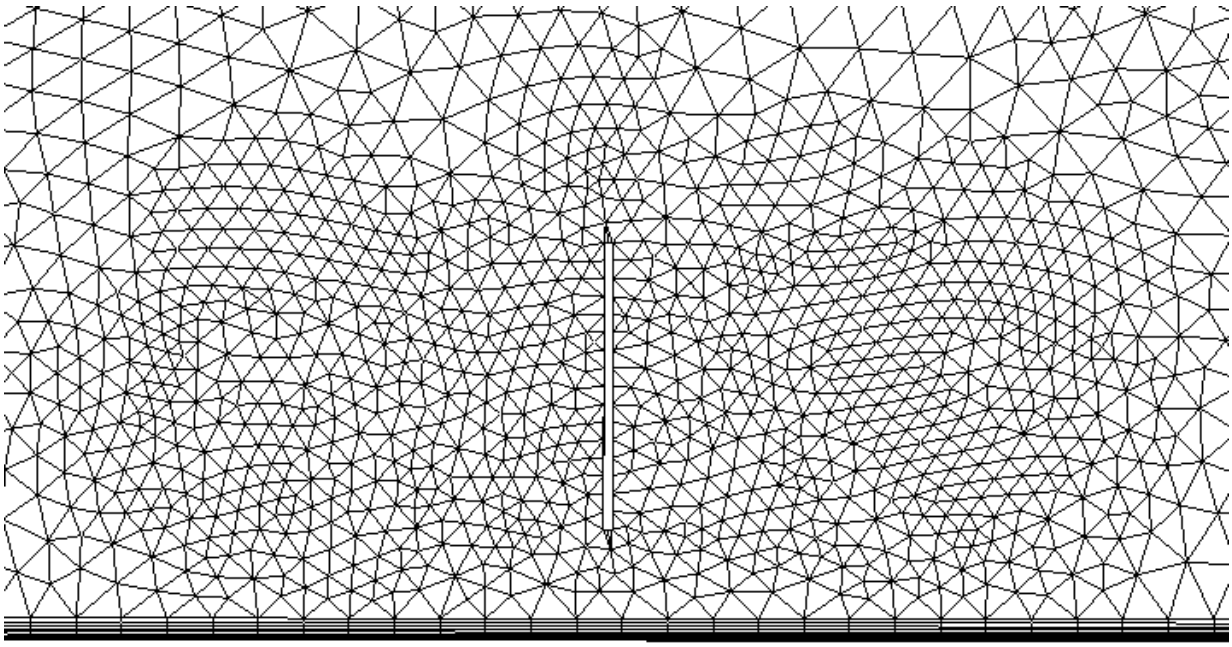

Figure H.7: Refined Mesh about the Rotor for the Wind Tunnel Flow Models

For each set of Fourier data the true location of the highest peak was found by performing a weighted interpolation between the two highest points. The peak location was averaged over all variables and elements to give a final peak frequency of 2.27 events per 100 time steps. The periodic behavior could be a numerical artifact and be purely erroneous, or could be physical and reflect actual wind tunnel behavior.

The physical time step set between the 100 consecutive solutions was 0.1s. This and the mean peak frequency corresponds a period of 4.4s. The inlet speed for the model was set to 13 m/s. The time for the flow to traverse the test area is 2.27s, thus a period of 4.4s closely corresponds to the time it takes for two test volumes to pass through the test area. The close correspondence between the periods of flow passage and the solution variables suggests that the oscillation could be physical. The periodic behavior only appeared in fine mesh models. The absence of the periodic behavior in the course grid models suggests that it is not a numerical artifact. Consultation with Dr. Stubley, has revealed that typically in CFD models, with large open sections with fine meshing, turbulent fluctuations start

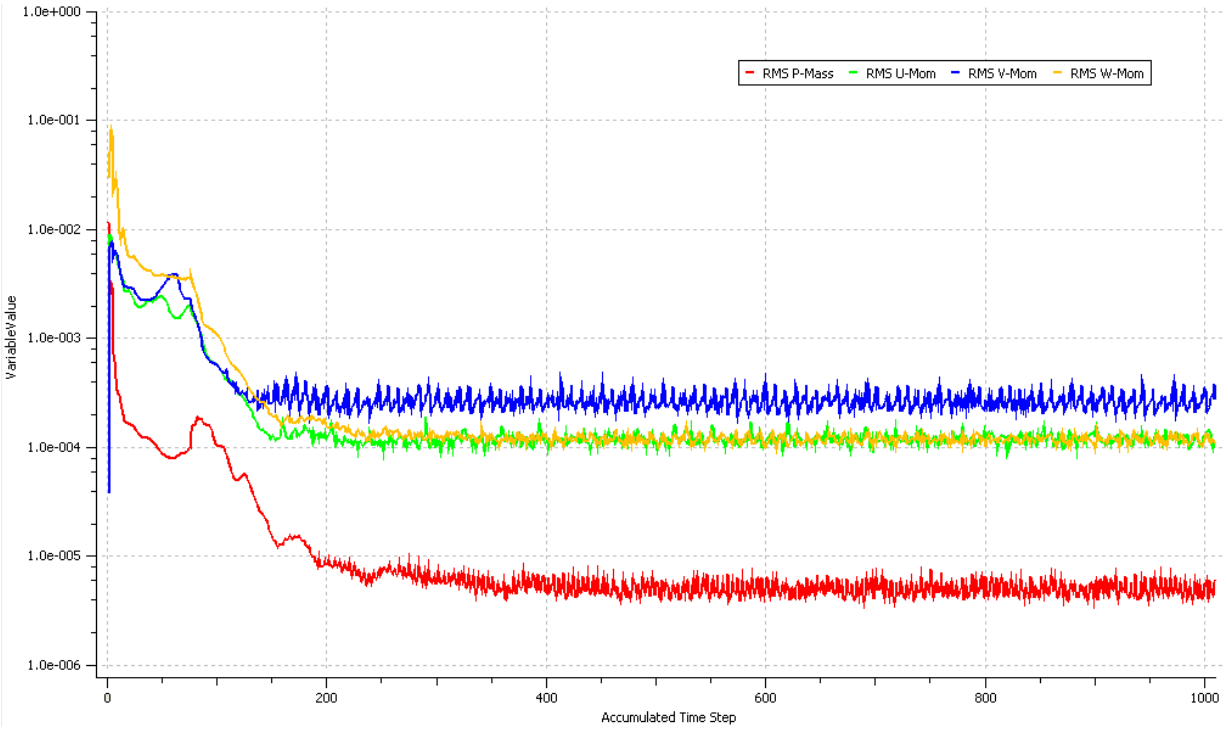

Figure H.8: Typical Residual Curve for a Tunnel Model

to be resolved in the flow. In this model it is possible that the flow is sufficiently far from domain surfaces to not be constrained by boundary conditions, yet the elements are small enough to resolve the larger turbulent structures. It is hypothesized that the fluctuations are physical. Physical measurements of the wind tunnel flow are required to confirm this hypothesis.

Overall the variation at the rotor inlet is very small compared to the overall velocity magnitude. With a small variation the results at the rotor inlet are likely accurate. Each model was executed over 1000 time steps to eliminate any decaying transient phenomenon. After 1000 time steps the periodic behavior is dominant. To get a representative steady state result, the results from 11 subsequent time steps were extracted. The time step over the 11 sets of results was 0.4s. This corresponded to one period of the periodic behavior. Since a full period is captured there would be no bias in the average of all 11 sets of

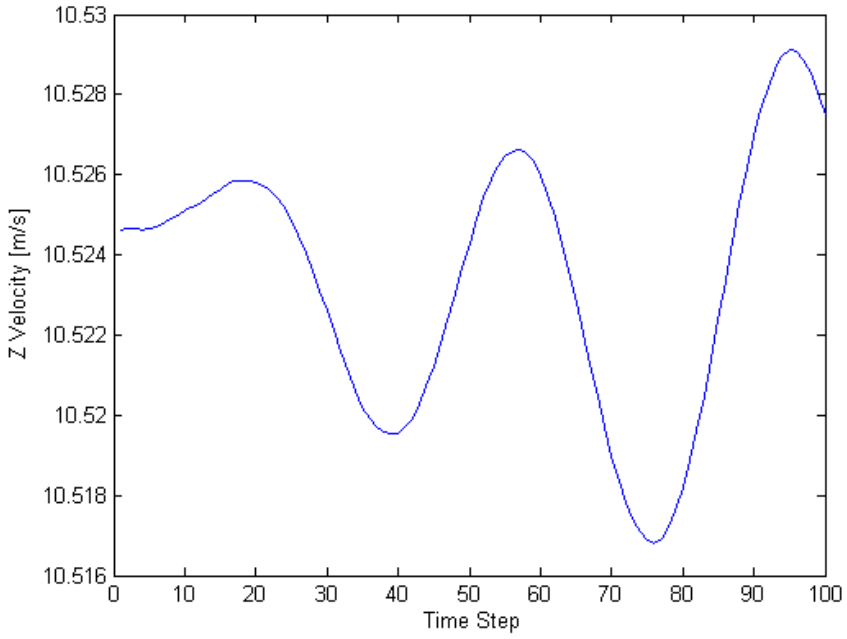

Figure H.9: Typical Variation of Flow Variables in Wind Tunnel Model

results. The steady state solution for the wind tunnel models is the average over the 11 sets of results.

H.2.6 Axial Location of the Wind Turbine

The lateral location within the wind tunnel is another variable. Ideally the wind tunnel flow will mimic an infinite domain. In an infinite domain with no obstructions the pressure is constant, thus a pressure gradient of 0. With a zero pressure gradient the flow would be straight an parallel with no divergence. Using this premise the ideal turbine location can be found without modeling the turbine.

The wind tunnel was modeled with the same geometry similar mesh and the same boundary conditions. The only difference between other models was the momentum sink representing the wind turbine was removed. Not all wind speeds were modeled, a higher

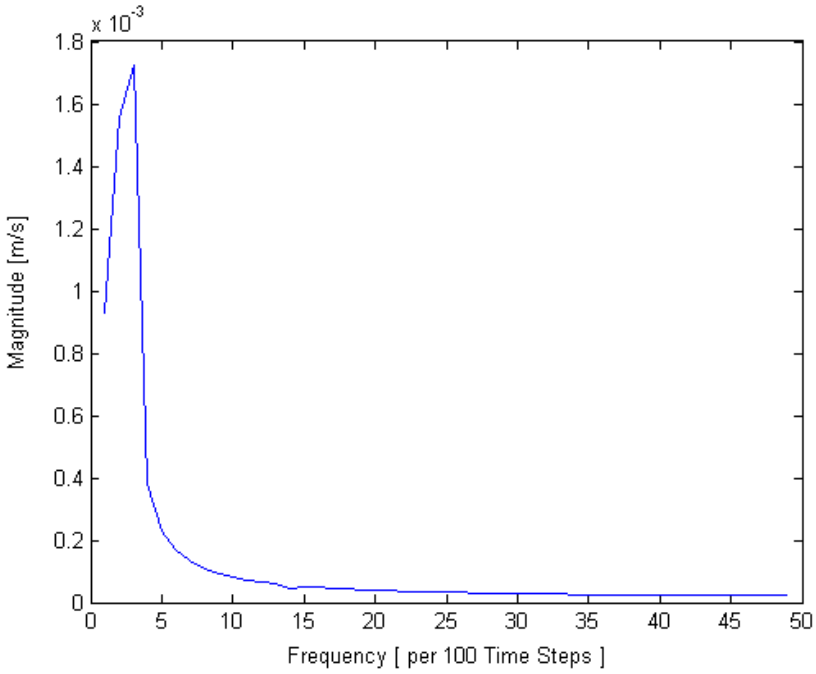

Figure H.10: Typical Fourier Transform of the Wind Tunnel Results

wind speed would produce a higher pressure gradient, thus would represent a worst case scenario. 13 m/s was chosen for the inlet velocity.

Figure H.11 shows a contour plot of pressure gradient on the plane of symmetry in the test area. The axial location of minimum pressure gradient represents the location of ideal turbine placement. The results given in figure H.11 show the ideal placement is 8.2m back from the jet exit.

The empty tunnel study was performed before the grid and domain study. The ideal turbine placement was applied to all the results in the grid and domain convergence studies. Once the study was complete, a second empty tunnel study was performed to determine if the ideal axial position was sensitive to the grid and domain variables. The second study confirmed the results of the first. The same ideal turbine placement was used in the final set of results.

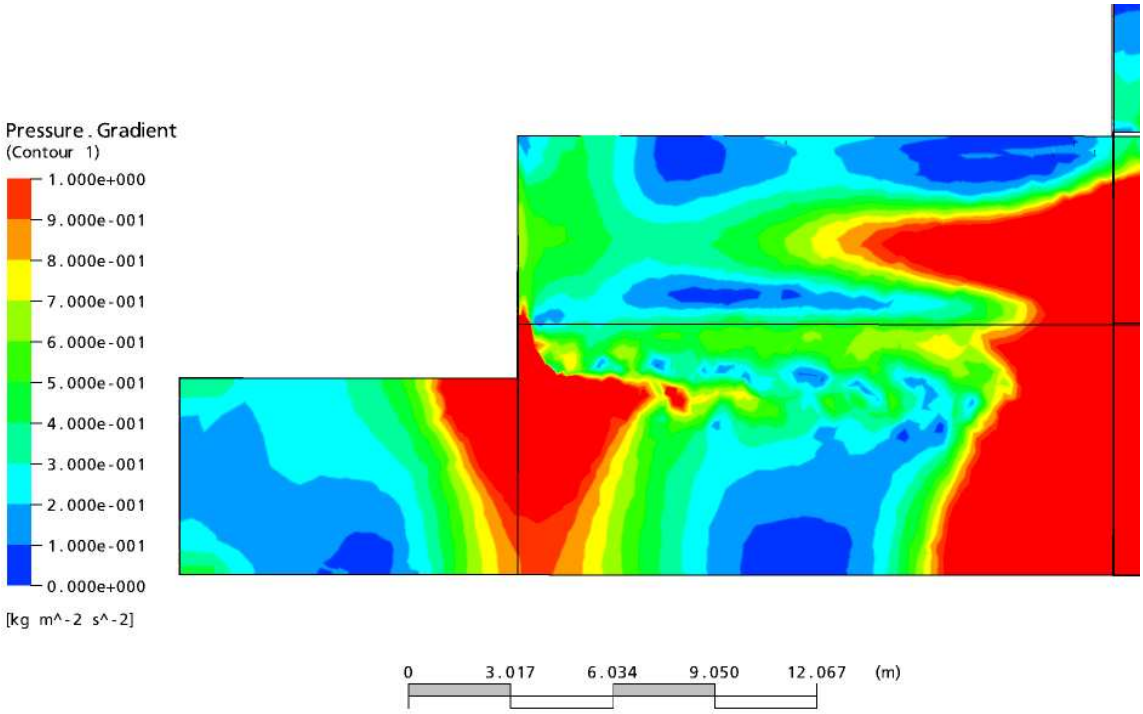

Figure H.11: Empty Wind Tunnel Pressure Gradient

H.2.7 An example of the Wind Tunnel Results

The experiment is likely to be conducted in high winds with a lightly loaded rotor. Figure H.12 gives the results for this case. Here the rotor has been vertically placed at the center axis of the jet. Several different sets of results are shown simultaneously. The color contour plot is the pressure, the gray scale shading is the shear strain rate while streamlines have been added to get a sense of fluid motion. The dominant flow direction is from right to left.

The results shown in figure H.12 correspond to the same conditions as the results in figure H.4. The types of plots are similar, thus the two figures are comparable. Many of the same features are common to both. Both have high pressure region upstream and low pressure regions down stream. Both results show a shear layer extending down stream from the rotor tip. Both results show small divergence of flow in the rotor.

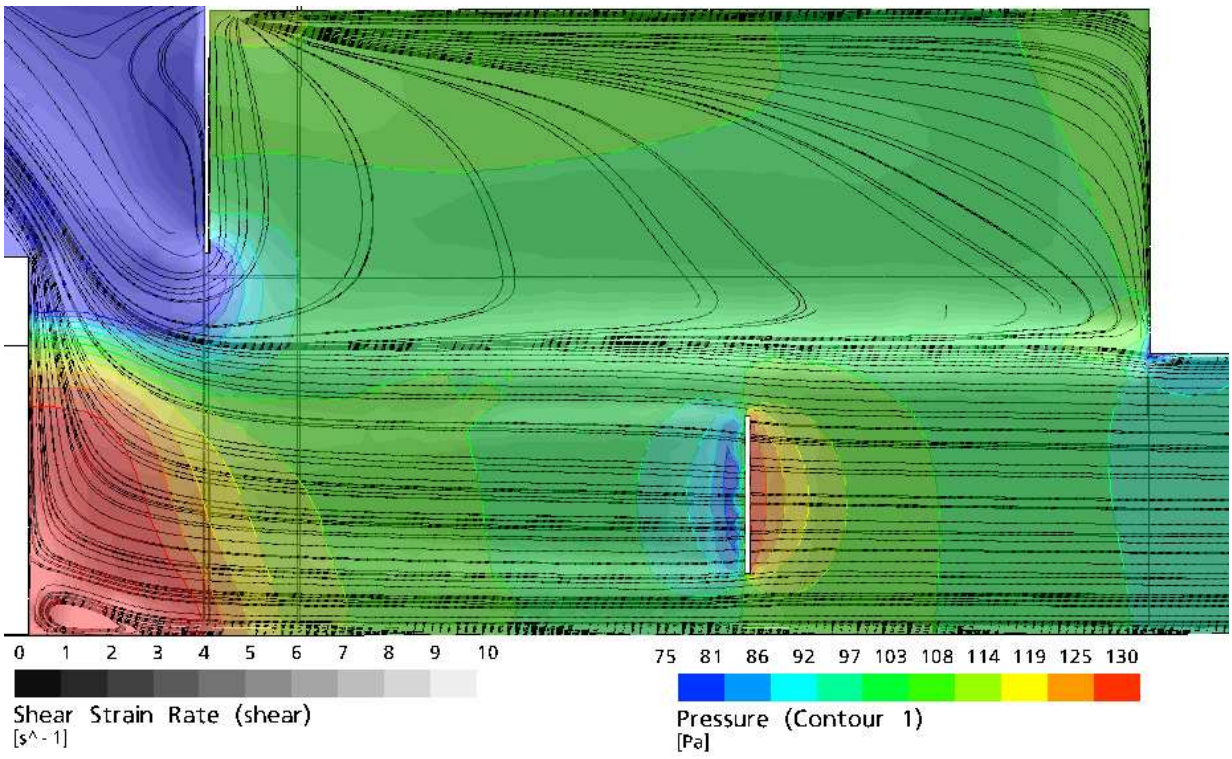

Figure H.12: An example of Wind Tunnel Model Results

The tunnel results have additional features as a result of all the obstructions and boundaries of the tunnel sections. A strong high pressure region is upstream from the obstacle, this is deflecting a lot of the flow in the turbine wake up, to flow up and over the obstacle. A second shear layer is present extending down stream from the jet exit, this shear lawyer is stronger than the one from the wind turbine. The stream lines closer to the floor do no diverge as much as the corresponding stream lines at the top of the rotor. The additional shear layer, constrained divergence at the floor, flow deflection and increased pressure from the obstacle are all sources of error in the wind tunnel flow.

Appendix I

Rotor Speed Sensitivity and Power

The main focus of the apparatus is to study dynamic stall. This will be achieved by loading a rotor within a wind tunnel. Dynamic stall is dependent on the variation of angle of attack with time. Angle of attack is dependent on the rotational speed of the rotor and the inflow conditions. Ideally wind turbine rotors typically operate at constant speed, in constant wind speeds. The variation in time of the angle of attack is due to the rotors misalignment to the flow causing a varying theta component on the rotor plane. For best results the variation of angle of attack should reflect actual operating conditions. For this to happen the rotor needs to be loaded such that it operates at constant speed.

I.1 Speed Sensitivity

The angle of attack is proportional to the inflow angle. Equation I.1 shows how the inflow angle varies with the rotational speed. The ratio of wind velocity to rotor velocity is known as the advance ratio, the inverse is known as the local tip speed ratio, the global tip speed ratio is the local tip speed ratio at the tip. Figure I.1 shows how the inflow angle varies with tip speed ratio. Wind turbines will exhibit dynamic stall as the tip speed ratio falls. On modern wind turbine dynamic stall is known to initiate at global tip speed ratios of around 4. Modern wind turbines will operate at global tip speed ratios as low as 2.0. Dynamic stall typically occurs near the root. The local tip speed ratio at the root at the lowest global tip speed ratio is 0.5. Thus the largest inflow angle is 63.4 degrees.

$$\phi = \arctan\left(\frac{V}{\omega r}\right) \tag{I.1}$$

Dynamic stall is very sensitive to the angle of attack. The phenomenon is known to happen with angle variation as low as 3 degrees. Figure I.2 shows how the inflow angle variation varies with local tip speed ratio. The maximum variation always occurs at the local tip speed ratio of 1. Figure I.3 shows how the inflow angle variation varies with rotational speed variation. The variation of inflow angle due to the variation of rotor speed needs to be kept below 0.5° to ensure that dynamic stall is dependent on rotor misalignment and not the rotor speed. Figure I.3 shows that the speed variation must be within 0.8%.

I.2 Speed Variation

Dynamic stall is a transient phenomenon that introduces a hysteresis in the aerodynamic loading vs. the angle of attack. The hysteresis itself can cause great variation in the torque produced by the rotor. Thus a passively loaded rotor will experience some variation in the rotor speed due to dynamic stall. The effect of this hysteresis can be determined by solving how the aerodynamic forces change with the angle of attack. Figure I.4 shows the assumed hysteresis of a hypothetical airfoil.

The torque response from the lift hysteresis was found by assuming that the angle of attack varies with the sine of the phase angle. It was also assumed that the entire blade has the same angle of attack at any given phase angle. These assumptions along with the lift hysteresis curve allowed for the calculation of the local lift force. The local lift force was then integrated along the blade to determine the torque. The torque is dependent on the chord and radius of the rotor. The current experiment requirements show that a 2 bladed rotor will be used with a radius of 1.636m. A linear solidity distribution was assumed for the rotor. The active area of the assumed rotor started at r/R of 0.25 and a local solidity of 0.12, the local solidity of the tip is 0.012.

Figure I.5 shows a typical torque solution. This torque solution was found at a global tip speed ratio of 2. The sensitivity analysis shows that the global tip speed ratio influences the angle of attack. The variation of torque is defined by equation I.2. The sensitivity

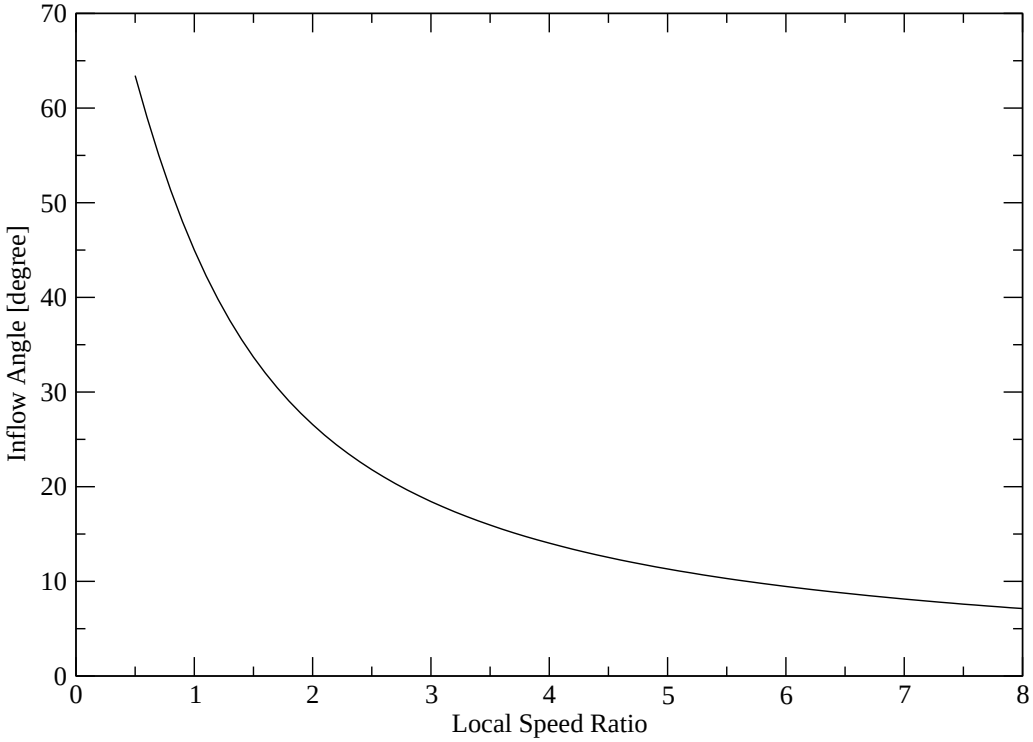

Figure I.1: Flow Angle vs. Local Speed Ratio

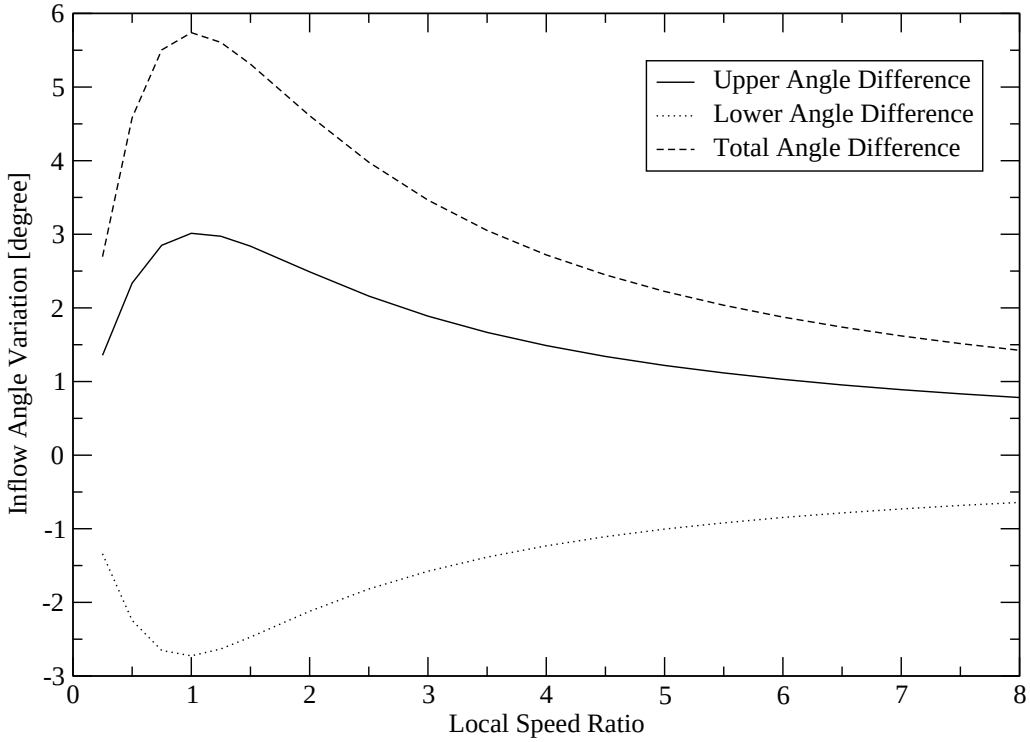

Figure I.2: Flow Angle Variation vs. Local Speed Ratio

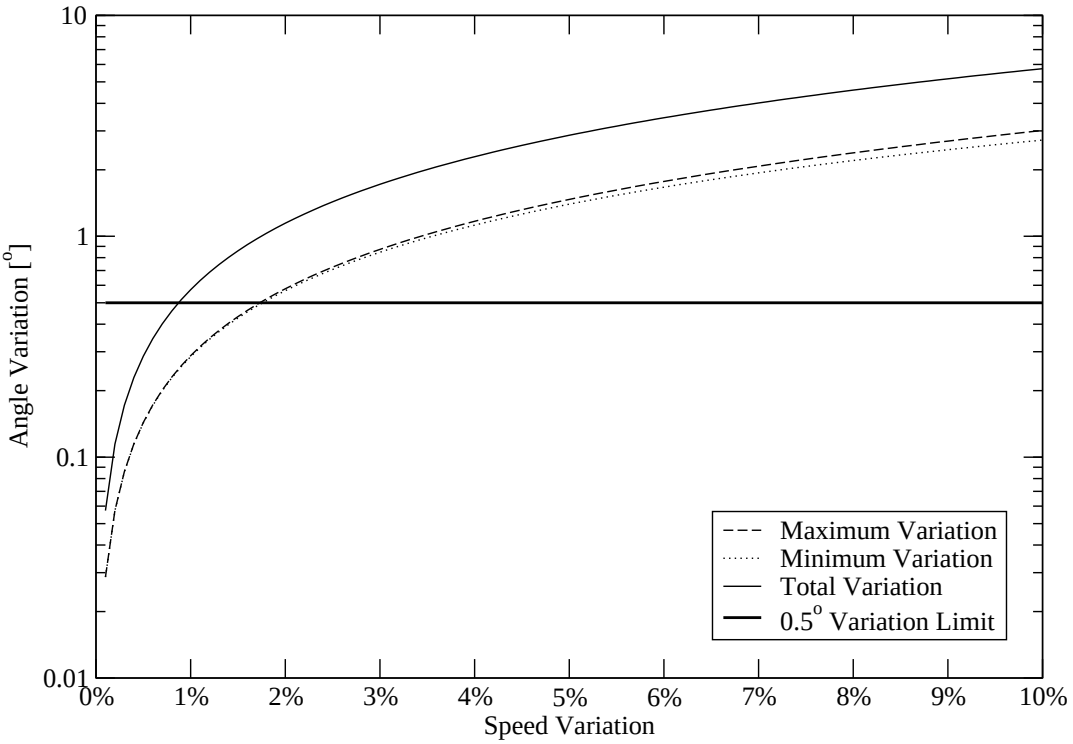

Figure I.3: Flow Angle Variation vs. Speed Variation

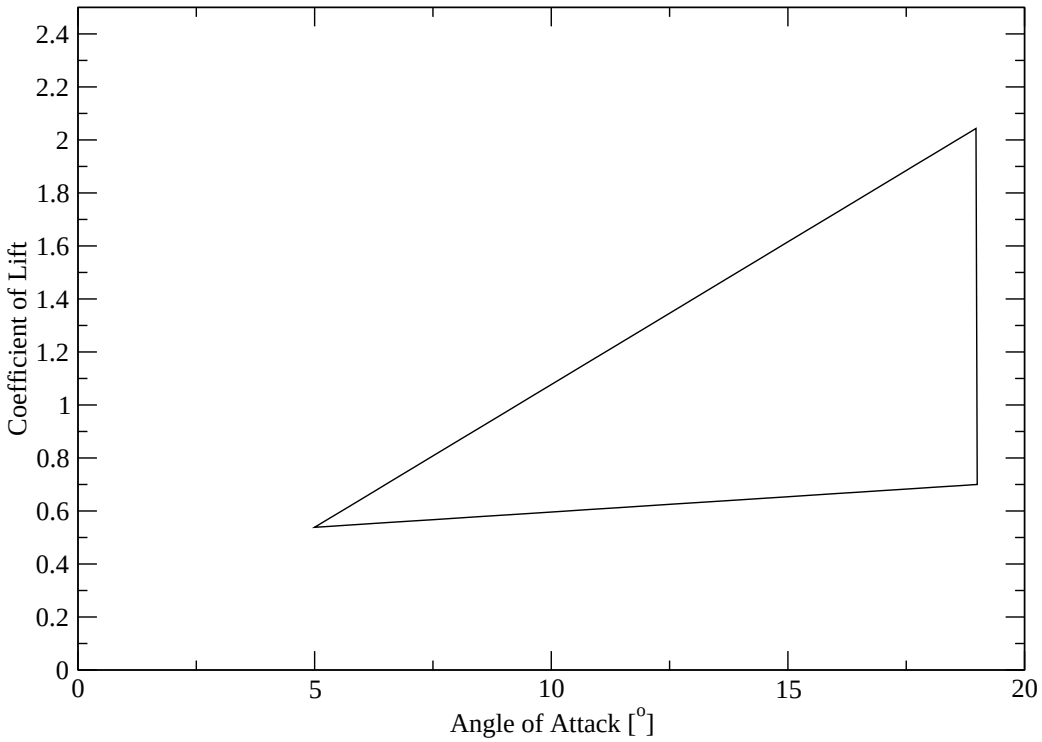

Figure I.4: Assumed Lift Hysteresis

analysis shows that the inflow angle variation is sensitive to the global tip speed ratio. Figure I.6 compares the torque variation with the global tip speed ratio. Figure I.6 shows that torque variation decreases with the global tip speed ratio. The smallest tip speed ratio for the experiment will be 2.0.

$$\Delta T \equiv \frac{T_{Max} - T_{Min}}{2T_{Mean}} \tag{I.2}$$

The variation of speed versus the variation of torque in a passive system is dependent of the rotational inertia of the various components. Equation I.3 governs how the rotational speed varies with the torque. Figure I.7 shows a schematic for the experimental rig. The inertia was estimated for all the components in rig. The only unknown is the inertia of the load device. Large DC motors are known to have inertia of 0.01 kg?m2. Second the inertia of the components on the high speed shaft varies with the square of the gear ratio. Depending on the load device the gear ratio could vary between 8 and 16.

$$\omega = \int_0^t \frac{T(\tau)}{I} d\tau \tag{I.3}$$

Figure I.8 shows how the rotational speed varies with phase angle at the tip speed ratio of 2, gear ratio of 1 and high speed inertia of 0.001. Speed variation is defined by equation I.4. Figure I.9 compares speed variation with the high speed inertia at three different gear ratios. The figure shows that the inertia of a large DC motor is insufficient to achieve the constant speed criteria. Figure I.10 shows the minimum inertia needed to meet the constant speed criteria at various gear ratios. The figure shows that for a passive system additional inertia is needed at all gear ratios. The other solution is to control the torque of the load device to maintain the speed.

$$\Delta\omega \equiv \frac{\omega_{Max} - \omega_{Min}}{2\omega_{Mean}} \tag{I.4}$$

The maximum radius of any component in the hub is 0.409m. Any additional inertia should be within half this limit. If these constraints are applied the minimum inertia criteria is achieved by having 1.22 kg or 0.31 kg of mass rotating at 0.205m with a gear ratio of 8 or 16 respectively. This shows that a fly wheel on the high speed shaft would be

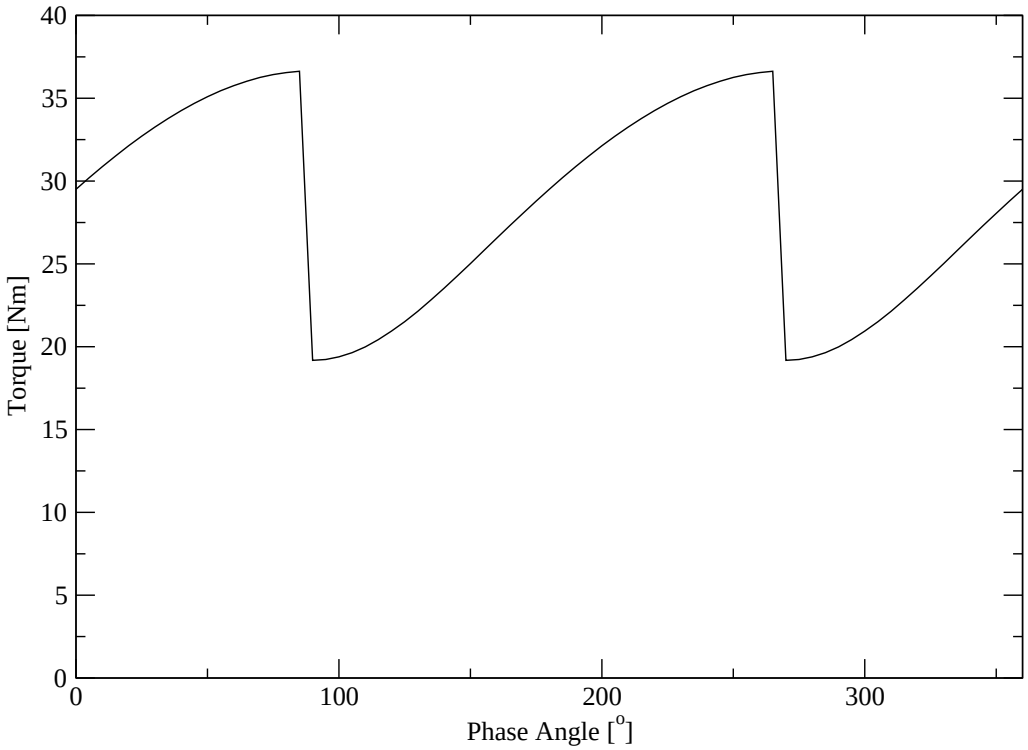

Figure I.5: Representative Torque Curve for Rotor Under Dynamic Stall

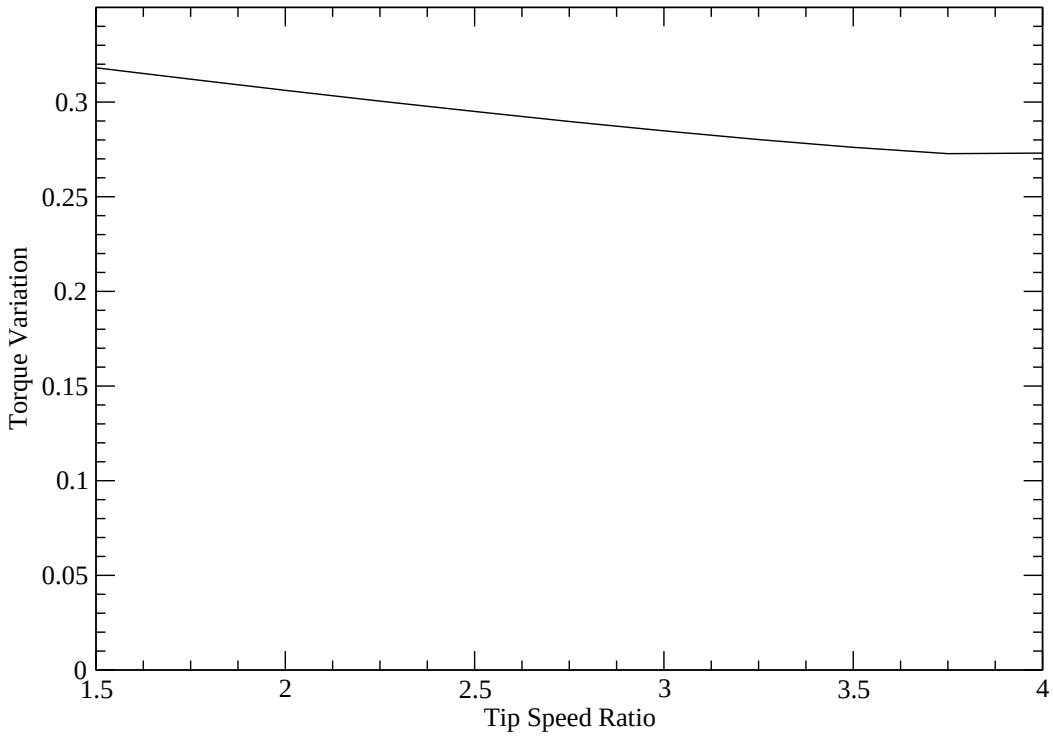

Figure I.6: Torque Variation vs. Tip Speed Ratio

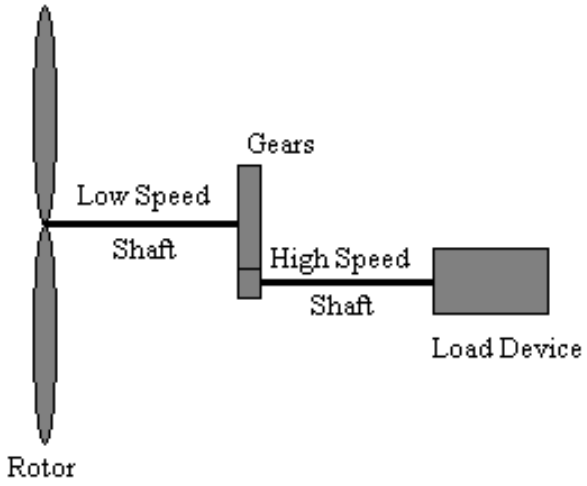

Figure I.7: Schematic of the Turbine Drive Train

sufficiently small and compact enough for the experiment. Thus a passive load device can be used.

There are still issues with a passive load device. The incoming flow could be unsteady and may introduce further variation in the torque. Also the speed of the rotor could drift. If the drift is fast enough the rotor speed could violate the speed requirements while the experiment is in progress. Only a controlled load device would be able to rectify these problems perfectly.

I.3 Power Requirements

The power needs of the load device will vary depending on the experiment. Equation 5.2 was used to evaluate the power of the load device. A computational fluid dynamic study discussed in chapter 4 showed that a rotor diameter of 3.272m will be applicable. The maximum speed of the wind tunnel is 13 m/s. The assumed maximum coefficient of power (C_p) is 16/27. With these assumptions the maximum power of the wind turbine is 6459 W.

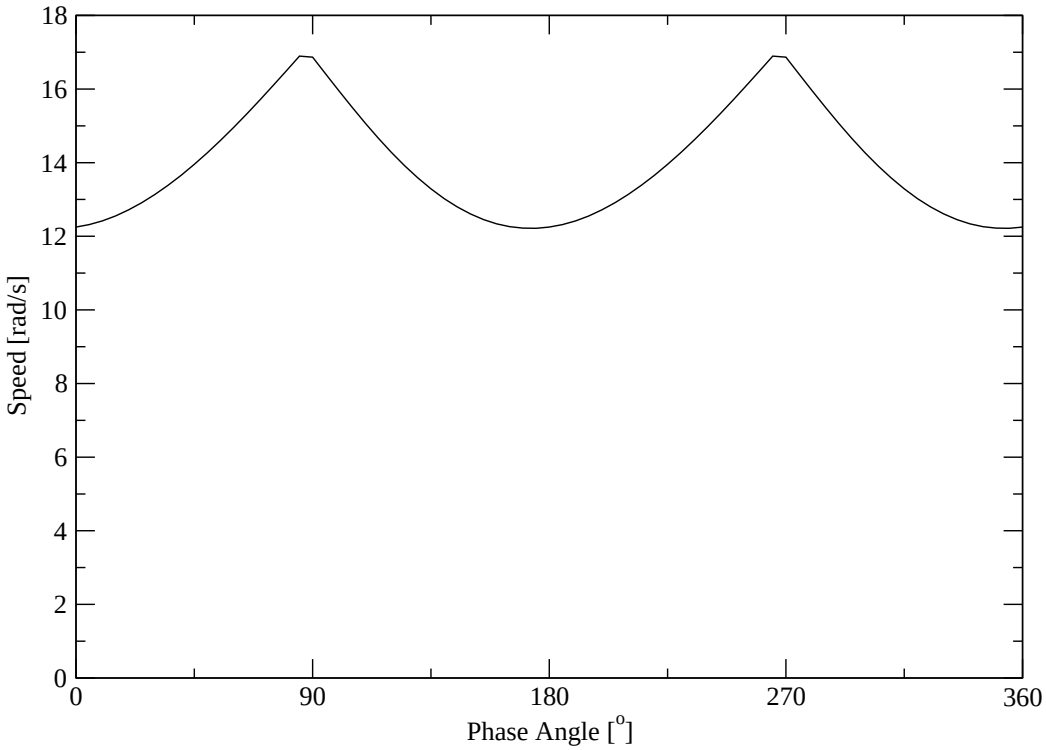

Figure I.8: Representative Rotor Speed Curve under Dynamic Stall

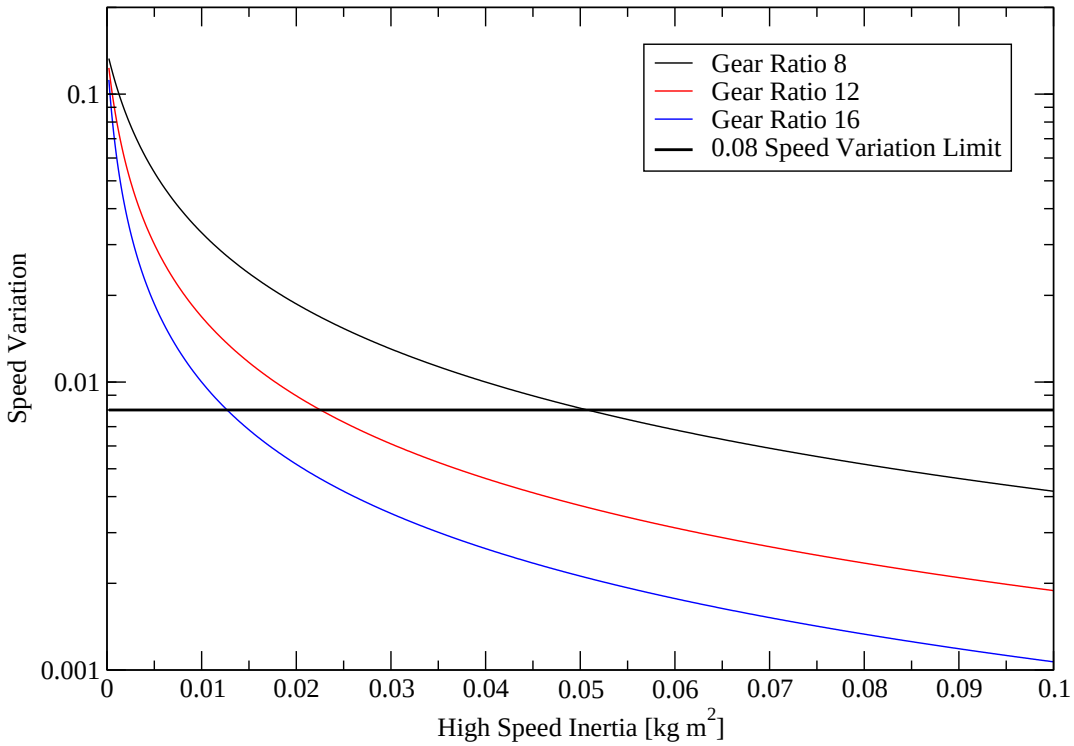

Figure I.9: Speed Variation vs. High Speed Inertia

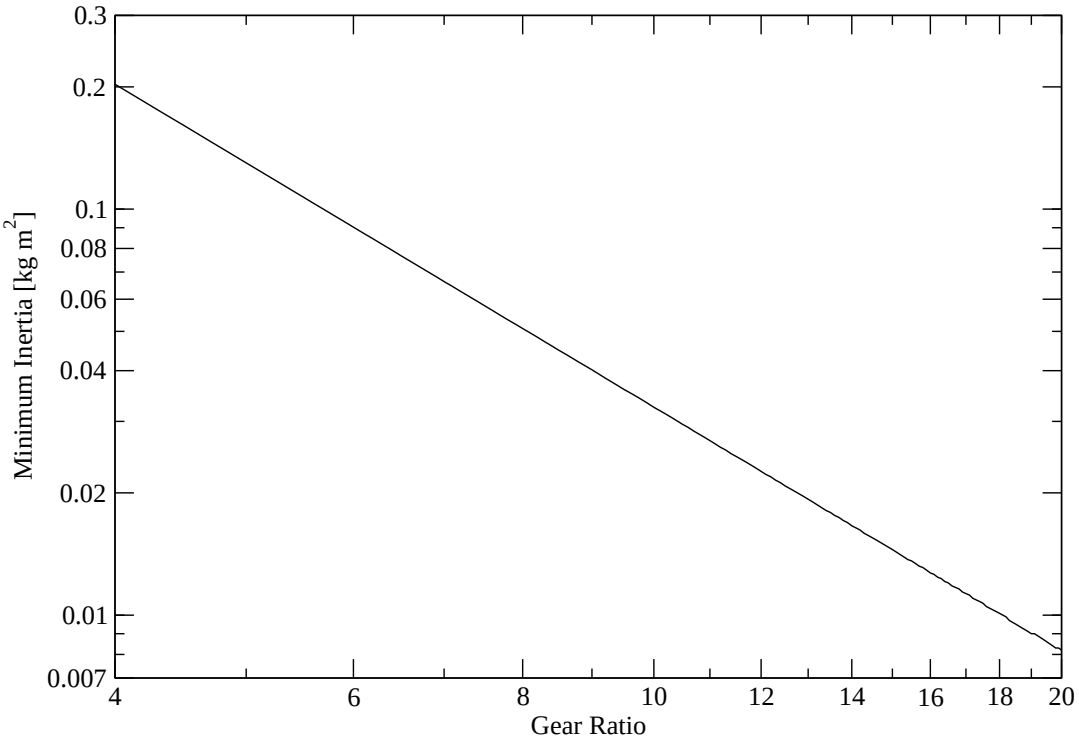

Figure I.10: Minimum Inertia vs. Gear Ratio

The power requirements for the proposed experiment will be different than the ideal power requirements. The proposed experiment is similar to one performed at the Ames test facility by National Renewable Energy Laboratory in the United States. The rotor geometry and the experimental conditions of the Ames test were used to solve the aerodynamics using Blade Element Momentum theory. The calculations showed that a maximum CP of 0.085. At best conditions and at this CP the maximum power for the experiment is 917 W.

Wind turbines are meant to operate in a wide range of conditions. There is potential for research in other areas aside from dynamic stall. One example is turbulent wake phenomenon. This phenomenon occurs when the axial thrust causes the wake to collapse and become turbulent. Under these conditions the wake flow is not streamlined and exhibits the wake of a bluff body. Currently there are few analytical models, all the relations are empirical. In the future this phenomenon may become a research interest. The significance of this phenomenon is that under certain circumstances the wind turbine will actually consume power to operate. This would require the ultimate load device to operate consuming power and also supplying power.

In summary for the current experiment the power requirements are low. A 2 kW load will be sufficient. For the long term research goals a 6.46 kW load capable of supply power and consuming power will be needed. There are two sets of requirements depending on the criteria of the load device. If the load device is for the current experiment than a 2 kW power consuming device will suffice. For all the possible experiments for wind turbine technology a 7 kW device that can operate in motor mode and generator mode is required.

Appendix J

Drive Train Flywheel

The rotor loading requires a large inertia to help maintain constant speed. A flywheel is readily available, the moment of inertia has been calculated using formula J.1. This formula is derived from the moment of inertia defined in equation J.2 for an axis-symmetric square cross section. The profile of the flywheel is given in figure J.1. The profile can be calculated by dividing it into the four squares shown in figure J.1. The total inertia of the flywheel is $0.313 kgm^2$. This inertia is sufficiently large enough for a system with a gear ratio of 4. The current system has a gear ratio of 10. Thus it is more than sufficient by a large margin.

$$I_M = \frac{1}{2}\pi\rho w \left(R_o^4 - R_i^4\right) \tag{J.1}$$

$$I_M \equiv \int R^2 dM \tag{J.2}$$

There are no performance specifications available on the flywheel. At a given rotational speed, the flywheel could face catastrophic failure if the centripetal forces exceed the limits of the material. Abaqus 6.5-1 was used to determine whether it was safe to use the flywheel.

The part was analyzed as an axis symmetric solid model. The assumed material properties are given in table J.1. A rotational body force was applied for a rotational speed of 345.575 radians per second. The speed is the fastest speed of the motor, thus the fastest

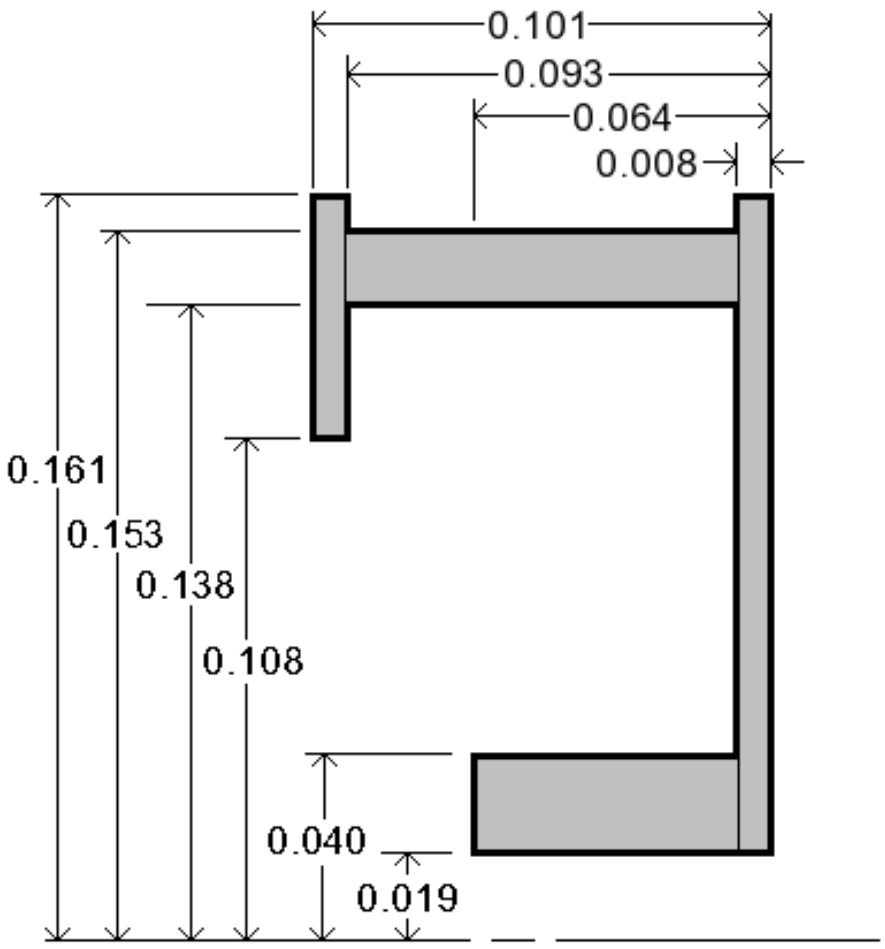

Figure J.1: Axis-Symmetric Profile of the Flywheel

Density $[kg/m^3]$	7800
Modulus of Elasticity $[Pa]$	$2 \cdot 10^{11}$
Poissons Ratio	0.23

Table J.1: Assumed Material Properties for the Steel Flywheel

speed in the system. The appropriate symmetry boundary conditions were applied on the partition faces. The surface mated with the shaft was constrained in all three directions.

The Von-Mises stress of the flywheel is given in figure J.2. The maximum stress is 24.33 MPa. Assuming a yield strength of 200 MPa this gives a safety factor of 8.22. Thus for this application the flywheel is operating well within safety limits.

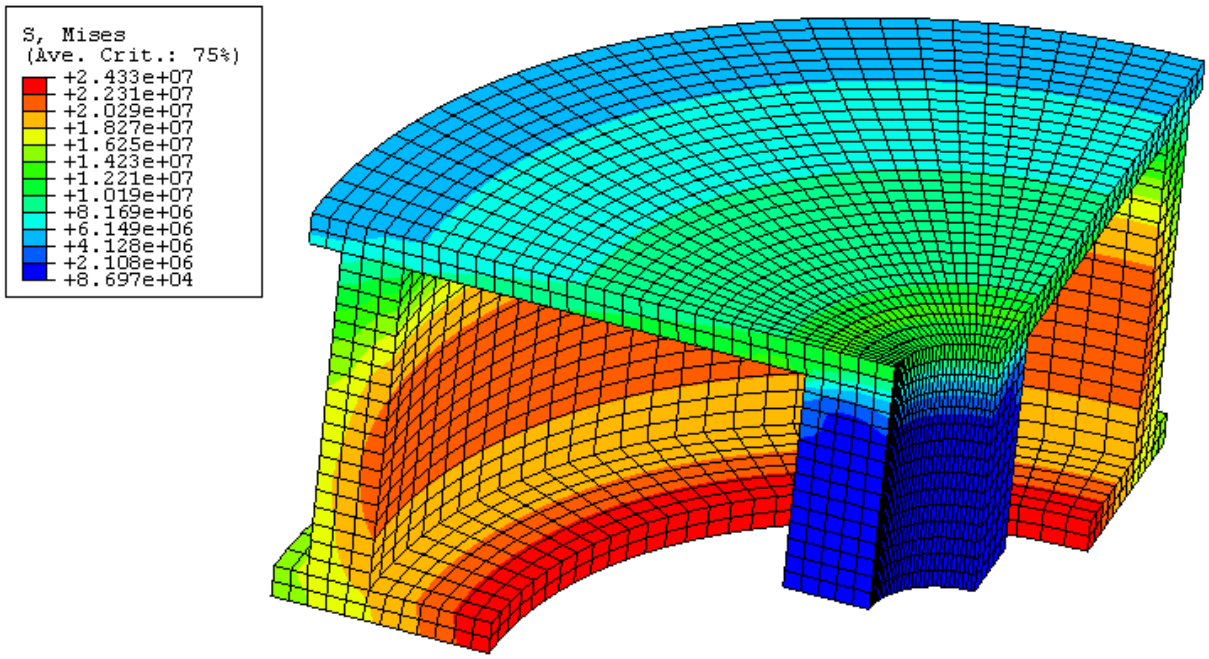

Figure J.2: Flywheel Stress

Appendix K

Rotor Speed Control

The two torque absorption devices and a pair of belt drives are not sufficient to load the rotor. The operating window requires the apparatus to operate over a wide range of speeds. It is important that the operator can configure the drive train so that for a given wind speed the rotor can operate over a range of wind speeds. In the cases where power needs to be supplied to the system there has to be a way of exciting the DC motor. This section describes the additional equipment required to provide energy to the DC motor and allow speed control.

Traditionally a DC motor is driven by an electronic motor drive. This is a power electronics appliance that conditions the electrical energy to drive the system at a specific speed. These drives have provisions to allow a sensory feedback to allow closed loop speed control. Typically these drives are designed to supply and absorb power. The drives absorb power by driving energy onto the grid or using power dissipation resisters.

An alternative controller uses equipment that is readily available. An alternating current electrical supply can be converted to a direct current supply using a rectifier. This allows the field windings to be excited without any power electronics. This is important, in either motor or generator mode the field windings need to be excited or the system will not work. The connection to the armature windings determines whether or not the device is loaded for motor mode or generator mode. Speed control is achieved by how the electrical energy at the armature windings is controlled.

In sections K.1 and K.2 a detailed discussion of both drive options is given. As the apparatus is built, tested then used for experiments it is expected that both drives will be used. Each architecture will be used at different stages. Section K.3 discusses how each drive architecture will be used at these stages.

K.1 Commercial Controller

There are two architectures for controlling electrical motors. The first uses an AC induction motor, the second a DC motor. The first is less expensive overall, if the DC motor is already purchased then the second is the least expensive choice. The current load devices cannot load the wind turbine over the full range of operating conditions. A controller for any architecture is a major investment, it would be prudent to invest in a control architecture that maximizes the overall abilities of the apparatus.

K.1.1 Direct Current Architecture

The wind turbine rig will most likely operate in both motor mode and generator mode in either direction. Accordingly a controller needs to control the speed in all four modes. Such a controller is referred to as a 4 quadrant controller. Saftronics provide a popular choice for controlling DC motors.

The controllers are designed for modern DC machines, in modern machines the voltage requirements on the field windings is half that of the armature. In the DC motor on hand the field windings use the same voltage. In these situations Saftronics recommended a small DC 2:1 autotransformer for the field windings.

The Saftronics DC controller that could connect to the current DC motor is the Quantum drive. The part number is TE 9500-8602, the cost is $5215.55. The REX RC3HC auto transformer is sufficient to step up the voltage on the field windings. The transformer can transform 3 kW of electricity from 240V to 480V. The cost of the transformer is $332.50. The total cost is $5548.05.

The Quantum drive given above has regenerative capabilities that would supply and absorb power. When absorbing power it transmits energy onto the grid. When transferring energy onto the grid the wave form is not perfectly sinusoidal. This can be a problem for

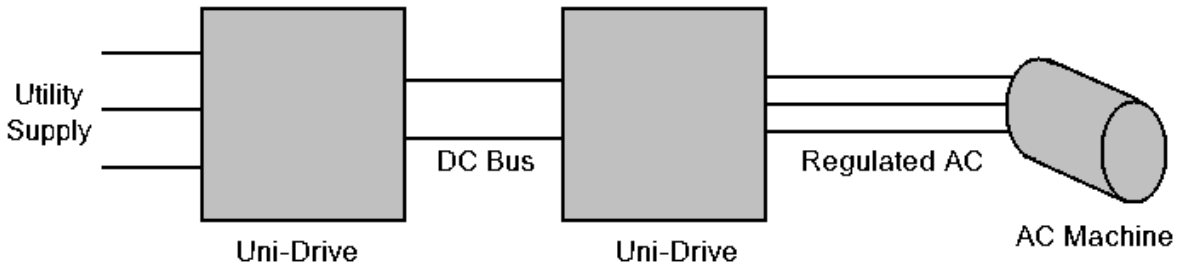

Figure K.1: Architecture of AC Drive

other sensitive electronic components. An alternative method of power absorption is to connect energy dissipating resisters to the drive. Instead of absorbing energy through the grid, offline resisters are used.

The less expensive single quadrant controllers can still absorb power in the same way that four quadrant can. The difference is it only operates in one direction. To reverse the directions of rotation a separate switch is required to switch the polarity on the armature windings. The direction could not be reversed on the fly. Wind turbine blades are typically designed to rotate in one direction. It is unlikely that a rotation reversal will be required in a test.

K.1.2 Alternating Current Architecture

The alternating current architecture will require that the DC motor be replaced by an AC induction machine. With the right drive and motor none of the drive train would have to be modified to accommodate a new drive. The architecture uses two drives, the first converts utility supply into DC electricity, the DC electricity is converted again into regulated AC electricity. The frequency of the regulated electricity varies according to what speed the AC motor is meant to operate at. Figure K.1 shows a schematic for this system.

The key benefit of the AC architecture is when it is absorbing power it does not require resisters to absorb energy. Instead the drive pushes the energy onto the utility grid. Unlike the DC drives the waveform of the electricity is sinusoidal, causing no harm to sensitive equipment. Another benefit is the drive is less expensive overall. If the current DC motor

is not powerful enough for future applications an AC drive would be the most economical replacement.

There is one limitation AC drives have compared to DC drives. DC drives can control the speed from 0 to full speed with high torque. The maximum torque of an AC drives drops off with speed. There is also a minimum speed that a an AC drive can operate at. These additional limitations could be a problem for testing low tip speed ratio phenomenon at low wind speeds.

K.2 Passive Controller

A surplus of electrical hardware is freely available. The hardware can be used to make a simple controller. The controller will not be sophisticated to provide closed loop speed control. An operator will be required to continuously monitor the speed and adjust the controller to maintain the speed. Using the freely available equipment a circuit has been designed that would allow operator control of the motor speed.

The passive control architecture relies on both the DC motor and the mechanical brake. The flywheel has been sized to limit short term variation in speed. Over the long term the speed will drift, the operator will need to continuously need to adjust the controller to maintain speed. The mechanical brake is best suited for constant torque, it would not be safe to vary the mechanical load while the apparatus is in operation. The best means of control is through the motor.

The speed of the motor is controlled by varying the voltage at the armature. When the motor is absorbing power, the voltage can be varied by varying the resistive load. When the motor is supplying power to the apparatus the voltage can be controlled with a variable transformer then rectified. The equipment used in voltage control is different, depending on what mode the DC machine is operating in. The BEM results for the UW blade show that it is highly likely that power levels will be so low that power will need to be absorbed and supplied over a given run. It will be very difficult and potentially unsafe to operate in a condition where the armature connections are switched between electrical supplies and resistive loads. Under these conditions the mechanical brake can absorb extra power forcing the DC machine to always supply power to the system.

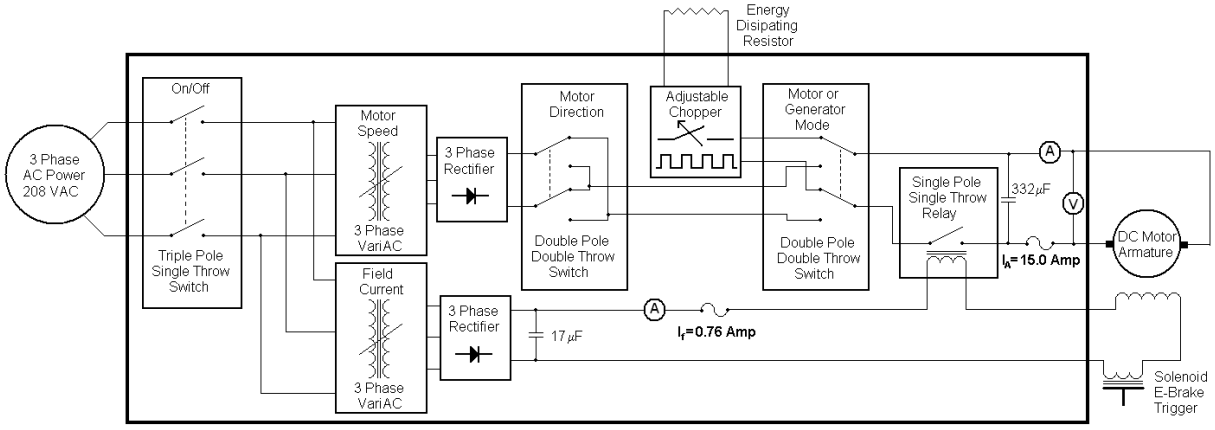

Figure K.2: Passive Controller Circuit

The motor is kept in motor mode by applying a constant torque with the mechanical load. The torque has to be set such that it is greater than the greatest positive torque of the experiment. The motor then adds further torque to drive the rotor at constant speed. The constant torque load is directional so its configuration will always have to be changed with different direction rotors. Motor direction is controlled by a mechanical switch in the circuit.

Figure K.2 shows the circuit diagram for the motor controller. Everything within the large black box can be contained within one case close to the operator. The energy dissipating resisters will produce a significant amount of heat and need to be placed where they could be cooled. The armature, field windings and the solenoid emergency brake trigger needs to be attached to apparatus.

The controller uses one mechanical switch on the input power to turn the motor on and off. The first double pole double throw switch on the armature circuit controls the direction of the motor. The second double pole double throw switch allows the motor to be connected to either the resistive load or the electrical supply. Fusing is added to both the armature and field circuits in the event that the motor short circuits or the current exceeds safe limits.

When the motor is supplying power it is controlled by changing the armature voltage with the variable transformer. When the motor is absorbing power the armature is con-

nected to the resisters. Variable resisters capable of absorbing 3.5 kW over a wide range of resistances are not readily available. One way of providing the effect of a variable resister is to use a chopper circuit. The chopper circuit continuously switches on and off at a high frequency. The time the switch is closed and opened can be adjusted. When the switch is always open the effective resistance is infinite, when the switch is always closed the effective resistance is the resistance selected for the energy dissipating resisters. Varying the switch timing between these extremes will vary the effective resistance. For maximum range of control, the dissipating resistance should be very low.

A second variable transformer is connected to the field windings. This transformer will reduce the field voltage and the field itself. With a weakened field the motor will rotate faster at a given voltage and draw more current to absorb the same torque. This control is useful when current and speed limits have not been exceeded, the voltage is at its maximum and more speed is required. Using this transformer to control speed should be avoided. Weakening the field can reduce the torque, potentially creating an rotor over speed condition, at constant torque more current is drawn, potentially exceeding the current limits of the motor and circuit overall.

In DC motors it is critical that the field windings are always excited. Without excitement there are two potential dangers. Mechanically the motor will start to turn beyond the rated speed. Electrically the armature impedance will drop off and the armature current will exceed current limits. Fusing will protect from electrical dangers. For additional safety, the single pole single throw relay is placed in series with the field windings to ensure that the armature is only excited when the field windings are excited.

When the armature and field windings are disconnected the system can no longer load the rotor. The aerodynamic torque can accelerate the system beyond safe limits. To prevent this a solenoid trigger is in series with the field windings. The solenoid trigger engages a mechanical brake that is connected to the low speed shaft. In an emergency situation where a belt may break the operator could stop the entire apparatus by switching the on/off switch.

The capacitors were added to act as low-pass filters. The 3 phase rectifier introduces a ripple at a frequency of 360 Hz. The capacitors are sized based on a cut-off frequency of

30Hz to ensure minimal DC fluctuation. The capacitors are over-sized, however cost is a minor issue at these sizes, overall this will extend the life of the motor.

Further engineering is needed to select the heat sink for the rectifiers. The rectifier for the armature circuit will have a maximum heat generation of 315W while the rectifier for the field windings will generate heat at a rate less than one watt.

K.3 Drive Selection

Implementing the commercial controller is expensive, once implemented it would be difficult to alter the capabilities of the system. The current system cannot load a rotor over all possible operating conditions. There is a good possibility that long term research goals will require a more powerful motor. To avoid the complication of installing two motor controllers the implementation needs to be delayed.

The range of operating conditions was estimated based on typical conditions presented in literature. With increased experience with apparatus a better set of operating parameters will be known. At this time it would be suitable to select the suitable motor controller.

Using the passive controller will allow the implementation of the commercial controller to be delayed. The passive controller should capable of operating the apparatus for immediate needs. The lack of closed loop speed control and the requirement for separate systems based on the rotor power makes the controller awkward for long term research. Future experiments may require a wide range or torsion loads, other experiments may be highly sensitive to speed variation. For these circumstances the passive controller is not suitable. Eventually the passive controller will be replaced by a commercial controller.

Appendix L

Truss Analysis Tools

L.1 Three Dimensional Rod Based Method

Finite element method can be employed to analyze truss structures. One dimensional rod elements were used to represent each member of the truss. Hooke's law applied to a one dimensional element is given in equation L.1. Figure L.1 was used to derive the stiffness matrix, given in equation L.2 for the element. The rod only responds to axial forces so only one component of force is needed, the variable r, s and t are the local coordinate system, while u, v and w is the deflection in this coordinate system. Figure L.2 shows the geometric convention for rotation in three dimensional space used to define the transformation matrices in equations L.3 and L.4. The vectors X, Y and Z represent the global coordinate system, vectors x, y and z represent the local coordinate system be rotated into the global coordinate system, at angles of θ and ϕ. Equation L.5 was applied for the stiffness matrix given in equation L.2 to be transformed with equations L.3 and L.4 to accept global deflection vectors and give global force vectors. Equation L.6 gives the results of equation L.5 where C_θ is $\cos\theta$, S_θ is $\sin\theta$, C_ϕ is $\cos\phi$ and S_ϕ is $\sin\phi$.

$$\vec{f_l} = [k]_{le}\,\vec{u_l} \tag{L.1}$$

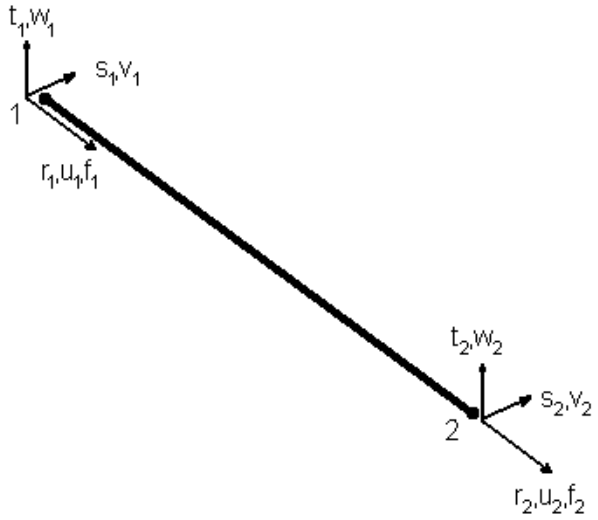

Figure L.1: Schematic of the Rod Element

$$[k]_{le} = \frac{EA}{L}\begin{bmatrix} 1 & 0 & 0 & -1 & 0 & 0 \\ 0 & 0 & 0 & 0 & 0 & 0 \\ 0 & 0 & 0 & 0 & 0 & 0 \\ -1 & 0 & 0 & 1 & 0 & 0 \\ 0 & 0 & 0 & 0 & 0 & 0 \\ 0 & 0 & 0 & 0 & 0 & 0 \end{bmatrix} \tag{L.2}$$

$$[\theta] = \begin{bmatrix} \cos\theta & 0 & -\sin\theta & 0 & 0 & 0 \\ 0 & 1 & 0 & 0 & 0 & 0 \\ \sin\theta & 0 & \cos\theta & 0 & 0 & 0 \\ 0 & 0 & 0 & \cos\theta & 0 & -\sin\theta \\ 0 & 0 & 0 & 0 & 1 & 0 \\ 0 & 0 & 0 & \sin\theta & 0 & \cos\theta \end{bmatrix} \tag{L.3}$$

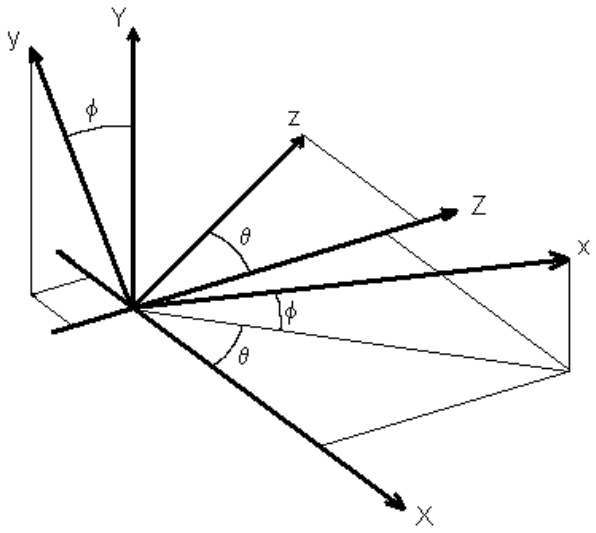

Figure L.2: Rotation in 3 Dimensional Space

$$[\phi] = \begin{bmatrix} \cos\phi & -\sin\phi & 0 & 0 & 0 & 0 \\ \sin\phi & \cos\phi & 0 & 0 & 0 & 0 \\ 0 & 0 & 1 & 0 & 0 & 0 \\ 0 & 0 & 0 & \cos\phi & -\sin\phi & 0 \\ 0 & 0 & 0 & \sin\phi & \cos\phi & 0 \\ 0 & 0 & 0 & 0 & 0 & 1 \end{bmatrix} \tag{L.4}$$

$$[k]_{ge} = [\theta]\,[\phi]\,[k]_l\,[\phi]^T\,[\theta]^T \tag{L.5}$$

$$\frac{EA}{L} \begin{bmatrix} C_\theta^2 C_\phi^2 & C_\theta C_\phi S_\phi & C_\theta S_\theta C_\phi^2 & -C_\theta^2 C_\phi^2 & -C_\theta C_\phi S_\phi & -C_\theta S_\theta C_\phi^2 \\ C_\theta C_\phi S_\phi & S_\phi^2 & S_\theta C_\phi S_\phi & -C_\theta C_\phi S_\phi & -S_\phi^2 & -S_\theta C_\phi S_\phi \\ C_\theta S_\theta C_\phi^2 & S_\theta C_\phi S_\phi & S_\theta^2 C_\phi^2 & -C_\theta S_\theta C_\phi^2 & -S_\theta C_\phi S_\phi & -S_\theta^2 C_\phi^2 \\ -C_\theta^2 C_\phi^2 & -C_\theta C_\phi S_\phi & -C_\theta S_\theta C_\phi^2 & C_\theta^2 C_\phi^2 & C_\theta C_\phi S_\phi & C_\theta S_\theta C_\phi^2 \\ -C_\theta C_\phi S_\phi & -S_\phi^2 & -S_\theta C_\phi S_\phi & C_\theta C_\phi S_\phi & S_\phi^2 & S_\theta C_\phi S_\phi \\ -C_\theta S_\theta C_\phi^2 & -S_\theta C_\phi S_\phi & -S_\theta^2 C_\phi^2 & C_\theta S_\theta C_\phi^2 & S_\theta C_\phi S_\phi & S_\theta^2 C_\phi^2 \end{bmatrix} \tag{L.6}$$

The stiffness matrix given in equation L.6 is determined for every element in the model. These stiffness matrices are used to form a similar stiffness matrix for the entire structure. Every node in the element domain corresponds to a node in the model domain. These node relationships are used to determine how the terms in the element matrices correspond to terms in the model matrix. Each element of the model matrix is formed by summing all the element terms that correspond to the same deflection and force. The final model matrix is the stiffness matrix for the entire structure, the stiffness matrix is important for both static and dynamic analysis.

Natural vibration occurs when the motion of the body is driven by its own deflection in the absence of external forces. This means that the product of acceleration and mass of any discrete element in the structure is equal to the force due to deformation, equation L.7. Under free vibration equation L.8 can be used to represent the deflection of discrete element, in time and space. $\vec{u}_0$ is the deflection for a particular mode of vibration and ω is the natural frequency for that mode. The acceleration of discrete elements is the double derivative of deflection with respect to time, equation L.9. Substituting equation L.8 and L.9 into L.7 and dividing through by $\cos \omega t$ gives equation L.10. Equation L.10 can be solved as an Eigen value problem, the Eigen vector is the deflection for a given mode, the Eigen value is the square of the corresponding natural frequency in radians per second.

$$[M] \frac{\partial^2}{\partial t^2} \vec{u} + [k]_{gm} \vec{u} = 0 \tag{L.7}$$

$$\vec{u} = \vec{u}_0 \cos \omega t \tag{L.8}$$

$$a_i = \frac{\partial^2}{\partial t^2} \vec{u} = -\omega^2 \vec{u}_0 \cos \omega t \tag{L.9}$$

$$[M]^{-1} [k]_{gm} \vec{u}_0 = \omega^2 \vec{u}_0 \tag{L.10}$$

L.2 Two Dimensional Beam Based Method

In structural problems the solution and problems are defined in terms of the external loading and the deflection within the structure. Hooke's law is applied to relate the loading and the deflection. The relationship between load and deflection is not linear, buckling is one example of a non-linearity. Linear algebra can be used to solve the problem when linearization is applied. Linearization assumes that the relation between force and deflection is linear when the change in both is sufficiently small. Instead of solving the problem by applying the full force to solve the full deflection, an incremental change in deflection is solved with and incremental application of force. Equation L.11 is used to solve an increment of deflection from an increment force, the k matrix is referred to as the stiffness matrix and linearly relates deflection and force.

$$\Delta\vec{F} = [k]_{gm}\,\Delta\vec{u} \tag{L.11}$$

When the deflection or force is large, equation L.11 cannot yield an accurate solution when applied once. Instead it is applied repeatedly until the full force has been applied. The total deflection of the structure is tracked using equation L.12, the subscripts number the applications of equation L.11. The stiffness matrix is dependent on the geometry of the structure, so as it deforms so does the stiffness equation, the variation of the stiffness matrix is the source of the non-linearity's. This variation in the stiffness matrix requires it to be reformulated with every application of equation L.11.

$$\vec{u}_j = \sum_{i=1}^{j} \Delta\vec{u}_i \tag{L.12}$$

The formulation of the stiffness matrix is based on the discretization. The physics at each discretized point in space is inter-related through the elements that connect the dicretized points. An element is represented as a simple structural member under a prescribed loading and deflection at the discretized points. There are many types of elements, varying in the dimensions of space it occupies, loading situation and the number of discretized points it connects. For this tool the structure is represented by one dimensional beam, rod and hybrid elements. Each of these elements have their own stiffness matrix, these element stiffness matrices are combined to form the stiffness matrix for the structure.

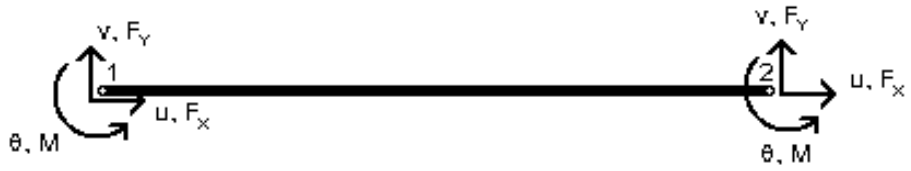

Figure L.3: Schematic of Beam Element

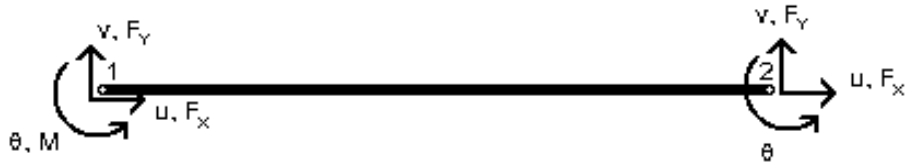

Figure L.4: Schematic of the First Hybrid Element

The schematics in figures L.3, L.4, L.5 and L.6 are used to formulate the beam, hybrid and rod element respectively. The beam element assumes a fixed connection at both ends thus the element can react to external moment forces. The hybrid elements assume that the element is fixed at one end like the beam elements but pinned at the other end. A pinned connection cannot transmit a moment force thus the element cannot be affected by a moment at the pinned end. The difference between the two hybrid elements is what end is pinned. The rod element is pinned at both ends, such an element cannot transmit any moments at either end. Since moments are reactions to lateral forces the element can not yield reactions to lateral forces, hence the element is insensitive to these forces as well. The difference between the rod element in figure L.6 and figure L.1, is the rod element here can only deflect in two dimensions. The structure can be represented in two dimensional space, the third dimensions is ignored.

Equation L.13 applies to every element in the problem. The only difference is the terms in the stiffness matrices. The local element stiffness matrix for the beam elements is given in equation L.14, for the first hybrid element it is given in equation L.15, for the second hybrid element it is given in equation L.16, for the rod element it is given in equation L.17. The stiffness matrices are given in terms of α and ζ, the definitions are given in

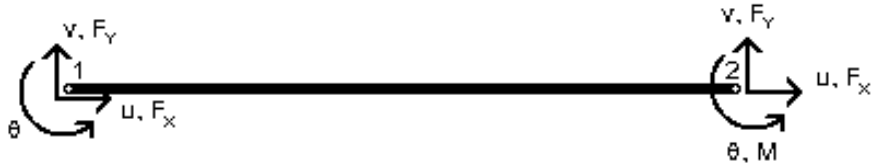

Figure L.5: Schematic of Second Hybrid Element

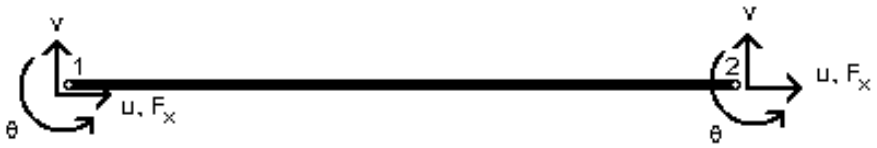

Figure L.6: Schematic of Rod Element

equation L.18 and L.19. The length in the α and ζ is the original length of the element. The subscript l denotes that the terms are expressed in the local coordinate system of the element, g is the coordinate system of the structure. The subscript e denotes that the term is specific to the element, while m denotes the term is specific to the entire structure.

$$\begin{bmatrix} F_{x1} \\ F_{y1} \\ M_1 \\ F_{x2} \\ F_{y2} \\ M_2 \end{bmatrix}_{le} = [k]_{le} \begin{bmatrix} u_1 \\ v_1 \\ \theta_1 \\ u_2 \\ v_2 \\ \theta_2 \end{bmatrix}_{le} \tag{L.13}$$

$$[k]_{le} = \begin{bmatrix} \alpha & 0 & 0 & -\alpha & 0 & 0 \\ 0 & 12\zeta & 6L_0\zeta & 0 & -12\zeta & 6L_0\zeta \\ 0 & 6L_0\zeta & 4L_0^2\zeta & 0 & -6L_0\zeta & 2L_0^2\zeta \\ -\alpha & 0 & 0 & \alpha & 0 & 0 \\ 0 & -12\zeta & -6L_0\zeta & 0 & 12\zeta & -6L_0\zeta \\ 0 & 6L_0\zeta & 2L_0^2\zeta & 0 & -6L_0\zeta & 4L_0^2\zeta \end{bmatrix} \tag{L.14}$$

$$[k]_{le} = \begin{bmatrix} \alpha & 0 & 0 & -\alpha & 0 & 0 \\ 0 & 3\zeta & 3L_0\zeta & 0 & -3\zeta & 0 \\ 0 & 3L_0\zeta & 3L_0^2\zeta & 0 & -3L_0\zeta & 0 \\ -\alpha & 0 & 0 & \alpha & 0 & 0 \\ 0 & -3\zeta & -3L_0\zeta & 0 & 3\zeta & 0 \\ 0 & 0 & 0 & 0 & 0 & 0 \end{bmatrix} \tag{L.15}$$

$$[k]_{le} = \begin{bmatrix} \alpha & 0 & 0 & -\alpha & 0 & 0 \\ 0 & 3\zeta & 0 & 0 & -3\zeta & 3L_0\zeta \\ 0 & 0 & 0 & 0 & 0 & 0 \\ -\alpha & 0 & 0 & \alpha & 0 & 0 \\ 0 & -3\zeta & 0 & 0 & 3\zeta & -3L_0\zeta \\ 0 & 3L_0\zeta & 0 & 0 & -3L_0\zeta & 3L_0^2\zeta \end{bmatrix} \tag{L.16}$$

$$[k]_{le} = \begin{bmatrix} \alpha & 0 & 0 & -\alpha & 0 & 0 \\ 0 & 0 & 0 & 0 & 0 & 0 \\ 0 & 0 & 0 & 0 & 0 & 0 \\ -\alpha & 0 & 0 & \alpha & 0 & 0 \\ 0 & 0 & 0 & 0 & 0 & 0 \\ 0 & 0 & 0 & 0 & 0 & 0 \end{bmatrix} \tag{L.17}$$

$$\alpha \equiv \frac{AE}{L_0} \tag{L.18}$$

$$\zeta \equiv \frac{IE}{L_0^3} \tag{L.19}$$

Before the terms of the element stiffness matrices can be added to the model stiffness matrix, they need to be transformed to the global coordinate system using equation L.20. The rotation matrix is given in equation L.21, θ is the angle in the counter-clockwise direction of the element in the global coordinate system. The matrices in equations L.14 through L.17 do not change with deformation, the angle in equation L.21. The angle is found by adjusting the discretized locations of the solution with the total deflection in equation L.12 and recalculating the angles of each element. The stiffness matrix for the

structure is assembled by summing the terms in all the element stiffness matrices that correspond to the same deflection and force.

$$[k]_{ge} = [\theta]^T [k]_{le} [\theta] \tag{L.20}$$

$$[\theta] = \begin{bmatrix} \cos\phi & \sin\phi & 0 & 0 & 0 & 0 \\ -\sin\phi & \cos\phi & 0 & 0 & 0 & 0 \\ 0 & 0 & 1 & 0 & 0 & 0 \\ 0 & 0 & 0 & \cos\phi & \sin\phi & 0 \\ 0 & 0 & 0 & -\sin\phi & \cos\phi & 0 \\ 0 & 0 & 0 & 0 & 0 & 1 \end{bmatrix} \tag{L.21}$$

The forces on each element is found with equation L.13 with the total deflection in the local coordinate system. The total deflection is found with equation L.12 except that $\Delta\vec{u}_i$ is transferred in the local coordinate system with equation L.22. The stress at each end of the element is found with equation L.23. The symbol w is the largest distance from the neutral axis in the profile.

$$\vec{u}_{le} = [\theta]\, \vec{u}_{ge} \tag{L.22}$$

$$\sigma = \frac{F_x}{A} \pm \frac{Mw}{I} \tag{L.23}$$

Appendix M

Tower Structural Analysis

M.1 Structural Analysis of Lightly Loaded Tower

Figure M.1 gives the loading schematic of the overall tower structure. Having forces in two directions requires a conservation of momentum in both directions. Given that the forces are expected to be steady there is no momentum, thus all forces in any direction should sum to 0. The beam elements of the tower are experiencing shear, with a rigid connection top and bottom the beam elements should not experience any angular displacement at the top or bottom. With a rigid top, both tower elements should experience the same lateral displacement. Being the structurally the same the thrust force is evenly distributed across both tower members. Figure M.2 show the free body diagram of a tower member with only lateral force applied, for zero angular displacement at the top there has to be a moment force countering the bending. Equation M.1 gives the moment force at the top of the tower. Knowledge of this moment force allows the knowledge of the free body diagram for the rigid top section given in figure M.3. Conservation of vertical forces on the top section is given in equation M.2. Conservation of angular momentum is necessary to solve all the forces in the structure. Equation M.3 gives the angular momentum balance of the top section about point 1. Knowing F_T, F_w, X and d the distance between tower members, equations M.1, M.2 and M.3 are all that is needed to solve the overall forces on the tower members.

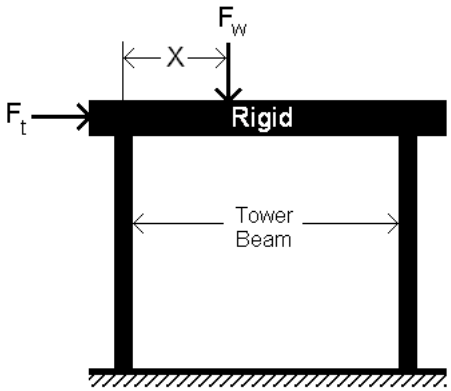

Figure M.1: Loading Schematic for Tower Structure

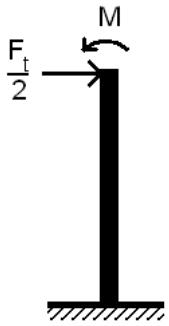

Figure M.2: Tower Member Free Body Diagram under Lateral Loading

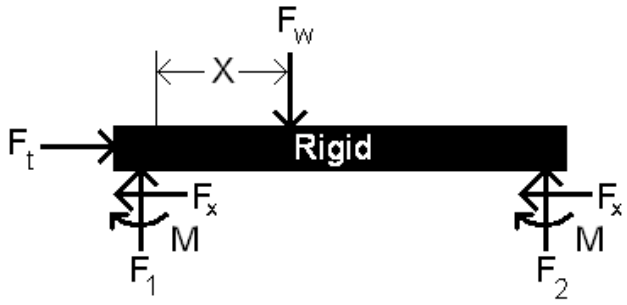

Figure M.3: Free Body Diagram of the Tower Top Section

$$M = \frac{F_T l}{4} \tag{M.1}$$

$$0 = F_w - F_1 - F_2 \tag{M.2}$$

$$0 = F_2 d - F_w X - 2M \tag{M.3}$$

The assumed weight of 1kN was too small. Once the entire structure was designed the final mass of the nacelle hub and other equipment was 359kg, resulting in a weight of 3518.2N. The spacing d of the tower elements was set at 0.949m to satisfy the minimum distance between tower and rotor place constraint. The maximum stress in the tower elements occurs at the front and top of the rear tower element, here the material is under compression from the weight moment balance and additional compression from the moment in the tower itself. The stress at this element is given in equation M.4, equation M.4 is derived from equations M.1, M.3 and M.5. The weight of the structure cannot change, however the maximum stress can be reduced by reducing the thrust and moving the nacelle assembly forward on the tower. Assuming a yield strength of 200MPa table M.1 gives the safety factor for the tower at varying thrust and nacelle positions.

$$\sigma_{max} = \frac{Mr}{I} + \frac{F_w X + 2M}{dA} \tag{M.4}$$

$$\sigma_m = \frac{Mr}{I} \tag{M.5}$$

		Thrust Force [N]			
		500	1000	1500	2000
$\frac{X}{d}$	0.00	7.1	3.6	2.4	1.8
	0.10	7.0	3.5	2.4	1.8
	0.20	6.8	3.5	2.3	1.8
	0.25	6.8	3.5	2.3	1.8
	0.30	6.7	3.5	2.3	1.8
	0.40	6.6	3.4	2.3	1.7
	0.50	6.5	3.4	2.3	1.7
	0.75	6.2	3.3	2.3	1.7
	1.00	6.0	3.2	2.2	1.7

Table M.1: Tower Safety Factor under Various Loading Conditions

Table M.1 shows that as the thrust force increases the effect of position of the nacelle on the tower diminishes. With increasing thrust force the moment forces on the beams increases, these moments become the dominant contribution of axial compression on the rearward tower element. At 2kN thrust force the front tower member is under tensile strain. Given that at high thrust forces the effect of position is negligible, the nacelle position was placed in the center. Future experiments could have the apparatus producing negative thrust, thus the effect of position would be reversed. Operating with a thrust force greater than 1kN will result in safety factors too small for safe operation.

The thrust force for this experiment was estimated using a high coefficient of thrust at maximum wind speed. The thrust of the intended experiment will be much less, since the purpose is to test the rotor in less than ideal conditions. In cases otherwise reinforcements can be added to strengthen the tower.

M.2 Structural Analysis of Tower Gusset Connections

The vertical members in the two strut tower are under strong bending moment loads. In section M.1 these members were analyzed as a cantilevered beam, stress concentrations at

Density $[kg/m^3]$	7800
Modulus of Elasticity $[Pa]$	$2 \cdot 10^{11}$
Poisson's Ratio	0.23

Table M.2: Alternate Material Properties for Steel

the connection points were ignored. Further analysis is required to determine whether the connection is sufficiently strong. A model was developed within Abaqus 6.5-1 to determine the stress of the gusseted tower connections.

To simplify the model many changes were made to the solid model. The meshing was simplified when the tube was modeled as an octagon. There is also symmetry from left to right of the tower so only one half was meshed. Extending the analysis in section M.1 will show that the member transmits no moments at its mid point. Knowing the loading at this intermediate point allowed the bottom half to be modeled independently.

The member has gussets welded to it, which bolt into a plate on either end of the member. The ideal gusset geometry is unknown. The width of the gusset is constrained by the size of the plates it bolts to. Several variations of this model were used to find how thickness and height affected the strength. The ideal gusset is 0.145m wide and 0.2 m tall and 6.35 mm thick. The model presented here is with the ideal gusset geometry.

The tower was modeled as steel. The assumed properties are given in table M.2

A lateral load was applied evenly across all the points on the top of the tower. The lateral load is for a 2000 N thrust force. The axial force varies whether the member is at the front or rear. The analysis in section M.1, shows that with a 2000 N thrust and a nacelle weight of 3518 N, the front member is being compressed by 907 N and the rear by 2611 N. Two load cases were considered to account for both compressive forces. The axial forces were distributed evenly over the top section of the model. The model was constrained in all three directions at the base. The appropriate symmetry boundary condition was applied on the partitioned faces.

Figure M.4 shows the Von-Mises stress of the tower at the gusseted region for the worst load case. Here the peak stress is 79 MPa at the rear of the tower. This is the expected location of peak stress in the analysis in section M.1. The plot shows negligible stress

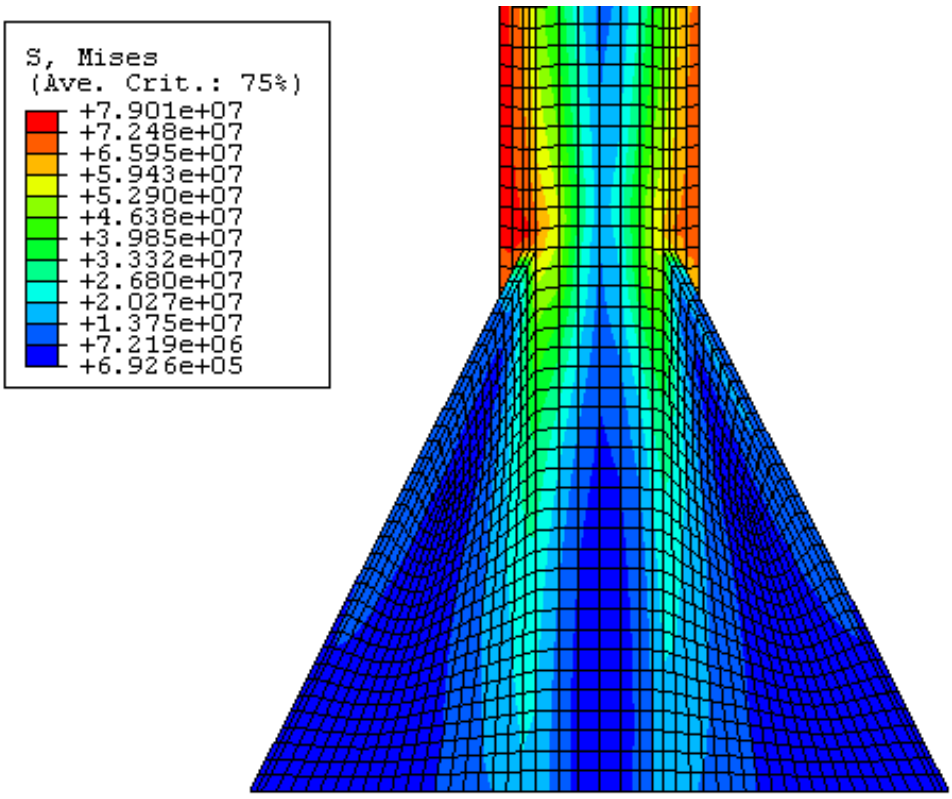

Figure M.4: Stress of the Vertical Tower Member

concentration at the end of the gusset hence it is safe to assume that the gusset has no effect on the maximum stress. The analysis in section M.1 is valid. One interesting result is the peak stress for the other load case is 76 MPa. This confirms that at the high thrust loads the peak stress is desensitized to the axial loading.

M.3 Structural Analysis of Highly Loaded Tower

Section 6.3.2 explains the overall architecture of the highly loaded tower. The additional struts make this tower structure indeterminate and cannot be solved with the same methods used in section M.1 for the lightly loaded tower. Hooke's law needs to be applied to give additional equations to enable a solution to the problem.

The structural analysis is further complicated by the fact that higher loads lead to greater deflection introducing non-linearity's. A given member can withstand greater loads when applied axially, as appose to laterally. The lateral loading will produce shear and bending moments, which does not stress the materially equally, resulting in inefficient loading. Axial loading will yield additional lateral loading when the member is subjected to lateral deformation. Under tensile conditions the additional lateral deformation acts in opposite direction to the original deflection minimizing its effect. The opposite is true for compressive loading, the additional lateral deflection augments the original deflection weakening the structure further. Under extreme situations this leads to buckling, a failure mode under compressive loading.

There are two known analytical solutions to buckling, the first is the Euler buckling formula that solves the instability from purely axial buckling. The second is the secant formula that solves the maximum stress from eccentric axial loading. Both formulas cannot be applied when there is a distributed load causing lateral deflection. The lack of analytical tools requires finite element methods to be employed.

The solution to a given structural problem, is continuously varying across the entire solution domain. Analytically these problems are very complicated and exceedingly difficult to solve. Thus there are very few analytical solutions. The complexity of continuum can be eliminated by solving a discretized system similar to the original problem. The discretized system has discrete forces and deflections at discrete points in the solution. A detailed discussion of the discretized solution method is given in section L.2 in appendix L.

The method described in section L.2 was used to analyze the reinforced structure over a wide range of axial loads. The gravitational load was kept constant at 3518N. The axial load was varied from 0N to 4000N at 500N increments. Table M.3 shows how the maximum stress and safety factor varied with axial load. The maximum stress varied little with increased axial loading. The axial load is transmitted axially through the top section then through the reinforcements. The mode of loading is more efficient and lead to small increases in the stress. The bending stress from the gravitation loads yields the largest contribution to the maximum stress. Thus the highly loaded tower can withstand very high axial loads.

Axial Load [N]	Maximum Stress [MPa]	Safety Factor
0	26.5	7.53
500	27.0	7.41
1000	27.4	7.29
1500	27.9	7.18
2000	28.3	7.07
2500	28.7	6.96
3000	29.2	6.86
3500	29.6	6.75
4000	30.0	6.66

Table M.3: Structural Integrity of Highly Loaded Tower

Appendix N

Nacelle Structural Frame

The design of the nacelle was largely based on material freely available as scrap metal. Table N.1 lists all the members available for the design of the nacelle. The stiffness columns give the spring constant for a meter length of material under various loading conditions, K_x and K_y is for cantilever loading about the corresponding cross section axis, equation N.1, K_z is for axial loading, equation N.2. To prevent the smallest of laser distortion the second stiffest members, item 2, were used to span between the bearings of the main shaft and the laser head. The drive train requires structural member below those of the main shaft to hold the motor and the secondary shaft. Being the lowest set members these would connect to the tower. All the forces from the rotor are transmitted to the bearings, for increased stiffness the lower members would extend forward to support these bearings. The lower members span the length of the nacelle and support all the components thus the strongest members were used, item 1. A majority of the forces of the apparatus are from the rotor itself, the third strongest members, items 3 and 4, were used to support the bearings, and connect the main frame with the bearing support structure. The remainder of the material was used for reinforcements and other frame elements.

$$K_i = \frac{6EI_i}{L^3} \tag{N.1}$$

$$K_z = \frac{EA}{L} \tag{N.2}$$

			Cross Section				Stiffness		
Item	Qty	Length [m]	Shape	H [mm]	W [mm]	Thickness [mm]	K_x [kN/m]	K_y [kN/m]	K_z [MN/m]
1	2	2.000	L	64	64	6.5	367	367	158
2	1	3.052	▯	38	64	3.0	78	197	92
3	1	0.920	L	50	50	6.0	158	158	113
4	1	1.370	L	50	50	6.0	158	158	113
5	4	1.375	□	32	32	2.5	52	52	59
6	6	0.830	□	32	32	2.5	52	52	59
7	3	0.633	□	32	32	2.5	52	52	59
8	1	1.200	L	25	25	5.0	15	15	45

Table N.1: Properties of Available Structural Members

Appendix O

Dynamics of the Shaft and Rotor

The dynamic stall experiment will uses laser Particle Image Velocimetry (PIV) to collect data. The route of the laser beam will pass through several mirrors connected to different parts before getting to the target area. To preserve the integrity of the PIV data the laser must not deviate from the target area. Vibrations pose a potential source of deviation. A modal analysis was performed on the rotor rig to gauge the potential influence of vibrations.

Vibrations are suppressed when the fundamental frequency is kept high. High frequencies will increase the influence of damping and reduce the amplitude. Both of these effects reduce the potential laser deviation. The rotor rig itself will have rotating components that may induce their own vibrations. The fundamental frequency of the rig needs to be greater than these rotations to ensure that the rotations themselves do not excite these fundamental frequencies.

The laser beam will be emitted from the end of the shaft and will strike the blade perpendicular to the rotor plane. The first analysis focused on the vibrations inherent in the shaft and blade system. This system is simplified from the overall system. The overall system would include the effect of the tower and the nacelle frame. The nacelle frame can be ignored given that it is being designed very stiff. The effect of the tower is being ignored because it can be reinforced, to the point of being rigid. The schematic for the system is given in Figure O.1.

All models were implemented in Abaqus 6.5-1. 2 dimensional beam elements were used to model all components. The S809 airfoil profile, along with the Ames test turbine rotor

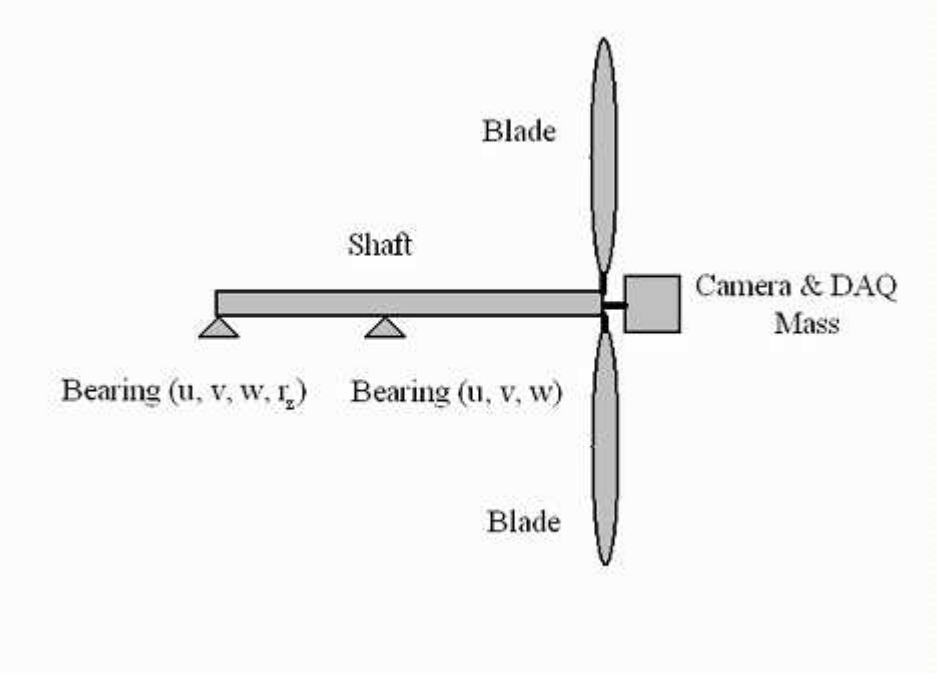

Figure O.1: Schematic of the Blade and Vibration System

	Steel	Carbon Fiber
Density $[kg/m^3]$	7800	1600
Young's Modulus $[GPa]$	200	70
Poisson's Ratio	0.25	0.361

Table O.1: Assumed Material Properties in Dynamic Analysis

shape was used to determine the beam properties of the blade. It was assumed that the blade was made of carbon fiber. The properties of mild steel were assumed for the shaft. The properties of all the materials are given in Table O.1.

Figure O.2 showed the deformed state of the first mode of vibration. At this mode the blade is oscillating about the flap-wise moment. The blade itself has a low flap wise moment of inertia hence the overall stiffness is low, contributing to the low frequency. The frequency of this moment is sensitive to the stiffness mass characteristics of the blade and the length of the shaft. Ideally the blade would be connected to the shaft at the first bearing and the shaft would have negligible influence on the vibration mode. Under these conditions the fundamental frequency of the blade governs the frequency of the system. Thus under any condition the blade characteristics are going to have a significant influence on the system.

The fundamental frequency is proportional to the root of the effective stiffness and the inverse root of the effective mass. The effective stiffness is effectively a weighted average of the overall stiffness. The stiffness at the tip of the blade will have little influence on the deformation of the overall system. Stiffness at the root will have a greater influence on the deformation of the system. The effective mass is a similar weighted average of the overall mass. In the effective mass the weighting trends are opposite to that in stiffness. Hence the mass distribution should be concentrated in the center than towards the outside.

Removing material near the tip will reduce the effective mass with little reduction in the effective stiffness. This in turn will increase the frequency. The mass distribution can be controlled by varying the thickness of the skin with radius. The ideal mass distribution was found by analyzing the rotor blade under static conditions. Three loads were considered in static conditions, gravity, centrifugal and distributed load from aerodynamic forces. The

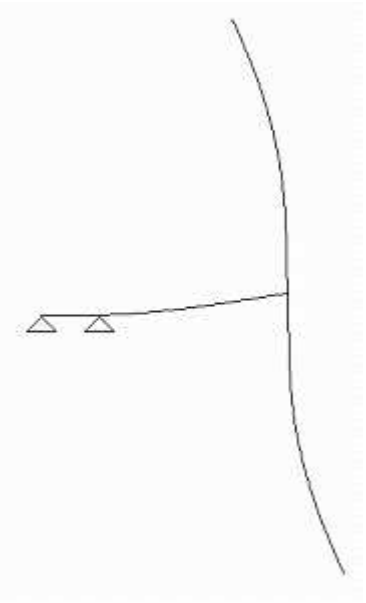

Figure O.2: First Vibration Mode for the Blade and Shaft

objective was to reduce the load in the blade such that the bending moment versus flap-wise moment of inertia (BMIR) was kept constant. Three mass distributions were considered, constant thickness, linear variation in thickness and parabolic variation in thickness. Only the parabolic distribution gave a constant BMIR. The fundamental frequency of the various blades is given in Table O.2. The parabolic blade has the best frequency at 29.208 Hz.

Ideal aerodynamic conditions are met when the blades are farthest from the nacelle assembly. A modal analysis was performed on several shaft lengths to determine the best compromise between aerodynamics and vibrations. Figure O.3 shows the first mode

Blade	Frequency $[Hz]$
Parabolic Thickness	29.208
Linear Thickness	25.881
Constant Thickness	21.191

Table O.2: Fundamental Frequency of Various Blades

frequency versus the shaft length. Up to the length of 1.4m the frequency trend shows negative concavity, beyond 1.4m the trend shows positive concavity. With increasing shaft length the deflection becomes more dependent on shaft properties than blade properties. Hence between lengths 1m and 2m the dominant influence is transferring from the blade to the shaft.

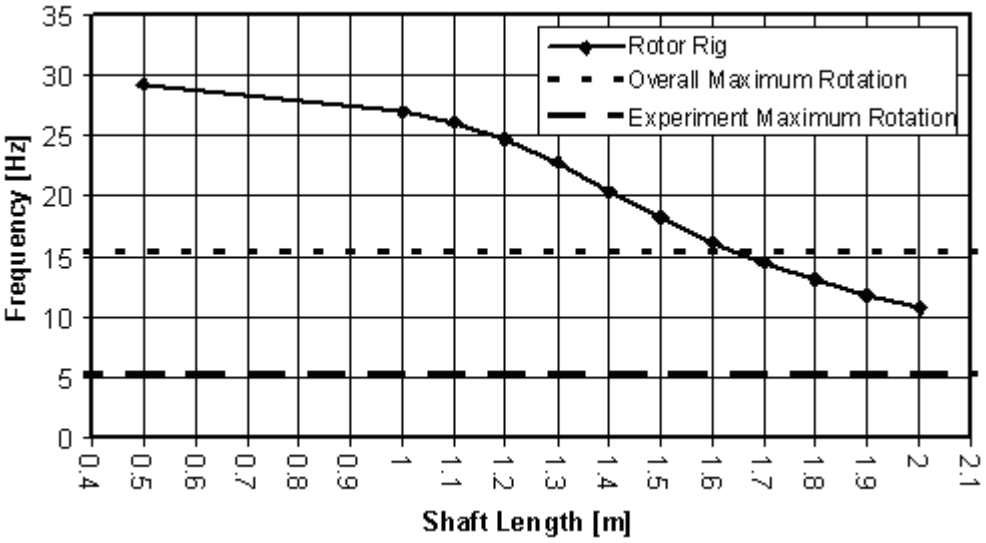

Figure O.3: Effect of Shaft Length on Vibrations

The maximum shaft length is 1.6m, beyond that length the fundamental frequency is equal to or less than the maximum rotational rate of the shaft. Ideal aerodynamic conditions are met when the rotor plane is 10 tower diameters from the tower. The tower diameter is 0.0762m, thus the minimum distance is 0.762m. The farthest forward position of the tower with respect to the shaft is underneath the 0.5m point. At this point the minimum length of the shaft is 1.262m. At this point the frequency is 23.521 Hz. This is 1.5 the maximum rotational rate and 4.6 times the maximum experiment rotation rate. Thus a shaft length of 1.262m is acceptable for both aerodynamic and vibration considerations. Depending on the nacelle center of mass the tower position will likely fall aft of the 0.5m position on the shaft. Under these conditions the shaft length can be shortened to 1m to reduce vibrations further.

Figure O.4 shows how the amplitude varies with frequency. With a frequency ratio of 0.75 the amplitude ratio is 2.4. Thus the system will have adverse vibrations at the overall maximum rotational rate and a 1.262m shaft. However with a 1m shaft the amplitude ratio drops to 1.35 at the overall maximum rotational rate. For the maximum speed in the experiment the amplitude ratio is near unity for both shaft lengths.

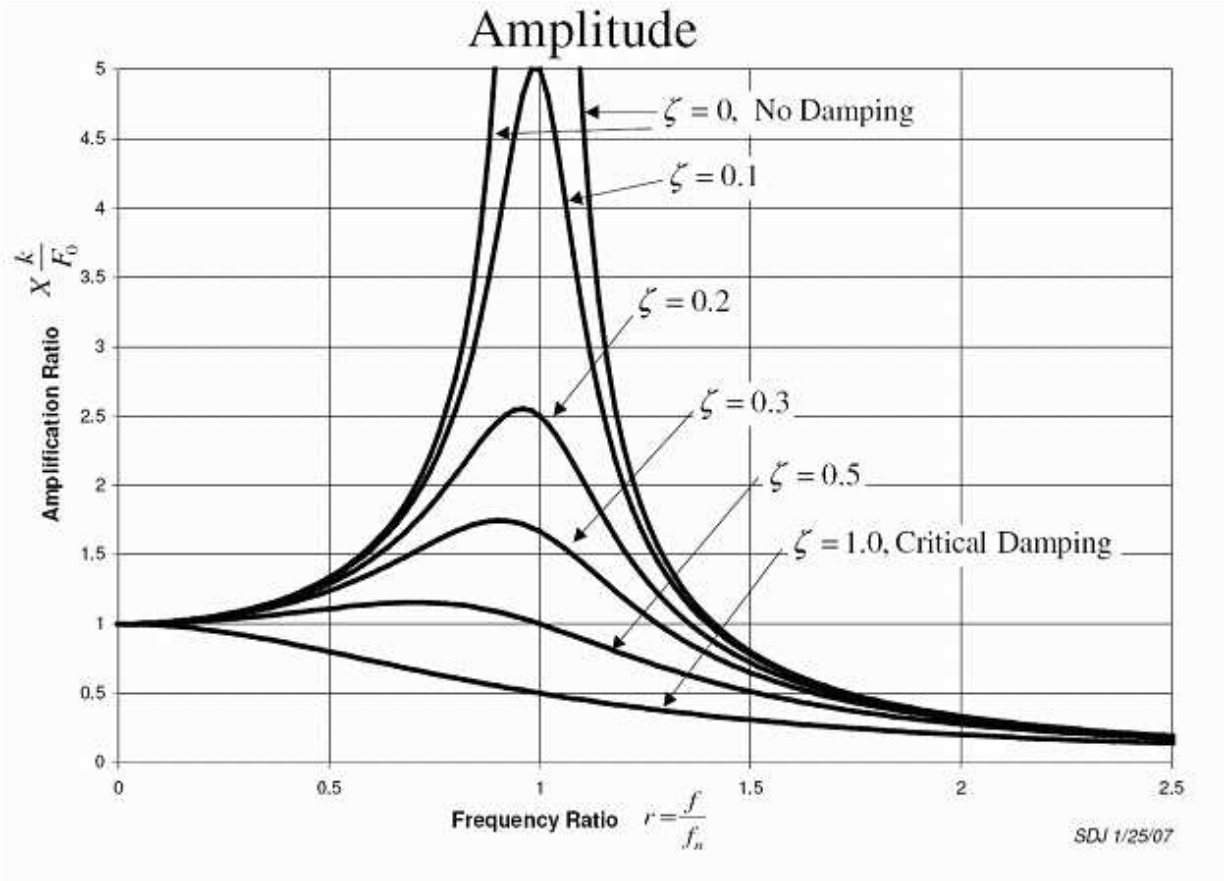

Figure O.4: Effect of Damping and Frequency [42]

The fundamental frequency of the system can be increased by increasing the blade wall thickness at the root. The blade in isolation and the system was analyzed with a parabolic thickness distribution and a 1m long shaft. Table O.3 compares the system frequency with overall blade wall thickness. Increasing the thickness of the blade increases the frequency

	Blade Frequency $[Hz]$	System Frequency $[Hz]$
Blade with 2mm Root Skin	29.208	27.000
Blade with 3mm Root Skin	35.742	30.574

Table O.3: Effect of Blade Material Thickness on Fundamental Frequency

of the system. However increasing the thickness also increases the weight at the end of the shaft. With a thicker blade the shaft deflection has a greater influence hence the reduced frequency in the system analysis.

Provided that the shaft is kept short the system frequency is most dependent on the blade fundamental frequency. The blade frequency is minimized when the material thickness applied with a parabolic distribution with decreasing thickness towards the tip. With a short shaft the frequency of the system can be increased with increasing skin thickness in the root of the blade. The analysis shows that a shaft length of 1.262m with a root skin thickness of 2mm is acceptable for the proposed experiment. A shorter shaft could be utilized if the tower is set aft of the forward bearing. This would further increase the stiffness so that PIV can be used with the overall maximum speed. Overall the analysis shows that the rig will be stiff enough that vibrations will have a minimal effect on the experiment.

Appendix P

Laser Optics Boom Geometry and Structural Properties

P.1 Forces Applied in Static Analysis

The FEM truss analysis described in section L.1 in appendix L was used to find the static response to the various forces. The discussion below describes how the forces were applied in the model.

For the static analysis the forces were applied for each member, each force was distributed evenly to it's to nodes. As stated above each member would be experiencing centrifugal acceleration, equation P.1, aerodynamic loading, equations P.2 and P.3, finally gravitational loading equation P.4. For these calculations ω was assumed to be 33.45 radians per second, C_D was one, and U was 13m/s. The forces form a vector that can be used to solve the final deflection by solving equation P.5. To ensure structural integrity it is important to confirm that stress is within the yield strength with an acceptable safety factor. Using the deflection solution equation P.6 was used to determine the stress within each member.

$$F_\omega = m\omega^2 r \tag{P.1}$$

$$F_{uAxial} = \frac{1}{2}\rho_{air} C_D D L U^2 \tag{P.2}$$

$$F_{uTheta} = \frac{1}{2}\rho_{air} C_D D L \left(\omega r\right)^2 \tag{P.3}$$

$$F_g = mg \tag{P.4}$$

$$\vec{f} = [k]_{gm}\, \vec{u} \tag{P.5}$$

$$\sigma = \frac{E\left(u_2 - u_1\right)}{AL_0} \tag{P.6}$$

P.2 Boom Optimization Results

The truss analysis tool described in section L.1 of appendix L was used to optimize the structure. The discussion below describes the results.

The boom was designed based on maximizing the lowest fundamental frequency. Table P.1 shows the frequency, deflection and stress properties of the optimized boom. As comparison the truss was optimized for minimum stress and minimum deflection, the properties of these structures are given for comparison. The overall structure has an acceptable minimum fundamental frequency being twice that of the maximum rotational rate. The maximum stress is half the yield strength of mild steel. This safety factor is small but acceptable, the load case for the stress is a worst case scenario. The deflection is high, the components of deflection are 0.298mm axially, 0.093mm radially and -3.636mm in azimuth. Deflection in the laser beam is most sensitive to radial and axial deflection, and has negligible sensitivity with azimuth deflection. Considering this sensitivity the deflection is acceptable. Much of the deflection would be steady and can be compensated for, the high fundamental frequency will reduce vibrations and other varying deflections. Table P.2 gives the properties of each member in the frequency optimized truss.

Optimization Criteria	Max. Frequency	Min. Stress	Min. Deflection
Min. Frequency [Hz]	69	62	55
Max. Stress [MPa]	98	35	39
Max. Deflection [mm]	3.65	1.99	1.87
Mass [g]	2362	971	1058

Table P.1: Properties of Various Optimized Truss Designs

Member	Length [m]	Diameter [mm]	Point 1 [m]	Point 2 [m]
1	0.235	6.4	(0, 0.083, 0)	(0.168, 0, 0.143)
2	0.235	6.4	(0, -0.083, 0)	(0.168, 0, 0.143)
3	0.165	1.6	(0.168, 0.083, 0)	(0.168, -0.083, 0)
4	0.165	1.6	(0.168, -0.083, 0)	(0.168, 0, 0.143)
5	0.165	1.6	(0.168, 0, 0.143)	(0.168, 0.083, 0)
6	0.147	6.4	(0.168, 0.083, 0)	(0.314, 0.073, 0)
7	0.147	6.4	(0.168, -0.083, 0)	(0.314, -0.073, 0)
8	0.147	6.4	(0.168, 0, 0.143)	(0.314, 0, 0.127)
9	0.214	1.6	(0.168, 0.083, 0)	(0.314, -0.073, 0)
10	0.211	1.6	(0.168, -0.083, 0)	(0.314, 0, 0.127)
11	0.217	1.6	(0.168, 0, 0.143)	(0.314, 0.073, 0)
12	0.147	1.6	(0.314, 0.073, 0)	(0.314, -0.073, 0)
13	0.147	1.6	(0.314, -0.073, 0)	(0.314, 0, 0.127)
14	0.147	1.6	(0.314, 0, 0.127)	(0.314, 0.073, 0)
15	0.13	6.4	(0.314, 0.073, 0)	(0.445, 0.065, 0)
16	0.13	6.4	(0.314, -0.073, 0)	(0.445, -0.065, 0)
17	0.131	6.4	(0.314, 0, 0.127)	(0.445, 0, 0.113)
18	0.19	1.6	(0.314, -0.073, 0)	(0.445, 0.065, 0)
19	0.193	1.6	(0.314, 0, 0.127)	(0.445, -0.065, 0)
20	0.187	1.6	(0.314, 0.073, 0)	(0.445, 0, 0.113)
21	0.131	1.6	(0.445, 0.065, 0)	(0.445, -0.065, 0)
22	0.131	1.6	(0.445, -0.065, 0)	(0.445, 0, 0.113)
23	0.131	1.6	(0.445, 0, 0.113)	(0.445, 0.065, 0)
24	0.116	6.4	(0.445, 0.065, 0)	(0.561, 0.058, 0)
25	0.116	6.4	(0.445, -0.065, 0)	(0.561, -0.058, 0)
26	0.117	6.4	(0.445, 0, 0.113)	(0.561, 0, 0.101)
27	0.169	1.6	(0.445, 0.065, 0)	(0.561, -0.058, 0)

Table P.2 – Continued on next page

Table P.2 – Continued from previous page

Member	Length [m]	Diameter [mm]	Point 1 [m]	Point 2 [m]
28	0.167	1.6	(0.445, -0.065, 0)	(0.561, 0, 0.101)
29	0.172	1.6	(0.445, 0, 0.113)	(0.561, 0.058, 0)
30	0.116	1.6	(0.561, 0.058, 0)	(0.561, -0.058, 0)
31	0.116	1.6	(0.561, -0.058, 0)	(0.561, 0, 0.101)
32	0.116	1.6	(0.561, 0, 0.101)	(0.561, 0.058, 0)
33	0.103	6.4	(0.561, 0.058, 0)	(0.664, 0.052, 0)
34	0.103	6.4	(0.561, -0.058, 0)	(0.664, -0.052, 0)
35	0.104	6.4	(0.561, 0, 0.101)	(0.664, 0, 0.09)
36	0.151	1.6	(0.561, -0.058, 0)	(0.664, 0.052, 0)
37	0.153	1.6	(0.561, 0, 0.101)	(0.664, -0.052, 0)
38	0.148	1.6	(0.561, 0.058, 0)	(0.664, 0, 0.09)
39	0.103	1.6	(0.664, 0.052, 0)	(0.664, -0.052, 0)
40	0.103	1.6	(0.664, -0.052, 0)	(0.664, 0, 0.09)
41	0.103	1.6	(0.664, 0, 0.09)	(0.664, 0.052, 0)
42	0.092	6.4	(0.664, 0.052, 0)	(0.755, 0.046, 0)
43	0.092	6.4	(0.664, -0.052, 0)	(0.755, -0.046, 0)
44	0.092	6.4	(0.664, 0, 0.09)	(0.755, 0, 0.08)
45	0.134	1.6	(0.664, 0.052, 0)	(0.755, -0.046, 0)
46	0.132	1.6	(0.664, -0.052, 0)	(0.755, 0, 0.08)
47	0.136	1.6	(0.664, 0, 0.09)	(0.755, 0.046, 0)
48	0.092	1.6	(0.755, 0.046, 0)	(0.755, -0.046, 0)
49	0.092	1.6	(0.755, -0.046, 0)	(0.755, 0, 0.08)
50	0.092	1.6	(0.755, 0, 0.08)	(0.755, 0.046, 0)
51	0.082	6.4	(0.755, 0.046, 0)	(0.837, 0.041, 0)
52	0.082	6.4	(0.755, -0.046, 0)	(0.837, -0.041, 0)
53	0.082	6.4	(0.755, 0, 0.08)	(0.837, 0, 0.071)
54	0.119	1.6	(0.755, -0.046, 0)	(0.837, 0.041, 0)
55	0.121	1.6	(0.755, 0, 0.08)	(0.837, -0.041, 0)

Table P.2 – Continued on next page

Table P.2 – Continued from previous page

Member	Length [m]	Diameter [mm]	Point 1 [m]	Point 2 [m]
56	0.117	1.6	(0.755, 0.046, 0)	(0.837, 0, 0.071)
57	0.082	1.6	(0.837, 0.041, 0)	(0.837, -0.041, 0)
58	0.082	1.6	(0.837, -0.041, 0)	(0.837, 0, 0.071)
59	0.082	1.6	(0.837, 0, 0.071)	(0.837, 0.041, 0)
60	0.073	6.4	(0.837, 0.041, 0)	(0.91, 0.036, 0)
61	0.073	6.4	(0.837, -0.041, 0)	(0.91, -0.036, 0)
62	0.073	6.4	(0.837, 0, 0.071)	(0.91, 0, 0.063)
63	0.106	1.6	(0.837, 0.041, 0)	(0.91, -0.036, 0)
64	0.104	1.6	(0.837, -0.041, 0)	(0.91, 0, 0.063)
65	0.108	1.6	(0.837, 0, 0.071)	(0.91, 0.036, 0)
66	0.073	1.6	(0.91, 0.036, 0)	(0.91, -0.036, 0)
67	0.073	1.6	(0.91, -0.036, 0)	(0.91, 0, 0.063)
68	0.073	1.6	(0.91, 0, 0.063)	(0.91, 0.036, 0)
69	0.065	6.4	(0.91, 0.036, 0)	(0.974, 0.032, 0)
70	0.065	6.4	(0.91, -0.036, 0)	(0.974, -0.032, 0)
71	0.065	6.4	(0.91, 0, 0.063)	(0.974, 0, 0.056)
72	0.094	1.6	(0.91, -0.036, 0)	(0.974, 0.032, 0)
73	0.096	1.6	(0.91, 0, 0.063)	(0.974, -0.032, 0)
74	0.093	1.6	(0.91, 0.036, 0)	(0.974, 0, 0.056)
75	0.065	1.6	(0.974, 0.032, 0)	(0.974, -0.032, 0)
76	0.065	1.6	(0.974, -0.032, 0)	(0.974, 0, 0.056)
77	0.065	1.6	(0.974, 0, 0.056)	(0.974, 0.032, 0)
78	0.058	6.4	(0.974, 0.032, 0)	(1.032, 0.029, 0)
79	0.058	6.4	(0.974, -0.032, 0)	(1.032, -0.029, 0)
80	0.058	6.4	(0.974, 0, 0.056)	(1.032, 0, 0.05)
81	0.084	1.6	(0.974, 0.032, 0)	(1.032, -0.029, 0)
82	0.083	1.6	(0.974, -0.032, 0)	(1.032, 0, 0.05)
83	0.085	1.6	(0.974, 0, 0.056)	(1.032, 0.029, 0)

Table P.2 – Continued on next page

Table P.2 – Continued from previous page

Member	Length [m]	Diameter [mm]	Point 1 [m]	Point 2 [m]
84	0.058	1.6	(1.032, 0.029, 0)	(1.032, -0.029, 0)
85	0.058	1.6	(1.032, -0.029, 0)	(1.032, 0, 0.05)
86	0.058	1.6	(1.032, 0, 0.05)	(1.032, 0.029, 0)
87	0.051	6.4	(1.032, 0.029, 0)	(1.083, 0.026, 0)
88	0.051	3.2	(1.032, -0.029, 0)	(1.083, -0.026, 0)
89	0.051	3.2	(1.032, 0, 0.05)	(1.083, 0, 0.044)
90	0.075	1.6	(1.032, -0.029, 0)	(1.083, 0.026, 0)
91	0.076	1.6	(1.032, 0, 0.05)	(1.083, -0.026, 0)
92	0.074	1.6	(1.032, 0.029, 0)	(1.083, 0, 0.044)
93	0.051	1.6	(1.083, 0.026, 0)	(1.083, -0.026, 0)
94	0.051	1.6	(1.083, -0.026, 0)	(1.083, 0, 0.044)
95	0.051	1.6	(1.083, 0, 0.044)	(1.083, 0.026, 0)
96	0.046	3.2	(1.083, 0.026, 0)	(1.128, 0.023, 0)
97	0.046	3.2	(1.083, -0.026, 0)	(1.128, -0.023, 0)
98	0.046	3.2	(1.083, 0, 0.044)	(1.128, 0, 0.039)
99	0.066	1.6	(1.083, 0.026, 0)	(1.128, -0.023, 0)
100	0.065	1.6	(1.083, -0.026, 0)	(1.128, 0, 0.039)
101	0.068	1.6	(1.083, 0, 0.044)	(1.128, 0.023, 0)
102	0.046	1.6	(1.128, 0.023, 0)	(1.128, -0.023, 0)
103	0.046	1.6	(1.128, -0.023, 0)	(1.128, 0, 0.039)
104	0.046	1.6	(1.128, 0, 0.039)	(1.128, 0.023, 0)
105	0.041	3.2	(1.128, 0.023, 0)	(1.169, 0.02, 0)
106	0.041	3.2	(1.128, -0.023, 0)	(1.169, -0.02, 0)
107	0.041	3.2	(1.128, 0, 0.039)	(1.169, 0, 0.035)
108	0.059	1.6	(1.128, -0.023, 0)	(1.169, 0.02, 0)
109	0.06	1.6	(1.128, 0, 0.039)	(1.169, -0.02, 0)
110	0.058	1.6	(1.128, 0.023, 0)	(1.169, 0, 0.035)
111	0.041	1.6	(1.169, 0.02, 0)	(1.169, -0.02, 0)

Table P.2 – Continued on next page

Table P.2 – Continued from previous page

Member	Length [m]	Diameter [mm]	Point 1 [m]	Point 2 [m]
112	0.041	1.6	(1.169, -0.02, 0)	(1.169, 0, 0.035)
113	0.041	1.6	(1.169, 0, 0.035)	(1.169, 0.02, 0)
114	0.036	3.2	(1.169, 0.02, 0)	(1.205, 0.018, 0)
115	0.036	3.2	(1.169, -0.02, 0)	(1.205, -0.018, 0)
116	0.036	3.2	(1.169, 0, 0.035)	(1.205, 0, 0.031)
117	0.053	1.6	(1.169, 0.02, 0)	(1.205, -0.018, 0)
118	0.052	1.6	(1.169, -0.02, 0)	(1.205, 0, 0.031)
119	0.053	1.6	(1.169, 0, 0.035)	(1.205, 0.018, 0)
120	0.036	1.6	(1.205, 0.018, 0)	(1.205, -0.018, 0)
121	0.036	1.6	(1.205, -0.018, 0)	(1.205, 0, 0.031)
122	0.036	1.6	(1.205, 0, 0.031)	(1.205, 0.018, 0)
123	0.032	3.2	(1.205, 0.018, 0)	(1.237, 0.016, 0)
124	0.032	3.2	(1.205, -0.018, 0)	(1.237, -0.016, 0)
125	0.032	3.2	(1.205, 0, 0.031)	(1.237, 0, 0.028)
126	0.047	1.6	(1.205, -0.018, 0)	(1.237, 0.016, 0)
127	0.048	1.6	(1.205, 0, 0.031)	(1.237, -0.016, 0)
128	0.046	1.6	(1.205, 0.018, 0)	(1.237, 0, 0.028)
129	0.032	1.6	(1.237, 0.016, 0)	(1.237, -0.016, 0)
130	0.032	1.6	(1.237, -0.016, 0)	(1.237, 0, 0.028)
131	0.032	1.6	(1.237, 0, 0.028)	(1.237, 0.016, 0)
132	0.029	3.2	(1.237, 0.016, 0)	(1.265, 0.014, 0)
133	0.029	3.2	(1.237, -0.016, 0)	(1.265, -0.014, 0)
134	0.029	3.2	(1.237, 0, 0.028)	(1.265, 0, 0.025)
135	0.042	1.6	(1.237, 0.016, 0)	(1.265, -0.014, 0)
136	0.041	1.6	(1.237, -0.016, 0)	(1.265, 0, 0.025)
137	0.042	1.6	(1.237, 0, 0.028)	(1.265, 0.014, 0)
138	0.029	1.6	(1.265, 0.014, 0)	(1.265, -0.014, 0)
139	0.029	1.6	(1.265, -0.014, 0)	(1.265, 0, 0.025)

Table P.2 – Continued on next page

Table P.2 – Continued from previous page

Member	Length [m]	Diameter [mm]	Point 1 [m]	Point 2 [m]
140	0.029	1.6	(1.265, 0, 0.025)	(1.265, 0.014, 0)
141	0.025	3.2	(1.265, 0.014, 0)	(1.291, 0.013, 0)
142	0.025	3.2	(1.265, -0.014, 0)	(1.291, -0.013, 0)
143	0.025	3.2	(1.265, 0, 0.025)	(1.291, 0, 0.022)
144	0.037	1.6	(1.265, -0.014, 0)	(1.291, 0.013, 0)
145	0.038	1.6	(1.265, 0, 0.025)	(1.291, -0.013, 0)
146	0.036	1.6	(1.265, 0.014, 0)	(1.291, 0, 0.022)
147	0.025	1.6	(1.291, 0.013, 0)	(1.291, -0.013, 0)
148	0.025	1.6	(1.291, -0.013, 0)	(1.291, 0, 0.022)
149	0.025	1.6	(1.291, 0, 0.022)	(1.291, 0.013, 0)
150	0.023	3.2	(1.291, 0.013, 0)	(1.313, 0.011, 0)
151	0.023	1.6	(1.291, -0.013, 0)	(1.313, -0.011, 0)
152	0.023	1.6	(1.291, 0, 0.022)	(1.313, 0, 0.02)
153	0.033	1.6	(1.291, 0.013, 0)	(1.313, -0.011, 0)
154	0.032	1.6	(1.291, -0.013, 0)	(1.313, 0, 0.02)
155	0.033	1.6	(1.291, 0, 0.022)	(1.313, 0.011, 0)
156	0.023	1.6	(1.313, 0.011, 0)	(1.313, -0.011, 0)
157	0.023	1.6	(1.313, -0.011, 0)	(1.313, 0, 0.02)
158	0.023	1.6	(1.313, 0, 0.02)	(1.313, 0.011, 0)
159	0.02	1.6	(1.313, 0.011, 0)	(1.333, 0.01, 0)
160	0.02	1.6	(1.313, -0.011, 0)	(1.333, -0.01, 0)
161	0.02	1.6	(1.313, 0, 0.02)	(1.333, 0, 0.017)
162	0.029	1.6	(1.313, -0.011, 0)	(1.333, 0.01, 0)
163	0.03	1.6	(1.313, 0, 0.02)	(1.333, -0.01, 0)
164	0.029	1.6	(1.313, 0.011, 0)	(1.333, 0, 0.017)
165	0.02	1.6	(1.333, 0.01, 0)	(1.333, -0.01, 0)
166	0.02	1.6	(1.333, -0.01, 0)	(1.333, 0, 0.017)
167	0.02	1.6	(1.333, 0, 0.017)	(1.333, 0.01, 0)

Table P.2 – Continued on next page

Table P.2 – Concluded from previous page

Member	Length [m]	Diameter [mm]	Point 1 [m]	Point 2 [m]
168	0.018	1.6	(1.333, 0.01, 0)	(1.351, 0.009, 0)
169	0.018	1.6	(1.333, -0.01, 0)	(1.351, -0.009, 0)
170	0.018	1.6	(1.333, 0, 0.017)	(1.351, 0, 0.016)
171	0.026	1.6	(1.333, 0.01, 0)	(1.351, -0.009, 0)
172	0.026	1.6	(1.333, -0.01, 0)	(1.351, 0, 0.016)
173	0.027	1.6	(1.333, 0, 0.017)	(1.351, 0.009, 0)
174	0.018	1.6	(1.351, 0.009, 0)	(1.351, -0.009, 0)
175	0.018	1.6	(1.351, -0.009, 0)	(1.351, 0, 0.016)
176	0.018	1.6	(1.351, 0, 0.016)	(1.351, 0.009, 0)
177	0.016	1.6	(1.351, 0.009, 0)	(1.367, 0.008, 0)
178	0.016	1.6	(1.351, -0.009, 0)	(1.367, -0.008, 0)
179	0.016	1.6	(1.351, 0, 0.016)	(1.367, 0, 0.014)
180	0.023	1.6	(1.351, -0.009, 0)	(1.367, 0.008, 0)
181	0.024	1.6	(1.351, 0, 0.016)	(1.367, -0.008, 0)
182	0.023	1.6	(1.351, 0.009, 0)	(1.367, 0, 0.014)
183	0.016	1.6	(1.367, 0.008, 0)	(1.367, -0.008, 0)
184	0.016	1.6	(1.367, -0.008, 0)	(1.367, 0, 0.014)
185	0.016	1.6	(1.367, 0, 0.014)	(1.367, 0.008, 0)
186	0.128	1.6	(1.367, 0.008, 0)	(1.495, 0, 0)
187	0.128	1.6	(1.367, -0.008, 0)	(1.495, 0, 0)
188	0.129	1.6	(1.367, 0, 0.014)	(1.495, 0, 0)

Table P.2: Member Properties of the Optimized Truss

Appendix Q

Structural Analysis of the Hub

Q.1 Structural Analysis Methods and Standards

Stringent requirements were set on the rotary components. These components hold the blades the main component of interest, the laser illumination relies on optics within the rotary components. It is critical that vibrations and other deflections are minimized. The rotation of the rotary domain causes periodic loading and increases the probability of fatigue failure.

Abaqus was relied on heavily for much of the stress analysis. The license limits the number of nodes to a maximum of 10000. This makes it impossible to analyze all the rotary components impossible. As such determining the modes of vibrations and their frequency and the total deflection of the system is very difficult. The material chosen for many of the rotary components is steel. The material has excellent fatigue properties, however to avoid extensive fatigue analysis a stringent stress limit was chosen.

To avoid extensive fatigue and dynamic analysis a tight stress limit is chosen for all the components on the rotary domain. The yield strength for a mild steel is approximately 200 MPa, a safety factor of 10 is sufficiently high, hence 20 MPa is the maximum stress of these components.

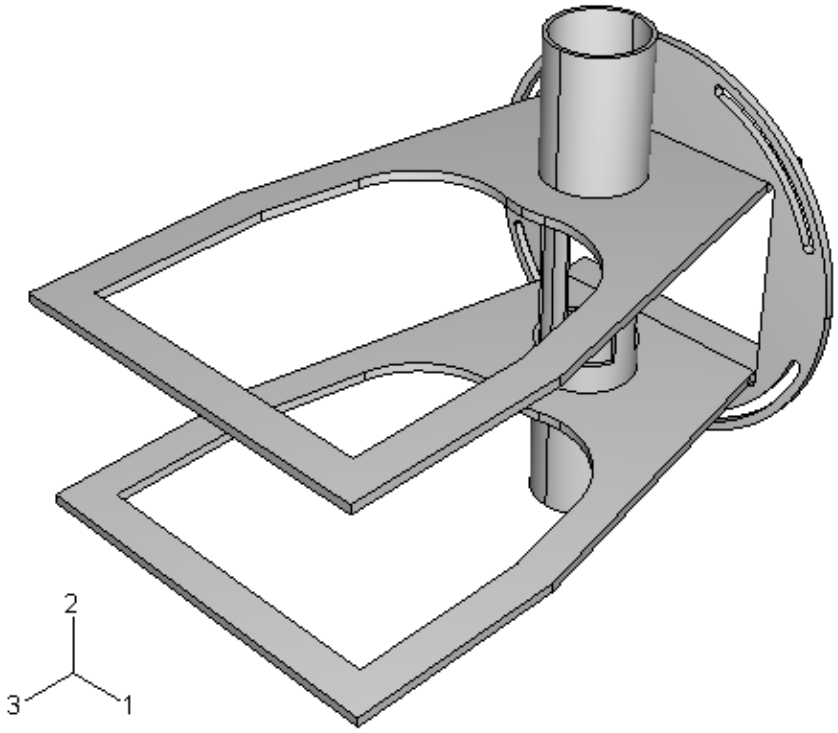

Figure Q.1: Geometry of the Front Frame Assembly

Q.2 Structural Analysis of the Front Frame Assembly

The front frame assemble is attached to the hub frame. It holds the blade and the data acquisition system. The part allows the blades to be pitched and allows access to the inside of the blade so the data acquisition system can sample any sensors in the blade. The stress of this assembly was determined with Abaqus version 6.5-1. The solid model used in the analysis is in figure Q.1.

The material for the frame is steel. The assumed properties are given in table Q.1.

Two load cases were considered for the model. The first where gravity acts in the positive 1 direction, the second where it acts in the positive 2 direction. The frame supports the blades and the data acquisition system. The weight of these components add forces, the blades add additional forces from rotation and aerodynamic loading.

Density $[kg/m^3]$	7800
Modulus of Elasticity $[Pa]$	$2 \cdot 10^{11}$
Poisson's Ratio	0.29

Table Q.1: Assumed Material Properties for Steel

The data acquisition system is housed in a frame to prevent it from moving around. This additional frame is heavy enough to be considered rigid, accordingly it was not modeled. The weight of these additional parts contribute to the weight forces from the data acquisition system. In total the mass of the additional frame and the data acquisition system is 10.16 kg, giving a weight of 99.66 N. These forces are distributed over 40 points at the far front end of the frame assembly.

The forces applied from the blades includes the weight but also the centrifugal and aerodynamic loads. The centrifugal loading was calculated assuming a mass of 10.2 kg per blade and a center of gravity of 0.55m from the axis of rotation. This is conservative since the actual center of gravity will be more inbound. The rotational rate used in the calculation is 33.45 radians per second. This resulted in a very high axial loading from the blades. The blades generate 1029.83 N and 142 Nm of torque, this and the weight of the blades act as a shear force on the blade mounts of the frame. The moment effect of the blade weight was ignored since it would be insignificant to the tensile loading. These forces were distributed over 60 points on the end of the blade mounts in the solid model. The distance between blade mounts is 0.326 m. The details of all forces applied in the model is given in table Q.2.

The front frame assembly is supported by the remainder of the hub assembly. This assembly connects through the slotted bolt holes. To simulate this support, the inside surface of the slots were constrained in all three directions.

Figure Q.2 and Q.3 shows the Von-Mises stress, of the front frame, for the first and second load cases respectively. The maximum stress is in the corner of the webbing between the two blade mounts. The maximum stress of both load cases is 52 MPa. A large component of this high stress is the tensile loading from the centrifugal forces in the blades. This loading causes the same stress in middle of the webbing, where it is approximately

Load Case	Gravity Along 1			Gravity Along 2		
Component	1 [N]	2 [N]	3 [N]	1 [N]	2 [N]	3 [N]
Data Acquisition	2.49	0.00	0.00	0.00	2.49	54.36
Left Blade	-5.52	-106.72	-8.58	-7.23	104.99	-8.58
Right Blade	8.95	106.72	-8.58	7.23	108.43	-8.58

Table Q.2: Forces applied in Front Frame Analysis

39 MPa. The further increase in stress from 39 MPa to 52 MPa would be a result of the stress concentration from the sharp corner.

The thickness of the material in the webbing in the model is 3.175 mm. In the design it has been increased to 6.35 mm. This should reduce the overall webbing stress to below 20 MPa. The design has been further altered to reduce the effect of the stress concentration. A filleted corner has replaced the sharp corners of the webbing. These design changes should be sufficient to reduce the stress in the front frame, thus it is considered acceptable.

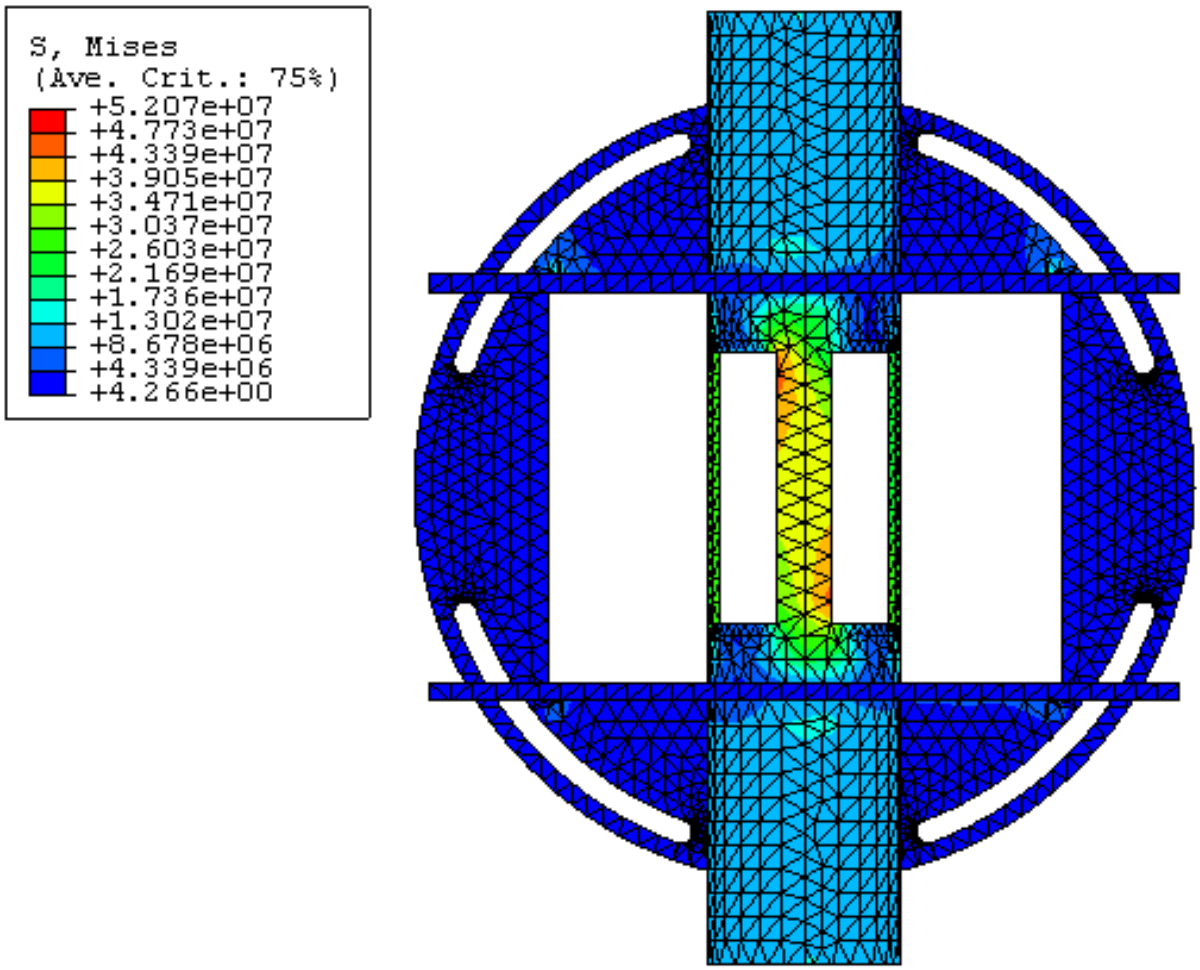

Figure Q.2: Front Frame Stress - Load Case 1

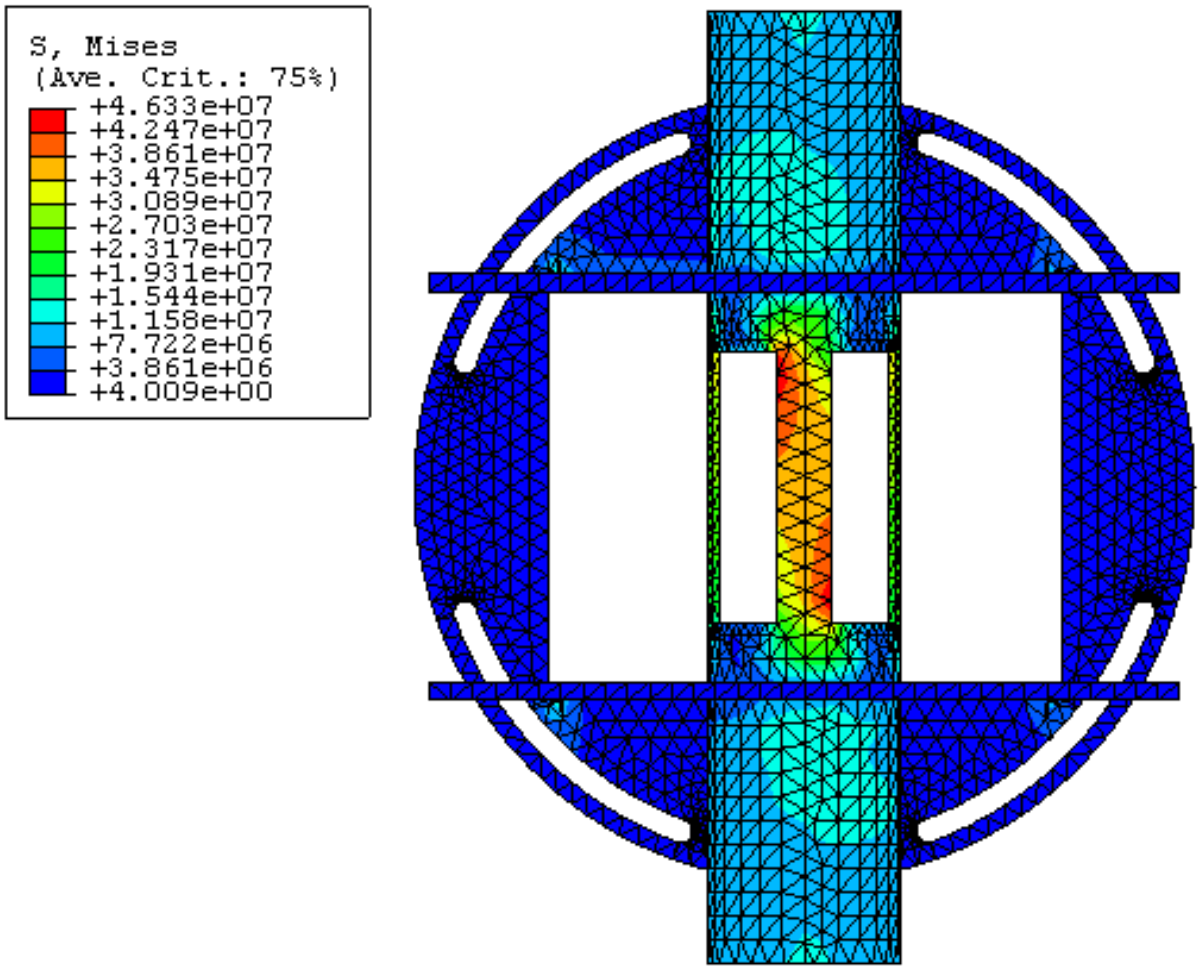

Figure Q.3: Front Frame Stress - Load Case 2

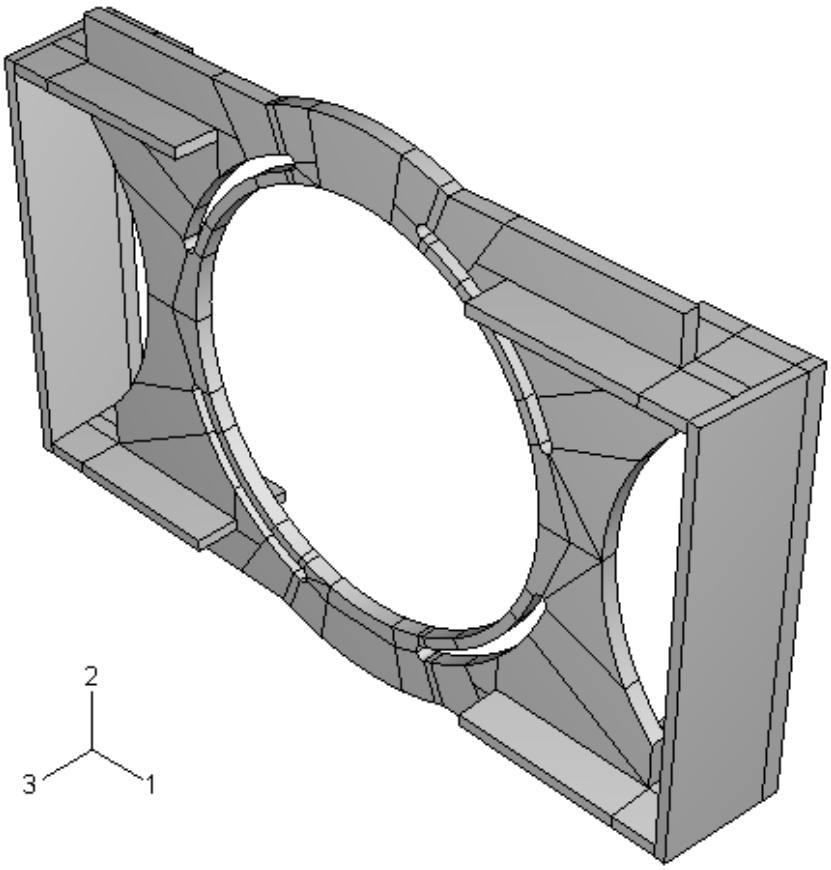

Figure Q.4: Geometry of the Front Plate Model

Q.3 Structural Analysis of Hub Frame Front Plate

The front plate of the hub frame connects the frame assembly that holds the blades and data acquisition system to the remainder of the hub. This part is designed to allow the blades to rotate about the axis of rotation so the camera can image different azimuth positions of the flow. The stress and strain in this component is analyzed in Abaqus version 6.5-1. The solid model used in the analysis is given in figure Q.4.

The material for the hub is steel, the assumed properties for the material are given in table Q.1.

Component	Mass $[kg]$	Moment Arm $[m]$
Front Plate	6.34	0.04
Hub Frame	13.41	0.20
Blades	21.00	0.32
Data Acquisition	2.00	0.93

Table Q.3: Mass and Moment Arms of Hub Components for Hub Plate

Component	Shear $[N]$	Moment $[Nm]$	Compression $[N]$	Torsion $[Nm]$
Solid Model	62.20	2.21	0.00	0.00
Front Frame	128.90	31.58	0.00	0.00
Blades	206.01	14.08	1029.83	142.00
Data Acquisition	19.62	7.03	0.00	0.00
Total	416.73	54.91	1029.83	142.00

Table Q.4: Overall Loading on the Hub Front Plate

Two load cases were considered for analysis. The first is where gravity is acting in the positive one direction, the second where it is acting in the positive two direction. The frame supports the front frame assembly, the blades and the data acquisition system. The weight of these components add a shear and moment to the part. The mass and moment arms of these components is given in table Q.3. The mass and moment arm of the solid model are included since the forces are applied on side that would support the weight of the solid model. Additional forces are a result of the aerodynamic loading, adding thrust and torsion loads. The resulting forces of all these components is given in table Q.4.

All the loads in table Q.4 are applied over four groups of points. These groups are located at the connections of the 4 forks of the hub frame to the solid model. At each group the loads are further distributed over 7 points. Each of the groups are 0.194m in the first direction and 0.113 in the second direction from the axis of rotation. Each of the groups are referred to by their location, where top is in the negative 1 direction and

Load Case	Gravity Along 1			Gravity Along 2		
Component	1 [N]	2 [N]	3 [N]	1 [N]	2 [N]	3 [N]
Bottom Left	3.56	19.47	26.69	-11.33	34.36	54.36
Bottom Right	26.21	19.47	26.67	11.33	34.36	19.42
Top Left	3.56	-19.47	46.87	-11.33	-4.59	54.13
Top Right	26.21	-19.47	46.87	11.33	-4.59	19.42

Table Q.5: Point Forces in the Front Plate Model

Load Case	Gravity Along 1			Gravity Along 2		
Component	1	2	3	1	2	3
Gravity $[m/s]$	9.81	0.00	0.00	0.00	9.81	0.00
Rotation $[rad/s]$	0.00	0.00	33.45	0.00	0.00	33.45

Table Q.6: Additional Loads Applied in the Front Plate Model

left is in the positive 2 direction. The magnitude of the point loads applied in the model are given in table Q.5. The effect of gravity is modeled as an overall acceleration and the effect of rotation is specified as an angular velocity. The details of these loading modes is given in table Q.6. The model was constrained in all directions on the inner surface of the slotted bolt connections for the front frame assembly.

The Von-Mises stress of the model is given in figures Q.5 and Q.6. The maximum stress in both load cases is below the 20 MPa limit. The design for the front plate is acceptable.

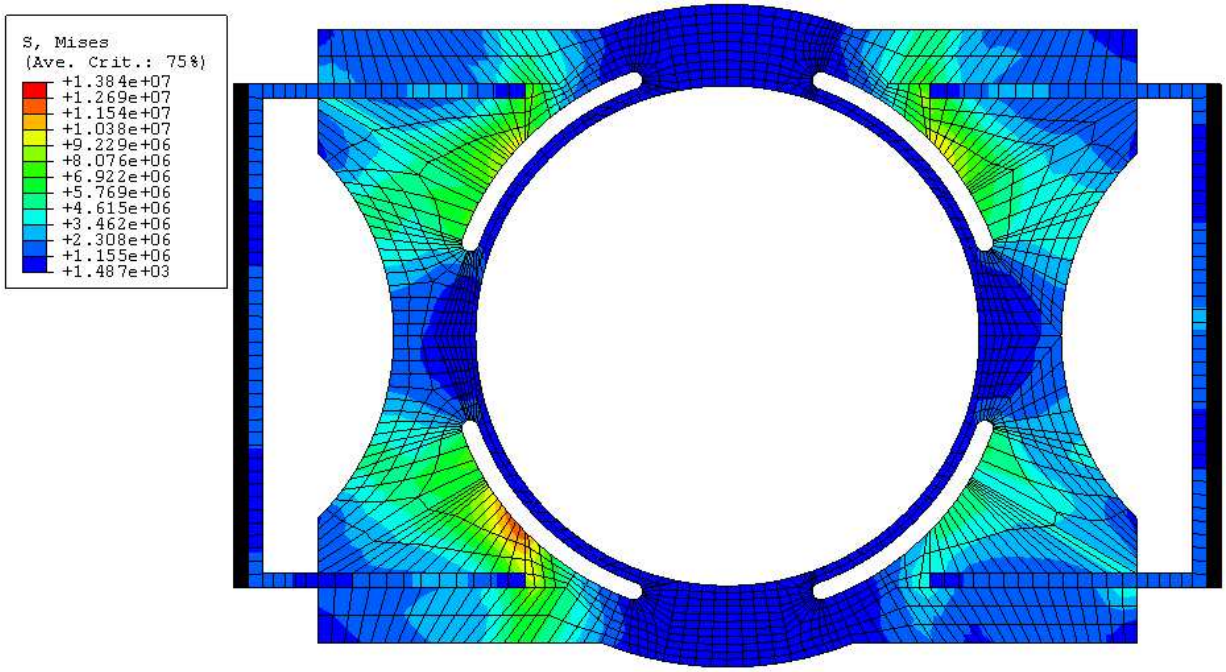

Figure Q.5: Front Plate Stress - Load Case 1

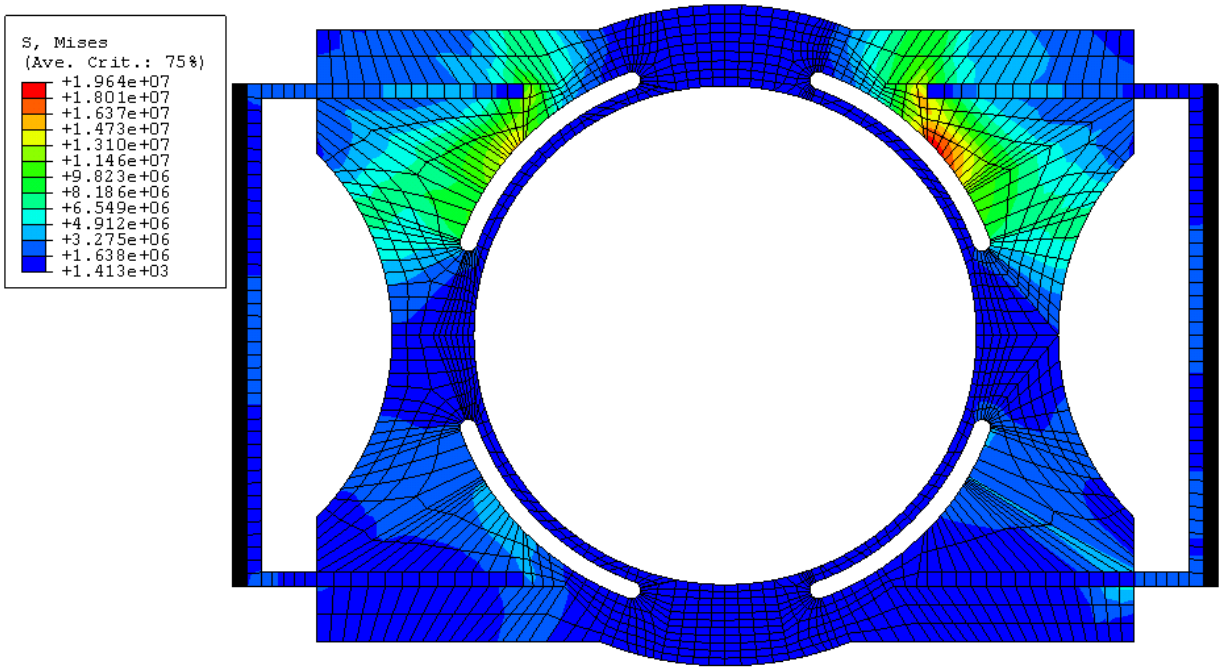

Figure Q.6: Front Plate Stress - Load Case 2

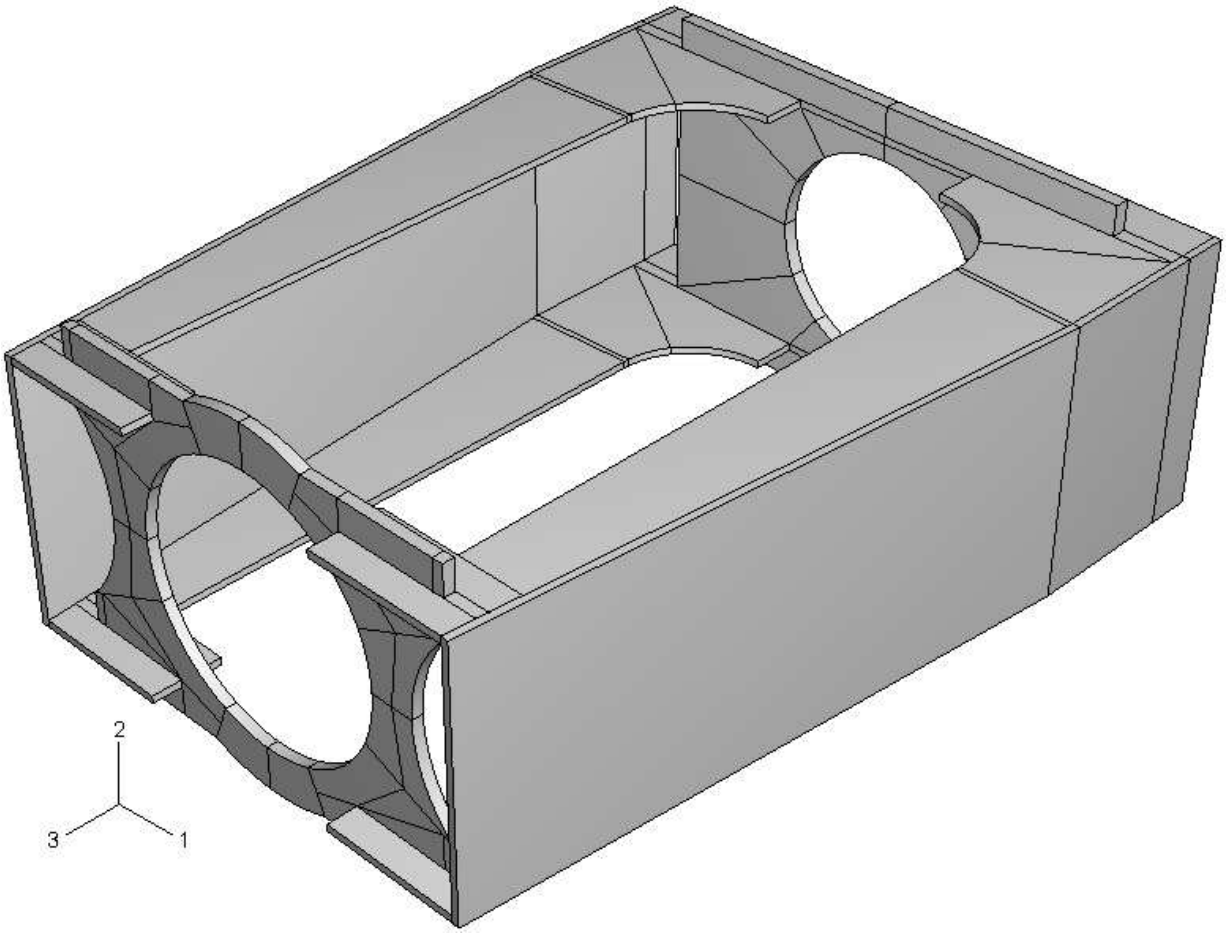

Figure Q.7: Geometry of the Hub Frame Model Solid

Q.4 Structural Analysis of the Hub Frame

The hub frame holds the camera gimbal the blades and the data acquisition system. It is the main structural element supporting all the components and transmitting the forces to the shaft. It is critical that there is minimal deflection and high fatigue resistance. The geometry of the hub was simplified to mesh within the node limits of the license available for Abaqus. The solid model used is given in figure Q.7.

Component	Mass $[kg]$	Moment Arm $[m]$
Hub Frame	13.41	0.20
Blades	21.00	0.32
Data Acquisition	2.00	0.93

Table Q.7: Mass and Moment Arms of Hub Components for Hub Plate

Component	Force $[N]$	Shear $[N]$	Moment $[Nm]$	Thrust $[N]$	Torque $[Nm]$
Hub Frame	0.00	128.90	26.20	0.00	0.00
Camera	160.39	0.00	0.00	0.00	0.00
Blades	0.00	206.01	14.08	1029.83	142.00
DAQ	0.00	19.62	6.21	0.00	0.00
Total	160.39	354.53	46.49	1029.83	142.00

Table Q.8: Overall Loading on the Hub Side Shaft Connection Plate

The material for the hub is steel, the assumed properties for the material are given in table Q.1.

Two load cases were considered for modeling the hub frame. The first is where gravity is acting in the positive 1 direction, the second where gravity is acting in the positive 2 direction. The hub frame in this model supports the camera gimbal between the forks and the components that make up the remaining frame assembly at the front. The weight of these components add point load forces along with shear and bending moment forces. Additional forces are a result of the aerodynamics of the blade. Here a thrust and a torque is generated from the blades. Finally the effect of gravity and rotation on the solid model itself. The mass and the moment arms of all the components front of the frame are given in table Q.7. The resulting forces of all the components are given in table Q.8

The forces of the camera were distributed over 8 points at the farthest forward extent of its axial translation track. This would represent a worst case situation. The other forces were distributed over four locations. At each of these locations the forces were further

Load Case	Gravity Along 1			Gravity Along 2		
Component	1 [N]	2 [N]	3 [N]	1 [N]	2 [N]	3 [N]
Top	22.1583	65.1615	-21.6943	0.0000	87.3199	64.3641
Bottom	22.1583	-65.1615	-107.0340	0.0000	-43.0032	-64.3641
Left	-43.0032	0.0000	-64.3641	-65.1615	22.1583	-21.6943
Right	87.3199	0.0000	-64.3641	65.1615	22.1583	-107.0340
Camera	20.0492	0.0000	0.0000	0.0000	20.0492	0.0000

Table Q.9: Point Forces in the Hub Side Shaft Connection

Load Case	Gravity Along 1			Gravity Along 2		
Component	1	2	3	1	2	3
Gravity $[m/s]$	9.81	0.00	0.00	0.00	9.81	0.00
Rotation $[rad/s]$	0.00	0.00	33.45	0.00	0.00	33.45

Table Q.10: Additional Loads Applied in the Hub Side Shaft Connection

distributed over 4 points. The four location are about the circular cavity at the front plate of the frame. The locations are referred by their location, top is the region in the negative 1 direction while left is in the negative 2 direction. The respective opposite directions hold for the bottom and right locations. The point loads applied at each of these locations for each load case is given in table Q.9. The details of how gravitational and rotational effects were modeled are in table Q.10. The frame is anchored by the shaft, at the rear mounting plate the inside surface of the circular cavity was constrained in all directions.

Figures Q.8 and Q.9 show the resulting Von-Mises stress of the hub frame. Overall the stress in all the components is below the maximum. There is one location where the stress is greater, that is on the rear plate at the end of the fork. This is a result of a stress concentration. Further detailed modeling has been performed on this region to deal with this issue. Overall the frame is acceptable.

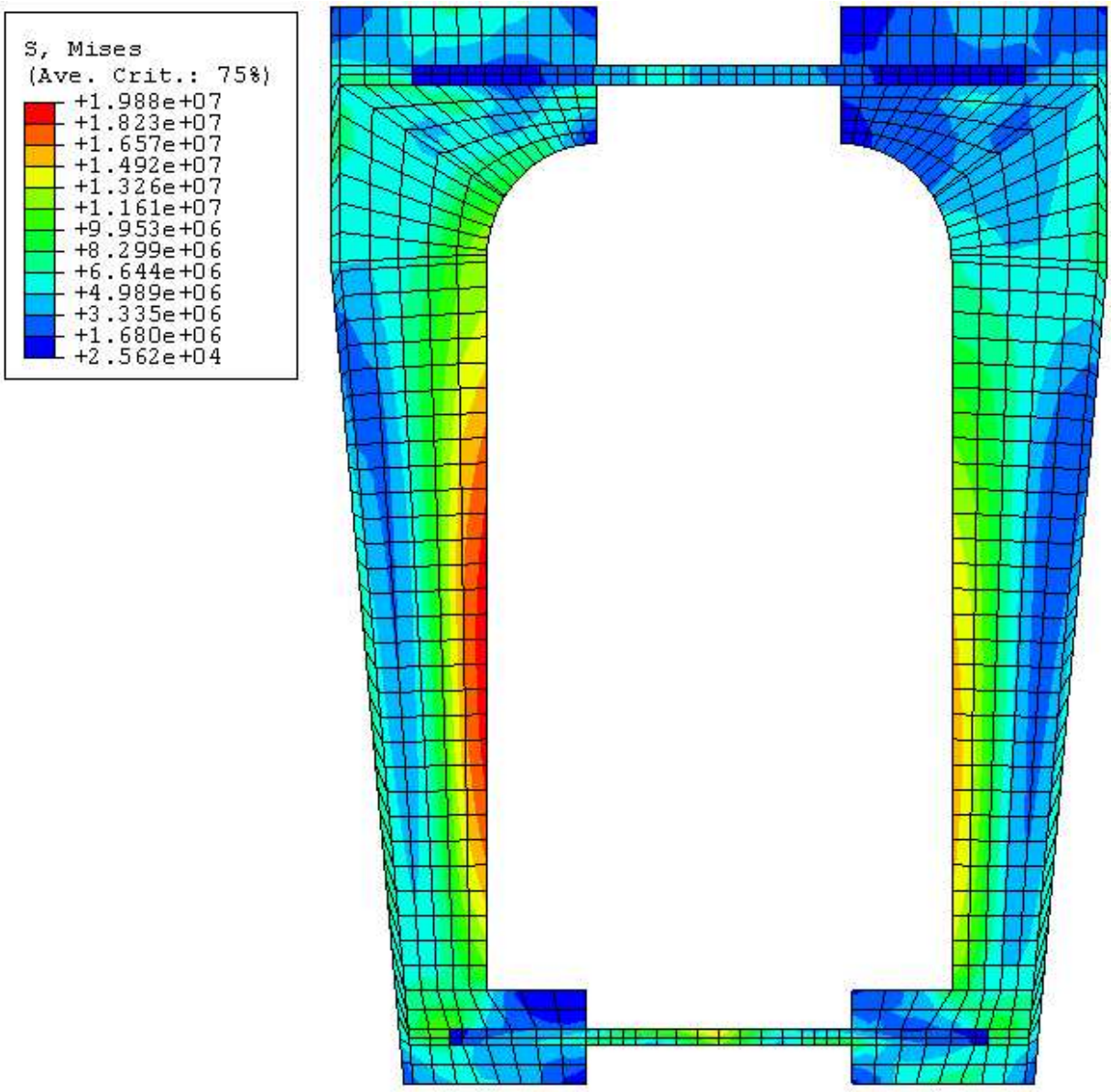

(a) 1-3 Plane

Figure Q.8: Hub Frame Stress - Load Case 1

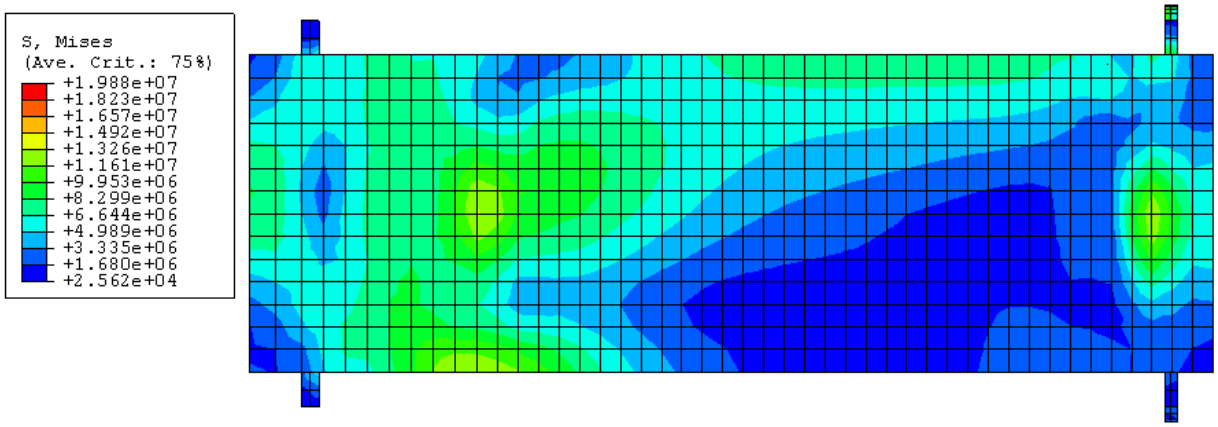

(b) 2-3 Plane

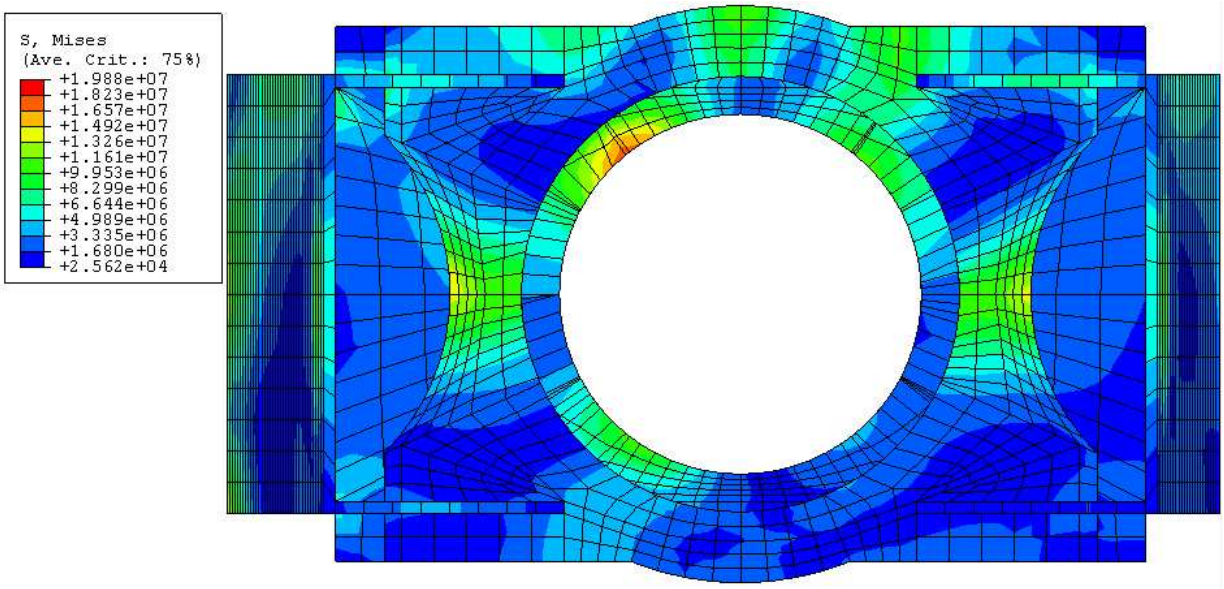

(c) Front

Figure Q.8: Hub Frame Stress - Load Case 1 - Continued

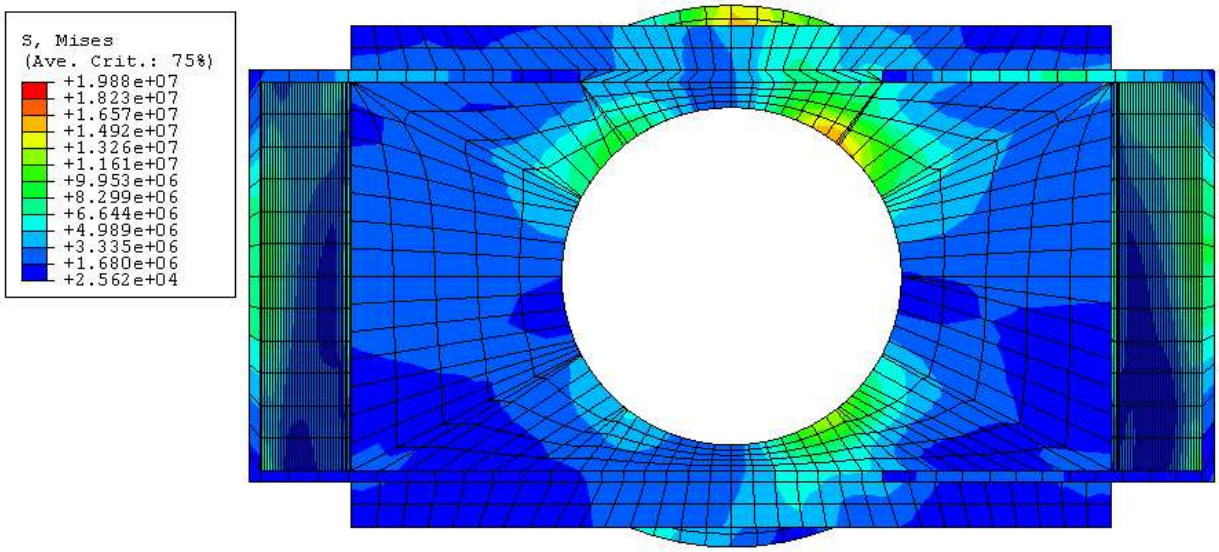

(d) Rear

Figure Q.8: Hub Frame Stress - Load Case 1 - Continued

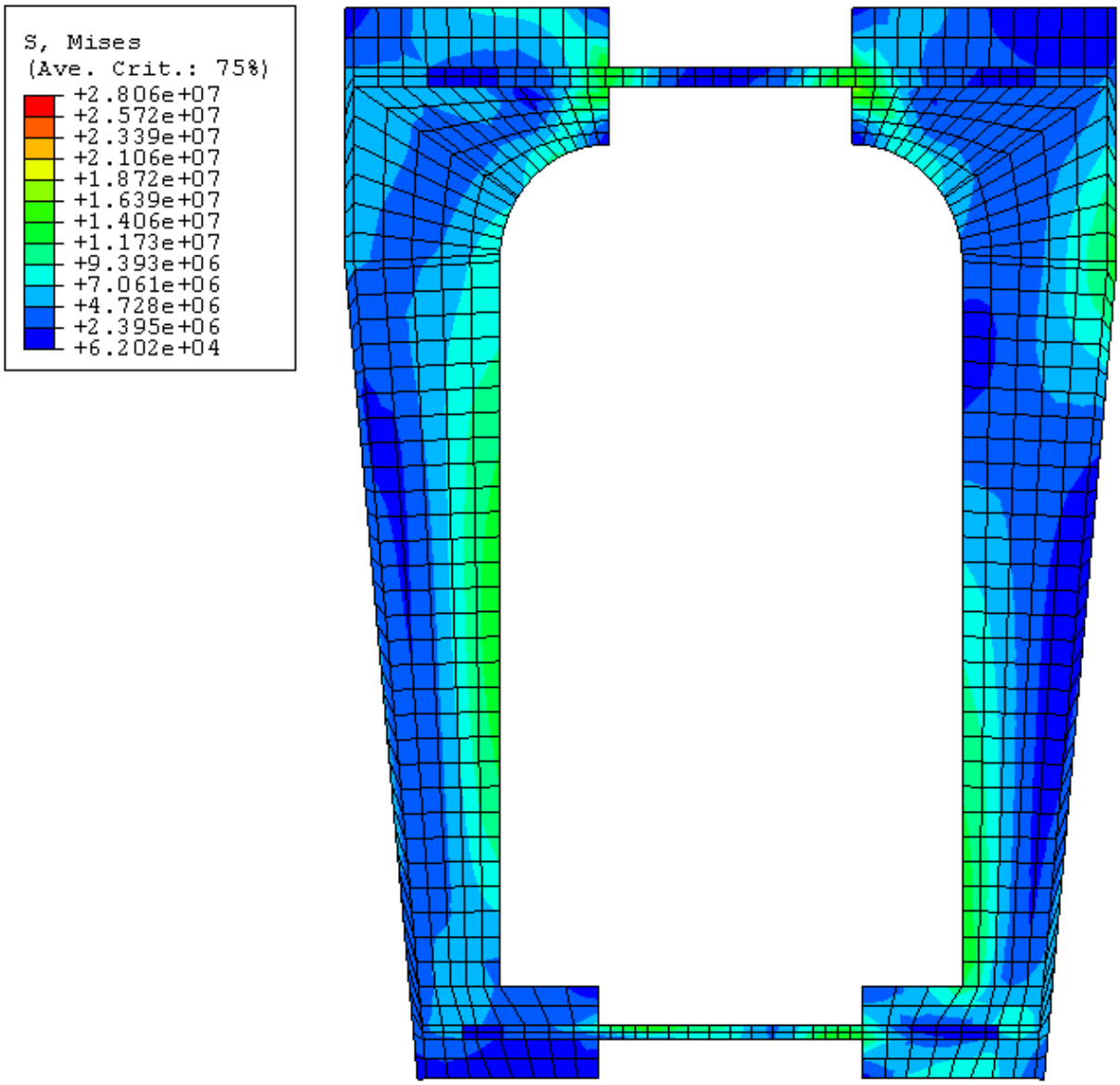

(a) 1-3 Plane

Figure Q.9: Hub Frame Stress - Load Case 2

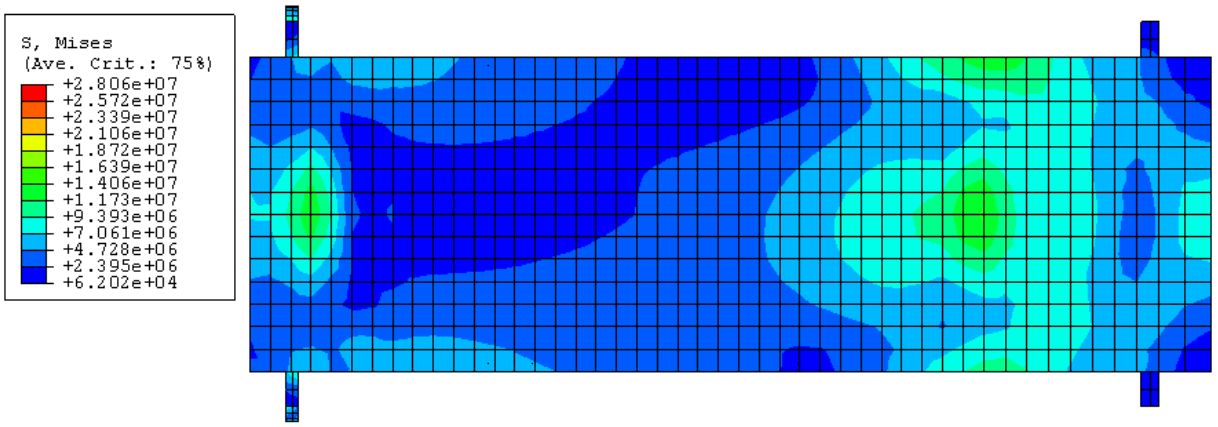

(b) 2-3 Plane

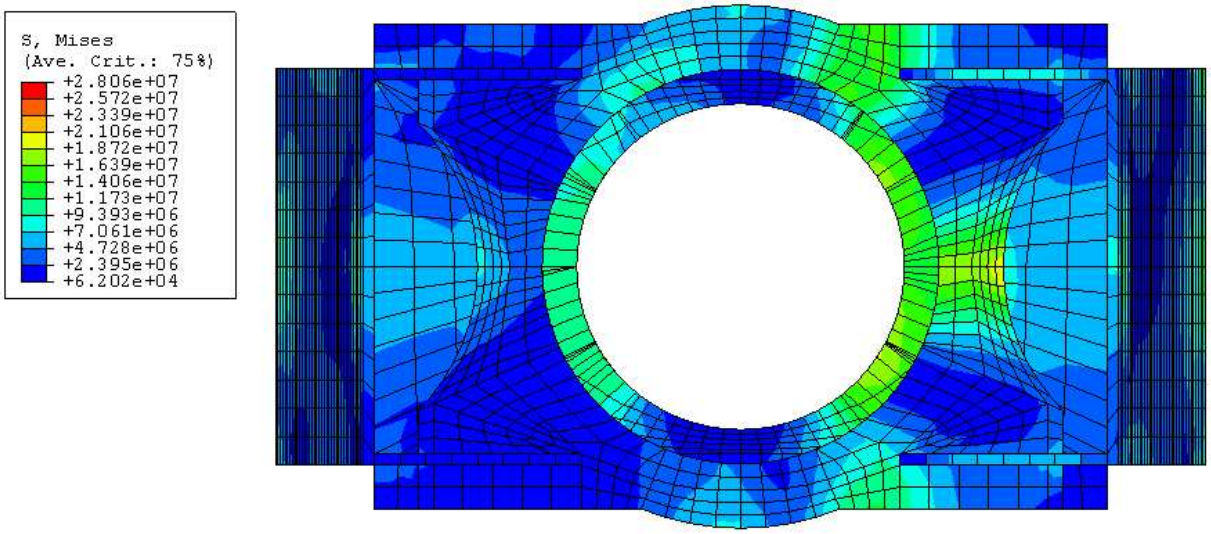

(c) Front

Figure Q.9: Hub Frame Stress - Load Case 2 - Continued

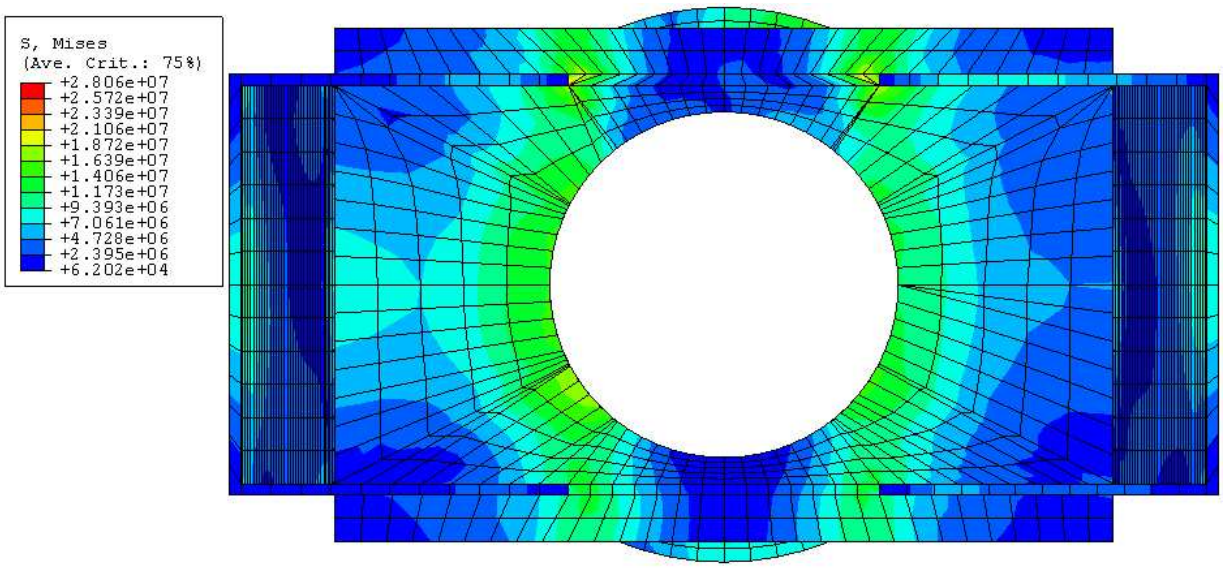

(d) Rear

Figure Q.9: Hub Frame Stress - Load Case 2 - Continued

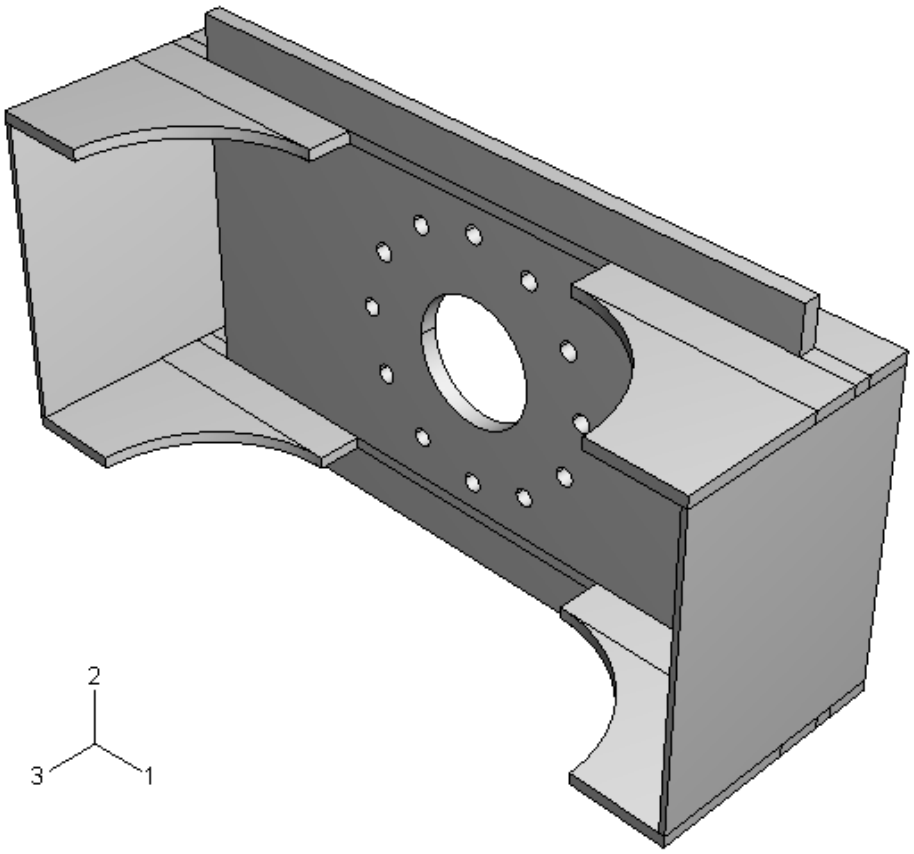

Figure Q.10: Geometry of the Hub Side, Hub Shaft Connection, FEM Model

Q.5 Structural Analysis of Hub Frame Connection to the Shaft

The connection between the shaft and the hub, on the hub side, was modeled in Abaqus. The simulations tested whether the bolt pattern was sufficiently strong enough, and the effect of the fork connection length. Figure Q.10 shows the geometry modeled.

The material for the part is steel. The assumed properties for the model are given in table Q.1.

Component	Mass $[kg]$	Moment Arm $[m]$
Hub Frame	36.99	0.51
Camera Assembly	16.35	0.47
Blades	21.00	0.68
Data Acquisition	2.00	0.93

Table Q.11: Mass and Moment Arms of Hub Components for Hub Plate

Component	Shear $[N]$	Moment $[Nm]$	Compression $[N]$	Torsion $[Nm]$
Hub Frame	362.84	184.25	0.00	0.00
Camera Assembly	160.39	75.48	0.00	0.00
Blades	206.01	140.02	1029.83	142.00
Data Acquisition	19.62	18.21	0.00	0.00
Total	748.87	417.97	1029.83	142.00

Table Q.12: Overall Loading on the Hub Side Shaft Connection Plate

Two load cases were considered for the connection plate. The first case is where gravity is acting in the positive one direction and the second case acting in the positive 2 direction. The plate is supporting all the components forward of the plate. Under gravity these components exert and a shear and moment. The mass of the components and their moment arms is given in table Q.11. The datum for the moment arms is the partition plane farthest in the positive third direction. The rotor generates axial and torsion forces aerodynamically. The resulting forces of the blade and other components are given in table Q.12.

The loads in table Q.12 were distributed over several points on the partition plane. The points of applied forces were grouped about one of four locations. The same forces were applied to all the points within a group. Within each group there were 5 points. Each grouping was located at the corners of the partition plane. The groupings are identified by what corner they were located on. Left is considered the negative 2 direction, while bottom is the positive 1 direction, right and top are opposite. Each grouping was approximately

Load Case	Gravity Along 1			Gravity Along 2		
Component	1 [N]	2 [N]	3 [N]	1 [N]	2 [N]	3 [N]
Bottom Left	23.68	-30.37	159.58	-13.77	7.08	186.94
Bottom Right	51.21	-30.37	159.58	13.77	7.08	-289.92
Top Left	23.68	30.37	56.59	-13.77	67.81	186.94
Top Right	51.21	30.37	56.59	13.77	67.81	289.92

Table Q.13: Point Forces in the Hub Side Shaft Connection

Load Case	Gravity Along 1			Gravity Along 2		
Component	1	2	3	1	2	3
Gravity $[m/s]$	9.81	0.00	0.00	0.00	9.81	0.00
Rotation $[rad/s]$	0.00	0.00	33.45	0.00	0.00	33.45

Table Q.14: Additional Loads Applied in the Hub Side Shaft Connection

0.193m in the first direction, and 0.088m in the second direction, from the axis of rotation. The forces applied at each grouping is given in table Q.13. There are additional loading from gravity and rotation, the details of which are given in table Q.14. The model is constrained in all three directions at all point about the bolt holes in the mounting plate.

The forks are the plates perpendicular to the mounting plate holding it in place. The forks could reinforce the mounting plate or add stress concentrations. Several different fork lengths were explored to determine what effect was dominant. The results showed that the stress concentration effect was more dominant than the reinforcing effect. As such the model with the shorter forks was the strongest.

The Von Mises stress results for the model with the shortest forks is given in figures Q.11 and Q.12. The results show that the stress in the plate exceeds the acceptable maximum. The thickness of the mounting plate in the model is 9.525 mm, to reduce the stress the thickness has been increased to 12.7mm. The number of bolts used to mount the plate has been increased from 12 to 16 to distribute the load better and reduce stress concentrations.

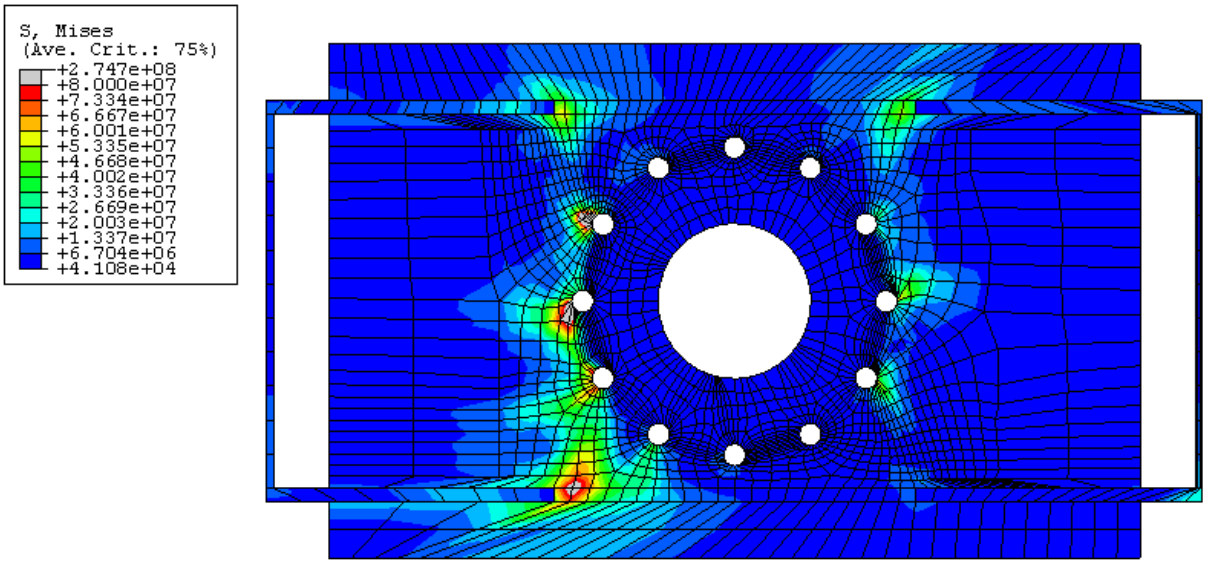

Figure Q.11: Hub Side Shaft Mounting Plate Stress, Load Case 1

The stress about the bolt holes should be further reduced since the washers on the bolts will distribute the load. Also the plate is mounted against a highly reinforced plate, this will distribute the forces even more. The stress concentrations near the forks will be eliminated by using filleted connectors that will distribute the load 25.4mm out from the forks.

Ignoring the stress concentrations the overall stress through the plate is approaching 40 MPa. Thickening it to 12.7mm should decrease the stress to 30 MPa. The load distribution should further reduce the stress even further. A second model is needed to confirm whether these changes will reduce the peak stress to acceptable levels.

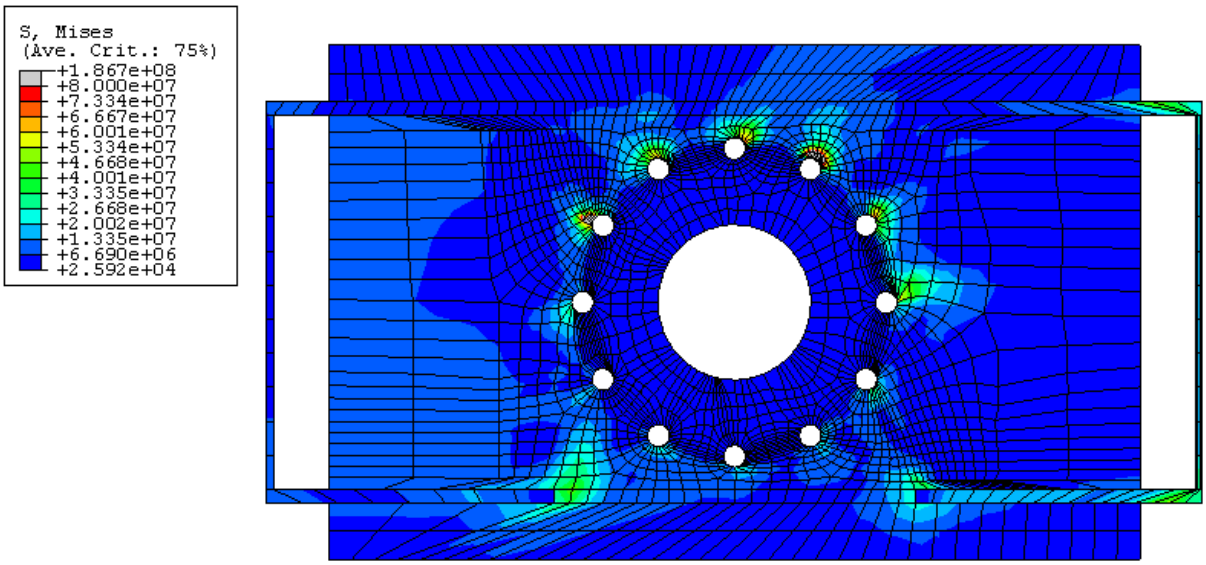

Figure Q.12: Hub Side Shaft Mounting Plate Stress, Load Case 2

Component	Mass $[kg]$	Moment Arm $[m]$
Hub Frame	75.41	0.35
Camera Assembly	18.39	0.52
Blades	21.00	0.71
Data Acquisition	2.00	0.95

Table Q.15: Mass and Moment Arms of Hub Components for Connection Plate Model

Q.6 Structural Analysis of Shaft Connection Plate

The plate that connects the hub to the shaft has been modeled and the results have shown that there is a lot of stress concentrations increasing the stress to unacceptable levels. The design was changed to reduce the stress. The first model was simplified and showed many potential stress concentrations. There is uncertainty in whether the stress concentrations are physical or from the simplifications. A second model was built just to test the stress in the plate alone to confirm the actual stress in the plate.

The complete geometry of the plate was used to build the model. Some modifications were made to simplify the meshing. All the holes were replaced with octagons of equal area. The octagon and the circle are very close in shape so this modification should have a minor effect. The solid model geometry used is shown in figure Q.13.

The material for the part was steel, the assumed properties are given in table Q.1.

The part connects directly to the shaft through a circular bolt pattern. The rest of the hub connects through a more complicated bolt pattern. Given that the stress through a cantilevered beam is well understood it is easier to specify the forces on the connections to the shaft. Majority of the forces are from the weight of the components and the shear and bending moments therein. The shaft supports the weight of the hub and the part of interest. Thus these forces were determined including the weight of the part in question. The resulting reaction was applied to the plate on the connection to the shaft. The mass and moment arms for the various components are given in table Q.15. The blades add aerodynamic loading as thrust and torsion. The resulting loads are given in table Q.16.

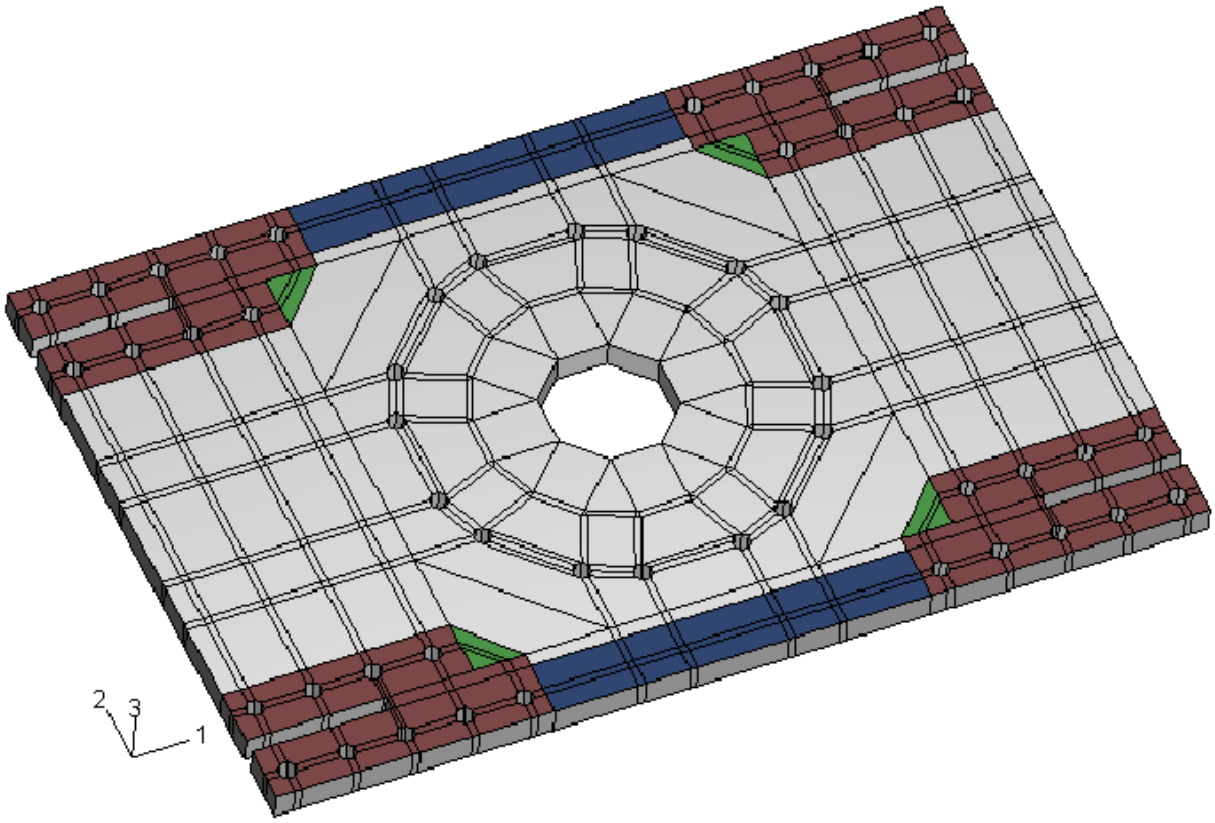

Figure Q.13: Solid Model Geometry for the Shaft Connection Plate

Component	Shear $[N]$	Moment $[Nm]$	Compression $[N]$	Torsion $[Nm]$
Hub Frame	739.77	260.54	0.00	0.00
Camera Assembly	180.44	94.29	0.00	0.00
Blades	206.01	145.36	1029.83	142.00
Data Acquisition	19.62	18.66	0.00	0.00
Total	1145.84	518.85	1029.83	142.00

Table Q.16: Overall Loading on the Shaft

Point	Axis 1 [mm]	Axis 2 [mm]
1	-87.177	-22.364
2	-77.457	-45.830
3	-45.830	-77.457
4	-22.364	-87.177
5	22.364	-87.177
6	45.830	-77.457
7	77.457	-45.830
8	87.177	-22.364
9	87.177	22.364
10	77.457	45.830
11	45.830	77.457
12	22.364	87.177
13	-22.364	87.177
14	-45.830	77.457
15	-77.457	45.830
16	-87.177	22.364

Table Q.17: Location of Bolt Holes in Rear Plate Analysis

To load cases were considered. The first is where gravity is acting in the positive 1 direction, the second where it acts in the positive 2 direction. The solid model for each load case was different due to the differences in symmetry. The forces were applied about 8 bolt holes, the loads were further distributed about 16 points for each hole. The locations of those bolt holes in the 1-2 plane are given in table Q.17. The loads applied at the locations are given in table Q.18. There is additional loading from gravity and the rotation, the details of this loading is given in table Q.19.

The boundary conditions are defined by how the plate connects with the hub. The bolt holes constrain the plate in the first and second direction. About the bolts the plate is held between a set of angle brackets that constrain the plate in the third direction. These

Load Case	Gravity along 1			Gravity along 2		
Component	1 [N]	2 [N]	3 [N]	1 [N]	2 [N]	3 [N]
Point 1	-6.00742	5.96989	-39.60333	-1.53149	1.49396	15.21440
Point 2	-7.61437	5.30427	-34.73914	-3.13844	0.82834	26.95752
Point 3	-9.78019	3.13844	-18.91200	-5.30427	-1.33748	42.78466
Point 4	-10.44582	1.53149	-7.16888	-5.96989	-2.94444	47.64885
Point 5	-10.44582	-1.53149	15.21440	-5.96989	-6.00742	47.64885
Point 6	-9.78019	-3.13844	26.95752	-5.30427	-7.61437	42.78466
Point 7	-7.61437	-5.30427	42.78466	-3.13844	-9.78019	26.95752
Point 8	-6.00742	-5.96989	47.64885	-1.53149	-10.44582	15.21440
Point 9	-2.94444	-5.96989	47.64885	1.53149	-10.44582	-7.16888
Point 10	-1.33748	-5.30427	42.78466	3.13844	-9.78019	-18.91200
Point 11	0.82834	-3.13844	26.95752	5.30427	-7.61437	-34.73914
Point 12	1.49396	-1.53149	15.21440	5.96989	-6.00742	-39.60333
Point 13	1.49396	1.53149	-7.16888	5.96989	-2.94444	-39.60333
Point 14	0.82834	3.13844	-18.91200	5.30427	-1.33748	-34.73914
Point 15	-1.33748	5.30427	-34.73914	3.13844	0.82834	-18.91200
Point 16	-2.94444	5.96989	-39.60333	1.53149	1.49396	-7.16888

Table Q.18: Point Loads in the Rear Plate Analysis

Load Case	Gravity Along 1			Gravity Along 2		
Component	1	2	3	1	2	3
Gravity $[m/s]$	9.81	0.00	0.00	0.00	9.81	0.00
Rotation $[rad/s]$	0.00	0.00	33.45	0.00	0.00	33.45

Table Q.19: Additional Loads Applied in the Rear Plate Analysis

brackets could be formed in various shapes to provide a range of different supports. Three different supports were considered in this model. The color tinting in Q.13 shows where the brackets could support the plate. The red tint is a base case, in all cases the brackets provided support in this area. The second case extends the support to the green region, this case is referred to as angle support. The final case supports the plate in all the colored regions, this case is referred to as the full support case.

Figures Q.14 and Q.15 show the Von-Mises stress in the plate for load case 1 and 2 respectively. In all cases the stress is below 20 MPa. Angle support is stronger than the base support, it has a peak stress of 15.4 MPa, where the base support has a peak stress of 16.5 MPa. Full support has the lowest peak stress of 12.3 MPa, however the full support brackets will interfere with the laser optics boom. The angle support is the best compromise of minimal stress and minimal interference. With this support the greatest stress in the connection plate is 15.4 MPa. The increase thickness and additional bolts recommended in section Q.5 will bring stress down to acceptable levels.

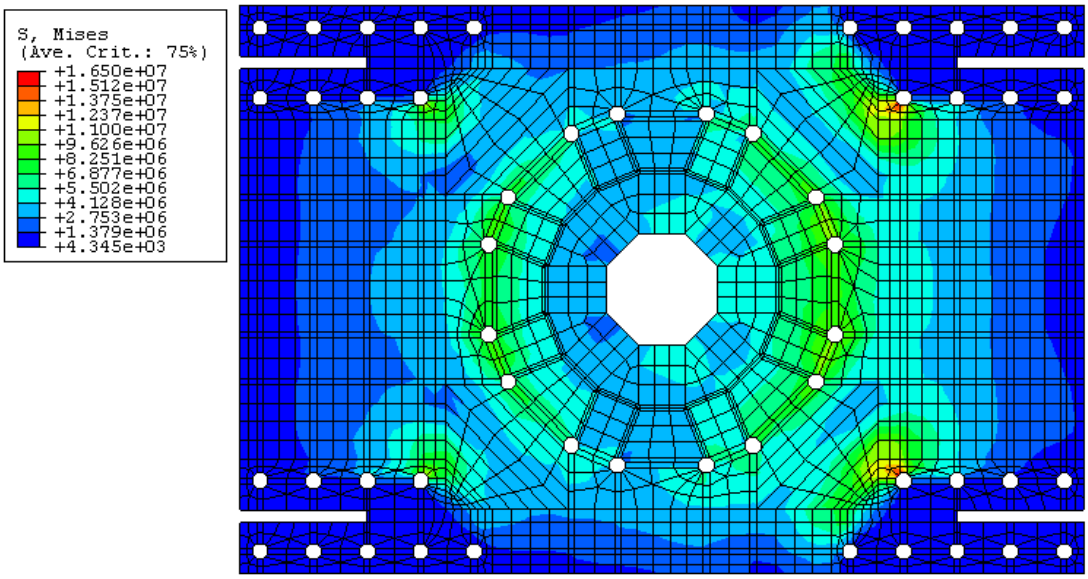

(a) Base Support

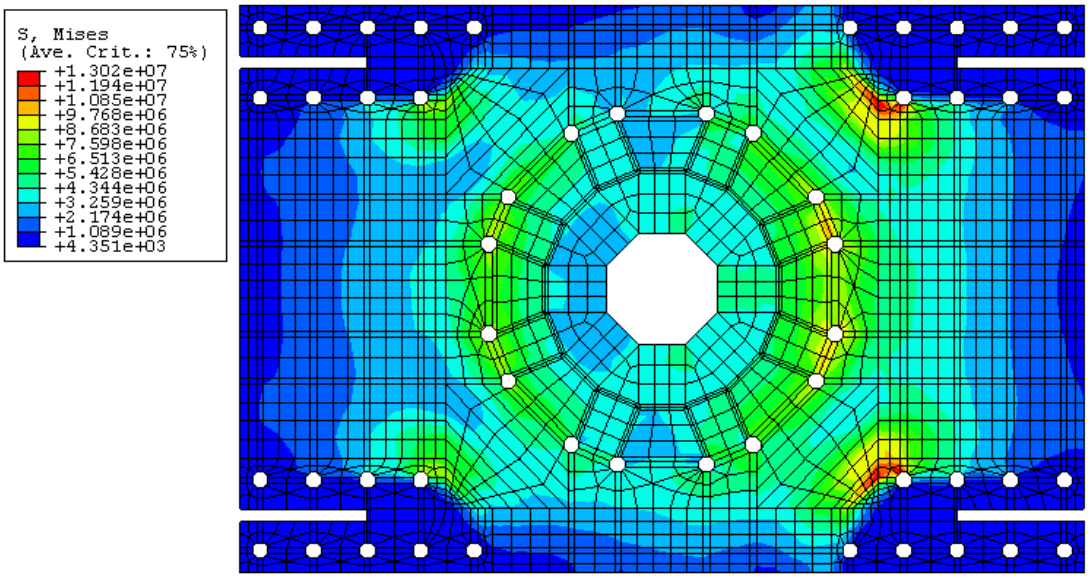

(b) Angle Support

Figure Q.14: Hub Shaft Connection Plate Stress - Load Case 1

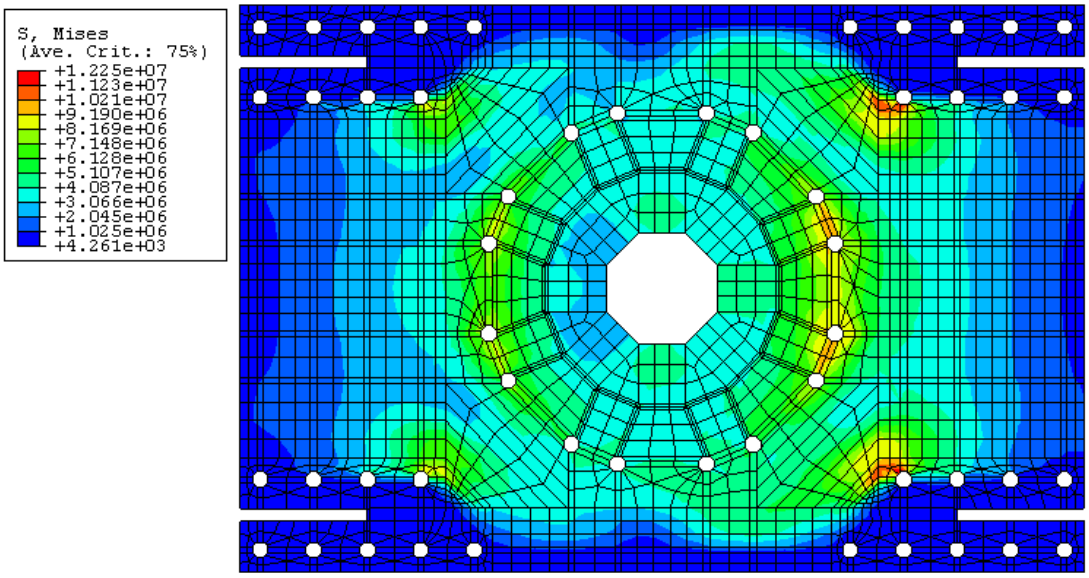

(c) Full Support

Figure Q.14: Hub Shaft Connection Plate Stress - Load Case 1 - Continued

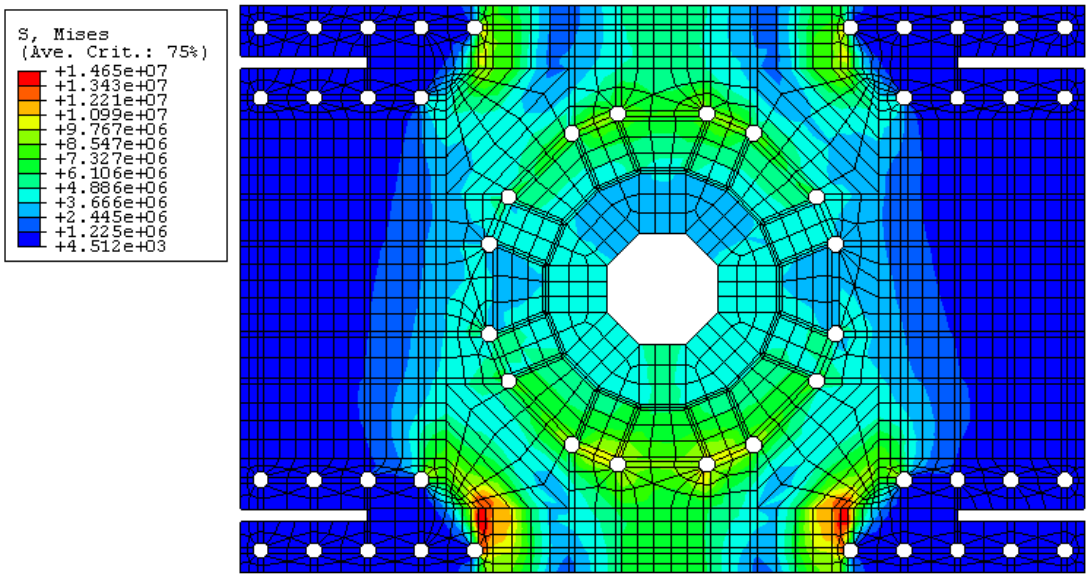

(a) Base Support

Figure Q.15: Hub Shaft Connection Plate Stress - Load Case 2

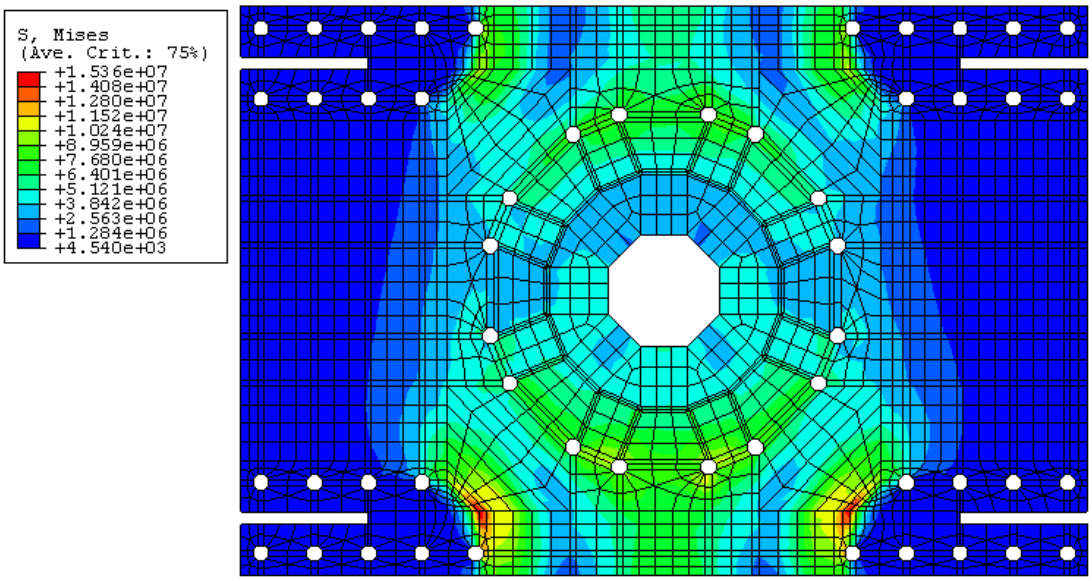

(b) Angle Support

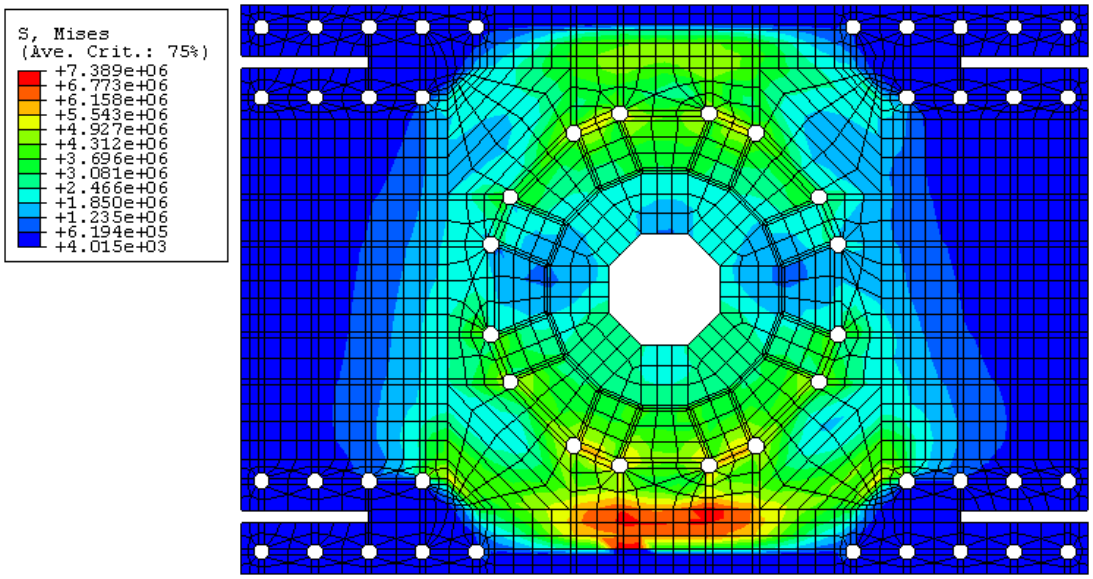

(c) Full Support

Figure Q.15: Hub Shaft Connection Plate Stress - Load Case 2 - Continued

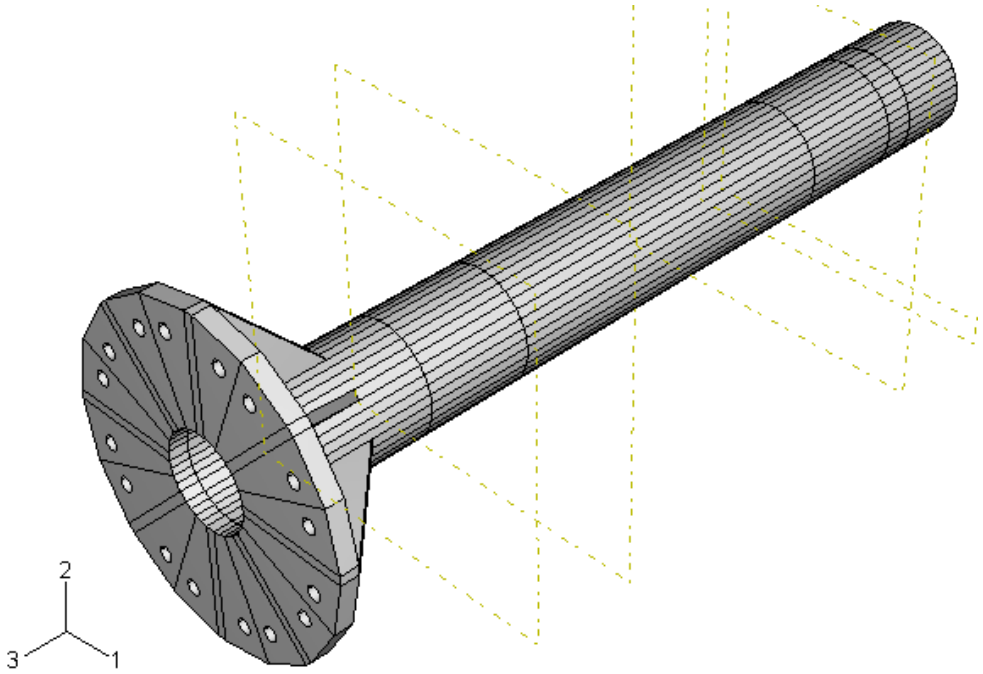

Figure Q.16: Geometry of the Shaft Side Hub Shaft Connection FEM Model

Q.7 Structural Analysis of Shaft Connection

The connection between the shaft and the hub, on the shaft side, was tested using Abaqus. Limitations with the license prevented analysis of the entire shaft with a sufficiently fine mesh. Instead the mesh about the flanges and the connection plate was fine, while else where it was course. A second FEM model was built to analyze the remainder of the shaft. Figure Q.16 shows the geometry used in the FEM model.

The material for the shaft is steel. The assumed properties for the model are given in table Q.1.

The model is close to being axis-symmetric. Hence only one load case was considered. There is loading from its own mass and the rotation. Also the shaft support the hub assembly. The weight of these parts exert a shear and bending moment load on the end of the shaft. The mass and moment arms of the components within the hub assembly is given in table Q.15. The datum for the moment arm is the end of the shaft where the hub

Point	Axis 1 [mm]	Axis 2 [mm]
1	-87.177	101.886
2	-77.457	78.420
3	-45.830	46.793
4	-22.364	37.073
5	22.364	37.073
6	45.830	46.793
7	77.457	78.420
8	87.177	101.886
9	87.177	146.614
10	77.457	170.080
11	45.830	201.707
12	22.364	211.427
13	-22.364	211.427
14	-45.830	201.707
15	-77.457	170.080
16	-87.177	146.614

Table Q.20: Location of Bolt Holes in Shaft Analysis

assembly connects. The blades generate an aerodynamic loading, there is a thrust force that acts in compression on the shaft and a torque that acts in torsion on the shaft. The resulting forces of all the components is given in table Q.16.

The loads in table Q.16 were applied at the 16 bolt holes at the mounting plate. The locations of the bolt holes in the 1-2 plane are given in table Q.20. At each hole the loads were distributed over 64 points. The loads applied at these points is given in table Q.21. The details of the gravitational loading and the rotation loading is given in table Q.22.

Shear and bending moments are taken up by the bearings by constraining the surfaces held by the bearings perpendicular to the surface. The torsion loading is taken up by the sprocket by constraining the surface holding the sprocket parallel to the surface. The

Component	1 [N]	2 [N]	3 [N]
Hole 1	0.736109	1.492470	9.900830
Hole 2	0.334371	1.326070	8.684790
Hole 3	-0.207085	0.784611	4.728000
Hole 4	-0.373491	0.382872	1.792220
Hole 5	-0.373491	-0.382872	-3.803600
Hole 6	-0.207085	-0.784611	-6.739380
Hole 7	0.334371	-1.326070	-10.696200
Hole 8	0.736109	-1.492470	-11.912200
Hole 9	1.501850	-1.492470	-11.912200
Hole 10	1.903590	-1.326070	-10.696200
Hole 11	2.445050	-0.784611	-6.739380
Hole 12	2.611450	-0.382872	-3.803600
Hole 13	2.611450	0.382872	1.792220
Hole 14	2.445050	0.784611	4.728000
Hole 15	1.903590	1.326070	8.684790
Hole 16	1.501850	1.492470	9.900830

Table Q.21: Point Loads in the Simple Shaft Analysis

Component	1	2	3
Gravity $[m/s]$	9.810	0.000	0.000
Rotation $[rad/s]$	0.000	0.000	33.450

Table Q.22: Additional Loads Applied in the Simple Shaft Analysis

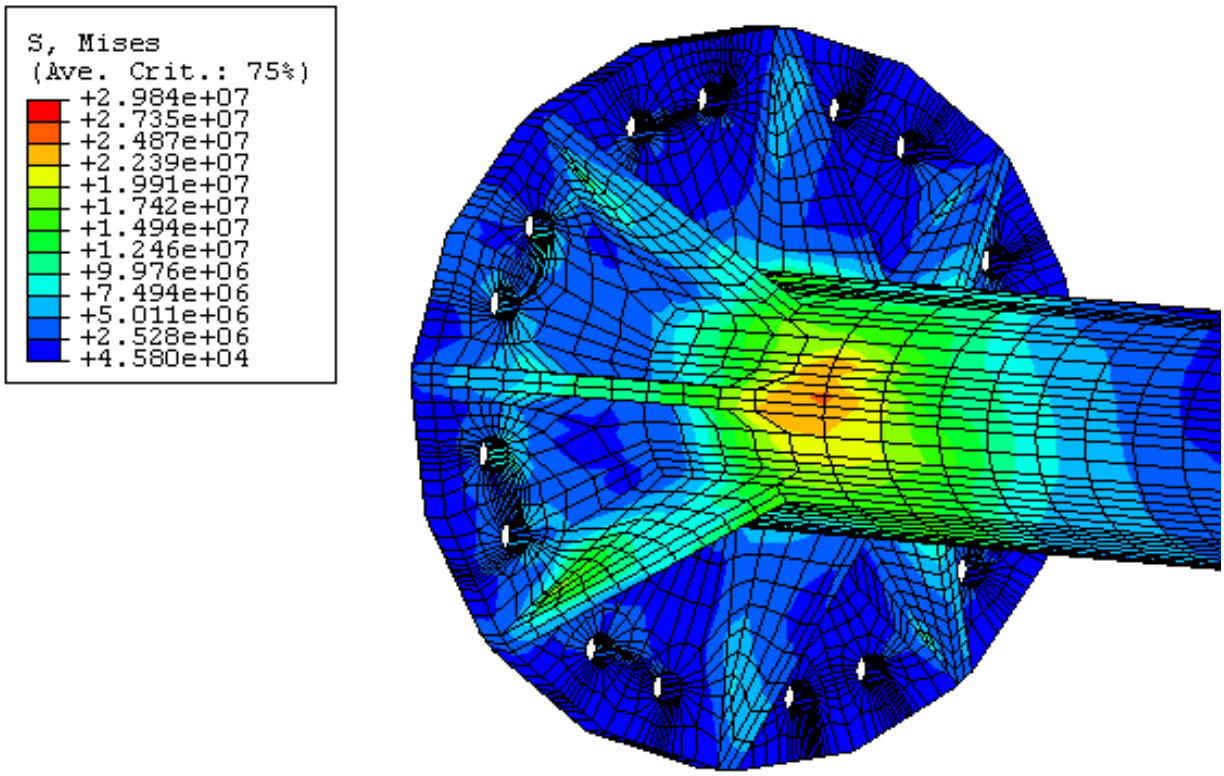

Figure Q.17: Stress within the Shaft Connection

compression forces are taken up by constraining the surface under the rear bearing mount in the axial direction.

Figure Q.17 shows the stress contained within the shaft connection. The highest stress is located where the front bearing supports the shaft. The solution there is based on a coarse mesh that will have high error. The results here should be ignored, a separate FEM model was built to get an accurate solution in this region. Within the flanges and the connection plate the maximum Von-Mises stress is 22 MPa at a small region, overall the stress is fairly low. The maximum is slightly greater than the maximum acceptable stress, however it is close enough that there should be no serious concerns.

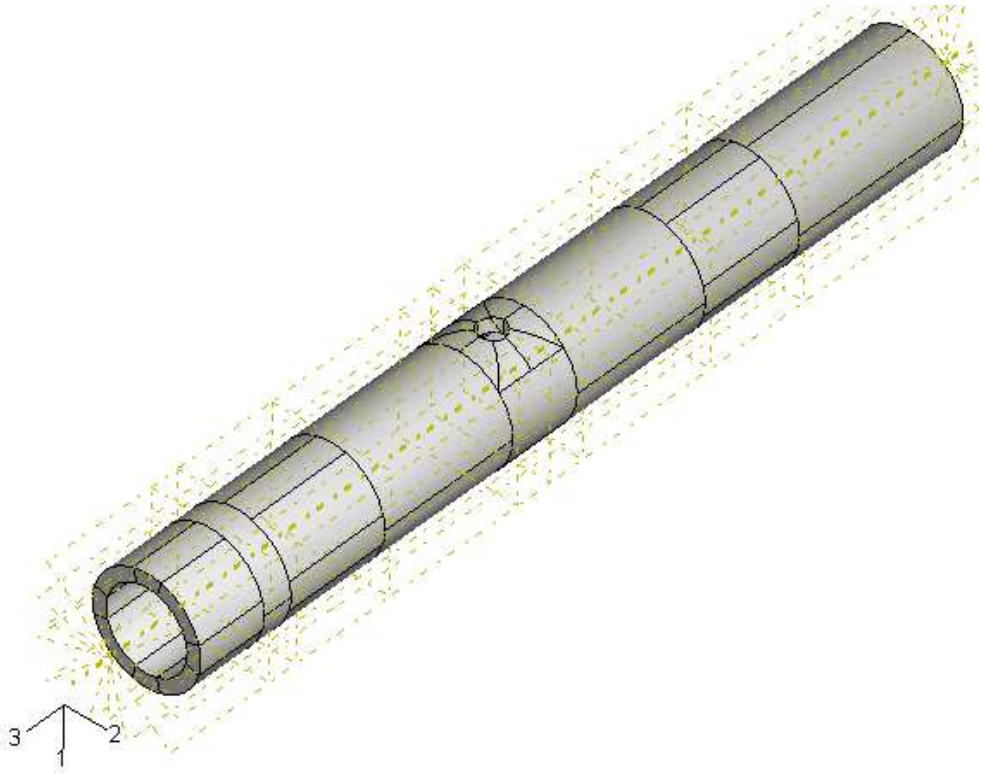

Figure Q.18: Geometry of the Simple Shaft FEM Model

Q.8 Structural Analysis of Shaft with a Hole

The purpose of this analysis is to determine the stress on the shaft. The license does not allow for the analysis of an effective mesh with all the flanges and mounting plate. These components were ignored to look at the stress in the shaft about the bearings, sprocket and the hole. Figure Q.18 shows the model used for the analysis. Several regions are shown in figure Q.18, the cylindrical region closer to the axis marker is where the sprocket is mounted. There is a small space between the next region where the rear bearing is mounted. A long space containing the hole separates the region for the front bearing from the rear bearing mount. The end furthest from the axis marker is where the forces are applied.

Point	Axis 1 [mm]	Axis 2 [mm]
1	0.000	-28.575
2	0.000	-38.100
3	28.575	0.000
4	38.100	0.000
5	0.000	28.575
6	0.000	38.100
7	-28.575	0.000
8	-38.100	0.000

Table Q.23: Location of Loading Points in Simple Shaft Analysis

The material for the shaft is steel, the assumed properties of steel used in the model are given in table Q.1.

The shaft is axis-symmetric with the exception of the hole on the side. Thus two load cases were considered for this analysis, one where the hole is pointing up, the second where the hole is pointing up.

The shaft is rotating and experiences gravitational loading. Additional loads are applied from the hub, rotor and the components therein. The rotor would be producing a thrust and a torque. The weight of all the components would add a shear force and a bending moment to the end of the shaft. The assumed mass and moment arms of all the components being supported by the shaft are given in table Q.15. The datum for the moment arm is the end of the shaft where the loads are to be applied. The resulting forces from all the components are given in table Q.16.

The loads in table Q.16 were applied at 8 points, the coordinates for those 8 points in the 1 2 plane are given in table Q.23. The loads at each point for each load case is given in table Q.24. Both gravitation load and centripetal acceleration is applied, the details are given in table Q.25.

The boundary conditions for both load cases was the same. To resist all forces except thrust and torsion the bearing regions were constrained in direction perpendicular to the surface. To resist torque the appropriate sides of the sprocket region were constrained in

Load Case	Hole Top			Hole Bottom		
Component	1 [N]	2 [N]	3 [N]	1 [N]	2 [N]	3 [N]
Point 1	-315.012	0.000	128.728	-601.472	0.000	128.728
Point 2	-406.661	0.000	128.728	-693.120	0.000	128.728
Point 3	143.230	-458.242	3477.430	-143.230	-458.242	-3219.700
Point 4	143.230	-549.890	4147.150	-143.230	-549.890	-3889.700
Point 5	601.472	0.000	128.728	315.012	0.000	128.728
Point 6	693.120	0.000	128.728	406.661	0.000	128.728
Point 7	143.230	458.242	-3219.960	-143.230	458.890	3477.420
Point 8	143.230	549.890	-3889.700	-143.230	459.890	4147.150

Table Q.24: Point Loads in the Simple Shaft Analysis

Load Case	Hole Top			Hole Bottom		
Component	1	2	3	1	2	3
Gravity $[m/s]$	9.810	0.000	0.000	-9.810	0.000	0.000
Rotation $[rad/s]$	0.000	0.000	33.450	0.000	0.000	33.450

Table Q.25: Additional Loads Applied in the Simple Shaft Analysis

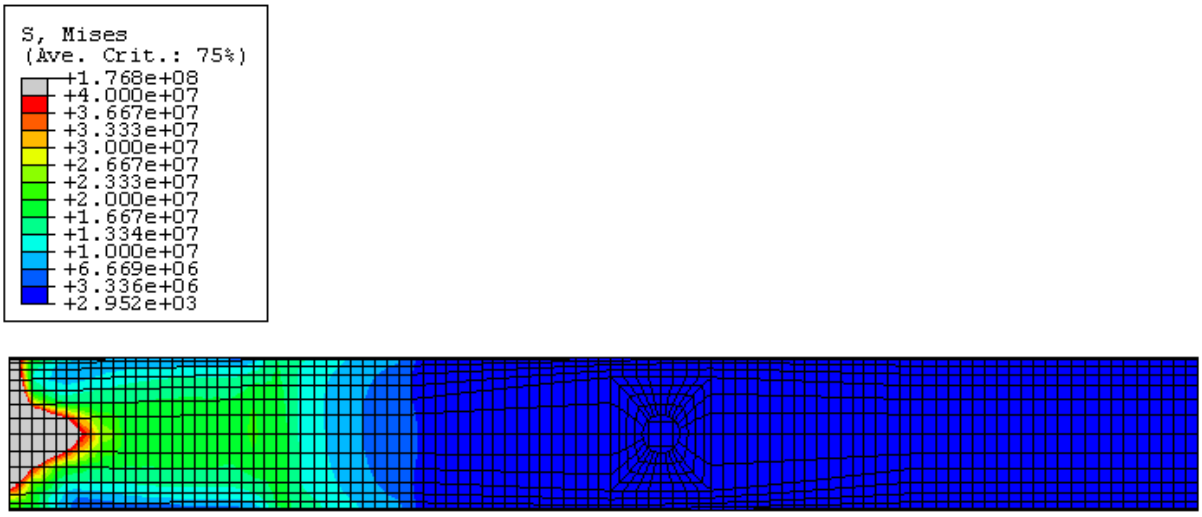

Figure Q.19: Simple Shaft Stress in Hole Top Load Case

direction tangent to the surface. The second bearing is meant to resist compression forces so the entire region there is constrained axially.

Originally the model was analyzed with a wall thickness of 6.35mm. It was found that stress in the first bearing region was too high. Increasing the thickness to 9.525mm brought the stress down to more reasonable level. The model was tested with different hole diameters with different placements along the shaft. Placing a 19.05mm diameter hole mid span between the two bearings would accommodate all the wires to the rotating domain and any slip rings and brake systems on the shaft. The results of this instance would best reflect the stress in the final part.

Figures Q.19 and Q.20 show the Von-Mises stress results in the model. The majority of stress in the shaft occurs near the bearings. Very little stress is present near the holes. The results show a large stress near where the loads are applied. This is not physical, the actual part has several flanges to reinforce this region. FEM modeling was applied to this reinforced region and the results of that model showed acceptable stress levels. Overall the stress is acceptable.

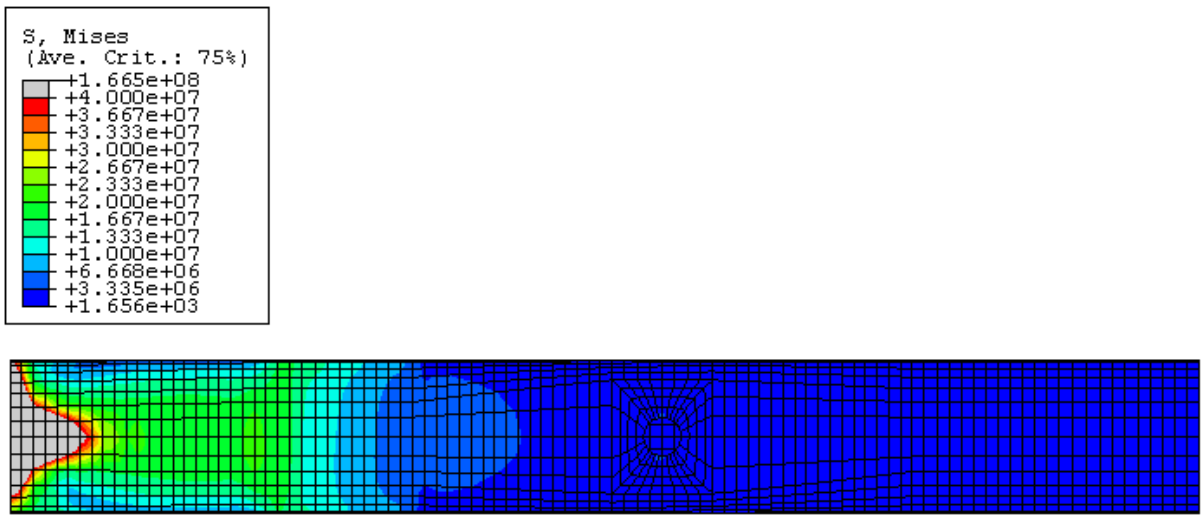

Figure Q.20: Simple Shaft Stress in Hole Bottom Load Case

Bibliography

[1] K. Abe, M. Nishida, A. Sakurai, Y. Ohya, H. Kihara, E. Wada, and K. Sato. Experimental and numerical investigations of flow fields behind a small wind turbine with a flanged diffuser. *Journal of Wind Engineering and Industrial Aerodynamics*, 93:951–970, 2005.

[2] Fabiano Daher Adegas, Gustavo de Marsillac Pena, Jorge Antonio Villar Ale, and Gabriel Sirilo Simioni. Power curve of small wind turbine generators - laboratory and field testing. In *RIO 3 - World Climate & Energy Event, 1-5 December 2003, Rio de Janeiro, Brazil*, 2003.

[3] X. Amandolese and E. Szechenyi. Experimental study of the effect of turbulence on a section model blade oscillating in stall. *Wind Energy*, 7:267–282, 2004.

[4] M. J. Barnsley and J. F. Wellicome. Wind tunnel investigation of stall aerodynamics for a 1.0 m horizontal axis rotor. *Journal of Wind Engineering and Industrial Aerodynamics*, 39:11–21, 1992.

[5] Rebecca Barthelmie, Ole Frost Hansen, Karen Enevoldsen, Jorgen Hojstrup, Sten Frandsen, Sara Pryor, Soren Larsen, Maurizio Motta, and Peter Sanderhoff. Ten years of meteorological measurements for offshore wind farms. *Journal of Solar Energy Engineering*, 127:170–176, 2005.

[6] F. Bet and H. Grassmann. Upgrading conventional wind turbines. *Renewable Energy*, 28:71–78, 2003.

[7] Ben F. Blackwell, Robert E. Sheldahl, and Louis V. Feltz. Wind tunnel performance data for two- and three-bucket savonius rotors. Technical report, Sandia Laboratories, 1977. SAND76-0131.

[8] Hugo Brouwer, Uwe Schroeder-Selbach, Jean-Claude Hulot, Demus King, Cristobal Burgos, Jun Arima, and Jonathan Coony. *Energy Policies of IEA Countries Denmark*. International Energy Agency, Paris, France, 2006.

[9] Tony Burton, David Sharpe, Nick Jenkins, and Ervin Bossanyi. *Wind Energy Handbook*. John Wiley and Sons, Chichester, England, 2001.

[10] Ken Chaney, Alfred J. Eggers Jr., Patrick J. Moriarty, and William E. Holley. Skewed wake induction effects on thrust distribution on small wind turbine rotors. *Journal of Solar Energy Engineering*, 123:290–295, 2001.

[11] Curran Crawford. Re-examining the precepts of the blade element momentum theory for coning rotors. *Wind Energy*, 9:457–478, 2006.

[12] Svend de Bruyn. Performance evaluation of southwest wind power air x wind turbine. Technical report, Detronics Limited, 2005. File 5221.

[13] Zhaohui Du and M. S. Selig. The effect of rotation on the boundary layer of a wind turbine blade. *Renewable Energy*, 20:167–181, 2000.

[14] Horia Dumitrescu and Vladimir Cardos. Rotational effects on the boundary-layer flow in wind turbines. *AIAA Journal*, 42(2):408–410, 2003.

[15] P. R. Ebert and D. H. Wood. The near wake of a model horizontal-axis wind turbine - i. experimental arrangements and initial results. *Renewable Energy*, 12(3):225–243, 1997.

[16] P. R. Ebert and D. H. Wood. Observations of the starting behaviour of a small horizontal-axis wind turbine. *Renewable Energy*, 12(3):245–257, 1997.

[17] P. R. Ebert and D. H. Wood. The near wake of a model horizontal-axis wind turbine at runaway. *Renewable Energy*, 25:41–54, 2002.

[18] Lars E. Ericsson. Revisiting unresolved dynamic stall phenomena. *Journal of Aircraft*, 17(6):1117–1122, 2000.

[19] Bernard Frankovic and Ivan Vrsalovic. New high profitable wind turbines. *Renewable Energy*, 24:491–499, 2001.

[20] Nobuyuki Fujisawa. On the torque mechanism of savonius rotors. *Journal of Wind Engineering and Industrial Aerodynamics*, 40:277–292, 1992.

[21] Nobuyuki Fujisawa. Velocity measurements and numerical calculations of flow fields in and around savonius rotors. *Journal of Wind Engineering and Industrial Aerodynamics*, 59:39–50, 1996.

[22] P. Giguere, M. S. Selig, and J. L. Tangler. Blade design trade-offs using low-lift airfoils for stall-regulated hawts. *Journal of Solar Energy Engineering*, 121:217–223, 1999.

[23] H. Glauert. *The Elements of Aerofoil and Airscrew Theory.* Cambridge University Press, Cambridge, England, 1959.

[24] I. Grant, G. McCutcheon, A. H. McColgan, and D. Hurst. Optical-velocimetry, wake measurements of lift and induced drag on a wing. *Optics and Lasers in Engineering*, 44:282–303, 2006.

[25] I. Grant, M. Mo, X. Pan, P. Parkin, J. Powell, H. Reinecke, K. Shuang, F. Coton, and D. Lee. An experimental and numerical study of the vortex filaments in the wake of an operational, horizontal-axis, wind turbine. *Journal of Wind Engineering and Industrial Aerodynamics*, 85:177–189, 2000.

[26] H. Grassmann, F. Bet, M. Ceschia, and M. L. Ganis. On the physics of partially static turbines. *Renewable Energy*, 29:491–499, 2003.

[27] Sandeep Gupta and J. Gordon Leishman. Dynamic stall modelling of the s809 aerofoil and comparison with experiments. *Wind Energy*, 9:521–547, 2006.

[28] Wouter Haans, Tonio Sant, and Gijs Van Kuik Gerard van Bussel. Stall in yawed flow conditions: A correlation of blade element momentum predictions with experiments. *Journal of Solar Energy Engineering*, 128:472–480, 2006.

[29] Wouter Haans, Tonio Sant, Gijs van Kuik, and Gerard van Bussel. Measurement of tip vortex paths in the wake of a hawt under yawed flow conditions. *Journal of Solar Energy Engineering*, 127:456–463, 2005.

[30] M. M. Hand, D. A. Simms, L. J. Fingersh, D. W. Jager, J. R. Cotrell, S. Schreck, and S. M. Larwood. Unsteady aerodynamics experiment phase vi: Wind tunnel test configurations and available data campaigns. Technical report, National Renewable Energy Laboratories, 1617 Cole Boulevard, Golden, Colorado, United States of America, 2001. NREL/TP-500-29955.

[31] Anca D. Hansen and Lars H. Hansen. Wind turbine concept market penetration over 10 years (1995-2004). *Wind Energy*, 10:81–97, 2007.

[32] M. H. Hansen. Improved modal dynamics of wind turbines to avoid stall-induced vibrations. *Wind Energy*, 6:179–195, 2003.

[33] M. O. L. Hansen, N. N. Sorensen, and R. G. J. Flay. Effect of placing a diffuser around a wind turbine. *Wind Energy*, 3:207–213, 2000.

[34] Martin O. L. Hansen. *Aerodynamics of Wind Turbines*. James & James, London, England, 2000.

[35] Andreas Heege, Jaume Betran, and Yvan Radovcic. Fatigue load computation of wind turbine gearboxes by coupled finite element, multi-body system and aerodynamic analysis. *Wind Energy*, 10:395–413, 2007.

[36] Pascal Hemon, Domenico Olivari, and Martin Wurmser. Experimental investigation of horizontal axis wind turbine dynamic stall in a wind tunnel. *Journal of Wind Engineering and Industrial Aerodynamics*, 19:73–82, 1992.

[37] Andrew R. Henderson, Colin Morgan, Bernie Smith, Hans C. Sorensen, Rebecca J. Barthelmie, and Bart Boesmans. Offshore wind energy in europe-a review of the state-of-the-art. *Wind Energy*, 6:35–52, 2003.

[38] Danmei Hu, Ouyang Hua, and Zhaohui Du. A study on stall-delay for horizontal axis wind turbine. *Renewable Energy*, 31:821–836, 2006.

[39] Ken ichi Abe and Yuji Ohya. An investigation of flow fields around flanged diffusers using cfd. *Journal of Wind Engineering and Industrial Aerodynamics*, 92:315–330, 2004.

[40] ANSYS Inc. Ansys cfx 10.0 website, September 2008. http://www.ansys.com/products/cfx.asp.

[41] Simulia Inc. Simulia abaqus website, 2008. http://www.simulia.com/products/abaqus_fea.html.

[42] Daniel J. Inman. *Engineering Vibrations, Second Edition.* Prentice-Hall, New York, United States of America, 2001.

[43] Eastman N. Jacobs and Albert Sherman. Airfoil section characteristics as affected by variations of the reynolds number. Technical report, National Advisory Committee for Aeronautics, 1937. NACA Report No. 586.

[44] Clemens Jauch, Poul Sorensen, and Birgitte Bak Jensen. The relevance of the dynamic stall effect for transient fault operations of active-stall wind turbines. *Wind Engineering*, 29(4):353–364, 2005.

[45] Sung Nam Jung, Tae-Soo No, and Ki-Wahn Ryu. Aerodynamic performance prediction of a 30 kw counter-rotating wind turbine system. *Renewable Energy*, 30:631–644, 2005.

[46] Norman Leece. Small wind turbine for built up areas. *REFocus*, September/October:13–13, 2003.

[47] T. Maeda, E. Ismaili, H. Kawabuchi, and Y. Kamada. Surface pressure distribution on a blade of a 10 m diameter hawt (field measurements versus wind tunnel measurements). *Journal of Solar Energy Engineering*, 127:185–191, 2005.

[48] J. F. Manwell, J. G. McGowan, and A. L. Rogers. *Wind Energy Explained, Theory, Design and Application*. John Wiley and Sons, Chichester, England, 2002.

[49] Toshio Matsushima, Shinya Takagi, and Seiichi Muroyama. Characteristics of a highly efficient propeller type small wind turbine with a diffuser. *Renewable Energy*, 31:1343–1354, 2006.

[50] C. Mayer, M. E. Bechly, M. Hampsey, and D. H. Wood. The starting behaviour of a small horizontal-axis wind turbine. *Renewable Energy*, 22:411–417, 2001.

[51] Michael McWilliam and David A. Johnson. Velocimetry measurement of flow around model vertical axis wind turbines. *International Journal of Green Energy*, 5:55–68, 2008.

[52] D. Medici and P. H. Alfredsson. Measurements on a wind turbine wake: 3d effects and bluff body vortex shedding. *Wind Energy*, 9:219–236, 2006.

[53] J.-L. Menet. A double-step savonius rotor for local production of electricity: a design study. *Renewable Energy*, 29:1843–1862, 2004.

[54] Andre L. Amarante Mesquita and Alex S. G. Alves. An improved approach for performance prediction of hawt using the strip theory. *Wind Engineering*, 24(6):417–430, 2000.

[55] V. J. Modi and M. S. U. K. Fernando. Unsteady aerodynamics and wake of the savonius wind turbine: A numerical study. *Journal of Wind Engineering and Industrial Aerodynamics*, 46 & 47:811–816, 1993.

[56] Xabier Munduate, Frank N. Coton, and Roderick A. McD. Galbraith. An investigation of the aerodynamic response of a wind turbine blade to tower shadow. *Journal of Solar Energy Engineering*, 126:1034–1040, 2004.

[57] Yuichi Murai, Taishi Nakada, Takao Suzuki, and Fujio Yamamoto. Particle tracking velocimetry applied to estimate the pressure field around a savonius turbine. *Measurement Science and Technology*, 18:2491–2503, 2007.

[58] T. F. Pedersen. On wind turbine power performance measurements at inclined airflow. *Wind Energy*, 7:163–176, 2004.

[59] D. G. Phillips, R. G. J. Flay, and T. A. Nash. Aerodynamic analysis and monitoring of the vortec 7 diffuser-augmented wind turbine. *IPENZ Transactions*, 26(1):13–19, 1999.

[60] K. Pierce and A. C. Hansen. Prediction of wind turbine rotor loads using the beddoes-leishman model for dynamic stall. *Journal of Solar Energy Engineering*, 117:200–204, 1995.

[61] S. C. Pryor and R. J. Barthelmie. Comparison of potential power production at on- and offshore sites. *Wind Energy*, 4:173–181, 2001.

[62] D. C. Quarton. The evolution of wind turbine design analysis - a twenty year progress review. *Wind Energy*, 1:5–24, 1998.

[63] William H. Rae and Alan Pope. *Low Speed Wind Tunnel Testing*. Wiley, New York, United States of America, 1984.

[64] U. K. Saha and M. Jaya Rajkumar. On the performance analysis of savonius rotor with twisted blades. *Renewable Energy*, 31:1776–1788, 2006.

[65] Ahmet Z. Sahin, Ahmed Z. Al-Garni, and Abdulghani Al-Farayedhi. Analysis of a small horizontal axis wind turbine performance. *International Journal of Energy Research*, 25:501–506, 2001.

[66] Korn Saranyasoontorn, Lance Manuel, and Paul S. Veers. A comparison of standard coherence models for inflow turbulence with estimates from field measurements. *Journal of Solar Energy Engineering*, 126:1069–1082, 2004.

[67] S. J. Savonius. The s-rotor and its applications. *Mechanical Engineering*, 53:333–338, 1931.

[68] J. G. Schepers, A. J. Brand, A. Bruining, J. M. R. Graham, M. M. Hand, D. G. Infield, H. A. Madsen, T. Maeda, J. H. Paynter, R. van Rooij, Y. Shimizu, D. A. Simms, and N. Stefanatos. Final report of iea annex xviii: 'enhanced field rotor aerodynamics database'. Technical report, International Energy Agency, 2002. ECN-C–02-018.

[69] J. G. Schepers and H. Snel. Model experiments in controlled conditions final report. Technical report, The Energy Research Center of the Netherlands (ECN), 1755 ZG Petten, Netherlands, 2007. ECN-E07-042.

[70] S. Schreck and M. Robinson. Rotational augmentation of horizontal axis wind turbine blade aerodynamic response. *Wind Energy*, 5:133–150, 2002.

[71] S. Schreck and M. Robinson. Boundary layer state and flow field structure underlying rotational augmentation of blade aerodynamic response. *Journal of Solar Energy Engineering*, 125:448–456, 2003.

[72] S. Schreck and M. Robinson. Tip speed ratio influences on rotationally augmented boundary layer topology and aerodynamic force generation. *Journal of Solar Energy Engineering*, 126:1025–1033, 2004.

[73] S. Schreck and M. Robinson. Blade three-dimensional dynamic stall response to wind turbine operating condition. *Journal of Solar Energy Engineering*, 127:488–495, 2005.

[74] S. J. Schreck, Niels N. Sorensen, and Michael C. Robinson. Aerodynamic structures and processes in rotationally augmented flow fields. *Wind Energy*, 10:159–178, 2007.

[75] Scott Schreck. The nrel full-scale wind tunnel experiment. *Wind Energy*, 5:77–84, 2002.

[76] Scott J. Schreck, William E. Faller, and Hank E. Helin. Pitch rate and reynolds number effects on unsteady boundary-layer transition and seperation. *Journal of Aircraft*, 35(1):46–52, 1998.

[77] Scott J. Schreck and Michael C. Robinson. Horizonal axis wind turbine blade aerodynamics in experiments and modeling. *IEEE Transactions on Energy Conversion*, 22(1):61–70, 2004.

[78] Scott J. Schreck, Michael C. Robinson, M. Maureen Hand, and David A. Simms. Blade dynamic stall vortex kinematics for a horizontal axis wind turbine in yawed conditions. *Journal of Solar Energy Engineering*, 123:272–281, 2001.

[79] K. K. Sharma, R. Gupta, S. K. Singh, and S. R. Singh. Experimental investigation of the characteristics of a savonius wind turbine. *Wind Engineering*, 29:77–82, 2005.

[80] Y. Shimizu, H. Imamura, S. Matsumura, T. Maeda, and G. J. W. van Bussel. Power augmentation of a horizontal axis turbine using a mie type tip vane: Velocity distribution around the tip of a hawt blade with and without a mie type tip vane. *Journal of Solar Energy Engineering*, 117:297–303, 1995.

[81] Y. Shimizu, E. Ismaili, Y. Kamada, and T. Maeda. Rotor configuration effects on the performance of a hawt with tip-mounted mie-type vanes. *Journal of Solar Energy Engineering*, 125:441–447, 2003.

[82] Christophe Sicot, Philippe Devinant, Thomas Laverne, Stephane Loyer, and Jacques Hureau. Experimental study of the effect of turbulence on horizontal axis wind turbine aerodynamics. *Wind Energy*, 9:361–370, 2006.

[83] D. Simms, M. Hand, L. J. Fingersh, and D. W. Jager. Unsteady aerodynamics experiment phases iiiv test configurations and available data campaigns. Technical report, National Renewable Energy Laboratories, 1617 Cole Boulevard, Golden, Colorado, United States of America, 1999. NREL/TP-500-25950.

[84] D. Simms, M. Hand, L. J. Fingersh, D. W. Jager, and J. R. Cotrell. Unsteady aerodynamics experiment phase v: Test configuration and available data campaigns. Technical report, National Renewable Energy Laboratories, 1617 Cole Boulevard, Golden, Colorado, United States of America, 2001. NREL/TP-500-29491.

[85] H. Snel. Review of the present status of rotor aerodynamics. *Wind Energy*, 1:46–69, 1998.

[86] H. Snel, J. G. Schepers, and B. Montgomeric. The mexico project (model experiments in controlled conditions): The database and first results of data processing and interpretation. *Journal of Physics: Conference Series*, 75:1–11, 2007.

[87] Herman Snel. Review of aerodynamics for wind turbines. *Wind Energy*, 6:203–211, 2003.

[88] N. N. Sorensen, J. A. Michelsen, and S. Schreck. Navier-stokes predictions of the nrel phase vi rotor in the nasa ames 80 ft x 120 ft wind tunnel. *Wind Energy*, 5:151–169, 2002.

[89] David A. Spera. *Wind Turbine Technology*. American Society of Mechanical Engineers, New York, United States of America, 1994.

[90] Bryan Sperandei. The application of particle image velocimetry in a small scale wind tunnel. Master's thesis, University of Waterloo, 200 University Ave West, Waterloo Ontario Canada, 2002.

[91] Nicholas Stern. *The Economics of Climate Change*. Cambridge University Press, Cambridge, England, 2007.

[92] James L. Tangler. The evolution of rotor and blade design. In *American Wind Energy Association WindPower 2000, Palm Springs, California April 30-May 4, 2000*, 2000.

[93] James L. Tangler. The nebulous art of using windtunnel airfoil data for predicting rotor performance. *Wind Energy*, 5:245–257, 2002.

[94] James L. Tangler. Insight into wind turbine stall and post-stall aerodynamics. *Wind Energy*, 7:247–260, 2004.

[95] James L. Tangler and Michael S. Selig. An evaluation of an empirical model for stall delay due to rotation for hawts. In *WINDPOWER '97 Conference Austin, Texas, June 15-18, 1997*, 1997.

[96] Sven-Erik Thor and Patricia Weis-Taylor. Long-term research and development needs for wind energy for the time frame 2000-2020. *Wind Energy*, 5:73–75, 2002.

[97] Chanin Tongchitpakdee, Sarun Benjanirat, and Lakshmi N. Sankar. Numerical simulation of the aerodynamics of horizontal axis wind turbines under yawed flow conditions. *Journal of Solar Energy Engineering*, 127:464–474, 2005.

[98] M. F. Unal, J.-C. Lin, and D. Rockwell. Force prediction by piv imaging: A momentum-based approach. *Journal of Fluids and Structures*, 11:965–971, 1997.

[99] Izumi Ushiyama, Toshihiko Shimota, and Yukihiro Miura. An experimental study of the two-staged wind turbines. *Renewable Energy*, 9(1-4):909–912, 1996.

[100] B. W. van Oudheusden, F. Scarano, and E. W. F. Casimiri. Non-intrusive load characterization of an airfoil using piv. *Experiments in Fluids*, 40(6):988–992, 2006.

[101] B. W. van Oudheusden, F. Scarano, E. W. M. Roosenboom, E. W. F. Casimiri, and L. J. Souverein. Evaluation of integral forces and pressure fields from planar velocimetry data for incompressible and compressible flowsr. *Experiments in Fluids*, 43(2 & 3):153–162, 2007.

[102] L. J. Vermeer, J. N. Sorensen, and A. Crespo. Wind turbine wake aerodynamics. *Progress in Aerospace Sciences*, 39:467–510, 2003.

[103] Tongguang Wang and Frank N. Coton. Numerical simulation of wind tunnel wall effects on wind turbine flows. *Wind Energy*, 3:134–148, 2000.

[104] Jennifer Weisinger. Characterization of the university of waterloo live fire research facitlity wind generation system. Master's thesis, University of Waterloo, 200 University Ave West, Waterloo Ontario Canada, 2004.

[105] J Westerweel. Fundamentals of digital particle image velocimetry. *Measurement Science and Technology*, 8:1379–1392, 1997.

[106] J. Whale, C. G. Anderson, R. Bareiss, and S. Wagner. An experimental and numerical study of the vortex structure in the wake of a wind turbine. *Journal of Wind Engineering and Industrial Aerodynamics*, 84:1–21, 2000.

[107] Frank M. White. *Fluid Mechanics 5th Edition*. McGraw Hill Higher Education, New York, United States of America, 2003.

[108] A. K. Wright and D. H. Wood. The starting and low wind speed behaviour of a small horizontal axis wind turbine. *Journal of Wind Engineering and Industrial Aerodynamics*, 92:1265–1279, 2004.

[109] A. Yeznasni, R. Derdelinckx, and Ch. Hirsch. Influence of dynamic stall in the aerodynamic study of hawts. *Journal of Wind Engineering and Industrial Aerodynamics*, 39:187–198, 1992.

[110] Arthouros Zervos and Steve Sawyer. Global wind 2006 report. *Global Wind Energy Council*, 2007.